Order of Magnitude Improved Limit on the Electric Dipole Moment of the Electron

Order of magnitude improved limit on the electric dipole moment of the electron

A DISSERTATION PRESENTED
BY
CRISTIAN DANIEL PANDA
TO
THE DEPARTMENT OF PHYSICS

IN PARTIAL FULFILLMENT OF THE REQUIREMENTS
FOR THE DEGREE OF
DOCTOR OF PHILOSOPHY
IN THE SUBJECT OF
PHYSICS

HARVARD UNIVERSITY
CAMBRIDGE, MASSACHUSETTS
NOVEMBER 2018

Order of magnitude improved limit on the electric dipole moment of the electron

Abstract

The Standard Model of particle physics accurately describes with amazing precision all particle physics measurements made in the laboratory. However, it is unable to answer many central questions that arise from cosmological observations, such as the nature of dark matter and why matter dominates over antimatter throughout the Universe. Theories containing particles and interactions beyond the standard model, such as models incorporating supersymmetry, may explain these phenomena. Such particles can come into virtual existence in the vacuum and then interact with real particles to modify their properties. For example, the existence of very massive particles whose interactions violate time-reversal symmetry, as needed to explain the cosmological matter–antimatter asymmetry, gives rise to an electric dipole moment along the spin axis of the electron. To date no electric dipole moments (EDM), of the electron or other fundamental particles, have been observed. However, dipole moments only slightly smaller than current bounds can arise from new particles more massive than any known to exist. Here we present a new measurement of the electron's electric dipole moment (eEDM), $d_e = (4.3 \pm 3.1_{\mathrm{stat}} \pm 2.6_{\mathrm{syst}}) \times 10^{-30}\ e \cdot \mathrm{cm}$, obtained by measuring the spin precession of electrons subjected to the huge intramolecular electric field accessible in the thorium monoxide molecule. The sensitivity of our measurement is one order of magnitude better than any previous work and probes for the existence of new particles with mass far beyond the direct reach of the Large Hadron Collider. Since our measurement is consistent with zero, we report an upper limit of $|d_e| < 1.1 \times 10^{-29}\ e \cdot \mathrm{cm}$, which sets very strong constraints on a wide range of theories that predict new physics at energy scales directly accessible to colliders.

Contents

Papers and Publications

1. "Order of magnitude smaller limit on the electric dipole moment of the electron"
   The ACME Collaboration: J. Baron, W. C. Campbell, D. DeMille, J. M. Doyle, G. Gabrielse, Y. V. Gurevich, P. W. Hess, N. R. Hutzler, E. Kirilov, I. Kozyryev, B. R. O'Leary, C. D. Panda, M. F. Parsons, E. S. Petrik, B. Spaun, A. C. Vutha, A. D. West, *Science* **343**, p. 269-272 (2014).

2. "Improved limit on the electric dipole moment of the electron"
   The ACME Collaboration: V. Andreev, D. G. Ang, D. DeMille, J. M. Doyle, G. Gabrielse, J. Haefner, N. R. Hutzler, Z. Lasner, C. Meisenhelder, B. R. O'Leary, C. D. Panda, A. D. West, E. P. West & X. Wu, *Nature* **562**, 355-360 (2018).

3. "Stimulated Raman adiabatic passage preparation of a coherent superposition of ThO $H^3\Delta_1$ states for an improved electron electric-dipole-moment measurement"
   C. D. Panda, B. R. O'Leary, A. D. West, J. Baron, P. W. Hess, C. Hoffman, E. Kirilov, C. B. Overstreet, E. P. West, D. DeMille, J. M. Doyle, and G. Gabrielse, *Phys. Rev. A* **93**, 052110 (2016).

4. " Methods, analysis, and the treatment of systematic errors for the electron electric dipole moment search in Thorium Monoxide"
   The ACME Collaboration: J. Baron, W. C. Campbell, D. DeMille, J. M. Doyle, G. Gabrielse, Y. V. Gurevich, P. W. Hess, N. R. Hutzler, E. Kirilov, I. Kozyryev, B. R. O'Leary, C. D. Panda, M. F. Parsons, E. P. West, B. Spaun, A. C. Vutha, A. D. West, *New Journal of Physics* **19**, 073029 (2017).

5. "An underappreciated radiation hazard from high voltage electrodes in vacuum"
   A. D. West, Z. Lasner, D. DeMille, E. P. West, C. D. Panda, J. M. Doyle, G. Gabrielse, A. Kryskow, C. Mitchell, *Health Physics* **112(1)**, 33-41 (2017).

6. "A self-calibrating polarimeter to measure Stokes parameters"
   V. Andreev, C. D. Panda, P. W. Hess, B. Spaun, G. Gabrielse, *ArXiv 1703.00963* (2018).

7. "Suppression of excess noise in the ACME II measurement of the electron electric dipole moment to below the shot-noise-limit" (in preparation) (2018).

List of Figures

List of Tables

Acknowledgments

It was great fun to complete this new measurement of the eEDM along a number of amazing professors, postdocs, and graduate and undergraduate students as part of the ACME Collaboration. Thanks go to my advisor Jerry Gabrielse for his tireless enthusiasm about fundamental physics research and for support throughout my PhD years. Dave DeMille and John Doyle, the other two ACME PIs, provided the advice and stability that kept the collaboration going through good and bad times. Acknowledgments go to Markus Greiner and Matt Reece, my committee members, for giving advice, both scientific and professional, along the way.

I am grateful to: Daniel Ang, Jonathan Haefner, Zack Lasner, Cole Meisenhelder and Xing Wu, for being there as we pushed the ACME II measurement across the finish line; Adam West, Paul Hess and Ben Spaun for teaching me how to align a fiber couple when I first started; Elizabeth West, Brendon O'Leary for doing tireless work on finishing ACME I and setting up ACME II. Also thanks to everyone else that joined the group for long or short and helped with parts of this complicated experiment, including Vitaly Andreev, Jacob Baron, Chris Overstreet and many others.

I am grateful to the entire Gabrielse Group for their support and advice, and for sharing in the experience of doing amazing work on some of the most complex experiments out there. Also thank you for being both friends and colleagues at the same time.

The Physics Department administration and technical staff provided much needed sup-

port. Jan Ragusa, Pattee McGarry, Silke Exner, Lisa Cacciabaudo and many others seamlessly helped us disentangle much of the paperwork needed to keep research going. Stan Cotreau and Steve Sansone taught me how to make amazing parts out of cut metal and sometimes made them for us. Jim McArthur designed custom magic electronic circuits that still worked more reliably than commercial ones.

I would like to thank friends in the Physics departments, including the incoming class of 2012, for fun times doing problem sets and getting through the good and bad of graduate school together. Thanks to the Doyle and DeMille groups for good chats and always being available to share their expertise.

I am grateful to my family, for supporting me in everything I do and for their sacrifices and to Mischka for her encouragements and for always being there for me. Thank you.

Science is made up of so many things that appear obvious after they are explained.

Pardot Kynes, *Dune* by Frank Herbert

1

Introduction to the electron EDM

The last century has seen a great expansion in our understanding of the properties and interactions of elementary particles, made possible by remarkable technological advances. At the Large Hadron Collider (LHC), protons are accelerated to relativistic speeds and collide with each other with immense energy. These collisions produce massive particles that can be either detected directly or inferred from their decay products.

We can open another window into the physics of elementary particles by measuring their properties with exquisite precision. Even when isolated in a vacuum at large distances

from any other particles, fundamental particles interact with quantum fields associated with every other type of elementary particles. These interactions produce minute changes in the properties of the measured particle. Such properties can typically be investigated with high precision for particles that are commonly available in the laboratory, for example the electrons in an atom or molecule. Properties of electrons in atoms and molecules are probed using electromagnetic fields with robust techniques that have been perfected over the last one hundred years.

High precision measurements of the properties of common particles allow us to look into the nature of new particles and interactions that might be difficult to produce directly at particle colliders. One example highlighting the success of this approach in testing our theory of particle physics, the Standard Model, is in the measurement of the electron's magnetic moment [1]. Here, precise measurements [1–3] and careful quantum field theory calculations [4] have been able to test and verify our understanding of the theory of particle physics with greater than ten decimal digits of fractional precision.

The electric dipole moment (EDM) of a fundamental particle is an asymmetric charge distribution along the particle's spin [5–8]. The existence of an EDM requires violation of the time-reversal symmetry (T-symmetry) (see discussion in Section 1.1). The Standard Model of particle physics predicts that the electron has such an EDM (eEDM), but with a magnitude far below current experimental sensitivities [5–9]. However, theories of physics beyond the Standard Model generally include new particles and interactions that can break T-symmetry [10–16]. If these new particles have masses of 1-100 TeV, theories typically predict that $d_e \sim 10^{-27} - 10^{-30}$ e cm (in S. I. units, 1 e cm$= 1.6 \times 10^{-21}$ C m) - orders of magnitude larger than the Standard Model predictions and now accessible by experiment.

The electric dipole moment, $\vec{d_e}$, in an electric field, $\vec{\mathcal{E}}$, leads to an interaction energy $U = -\vec{d_e} \cdot \vec{\mathcal{E}}$. Experiments typically measure d_e by observing the energy shift U, which is correlated with a reversal of the direction of the electric field experienced by the electron. Atoms and molecules with large nuclei prove to be good systems for the measurement of d_e.

In these species, the electrons can experience relativistic enhancement in the magnitude of the electric field, which can be a million times larger than that which can be applied in a laboratory (see Section 1.3).

1.1 Symmetries in physics

Symmetries are at the basis of modern physical theories and guide our understanding of physical phenomena. The interactions of particle physics are described by three fundamental near-symmetries: charge inversion (C), parity inversion (P), and time reversal (T). They are described by:

- C-symmetry: a universe where every particle is replaced by its antiparticle.
- P-symmetry: a universe where all three spatial coordinates are mirrored $(x, y, z) \rightarrow (-x, -y, -z)$.
- T-symmetry: a universe where the direction of time is reversed.

Time symmetry deserves a word, since it seems to counter-intuitively conflict with the idea prevalent in statistical mechanics, where the universe evolves along an "arrow of time" due to increasing entropy. Therefore, evolving time backwards from the current state would create a lower entropy state in the future. However, the Standard Model describes local and not global properties. Since there is no Standard Model prediction that physical systems should tend towards higher entropy, it would simply be the case of a redefinition of what past and future mean in these two universes, with no need to redefine of the microscopic physical laws that apply [17].

We refer to C, P, T as being "near-symmetries" because all of them have been measured to be broken in various physical systems. P symmetry was the first to be observed as broken, with the measurements of $\beta-$decay of the ^{60}Co nucleus [18]. Later, C, CP, and more recently T violation were measured [19–21]. However, the combined CPT symmetry

is believed to be an exact symmetry of nature at a fundamental level and is therefore at the foundation of many current quantum field theories. In addition, CPT symmetry holds for all physical phenomena where Lorentz invariance is preserved [22]. Lorentz symmetry has been tested in a large number of systems without any proof of its breaking [23].

1.1.1 EDM and matter-antimatter asymmetry

Let's consider a fundamental particle, such as the electron, which possesses both a spin, $\vec{s}$, and an EDM, $\vec{d_e}$. Since $\vec{d_e}$ is a vector quantity, it must be aligned with the only other vector quantity available, the spin, $\vec{d_e} \parallel \vec{s}$ (a consequence of the Wigner-Eckart theorem). Performing a P transformation reverses the direction of $\vec{d_e}$, since the dipole arises from a spatial distribution, but not $\vec{s}$ (see Fig. 1.1.1). In contrast, performing a T transformation reverses the direction of $\vec{s}$, which is an angular momentum, and leaves $\vec{d_e}$ unchanged. Therefore, either applying P or T results in a different type of electron, in which the $\vec{d_e}$ and $\vec{s}$ are anti-aligned (Fig. 1.1.1). Such a particle has not been discovered, as all physics measurements point towards all electrons being the same. For example, atomic spectra teaches us that electrons are indistinguishable from each other. Furthermore, only two electrons can occupy the same atomic s orbital, which is consistent with the spin being the electron's only internal degree of freedom ($+1/2$ or $-1/2$).

If CPT is a good symmetry, as suggested by experimental data [23], violation of T symmetry is equivalent to violation of CP symmetry. The breaking of CP symmetry brings us to another asymmetry of our universe: the fact that our universe is made out of matter instead of anti-matter, commonly referred to as the "baryon asymmetry" of the universe (BAU). The lack of anti-matter in our universe is supported by the lack of gamma radiation that would be common due to annihilation between matter and anti-matter.

A mechanism that can account for the abundance of matter in the universe was first described by Andrei Sakharov [24]. Violation of CP symmetry is one of the components

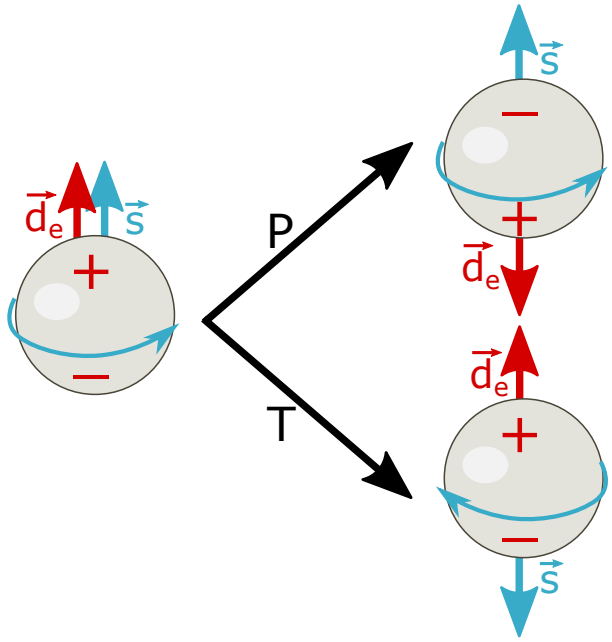

Figure 1.1.1: **The electron before and after applying P and T transformations.** P reverses the electron EDM, $\vec{d}_e$, while the spin $\vec{s}$ is invariant. T reverses $\vec{s}$, while $\vec{d}_e$ is invariant. The particles that result after either P or T transformations are distinguishable from the original, in contradiction with observation of electrons in nature. Therefore, a particle with a non-zero EDM has a preferred parity (P) configuration or time (T) direction.

of this mechanism. Some amount of CP violation is already accounted as part of the Standard Model through the Cabibbo-Kobayashi-Maskawa ("CKM") mechanism in the kaon system [25, 26]. However, the amount of CP violation present in the Standard Model at the moment is too small to explain the amount of BAU present in our universe [27]. It is therefore believed that additional sources of CP violation beyond the Standard Model should be present. EDMs, which are intrinsically T and CP violating, are probes into that new physics.

1.2 The electron EDM and Beyond the Standard Model physics

The predicted Standard Model value of the eEDM is many order of magnitudes smaller than current experimental limits, at $d_e < 10^{-38}$ e cm [7, 8]. This is because the CKM

matrix contribution resides in the quark sector and is heavily suppressed, with the highest order contributions requiring four-loop diagrams [28].

However, nearly every extension to the Standard Model [12–14] introduces the possibility for new particles and new T-violating phases, ϕ_{T}, that can lead to measurably large eEDMs. Within typical extensions to the Standard Model, an eEDM arising from new particles with rest-mass energy Λ in an n-loop Feynman diagram will have size [16, 28, 29]

$$\frac{d_e}{e} \sim \kappa \left(\frac{\alpha_{\mathrm{eff}}}{2\pi}\right)^n \left(\frac{m_e c^2}{\Lambda^2}\right) \sin(\phi_{\mathrm{T}})(\hbar c), \tag{1.1}$$

where α_{eff} (4/137 for electroweak interactions) encodes the strength with which the electron couples to new particles, m_e is the electron mass and $\kappa \sim 0.1$ to 1 is a dimensionless prefactor whose value depends on the specific model of new physics. In typical models where 1- or 2-loop diagrams produce d_e, with $\sin(\phi_{\mathrm{T}}) \sim 1$, the size of the eEDM due to T-violating new physics at energy scales $\Lambda \sim 1 - 100$ TeV is in the $10^{-28} - 10^{-30}$ $e \cdot$ cm range [12–16], which is accessible by current experiments. EDM measurements therefore represent low background probes of physics beyond the Standard Model.

1.3 Atomic and molecular EDM experiments

Precision measurements in atomic and molecular systems are sensitive probes of fundamental physics. Searches for the permanent EDM of fundamental particles have been a busy area of research in this field. Different atomic and molecular geometries can enhance the sensitivity of the measured energy shifts to the electron (paramagnetic species) or the nuclei (diamagnetic species) [28]. Measurements of the EDMs of free neutrons [30, 31], electron [5, 6], muon [32] and atomic species, such as mercury [33] or radium [34], are all complimentary tests of physics beyond the Standard Model.

The electron's EDM, $\vec{d_e}$, is a vector quantity that is aligned along the axis of the electron's spin, $\vec{s}$ [28]. In an electric field, $\vec{\mathcal{E}}$, this leads to an interaction Hamiltonian of the unpaired

electron moving non-relativistically:

$$U_{\mathrm{EDM}} = -\vec{d}_e \cdot \vec{\mathcal{E}} \propto \vec{s} \cdot \vec{\mathcal{E}}. \tag{1.2}$$

The energy shift of Eq. 1.2 is measured to quantify the size of the electron EDM.

1.3.1 Sensitivity scaling

From Eq. 1.2, the statistical uncertainty in $\vec{d}_e$ is given by:

$$\delta d_e = \frac{\delta U_{\mathrm{EDM}}}{\mathcal{E}}. \tag{1.3}$$

From the energy-time uncertainty principle, for a single measurement,

$$\delta U_{\mathrm{EDM}} = \frac{\hbar}{2\tau}, \tag{1.4}$$

where τ is the time over which the experiment is performed, called the "coherence time". Repeated measurements decrease the uncertainty even more. For N independent measurements that obey Poisson statistics, the uncertainty scales as $1/\sqrt{N} = 1/\sqrt{\dot{N}T}$, where $\dot{N}$ is the rate of measurements performed per unit time and T is the total integration time. Therefore, for an experiment that is limited by statistical noise ("shot-noise limited"), the statistical uncertainty of δd_e is given by:

$$\delta d_e = \frac{\hbar}{2\mathcal{E}\tau\sqrt{\dot{N}T}}. \tag{1.5}$$

1.3.2 $\mathcal{E}_{\mathrm{eff}}$ in molecules and atoms

Every improvement in the sensitivity to d_e in the last 50 years has been obtained by measuring the energy shifts of unpaired electrons bound in atoms and molecules (Fig. 1.3.1). As noted by Schiff [35], this large sensitivity of neutrals to the electron EDM seems

surprising at a first glance. Since electrons are charged particles, they cannot experience an electric field without being subject to acceleration. Orbiting electrons in neutrals do not experience a net acceleration in an applied electric field. This implies that the time-averaged electric field they experience is zero, $\langle\vec{\mathcal{E}}\rangle = 0$.

However, Schiff noted that this rule breaks down when relativistic effects are considered [35]. Salpeter showed that a neutral species can experience an energy shift, when in an external field, $\mathcal{E}_{\text{ext}}$ [36]. As noted by Sandars later, the energy shift can be much larger than the energy shift of the free electron, $d_e\mathcal{E}_{\text{ext}}$ [37]. The relativistic correction arises from taking into account the relativistic length contraction of the eEDM of the electrons in a neutral species when placed in an electric field,

$$H_{\text{EDM}} = -\vec{d_e}\cdot\vec{\mathcal{E}} + \frac{\gamma}{1+\gamma}\vec{\beta}\cdot\vec{d_e}\vec{\beta}\cdot\vec{\mathcal{E}}, \tag{1.6}$$

where $\vec{\beta} = \vec{v}/c$ and $\gamma = \frac{1}{\sqrt{1-\beta^2}}$ is the Lorentz factor [38].

The first term in Eq. 1.6, which describes the non-relativistic interaction, vanishes by Schiff's theorem. However, in neutral species polarized by external electric fields, electrons travel relativistically near the charged nucleus, so the electron's velocity and electric field are non-uniform in space. These effects are captured by the second term in Eq. 1.6, which is relativistic and results in a non-zero net expectation value of $\langle d_e\vec{\mathcal{E}}\rangle$. We typically group these efects in a factor that we refer to as the "effective electric field", $\mathcal{E}_{\text{eff}}$. The corresponding energy shift due to the EDM is then given by

$$U_{\text{EDM}} = \langle H^{\text{rel}}_{\text{EDM}}\rangle = -\langle\vec{d_e}\rangle\cdot\mathcal{E}_{\text{eff}}. \tag{1.7}$$

In both atoms and molecules, detailed calculations show that $\mathcal{E}_{\text{eff}}$ can be significantly larger in magnitude than the applied external field, $\mathcal{E}$ [39, 40]. The magnitude of $\mathcal{E}_{\text{eff}}$ is especially large for states which are superpositions of odd and even parity wavefunctions. In these states, the valence electron density has a significant gradient near the highly charged

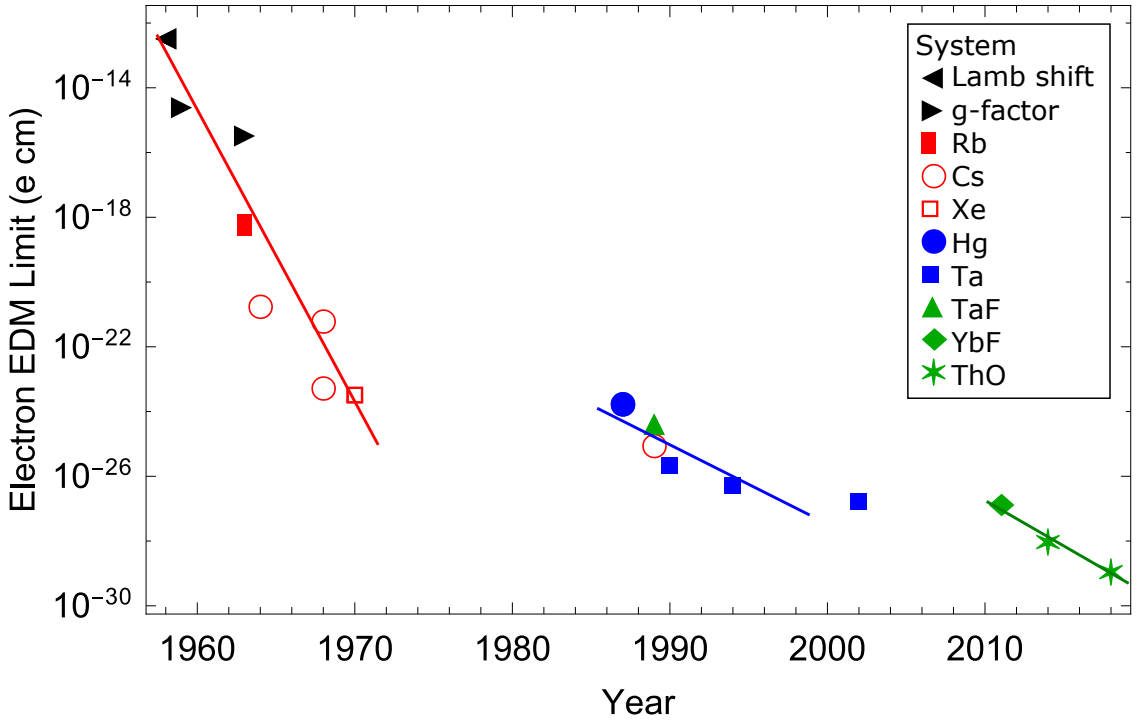

Figure 1.3.1: **Evolution of best eEDM limits (90% confidence) over time, grouped by the species used.** First measurements (black) used measurement of hydrogen Lamb shit and electron magnetic moment to limit the eEDM. Measurements with relatively light atomic species (red) in the 60-70s were followed by heavier species (blue) in the 80-90s, which used the large relativistic enhancement of atoms. Recent experiments with molecules (green) take advantage of the additional degrees of freedom available in molecules to achieve higher polarization factors and set more stringent limits on the magnitude of the eEDM.

nucleus. This corresponds to the atom or molecule being aligned with the external electric field. We quantify the alignment by the degree of electrical polarization, $P_{\mathcal{E}}$.

In addition, species with a nucleus of high atomic number Z have a large overlap between the valence electron wavefunction and the nucleus and therefore enhanced sensitivity to the eEDM [41]. For typical paramagnetic species with valence electrons in σ orbitals [28, 42],

$$\mathcal{E}_{\text{eff}} \propto P_{\mathcal{E}} \cdot Z^3. \tag{1.8}$$

For atomic or molecular systems with large $Z \approx 90$, the effective electric field can be

as large as $\approx$ 100 GV/cm. In practice, atomic polarization is limited by the typically large spacing between opposite parity levels, which limits the attainable polarization to $P_{\mathcal{E}} \sim 10^{-3}$. However, this can still lead to values of $\mathcal{E}_{\text{eff}}$ that are more than three orders of magnitude above that achievable in the laboratory (e. g. $\mathcal{E}_{\text{eff}} \sim 70$ MV/cm for Ta [43]).

Recent experiments use molecules to achieve $P_{\mathcal{E}} \sim 0.1 - 1$ by mixing closely spaced opposite parity states. These states are available in molecules due to increased number of degrees of freedom, either rotational [44] or due to Ω, Λ-doubling [6].

1.3.3 Historical Progress in the EDM field

As shown in Figure. 1.3.1, the electron EDM limit has been improved by more than 15 orders of magnitude since the first measurements performed in the 1950s. Given Eq. 1.5, experiments typically achieve higher sensitivity by improving three factors, $\mathcal{E}_{\text{eff}}$, τ or $\dot{N}$. At the same time, it is important to perform the experiment in a robust way that allows for increased duty cycle and therefore increased experiment integration time, T. Keeping systematic errors under control at levels much lower that the statistical uncertainty is another common feature of successful measurements.

Initial limits on the value of the eEDM were placed using measurements of the electron g-factor and by measuring the Lamb shift in the hydrogen atom [36, 45, 46]. However, after Sandars showed that molecules and atoms can provide effective electric fields much larger than applied laboratory electric fields [37], all the best limits on the eEDM were obtained in atomic or molecular systems. Initial experiments in the 1960s and 1970s were performed in alkali atoms, such as Rb or Cs [47–50], with large enhancement in sensitivity made possible by the increase in signal and polarization factor of these atoms. Experiments in the 1980s and 1990s shifted to heavier atoms, which took advantage of the larger $\mathcal{E}_{\text{eff}}$ present in such species and improvements in the experimental technique [51–55].

The sensitivity of eEDM limits obtained since the turn of the 21st century are shown

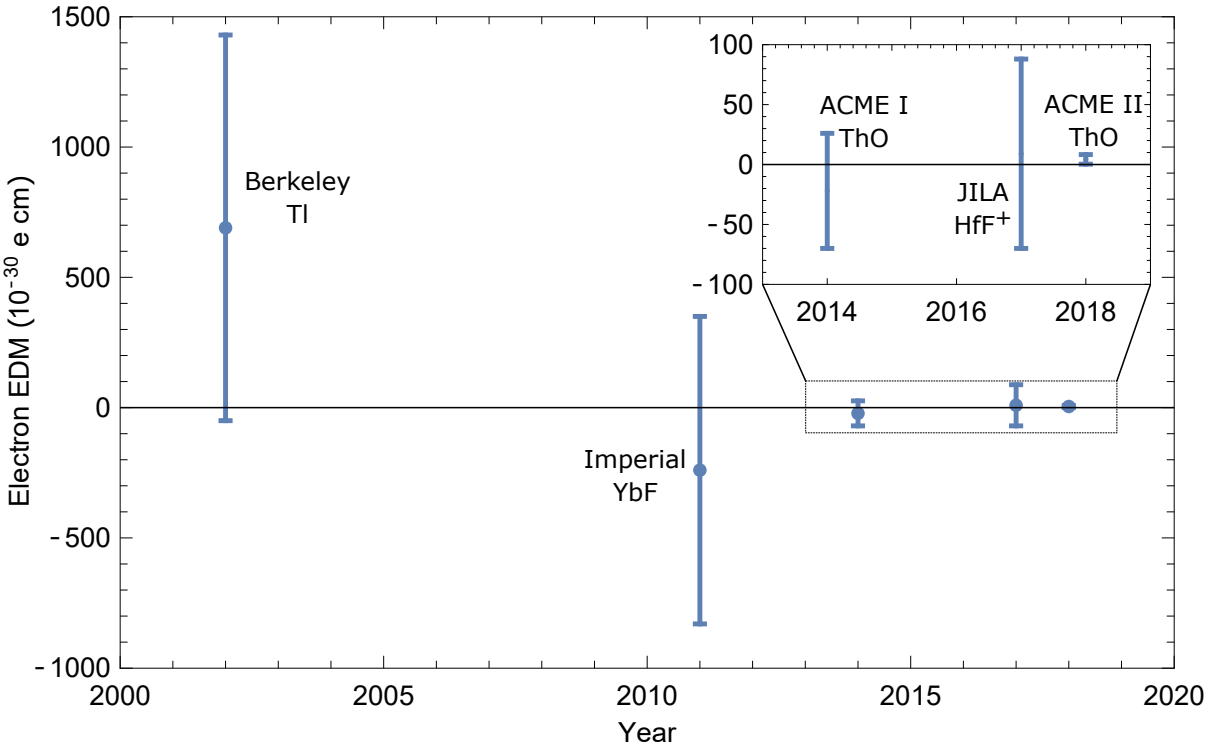

Figure 1.3.2: **eEDM measurements performed since the turn of the century.** Both the ACME I and ACME II experiments represent order of magnitude improvements in sensitivity over the previous systems. Error bars represent 1σ (68%) confidence intervals.

in Figure 1.3.2 and Table 1.3.1. Through careful experimental control and the use of the heavy Thallium atom ($\mathcal{E}_{\text{eff}} \sim 70$ MV/cm), experiments performed at Berkeley in the 1990s and early 2000s were able to reduce the eEDM limit by a few more orders of magnitude [43]. Recently, the best limits were achieved in polar molecules, which are more polarizable than atoms due to having much more closely spaced eEDM-sensitive levels of opposite parity due to the more complex molecular structure. Polarizations of $P_{\mathcal{E}} \sim 1$ are possible in molecules, which gives access to the full magnitude of the electric field ($\mathcal{E}_{\text{eff}} \approx 78$ GV/cm in ThO). Although sources of molecular beams produce count rates that are typically smaller than atoms, this larger electric field allowed experiments with YbF and ThO to improve the previous eEDM limit [5, 6, 9, 44].

A new technique measuring the eEDM in an molecular ion confined in a radio frequency

Experiment	Berkeley	Imperial	ACME I	JILA	ACME II
Year	2002	2011	2014	2017	2018
Species	Tl	YbF	ThO	HfF^+	ThO
$\mathcal{E}_{\text{eff}}$ (V/cm)	7.0×10^7	1.4×10^{10}	7.8×10^{10}	2.3×10^{10}	7.8×10^{10}
τ (ms)	2.4	0.64	1.1	700	1.1
$\dot{N}$ (s^{-1})	4.7×10^8	1.2×10^4	3×10^4	20	1×10^7
Shot-noise uncertainty ($e \cdot \text{cm}\sqrt{\text{day}}$)	3.1×10^{-28}	1.1×10^{-27}	7.5×10^{-29}	1.6×10^{-29}	4.1×10^{-30}
eEDM limit ($e \cdot$ cm 90% conf.)	1.6×10^{-27}	1.1×10^{-27}	9.4×10^{-29}	1.3×10^{-28}	1.1×10^{-29}

Table 1.3.1: **Comparison of shot-noise limited statistical sensitivity of recent eEDM measurements.** The shot-noise uncertainty is computed using Eq. 1.5. It is important to keep in mind that the final EDM limit is not only given by the experiment shot noise limited sensitivity, but can also be limited by other sources of noise or systematics and is a function of the integration time.

trap has recently offered a result with uncertainty that is higher, but comparable to the first generation result, ACME I [56]. The molecular ion trap allows for longer coherence times but with lower count rate than the ACME measurements (Table 1.3.1).

1.3.4 The ACME I and ACME II measurements

We completed the ACME I measurement in 2013 and measured $|d_e| < 9.4 \times 10^{-29}\ e \cdot$cm with 90% confidence [5, 6], an order of magnitude lower compared to the previous measurement [44]. This confirmed the potential of molecules, by representing the first leap in eEDM sensitivity by an order of magnitude over atoms. I was privileged enough to work as part of the ACME collaboration which comprises of a number of amazing students, postdocs and professors at Harvard, Yale and Northwestern Universities, to whom much of the credit is due.

A campaign to improve the sensitivity of the ACME technique resulted in the ACME II measurement, $d_e = (4.3 \pm 3.1_{\text{stat}} \pm 2.6_{\text{syst}}) \times 10^{-30}\ e \cdot \text{cm}$ ('stat', statistical uncertainty; 'syst', systematic uncertainty), which improved the ACME I result by another order of

magnitude [9]. This result is consistent with zero and corresponds to an upper limit of $|d_e| < 1.1 \times 10^{-29}\ e \cdot \text{cm}$ at 90% confidence. This constrains new T-symmetry-violating physics for broad classes of proposed beyond-Standard-Model particles with masses in the range 3–30 TeV c^{-2}.

Most of this thesis focuses on the description of the ACME II experiment, which achieved an order of magnitude higher precision over ACME I by improving the state preparation, experimental geometry, fluorescence collection and control of systematic uncertainties. We describe here the ACME II aparatus, experimental techniques, data acquisition and analysis, and our methods of measuring and limiting systematic errors. Since the ACME II measurement is a comprehensive upgrade rather than a full redesign, we will commonly refer to the ACME I experiment, to point out improved experimental techniques that we implemented or to refer to systematic effects that are common to both experiments. The ACME I experiment is described in detail in a number of references [6, 57–61].

So if you wake up one morning and it's a particularly beautiful day, you'll know we made it. Okay, I'm signing out.

Robert Capa, *Sunshine*

2

An electron EDM measurement in ThO

2.1 The $H^3\Delta_1$ ThO molecular state

The ThO molecule has a number of properties that makes it optimal for an eEDM measurement, both by allowing for high statistical sensitivity and rejection of systematic errors. We express ThO molecular states using the basis $|Y, J, M, \Omega\rangle$, where Y designates the electronic state, J is the angular momentum, M is its projection along a quantization axis $\hat{z}$ and Ω is the projection of the electronic angular momentum onto the internuclear axis, $\hat{n}$, which points from the lighter nucleus (oxygen) to the heavier nucleus (thorium). The states used for the ACME I or ACME II measurements and that are relevant for future

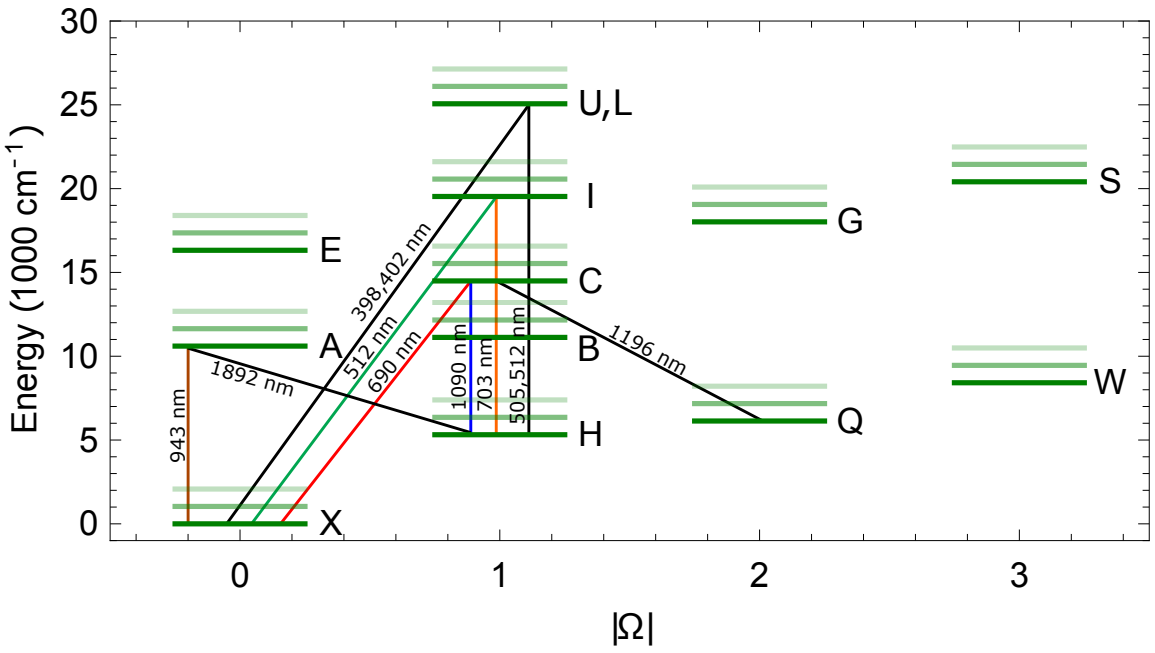

Figure 2.1.1: **ThO electronic states and transitions used in the ACME measurement.** The energies of labeled electronic states are shown, as a function of quantum number $|\Omega|$. The transitions used in ACME I and ACME II are shown with colored lines and labeled transition wavelength. Transitions that could be useful in a future ACME measurement are shown in black lines.

ACME measurements are shown in Figure 2.1.1.

We performed the ACME I and ACME II eEDM measurements in the $|J = 1, M = \pm 1\rangle$ sublevels of the $H^3\Delta_1$ electronic state of ThO [6]. The H state has two valence electrons in a $(\sigma\delta)$ configuration. The σ orbital valence electron wavefunction has a large amplitude near the heavy Th nucleus, which provides a large relativistic enhancement of the applied electric field, enhancing the sensitivity of the measurement to the eEDM. The H state provides an $\mathcal{E}_{\text{eff}} \approx 78$ GV/cm [39, 40], a factor of 3 (5) times larger than that available in the YbF (HF^+) molecular measurements, who set the nearest competitive limits [44, 56], and over 1000 times larger than available to experiments using Tl atoms [43].

The $|H, J = 1, |\Omega| = 1\rangle$ state manifold has closely spaced pairs of opposite-parity levels common to all $\Omega \neq 0$ states. The small splitting between the $|H, J = 1, \Omega = \pm 1\rangle$ states, $\Delta_{|\Omega|} = 2\pi \times 360$ kHz is given by the Coriolis effect in the rotating molecule [62]. To take

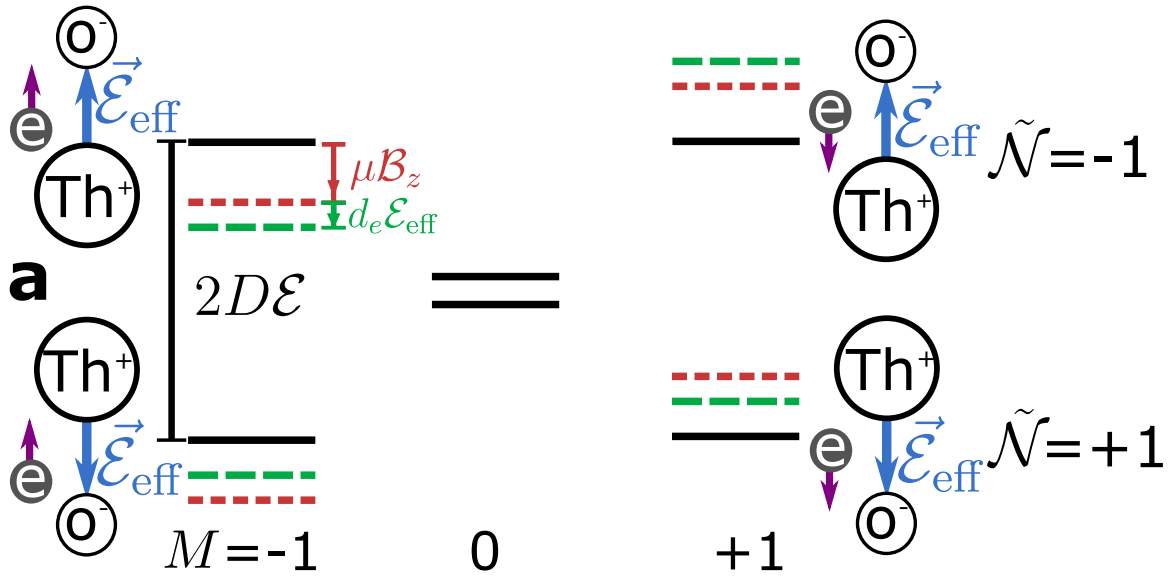

Figure 2.1.2: **Energy levels of the thorium monoxide H state.** $|H, J = 1, |\Omega| = 1\rangle$ state manifold in external $\vec{\mathcal{E}}$ and $\vec{\mathcal{B}}$ fields, accompanied by cartoons depicting the orientation of the effective electric field $\vec{\mathcal{E}}_{\rm eff}$ (blue arrows) and the spin of the electron $\vec{s}$ (purple arrows). The energy shifts $\mu\mathcal{B}_z$ (red) and $d_e\mathcal{E}_{\rm eff}$ (green) due to the magnetic moment μ and the EDM d_e, respectively, are shown. The $\tilde{\mathcal{N}} = \pm 1$ states are split by $2D\mathcal{E} \sim 200$ MHz due to the Stark effect.

advantage of the large $\mathcal{E}_{\rm eff}$, we apply an electric field $\vec{\mathcal{E}}$ that mixes the $M \neq 0$ opposite parity states via the Stark interaction, $-\vec{D}_H \cdot \vec{\mathcal{E}}$, where $D_H = 2\pi \times 1 \frac{\rm MHz}{\rm V/cm}$ is the electric field operator. For our typically applied electric fields, $|\vec{\mathcal{E}}| = 80$ V/cm ($1\mathcal{E}$) and $|\vec{\mathcal{E}}| = 140$ V/cm ($2\mathcal{E}$), these states mix completely such that the molecule is fully polarized ($P_{\mathcal{E}} > 99\%$) [63].

In this configuration, the internuclear axis $\hat{n}$, pointing from the oxygen to thorium nucleus, is either aligned or antialigned with $\vec{\mathcal{E}}$ (see Fig. 2.1.2). The direction of $\hat{n}$ corresponds to the direction of the field $\vec{\mathcal{E}}_{\rm eff}$ that acts on $\vec{d}_e$. States with opposite molecule orientation are described by the quantum number $\tilde{\mathcal{N}} = \text{sgn}(\vec{\mathcal{E}} \cdot \hat{n}) = \pm 1$. The direction of $\vec{\mathcal{E}}_{\rm eff}$ can be reversed either by reversing the laboratory field $\vec{\mathcal{E}}$ or by changing the state $\tilde{\mathcal{N}} = \pm 1$ used in the measurement. Each means of reversal allows us to reject a wide range of systematic errors [43, 64, 65].

2.2 EDM ENERGY SHIFT IN THE H STATE

The interaction between $\vec{\mathcal{E}}_{\text{eff}}$ and the electron EDM, $\vec{d}_e$, gives rise to an energy shift $U = -\vec{d}_e \cdot \vec{\mathcal{E}}_{\text{eff}}$, where $\vec{d}_e = d_e \vec{s}/(\hbar/2)$, $\vec{s}$ is the spin of the σ electron, and $\hbar$ is the reduced Planck constant. The electron spin, $\vec{s}$, is oriented along the spin of the molecular state, $\vec{S}$. We measure the energy difference between states with $M = \pm 1$, corresponding to $\vec{S}$ aligned or antialigned with $\vec{\mathcal{E}}_{\text{eff}}$ (Fig. 2.1.2), which contains a term proportional to U.

To do so, we prepare an initial coherent superposition of $M = \pm 1$ states, corresponding to the spin $\vec{S}$ aligned along a fixed direction in the xy plane (Fig. 2.2.1). The applied magnetic field, $\vec{\mathcal{B}} = \mathcal{B}_z \hat{z}$, and $\vec{\mathcal{E}}_{\text{eff}}$, exert torques on the magnetic and electric dipole moments associated with the spin, causing $\vec{S}$ to precess in the xy plane by angle ϕ as the molecules travel and evolve freely. The final value of ϕ is measured by laser excitation of the molecules, which induces fluorescence whose strength depends on the angle between $\vec{S}$ and the laser polarization. The angle ϕ is given by

$$\phi \approx \frac{-(\mu \tilde{\mathcal{B}} |\mathcal{B}_z| + \tilde{\mathcal{N}} \tilde{\mathcal{E}} d_e \mathcal{E}_{\text{eff}})\tau}{\hbar}, \tag{2.1}$$

where $|\mathcal{B}_z| = |\vec{\mathcal{B}} \cdot \hat{z}|$, $\tilde{\mathcal{B}} = \text{sgn}(\vec{\mathcal{B}} \cdot \hat{z})$, $\tilde{\mathcal{E}} = \text{sgn}(\vec{\mathcal{E}} \cdot \hat{z})$, τ is the spin precession time, and $\mu = \mu_{\text{B}} g_{\mathcal{N}}$, where $g_{\mathcal{N}} = -0.0044$ is the g-factor of the $|H, J = 1, \mathcal{N}\rangle$ state [66] and μ_{B} is the Bohr magneton.

The sign, $\tilde{\mathcal{N}}\tilde{\mathcal{E}}$, of the EDM contribution to the angle is given by the sign of the torque of $\vec{\mathcal{E}}_{\text{eff}}$ on $\vec{s}$. The spin precession frequency, $\omega = \phi/\tau$, is given by the energy shift between the $M = \pm 1$ states (divided by $\hbar$). The value of d_e is extracted from the change in ω correlated with the orientation of $\vec{\mathcal{E}}_{\text{eff}}$ in the lab frame, i.e. with the product $\tilde{\mathcal{N}}\tilde{\mathcal{E}}$. Denoting this correlated component as $\omega^{\mathcal{N}\mathcal{E}}$, we obtain $d_e = -\hbar\omega^{\mathcal{N}\mathcal{E}}/\mathcal{E}_{\text{eff}}$.

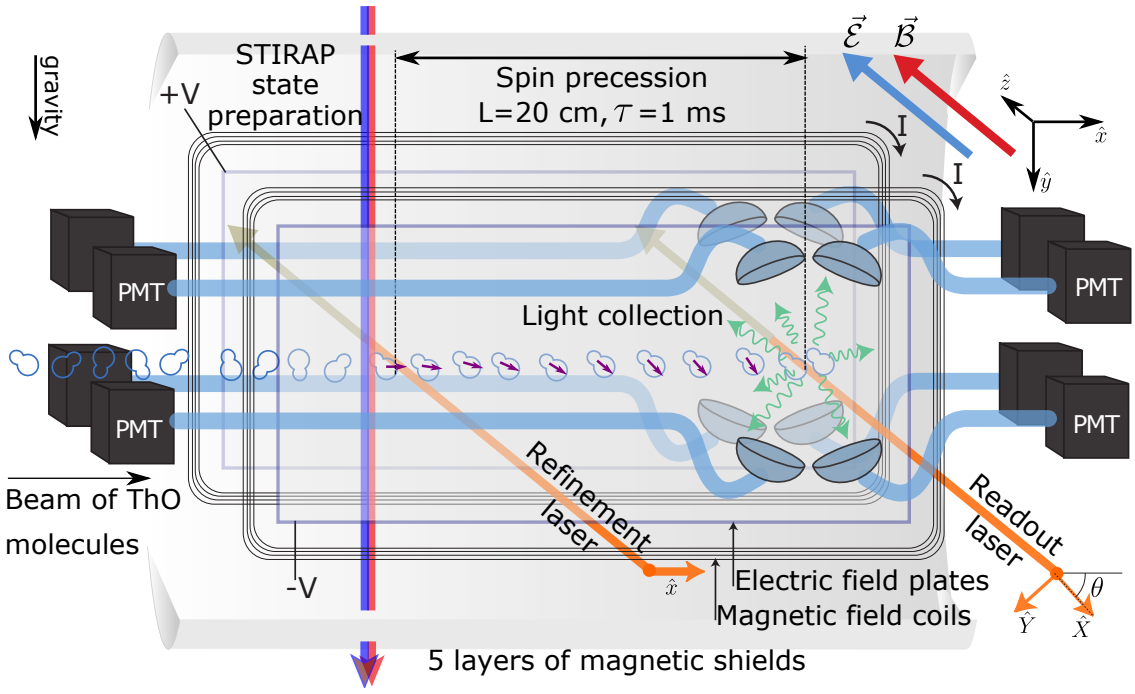

Figure 2.2.1: **Schematic of the measurement region.** A collimated pulse of ThO molecules enters a magnetically shielded region. An uniform electric field (oblique blue arrow) is applied using voltage $(+V,-V)$ on a set of transparent parallel plates and an uniform magnetic field (oblique red arrow) is applied using a current I through coils. A spin state aligned (purple) along $\hat{x}$, prepared by STIRAP (blue, red vertical arrows) and refined via an optical pumping laser beam (orange) polarized along $\hat{x}$, precesses over a length $L \approx 20$ cm (time $\tau \approx 1$ ms) in the applied electric ($\vec{\mathcal{E}}$) and magnetic ($\vec{\mathcal{B}}$) fields. The final spin alignment direction is read out by a laser (orange) with rapidly alternating linear polarizations, $\hat{\epsilon} = \hat{X}$, $\hat{Y}$ (with the former at an angle θ with respect to $\hat{x}$). The resulting fluorescence (green wavy arrow), whose intensity depends on the angle between $\vec{S}$ and $\hat{\epsilon}$, is collected and detected with photomultiplier tubes (PMTs).

2.3 Advantages of the ThO molecule

In addition to access to a large $\mathcal{E}_{\text{eff}}$ and the ability to reverse $\mathcal{E}_{\text{eff}}$ spectroscopically, through the $\tilde{\mathcal{N}}$ switch, $^3\Delta_1$ states have other advantages for performing eEDM measurements. $^3\Delta_1$ states are insensitive to magnetic fields, since the two units of angular momentum in the $\delta_{3/2}$ orbital cancel the spin angular momentum of the triplet $(\sigma\delta)^3$ state [67]. In the ThO molecule, the $|H, J = 1\rangle$ state has a small magnetic moment $\mu_H = g_H \mu_B M$, where $g_H = -0.00440(5)$ is the g-factor and μ_B is the Bohr magneton [68]. The deviation from zero is due to mixing with other states and the anomalous free electron g-factor [1].

The H state is metastable with a lifetime of $\tau_H \approx 1.8$ ms [63]. In diverging molecular beams such as ours, where the velocity of the molecules is order hundreds of m/s, this is rarely a limit. This is because, in such systems, the precession distance over which the applied electric and magnetic field have to be kept uniform can rarely be larger than that allowed by the lifetime of the H state. In the ACME experiment, the ThO molecules precess over 20 cm, corresponding to a precession time $\tau \approx 1$ ms.

As with many other species, ThO proved nicely compatible with a new approach to creating molecular beams, the hydrodynamically enhanced cryogenic buffer gas beam [69–71]. This method provides a cold, high-flux and low-divergence beam [72] yielding a large number of molecules in the few lowest-lying quantum states. The molecule beam's forward velocity (≈180 m/s) was also lower than a typical supersonic beam, which helped minimize the apparatus length for a given coherence time.

2.4 The ACME II spin precession measurement

In the absence of any experimental imperfections, we describe our system in terms of coordinate axes $+\hat{z}$ along $+\vec{\mathcal{E}}$ (for a specified sign of applied field that we denote as positive, pointing approximately east to west in the lab) and $+\hat{x}$ along the direction of the molecular

beam (which travels approximately south to north) such that $+\hat{y}$ is approximately aligned with gravity (Fig. 2.2.1). Note that when we reverse the direction of the electric field, by construction, the laboratory coordinate system does not change and the orientation of the electric field can be described by $\tilde{\mathcal{E}} \equiv \mathrm{sgn}(\hat{z}\cdot\vec{\mathcal{E}}) = \pm 1$. Analogously, we reverse the direction of the magnetic field between two $\tilde{\mathcal{B}} \equiv \mathrm{sgn}(\hat{z}\cdot\vec{\mathcal{B}}) = \pm 1$ states. Since the directions of the fields are encoded by $\tilde{\mathcal{E}}$ and $\tilde{\mathcal{B}}$, we define the magnitudes of the fields simply as $\mathcal{B}_z \equiv |\vec{\mathcal{B}}_z|$ and $\mathcal{E} \equiv |\vec{\mathcal{E}}|$.

We produce ThO molecules in a cryogenic buffer gas beam source [69, 70, 72]. The buffer gas used is neon. Similar to ACME I, each beam pulse contains $\sim 10^{11}$ ThO molecules in the $J = 0$ rotational level of the ground electronic (X) and vibrational state ($v = 0$). Molecular beam pulses are produced with a repetition rate of 50 Hz.

After leaving the beam source, the molecules are in a thermal distribution of rotational states at 4 K, residing mostly ($> 70\%$) in the $J = 0$–2 rotational levels. We use two stages of optical pumping for "rotational cooling," i.e. to enhance the population in the ground rotational level $|X, J = 0^+\rangle$, where the superscript denotes the parity quantum number of the state. The first stage is performed in electric field ≈ 0 V/cm, using 5–7 passes of a laser beam resonant with the $|X, J = 2^+\rangle \leftrightarrow |C, J = 1^-\rangle$ transition. Each pass has orthogonal polarization to the previous, addressing all M states in $|X, J = 2^+\rangle$. Due to parity and angular momentum selection rules, this results in optical pumping of population from $|X, J = 2^+\rangle$ to $|X, J = 0^+\rangle$. The second stage is performed in an applied electric field of ≈ 100 V/cm, which mixes the opposite-parity excited states $|C, J = 1^{\pm 1}, M = \pm 1\rangle$. A multipass, alternating polarization laser beam drives the $|X, J = 1^-\rangle \leftrightarrow |C, J = 1^{\mathrm{mixed}}, M = \pm 1\rangle$ transition, partially transferring population from $|X, J = 1^-\rangle$ to $|X, J = 0^+\rangle$. These two combined rotational cooling steps increase the population in the $|X, J = 0^+\rangle$ state by a factor of 2.5.

The molecules pass through fixed collimating apertures and enter a magnetically shielded region where the eEDM measurement is performed. The $\mathcal{E}$-field is produced by a pair of

parallel fused silica glass plates coated with a thin conductive layer (20 nm) of indium tin oxide (ITO) on one side and anti-reflection coating on the other side. The ITO-coated sides face each other with a gap of 45 mm and are connected to low-noise voltage supplies.

The vacuum chamber that houses the spin precession region is surrounded by five layers of μ-metal shielding. Current through coils generates the uniform magnetic field $\vec{\mathcal{B}}$ (Fig. 2.2.1). The coil design is optimized to create a uniform magnetic field along z. Additional coils allow us to apply $\mathcal{B}$-field offsets in the transverse directions (x and y), as well as all first-order gradients ($\partial\mathcal{B}_z/\partial z$, $\partial\mathcal{B}_z/\partial y$, $\partial\mathcal{B}_x/\partial x$, $\partial\mathcal{B}_y/\partial y$, $\partial\mathcal{B}_y/\partial x$, $\partial\mathcal{B}_z/\partial x$) for systematic error checks. The $\mathcal{B}$-field is monitored by four 3-axis fluxgate magnetometers, which are placed inside pockets inset in the vacuum chamber, 20–30 cm from the molecular beam. The electronic offset inherent to fluxgate magnetometers is subtracted by rotating them *in situ* by 180 degrees, and each can be translated along one axis. These magnetometers are used to infer changes in the $\mathcal{B}$-field as well as information about its gradients. The $\mathcal{B}$-field was also mapped before and after the EDM dataset by sliding a 3-axis fluxgate magnetometer down the beamline, along $\hat{x}$, at the position of the molecules and at positions offset vertically (along $\hat{y}$). The measurement of gradients along $\hat{x}$ and $\hat{y}$, along with Maxwell's equations, allowed us to also infer the gradients along $\hat{z}$, where the mechanical geometry of the field plates prevented a direct measurement.

We prepare the desired initial spin state using STIRAP, coherently transfering the molecules from the ground state $|X, J = 0\rangle$ to a specific sublevel of the lowest rotational level, $J = 1$, of the metastable (lifetime 2 ms) [63] electronic $H^3\Delta_1$ state manifold [73] (see Fig. 2.4.1a). This results in a coherent superposition of $M = \pm 1$ states. STIRAP is implemented through a pair of co-propagating laser beams (wavelengths 690, 1090 nm), resonant with electronic transitions $X - C$ and $C - H$. These beams are partially spatially overlapped and travel vertically (along $\hat{y}$), and with linear polarizations along $\hat{z}$ and $\hat{x}$, respectively. We choose which $\tilde{\mathcal{N}}$ state to address by tuning the frequency of the $H - C$

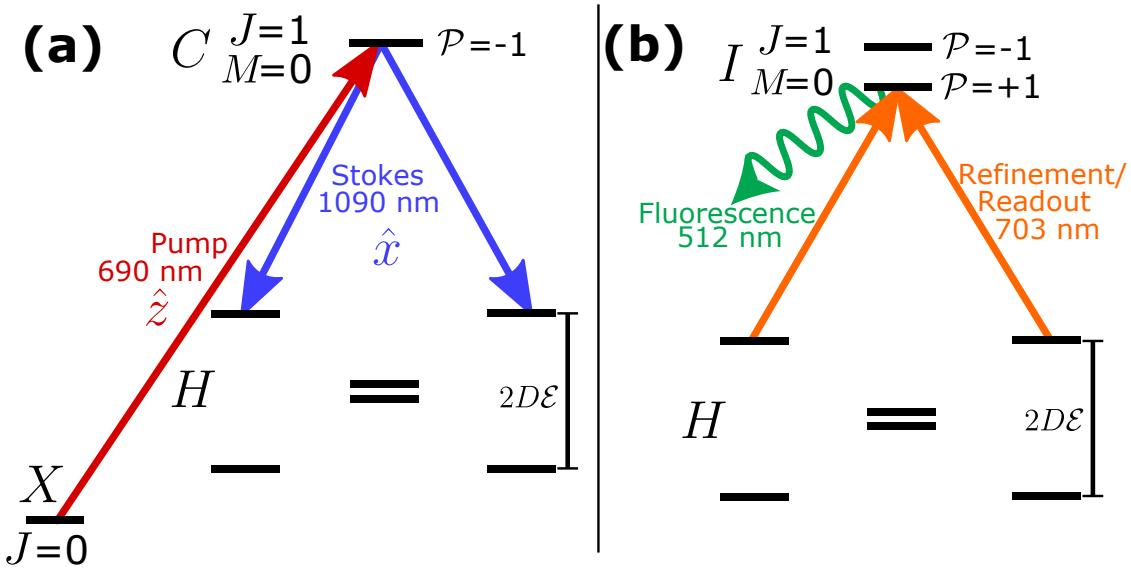

Figure 2.4.1: **Energy levels of thorium monoxide and laser transitions.** The addressed transitions are shown for one of several possible experimental states. **(a)** STIRAP transfers population from the ground state $|X, J = 0\rangle$ into a spin-aligned superposition of one molecule orientation $\tilde{\mathcal{N}} = +1$ or -1 (shown here with $\tilde{\mathcal{N}} = -1$). STIRAP uses two lasers, Pump ($X - C$, 690 nm, polarized along $\hat{z}$) and Stokes ($C - H$, 1090 nm, polarized along $\hat{x}$). **(b)** The refinement laser (orange) removes imperfections in the spin-aligned state prepared by STIRAP. The readout laser (orange) excites from the originally prepared molecule orientation, $\tilde{\mathcal{N}} = +1$ or -1 ($\tilde{\mathcal{N}} = -1$ shown here), to an isolated $J = 1, M = 0$ level in state I. This state can have either parity, $\tilde{\mathcal{P}} = +1$ or -1 ($\tilde{\mathcal{P}} = +1$ shown here). The I state decays via spontaneous emission, and we detect the resulting fluorescence (green wavy arrow).

STIRAP laser. More details on the STIRAP implementation are given in Section 3.2.

Imperfections in the STIRAP-prepared spin-aligned state can lead to systematic errors (see Section 5.5), but are suppressed with the following method. After leaving the STIRAP region, the molecules enter a linearly polarized "refinement" laser that optically pumps away the unwanted spin component and leaves behind a dark superposition of the two resonant $M = \pm 1$ sublevels of H [74]. The refinement laser is resonant with the $H - I$ transition (wavelength 703 nm; Fig. 2.4.1b). Within the short-lived (lifetime 115 ns) electronic I state, there are two well-resolved opposite-parity $\tilde{\mathcal{P}} = \pm 1$ states with $J = 1, M = 0$ [75, 76]. The refinement laser polarization is nominally aligned with the STIRAP-prepared spin $\vec{S}_{\mathrm{ST}}$ and

addresses the $\tilde{\mathcal{P}} = +1$ parity state in I. The resulting refined state, $|\psi(t=0), \tilde{\mathcal{N}}\rangle$, has $\vec{S}$ aligned along $\hat{x}$ more accurately than in the initial STIRAP-prepared state (Fig. 2.2.1).

Molecules travel over a distance of $L \approx 20$ cm (corresponding to $\tau \approx 1$ ms) so that $\vec{S}$ precesses in the xy plane by angle ϕ (given by Eq. 2.1). This yields the molecular state at time $t = \tau$,

$$|\psi(t=\tau), \tilde{\mathcal{N}}\rangle = \frac{e^{-i\phi}|M=+1, \tilde{\mathcal{N}}\rangle - e^{+i\phi}|M=-1, \tilde{\mathcal{N}}\rangle)}{\sqrt{2}}. \tag{2.2}$$

We measure ϕ by exciting the $H - I$ transition with laser light linearly polarized along direction $\hat{\epsilon}$. This yields fluorescence signals with intensity S_ϵ that depends on the angle between $\hat{\epsilon}$ and $\vec{S}$. To remove the effects of fluctuations in molecule number, we excite the molecules with two alternating orthogonal linear polarizations, $\hat{\epsilon} = \hat{X}$ and $\hat{Y}$, by modulating $\hat{\epsilon}$ sufficiently rapidly (period 5 μs) that each molecule is addressed by both polarizations as it flies through the laser beam [66]. To do so, we overlap two laser beams with orthogonal $\hat{X}$ and $\hat{Y}$ polarizations, which we switch on and off rapidly using AOMs. The $\hat{X}$ and $\hat{Y}$ pulses each have duration 1.9 μs, with a 0.6 μs delay between them to minimize the overlap of signal due to the finite lifetime of the I state (115 ns) [76] between successive pulses (Fig. 2.5.1a).

We record the corresponding fluorescence signals S_X and S_Y from the decay of I to the ground state X (wavelength 512 nm; see Fig. 2.5.1a). Fluorescence photons travel through the transparent field plates and are focused by one of eight lenses (four behind each field plate) into one of eight bent fused silica lightguides. Each lightguide carries the fluorescence to one of eight PMTs outside the magnetic shielding. The PMTs are optimized to detect fluorescence at 512 nm ($\sim 25\%$ quantum efficiency).

The PMT photocurrents are amplified and then recorded by a 14-bit digitizer operating at 16 megasamples/s. The digitizer signal is recorded by a computer, which communicates with a second computer that controls the slow switches (< 10 Hz).

We then compute the asymmetry [63],

$$\mathcal{A} \equiv \frac{S_X - S_Y}{S_X + S_Y} = \mathcal{C}\cos\left(2\left(\phi - \theta\right)\right), \tag{2.3}$$

where the experiment sensitivity is scaled by a "contrast" factor,

$$\mathcal{C} \equiv -\frac{1}{2}\frac{\partial \mathcal{A}}{\partial \theta} \approx \frac{1}{2}\frac{\partial \mathcal{A}}{\partial \phi}, \tag{2.4}$$

and $\hat{X}$ is defined to be at an angle θ with respect to $\hat{x}$ in the xy plane (Fig. 2.2.1). This procedure amounts to a projective measurement of the molecule alignment onto both $\hat{X}$ and $\hat{Y}$. We set $|\mathcal{B}_z|$ and θ such that $\phi - \theta \approx \frac{\pi}{4}(2n+1)$ for integer n, so that the asymmetry is linearly proportional to small changes in ϕ and thus maximally sensitive, and linearly proportional to, small changes in ϕ. We measure $\mathcal{C}$ by dithering θ between two nearby values, $\tilde{\theta} = \pm 1$, that differ by 0.2 rad. The measured contrast value is typically $\mathcal{C} \approx 0.95$. The value of the contrast is reduced from 1 by a variety of effects including decay from C back to H, elliptical laser polarization and forward velocity dispersion.

We then extract the measured phase, Φ, by normalizing the measured asymmetry by the measured contrast:

$$\Phi = \mathcal{A}/(2\mathcal{C}) + \pi/4(2n+1). \tag{2.5}$$

In the ideal case, the measured phase Φ is equal to the true phase ϕ, but as shown in Chapter 5, experimental imperfections can cause it to deviate from that.

2.5 Switches performed to extract the eEDM

We perform the spin precession measurement repeatedly under varying experimental conditions to (a) isolate the EDM phase from background phases and (b) search for and monitor possible systematic errors. Within a "block" of data (Fig. 2.5.1c) taken over 60 s, we perform 4 identical measurements of ϕ for each of a complete set of 2^4 experimental states

derived from 4 binary switches: $\tilde{\mathcal{N}}$, the molecule alignment; $\tilde{\mathcal{E}}$, the direction of the applied electric field; $\tilde{\theta}$, the readout laser polarization dither state; and $\tilde{\mathcal{B}}$, the magnetic field direction.

We form "switch parity components" of the phase, which are combinations of the measured phases that are odd or even under the selected switch operations [65]. We denote the experimental parity of a quantity with a superscript, u, that lists all the switch labels under which the quantity is odd; it is even under all unlabelled switches, and we use the superscript "nr" to show that the quantity is even under all considered switches. Using this formalism, we can write the phase for each $(\tilde{\mathcal{N}}, \tilde{\mathcal{E}}, \tilde{\mathcal{B}})$ state in terms of components with particular parity with respect to the experimental switches:

$$\Phi(\tilde{\mathcal{N}}, \tilde{\mathcal{E}}, \tilde{\mathcal{B}}) = \Phi^{\mathrm{nr}} + \Phi^{\mathcal{N}}\tilde{\mathcal{N}} + \Phi^{\mathcal{E}}\tilde{\mathcal{E}} + \Phi^{\mathcal{B}}\tilde{\mathcal{B}} + \Phi^{\mathcal{N}\mathcal{E}}\tilde{\mathcal{N}}\tilde{\mathcal{E}} + \Phi^{\mathcal{N}\mathcal{B}}\tilde{\mathcal{N}}\tilde{\mathcal{B}} + \Phi^{\mathcal{E}\mathcal{B}}\tilde{\mathcal{E}}\tilde{\mathcal{B}} + \Phi^{\mathcal{N}\mathcal{E}\mathcal{B}}\tilde{\mathcal{N}}\tilde{\mathcal{E}}\tilde{\mathcal{B}}. \quad (2.6)$$

The corresponding reverse transformation from the state into the parity basis is given by:

$$\Phi^{u}(\mathcal{N}, \mathcal{E}, \mathcal{B}) = \frac{1}{2^8} \sum_{\tilde{\mathcal{N}}', \tilde{\mathcal{E}}', \tilde{\mathcal{B}}' = \pm 1} (\tilde{\mathcal{N}}')^{\frac{1-\mathcal{N}}{2}} (\tilde{\mathcal{E}}')^{\frac{1-\mathcal{E}}{2}} (\tilde{\mathcal{B}}')^{\frac{1-\mathcal{B}}{2}} \Phi(\tilde{\mathcal{N}}, \tilde{\mathcal{E}}, \tilde{\mathcal{B}}). \quad (2.7)$$

For example, the $\tilde{\mathcal{N}}, \tilde{\mathcal{E}}$- odd component of the phase under the three considered $(\tilde{\mathcal{N}}, \tilde{\mathcal{E}}, \tilde{\mathcal{B}})$ switches can be extracted from the phase measured in all 8 possible states, $\Phi^{u}(\tilde{\mathcal{N}}, \tilde{\mathcal{E}}, \tilde{\mathcal{B}})$ as

$$\Phi^{\mathcal{N}\mathcal{E}} = \frac{1}{2^8} \sum_{\tilde{\mathcal{N}}', \tilde{\mathcal{E}}', \tilde{\mathcal{B}}' = \pm 1} (\tilde{\mathcal{N}}')(\tilde{\mathcal{E}}')\Phi(\tilde{\mathcal{N}}\tilde{\mathcal{E}}\tilde{\mathcal{B}}). \quad (2.8)$$

It is important to note that this formalism can be easily generalized to any number of switches and to any other quantities, not only Φ.

Some of these components arise from important measured physical quantities. We extract d_e from the $\Phi^{\mathcal{N}\mathcal{E}}$ component of phase (see Eq. 2.5), which is odd under the $\tilde{\mathcal{N}}$ and $\tilde{\mathcal{E}}$ switches and even under all other switches: $\Phi^{\mathcal{N}\mathcal{E}} = -d_e \mathcal{E}_{\mathrm{eff}} \tau / \hbar$. We extract the precession time τ

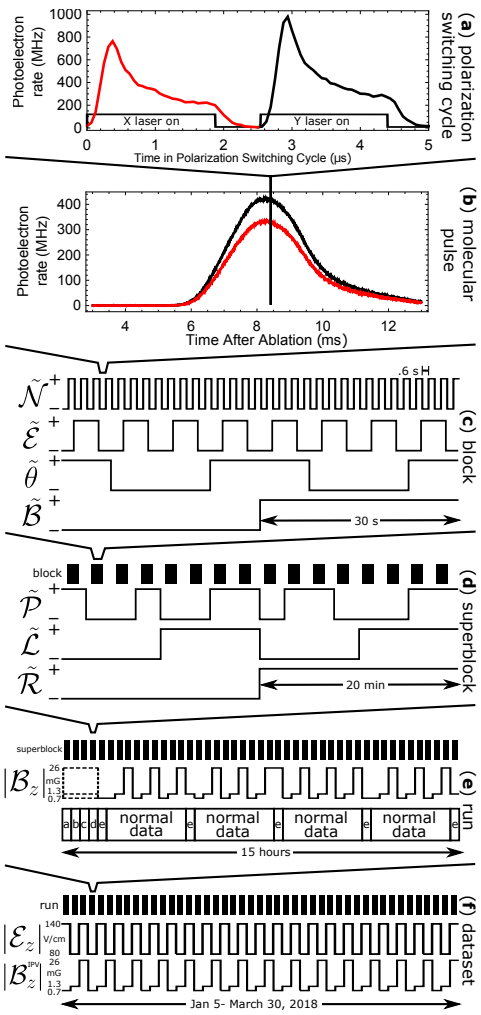

Figure 2.5.1: **Switching timescales**. **(a)** Fluorescence signal size vs. time in an $\hat{X}$, $\hat{Y}$ polarization cycle. **(b)** Measured molecular trace (25 averaged pulses) vs. time. Signal averaged over the entire $\hat{X}$ and $\hat{Y}$ polarization cycles from **(a)** are shown in red and black, respectively. **(c)** Switches performed within a block. The $\tilde{\mathcal{N}}$ and $\tilde{\mathcal{B}}$ switches randomly alternate between a $(-+)$ and $(+-)$ pattern, and the $\tilde{\mathcal{E}}$ and $\tilde{\theta}$ switches randomly alternate between $(-++-)$ and $(+--+)$ between blocks. **(d)** Switches performed within a superblock. The $\tilde{\mathcal{P}}$ state order is selected randomly, while $\tilde{\mathcal{L}}$ and $\tilde{\mathcal{R}}$ are deterministic. **(e)** Run data structure. We alternate between "normal" EDM data, taken at three values of $|\mathcal{B}_z|$, and monitoring of known systematic effects by performing Intentional Parameter Variations (IPV). Several days of data were taken with $|\mathcal{B}_z| = 2.6$ mG instead of $|\mathcal{B}_z| = 0.7$ mG shown in the figure. Each IPV corresponds to one superblock, where some control parameter (labeled $a - e$) is deliberately offset from its ideal value. Here, $a = P_{\text{ref}}$ (the refinement beam is completely blocked, to determine the intrinsic $\omega_{\text{STIRAP}}^{\mathcal{NE}}$), $b = \mathcal{E}^{\text{nr}}$, $c = P^{\mathcal{NE}}$, $d = \phi_{\text{STIRAP}}^{\mathcal{NE}}$, and $e = \partial\mathcal{B}_z/\partial z$. The $\mathcal{B}$-field magnitude for the e IPV was stepped through three experimental values within a run. **(f)** The EDM dataset. The $\mathcal{E}$-field magnitude was varied from day to day. The $\mathcal{B}$-field magnitude for the a, b, c, d IPVs was stepped through three experimental values.

from the component of phase that is odd under only the $\tilde{\mathcal{B}}$ switch, $\phi^{\mathcal{B}} = -\mu\,|\mathcal{B}_z|\,\tau/\hbar$, and use it to compute the frequency components $\omega^u \equiv \phi^u/\tau$ that are odd under chosen parity u. In certain cases we drop the superscript parity designation, as it is redundant. For example, we drop the superscript of the larger components of the applied electric and magnetic fields, $\mathcal{E} \equiv \mathcal{E}^{\mathcal{E}}$ and $\mathcal{B}_z \equiv \mathcal{B}_z^{\mathcal{B}}$.

On a slower timescale, we perform additional "superblock" binary switches to suppress known systematic errors and to search for unknown ones (Fig. 2.5.1d). These switches are: $\tilde{\mathcal{P}}$, the excited state parity addressed by the state readout laser; $\tilde{\mathcal{L}}$, reversal of the leads that supply the $\mathcal{E}$-field voltages along with reversal of the supply voltages; and $\tilde{\mathcal{R}}$, rotation of the readout $\hat{X}$-$\hat{Y}$ polarization basis by $\theta \to \theta + \pi/2$. Both the $\tilde{\mathcal{P}}$ and $\tilde{\mathcal{R}}$ switches interchange the role of $\hat{X}$ and $\hat{Y}$ and hence reject systematic errors associated with a small change in readout power, profile, or pointing when the polarization $\vec{\epsilon}$ is changed. The $\tilde{\mathcal{L}}$ switch rejects systematics that are proportional to an offset voltage in the $\mathcal{E}$-field power supplies. To compute d_e, we extract from the 2^7 block and superblock states $\omega^{\mathcal{N}\mathcal{E}}$, the component of the frequency that is odd under $\tilde{\mathcal{N}}$ and $\tilde{\mathcal{E}}$ and even under all other switches.

On these longer timescales, we also alternated between taking eEDM data under *Normal* conditions, in which all parameters were set to their ideal values, or taking data with *Intenional Parameter Variations* (IPVs), in which one or more of the experimental parameters were set to deviate from ideal (Fig. 2.5.1). This allowed us to monitor the EDM sensitivity to known systematic errors. Each IPV corresponds to one superblock, where some control parameter (labeled $a - e$) is deliberately offset from its ideal value. Here, $a = P_{\mathrm{ref}}$ (the refinement beam is completely blocked, to determine the intrinsic $\omega^{\mathcal{N}\mathcal{E}}_{\mathrm{STIRAP}}$), $b = \mathcal{E}^{\mathrm{nr}}$, $c = P^{\mathcal{N}\mathcal{E}}$, $d = \phi^{\mathcal{N}\mathcal{E}}_{\mathrm{STIRAP}}$, and $e = \partial\mathcal{B}_z/\partial z$. The $\mathcal{B}$-field magnitude for the e IPV was stepped through three experimental values within a run. The mechanisms leading to the systematic errors that we are monitoring using these IPVs are described in Chapter 5.

The EDM dataset consists of about 20,000 blocks, taken over the course of ∼2 months (Fig. 2.5.1f). During this dataset, in addition to the 7 switches described above, we

also varied the $\mathcal{B}$-field magnitude, $|\mathcal{B}_z| = 0.7,\ 1.3,\ 2.6,\ 26\,\mathrm{mG}$ (corresponding to $|\phi| \approx \frac{\pi}{160}, \frac{2\pi}{160}, \frac{4\pi}{160}$, and $\frac{\pi}{4}$, respectively), and the $\mathcal{E}$-field magnitude, $|\mathcal{E}_z| = 80,\ 140\,\mathrm{V/cm}$. 5% of data was taken with $|B_z| = 2.6$ mG; the rest was taken at $|B_z| = 0.7, 1.3, 26$ mG in approximately equal amounts. Equal amounts of data were taken with each of the two electric field magnitudes.

Yesterday is history, tomorrow is a mystery, but today is a gift. That is why it is called present.

Master Oogway, *Kung Fu Panda*

3

The ACME II apparatus and methods

The ACME I experiment achieved a factor of 12 increased precision [5, 6] compared to previous experiments [43, 44], significantly increasing the energy reach of eEDM measurements. The absence of an eEDM at the 10^{-29} $e \cdot$ cm level limited the parameter space available for many beyond the Standard Model theories [12–16]. A new eEDM measurement would increase the sensitivity to new particles, either by measuring a nonzero eEDM or by further decreasing the parameter space of viable theories.

The ACME I experiment was designed with simplicity and efficiency in mind, managing to achieve an order of magnitude increase in sensitivity in a 5 year measurement cycle. As

the first eEDM experiment performed with the ThO molecule, modularity and robustness were typical guiding factors in deciding on the experimental design and methods used to implement the spin precesion experiment. It was sometimes the case that designs and methods that gave lower signal were chosen for their easiness of implementation and increased robustness.

ACME II, the second generation experiment with ThO, was designed as an upgrade on the ACME I apparatus and measurement scheme, with the goal to achieve an order of magnitude improved eEDM measurement. ACME II achieved this goal by using new techniques and experiment design optimization, which increased the efficiency of components of the spin precession measurement, such as geometry, state preparation and detection. A diagram of the ACME II apparatus in its final running configuration is shown in Figure 3.1.1.

3.1 Sensitivity improvements

As derived in section 1.3.1, the shot-noise limited ACME eEDM sensitivity scales as

$$\delta d_e = \frac{\hbar}{2\mathcal{E}_{\text{eff}}\tau\sqrt{\dot{N}T}}. \tag{3.1}$$

Reducing δd_e therefore requires improving one of the following parameters: $\mathcal{E}_{\text{eff}}$, τ, $\dot{N}$ or T.

As described in section 1.3.2, the ThO molecule was already fully polarized in ACME I, taking advantage of the largest possible $\mathcal{E}_{\text{eff}} \approx 78$ GV/cm [5, 6]. The precesion time $\tau \approx 1.1$ ms is optimized for the lifetime of the H state, which was measured to be $\tau_H \approx 1.8$ ms and also limited by the spatial expansion of the ThO molecular beam which travel balistically once outside of the beam source, so significant improvements are unlikely.

The integration time T is limited by the duty cycle of the experiment. In total, eEDM data was only acquired during 5% of the time spent running the ACME I apparatus. This

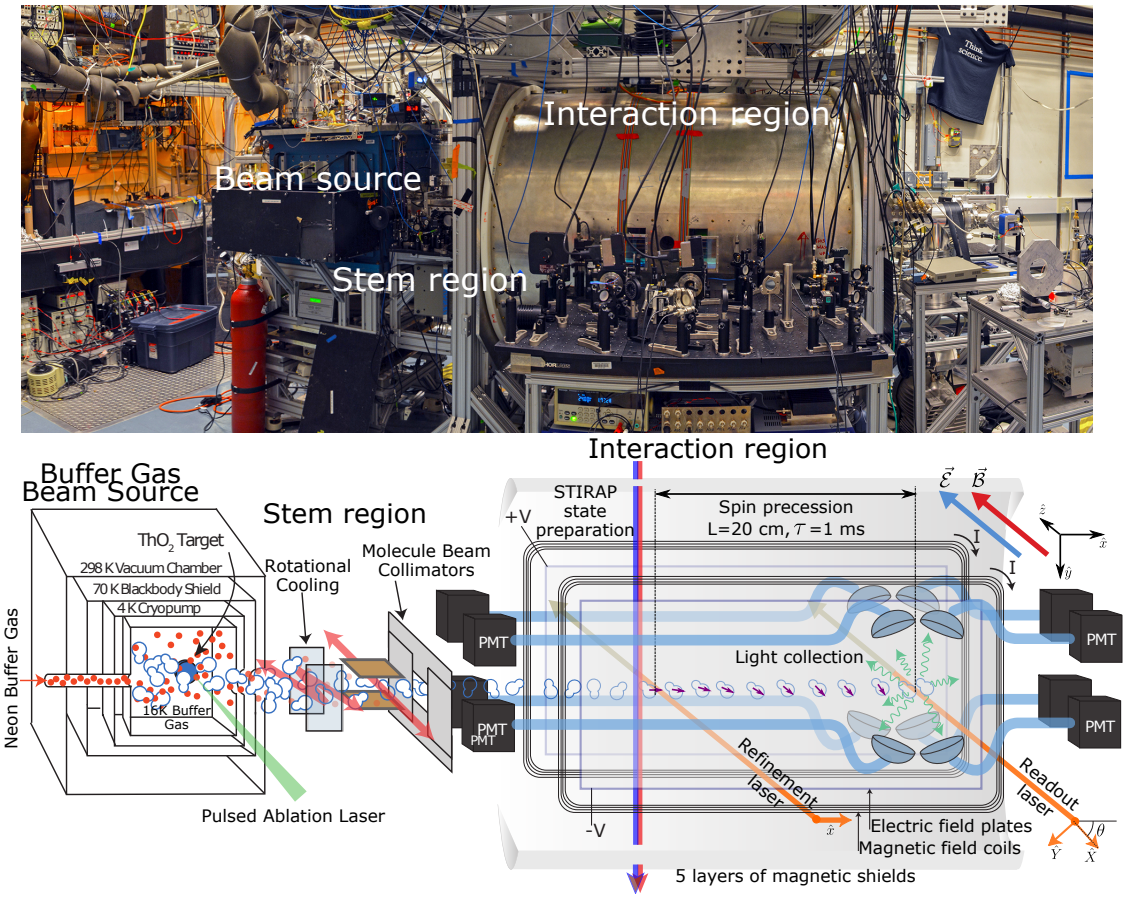

Figure 3.1.1: **The ACME II experimental apparatus.** Image of the physical apparatus (top) and schematic diagram (bottom). Pulsed laser ablation inside the buffer gas beam source creates a beam of ThO molecules. As they travel through the stem region, molecules are rotationally cooled by a pair of optical pumping lasers and collimated. They then enter a magnetically shielded region. An uniform electric field (oblique blue arrow) is applied using voltage $(+V, -V)$ on a set of transparent parallel plates and an uniform magnetic field (oblique red arrow) is applied using a current I through coils. A spin state aligned (purple) along $\hat{x}$, prepared by STIRAP (blue, red vertical arrows) and refined via an optical pumping laser beam (orange) polarized along $\hat{x}$, precesses over a length $L \approx 20$ cm (time $\tau \approx 1$ ms) in the applied electric ($\vec{\mathcal{E}}$) and magnetic ($\vec{\mathcal{B}}$) fields. The final spin alignment direction is read out by a laser (orange) with rapidly alternating linear polarizations, $\hat{\epsilon} = \hat{X}, \hat{Y}$ (with the former at an angle θ with respect to $\hat{x}$). The resulting fluorescence (green wavy arrow), whose intensity depends on the angle between $\vec{S}$ and $\hat{\epsilon}$, is collected and detected with photomultiplier tubes (PMTs).

low duty cycle results from a combination of two factors: 10 %, from the useful high signal region of the molecular pulse (2-3 ms) within the period between pulses (20 ms) (see Fig. 2.5.1b); 50%, from the settling time for the experiment switches and time to change and optimize the position of the ablation laser spot on the target.

We tried to increase the beam source duty cycle by increasing the repetition rate of the pulsed YAG ablation laser. However, due to unknown dynamics in the buffer gas beam source, the per-pulse molecular flux signals start to diminish above the ACME I ablation rate of 50 Hz. For example, increasing the YAG ablation rate to 100 Hz decreased the per-pulse signal by approximately a factor of 2. This makes the time averaged signal be optimal at a repetition rate of 50 Hz. The second factor limiting duty cycle occurs because we perform a large number of switches and we conservatively wait a significant amount of time for the experiment parameters to settle after each switch, typically many decay cycles (see Sec. 2.5). ACME II did not significantly improve this parameter over ACME I, but further improvements in the experiment timing structure might increase this duty cycle in the future by 10-20%.

With $\mathcal{E}_{\text{eff}}, \tau$ and T maxed out, the last available enhancement was in the count rate of the ACME measurement, $\dot{N}$. The count rate is a product of the number of molecules that are produced by the ACME beam source and the efficiency of using these molecules in the eEDM measurement. We considered increasing the first by upgrading to a higher-flux, quasi-CW thermochemical source that was largely the work of Elizabeth West and Jacob Baron. The thermochemical source offered higher time-averaged signal that the ablation source [77]. However, we eventually did not end up using this option, since it would require more frequent changing of targets and significantly modifying our experimental timing structure. The timing would need to be adjusted to account for the longer pulses. In addition, there were concerns that the larger variability in signal size over time could lead to increased phase measurement noise.

All of the statistical improvements that we implemented in ACME II improved the

fraction of ThO molecules produced by the beam source that are used in the spin precesion measurement, increasing the count-rate, $\dot{N}$.

The ACME II upgrades fall into three classes:

1. **Statistical improvements.** Since the ACME I systematic errors were small and under control, most efforts in increasing the ACME sensitivity reach revolved around improving the statistical sensitivity of the experiment. The statistical improvements to the ACME II experiment fall into three classes:

   (a) **Efficient Spin Aligned State Preparation through STIRAP:** ACME I used a lossy scheme (6% efficiency) with two steps of optical pumping to transfer population from the ground state X to the initial spin aligned state in the H state. ACME II achieves near unity (75%) transfer efficiency by using STImulated Rapid Adiabatic Passage (STIRAP), for a factor of 12 increase in the number of available molecules.

   (b) **Beamline Geometry Optimization:** We increased the separation of the experiment molecular collimators and reduced the distance between the beam source and the detection region, increasing the solid angle of beamsource produced molecules that enter the spin precession region. This increased the flux of molecules by a factor of 8.

   (c) **Fluorescence photon detection:** ACME II used a transition that allowed for detection of fluorescence photons at a shorter wavelength, 512 nm compared to 690 nm in ACME I. At this shorter wavelength, PMTs have a higher quantum efficiency (higher number of emitted photoelectrons per fluorescence photon). In addition, light guides and improvements in the geometry of the collection optics increase the proportion of emitted photons that were transferred to the PMTs. These improvements combine to increase the number of detected molecules by a factor of 5.

2. **Systematic error suppression.** The main systematic in ACME I resulted from a coupling of the non-reversing electric field ($\mathcal{E}^{\mathrm{nr}}$) to an ellipticity gradient in the preparation and readout laser beams. This ellipticity gradient was caused by thermal stress induced birefringence in the glass of the windows and electric field plates. In ACME II, we used improved electric field plates with a thinner absorptive layer of ITO for reduced absorption of the optical laser beam and fused silica rather than borosilicate for improved thermal conductivity of the glass substrate.

3. **Robustness and general experimental improvements.** A number of the described signal improvements required an increase in the experiment complexity. In order to maintain a favorable duty cycle, we reworked and improved many experimental systems with a goal to increase robustness and ease of use. The lasers are now low noise diode ECDLs with robust mechanical design locked to ULE cavities with typical locking times of over 1-2 weeks. The data acquisition system was updated and streamlined. The vacuum system of the region between the beam source and the spin precession region was improved. We added pocket insets to the vacuum chamber, allowing for the fluxgate magnetometers to be closer to the molecular precession region (only $20 - 30$ cm away) for improved magnetic field measurement and monitoring.

While each signal improvement was implemented and tested independently in separate setups before implementation in the final experimental configuration, we verified the combined ACME II increase in sensitivity at the beginning of the ACME II data-taking campaign. The results of these tests are shown in Fig. 3.1.2, where the signal in ACME II is increased by a factor of ~ 400 over ACME I, corresponding to a factor of 20 increase in shot-noise limited sensitivity. The larger signal to noise also made using the ACME apparatus much easier. For example, finding any fluorescence signal at all became much easier, since signal-to-noise over typical running timescales became large enough even when different parts of the system were not perfectly optimized. Also, the larger shot-noise corresponding

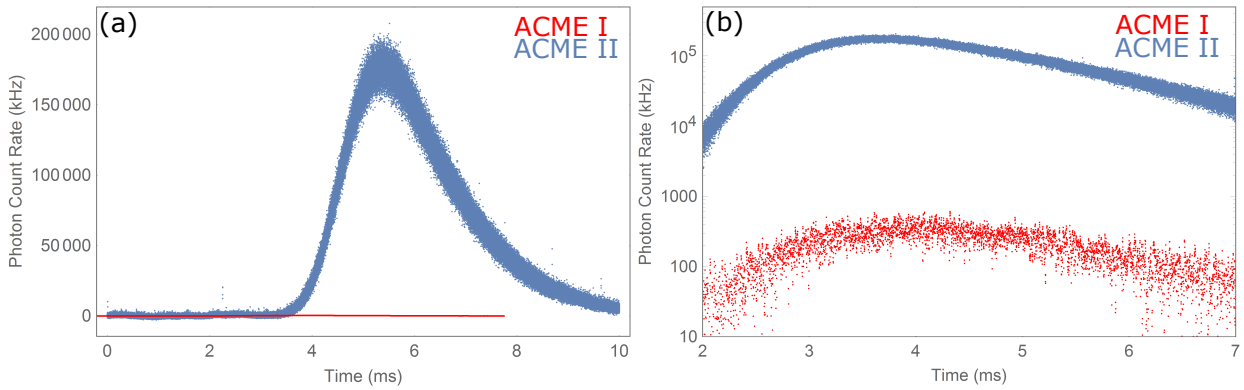

Figure 3.1.2: **Comparison between ACME I and ACME II signals.** Fluorescence traces showing signal levels obtained in ACME I and ACME II are displayed on **(a)** a linear plot and **(b)** a logarithmic plot.

to the larger signal made the experiment even less sensitive to background noise in our detection chain. This chapter describes the implementation of each of the improvements that contributed to the signal increase in detail.

3.2 Efficient state preparation through STIRAP

The largest individual signal gain in ACME II was from significantly increasing the number of useful ThO molecules by implementing STIRAP. STIRAP greatly boosts the preparation efficiency of the initial spin-aligned state of the $H^3\Delta_1$ "eEDM state", that represents the starting point of the ACME spin precession measurement. ACME I employed optical pumping to prepare this state, with an efficiency of approximately 6% [5, 6]. Using the STIRAP technique in ACME II, we have shown an increase in the population of the desired state by a factor of 12 ± 1, corresponding to a state transfer efficiency of $75 \pm 5\%$.

STIRAP is a population transfer scheme in a three-level system that relies on coherent two-photon coupling using time-varying electromagnetic fields [78]. Under appropriate experimental conditions, STIRAP can nearly completely transfer population from an initially populated state $|1\rangle$ to a final state $|3\rangle$ via a possibly lossy intermediary state $|2\rangle$. The process relies on the adiabatic evolution of a "dark" (i.e. not coupled to the radiation fields),

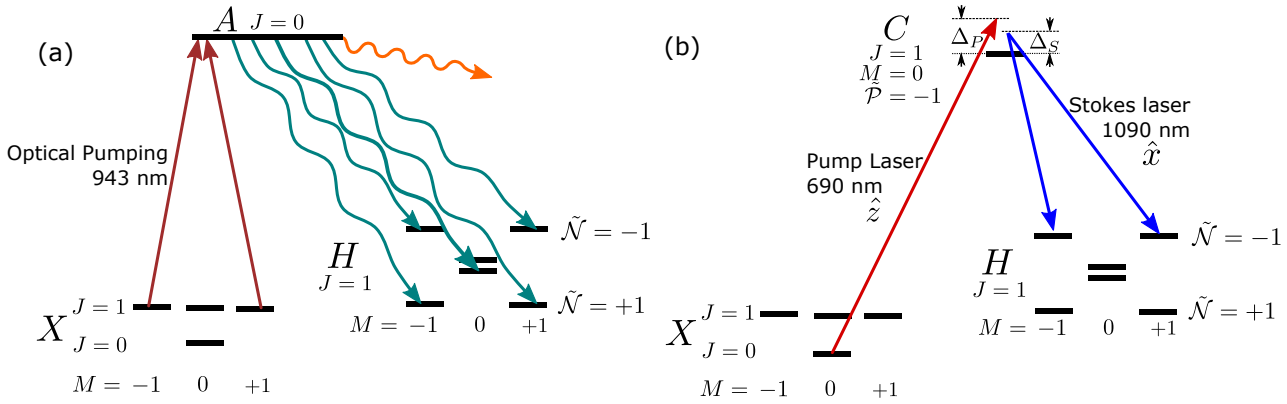

Figure 3.2.1: **Preparation of the initial spin-aligned state in $H^3\Delta_1$.** The state can be populated using either **(a)** an optical pumping scheme, as used in ACME I, or **(b)** a STIRAP scheme, as used in ACME II. For comparison purposes, we alternate between the two methods by blocking the corresponding laser beams. The detuningsof the STIRAP Stokes and Pump lasers are shown as Δ_S and Δ_P, respectively.

population-trapping state as molecules (or atoms) experience partially overlapping slowly varying fields: a Stokes pulse that introduces a dynamic Stark splitting of the unpopulated states $|2\rangle$ and $|3\rangle$ is followed by a pump pulse, coupling states $|1\rangle$ and $|2\rangle$. After its discovery and first demonstration with Na_2 dimers [79], STIRAP has been successfully applied to a number of experiments, such as in the preparation of ultracold dense gases of polar molecules [80, 81], creation of a well-defined photon number state in single-atom cavity quantum electrodynamics [82, 83], and quantum information processing [84, 85].

3.2.1 STIRAP implementation with the ThO energy level structure

In ACME I, the efficiency of preparing the initial state was limited by the incoherent nature of the optical pumping process that we used (partially illustrated in Fig. 3.2.1a) [5]. There, the $|X, J = 1^-, M = \pm 1\rangle$ states, where the superscript designates the parity quantum number, were optically pumped by two spatially separated 943 nm laser beams with orthogonal linear polarizations to the $|A, J = 0^+\rangle$ state. Approximately 35% of the population excited by the laser subsequently spontaneously decayed into the $|H, J = 1\rangle$ state

manifold[1]. Decay to each of the mixed-parity states $|H, J = 1, M = \pm 1, \tilde{\mathcal{N}}\rangle$ occurred with equal probability (1/6), with decay to the odd parity state $|H, J = 1^-, M = 0\rangle$ being twice as likely (1/3) and decay to the even parity state $|H, J = 1^+, M = 0\rangle$ being forbidden by the E1 parity selection rule. A linearly polarized 1090 nm laser beam, resonant with the $|H, J = 1, M = \pm 1, \tilde{\mathcal{N}}\rangle \rightarrow |C, J = 1, M = 0\rangle$ transition, addressed the spectrally unresolved states $|H, J = 1, M = \pm 1, \tilde{\mathcal{N}}\rangle$ of a particular $\tilde{\mathcal{N}} = \pm 1$ quantum number, pumping out half of the population and leaving behind a "dark" coherent superposition. This coherent superposition corresponds to an electron spin-aligned state [66]. For example, if the state preparation laser beam was linearly polarized along $\hat{x}$ and the $|C, J = 1^+, M = 0\rangle$ state was used, the prepared state was

$$|\psi(t = 0), \tilde{\mathcal{N}}\rangle = \frac{|M = +1, \tilde{\mathcal{N}}\rangle - |M = -1, \tilde{\mathcal{N}}\rangle}{\sqrt{2}}, \tag{3.2}$$

where $|M = \pm 1, \tilde{\mathcal{N}}\rangle$ is compact notation for $|H, J = 1, M = \pm 1, \tilde{\mathcal{N}}\rangle$.

The optical pumping transfer efficiency from the $|X, J = 1^-, M = \pm 1\rangle$ states to the H state manifold is $\sim 35\%$. One third of this population is contained in a pair of states with particular $\tilde{\mathcal{N}} = \pm 1$ and half of the population is in the selected spin-aligned state. We therefore estimate the efficiency of transferring population from the $|X, J = 1^-, M = \pm 1\rangle$ states to $|\psi(t = 0), \tilde{\mathcal{N}}\rangle$ to be approximately 6% in ACME I.

For ACME II, we use STIRAP to transfer population from the vibrionic ground state of the ThO molecule $|X, J = 0^+\rangle$ directly into the desired spin-aligned state of the H state with an efficiency of $75 \pm 5\%$ (Fig. 3.2.1b). We perform STIRAP via couplings to the $|C, J = 1^-, M = 0\rangle \equiv |2\rangle$ state, which has a lifetime of $\tau_C = 500$ ns [60]. The pump laser beam (690 nm) is linearly polarized along $\hat{z}$ and is near-resonant with the transition between states $|1\rangle$ and $|2\rangle$. The Stokes laser (1090 nm) is linearly polarized along $\hat{x}$ and is near-resonant with the transition between $|2\rangle$ and $|H, J = 1, M = \pm 1, \tilde{\mathcal{N}}\rangle$. Due to the

[1]This efficiency number uses an updated calculation, which includes all paths of decay from the excited A state, using data from the measurement discussed in Ref. [61]

parity of the intermediary state, population is transferred into the spin-aligned state $|3\rangle$ given in Eq. 3.2 [66].

In the ACME I optical pumping scheme, the orthogonal spin orientation could be prepared by choosing the opposite excited state parity, $|C, J = 1, M = 0\rangle$, or by rotating the polarization of the depletion 1090 nm laser to the $\hat{y}$-direction to address the opposite spin superposition. This was used as a "switch" for rejection of systematics [5]. In this STIRAP scheme, the orthogonal spin orientation cannot be prepared, but the lack of this switch did not affect our systematic error.

The radiative couplings between the three levels are characterized by the Rabi frequencies

$$\Omega_i(t) = \frac{\vec{D}_i \vec{E}_i(t)}{\hbar}, \tag{3.3}$$

where $i \in \{\mathrm{S}, \mathrm{P}\}$ corresponds to the Stokes or pump transition, $\vec{D}_i$ is the transition dipole moment, and $\vec{E}_i = E_i \hat{\epsilon}_i$ is the vector amplitude of the laser radiation field, which includes polarization. As shown in Figure 3.2.1b, the STIRAP efficiency is usually parametrized as a function of the detunings of the pump and Stokes lasers from their respective one-photon resonances Δ_P and Δ_S. The STIRAP transfer efficiency is in general significantly more sensitive to the two-photon detuning $\delta = (\Delta_P - \Delta_S)/2$ than the one-photon detuning $\Delta = (\Delta_P + \Delta_S)/2$ [78].

Choice of STIRAP intermediary state

STIRAP is a versatile process that can transfer population in a multitude of configurations. When the adiabatic criterion and power saturation condition are fulfilled, the coherent STIRAP process is not sensitive to the lifetime of the chosen intermediary state. As discussed in detail in Section 3.2.5, these two conditions for efficient transfer are significantly easier to accomplish when having access to larger Rabi frequencies. The Rabi frequencies of the Stokes and Pump transitions (Eq. 3.3) are proportional to the dipole moment of

the transition and the square-root of the laser intensity (through the electric field E). To achieve sufficiently high Rabi frequencies for the transfer, we chose transitions with high transition dipole moments and where relatively high power lasers are available.

The C state was carefully characterized for the ACME I experiment [5, 6, 60, 61]. The $X - C$ (690 nm) transition was used for initial ThO spectroscopy and molecule number measurements and later on for rotational cooling. The $C - H$ (1090 nm) transition was used as part of state preparation and for readout in ACME I. The knowledge from building laser systems at these wavelengths facilitated our design and implementation of the typically higher power and narrower line laser systems necessary for implementing STIRAP in ACME II. Simulations integrating the Schrodinger equation showed that the amount of available laser intensity with current technology (300 mW at 690 nm and 10 W at 1090 nm) was sufficient to achieve high efficiency STIRAP with parameter values that could be reasonably implemented in our system. Furthermore, tests with lower available laser power which were performed by Emil Kirilov in test configurations with less phase space densities showed promising STIRAP transfer efficiencies.

Choice of STIRAP starting rotational state

The choice of the rotational number J of the ground state X to perform STIRAP from was motivated by the desire to maximize the fraction of population that is available to the eEDM experiment. The ACME II experiment [5] uses a pulsed beam of ThO molecules generated by the same cryogenic buffer gas beam source used in ACME I [72]. The molecules exit the beam source with a forward velocity of $\sim$200 m/s along the $\hat{x}$ axis (Fig. 3.1.1). Their population is primarily concentrated in the electronic ground state X, in several rotational states with a Maxwell-Boltzmann distribution corresponding to a rotational temperature of about 4 K. At this temperature, the resulting fractions of molecules in the J=$\{0,1,2,3\}$ levels are $\{0.1,0.3,0.3,0.2\}$ respectively.

In ACME I, the useful population resided in the $M = \pm 1$ magnetic sub-levels of the

$|X, J = 1\rangle$ rotational level. This population was then transferred using a retro-reflected 943 nm optical pumping beam. To enhance signal, we increased the population in the $|X, J = 1, M = \pm 1\rangle$ states by transferring population from the other rotational levels through optical and microwave pumping. This increased signal by a factor of about 1.5–2.0 [5, 6].

In ACME II, when using STIRAP, a coherent process that maps a single non-degenerate quantum state into another, the population transfer has to start in a single quantum level. We could prepare, for example, a single magnetic level $|X, J = 1, M = 0\rangle$ through a second step of rotational cooling, but such a state would be remixed as the molecules travel from the stem into the interaction region, where no quantizing field is available. Rapidly changing electric field gradients would cause diabatic transfers to the other $|X, J = 1, M = \pm 1\rangle$ magnetic sub-levels, reducing the population in $|X, J = 1, M = 0\rangle$. To avoid such challenges, we instead decided to use the $|X, J = 0\rangle$ quantum state, which is completely non-degenerate due to the presence of a single $M = 0$ magnetic level. Another advantage of this $J = 0$ state is that is has a larger transition dipole moment to C than the $J = 1$ state, due to a larger Hohn-London factor. This reduced the power requirements for the STIRAP $X - C$ laser.

3.2.2 ACME II rotational cooling

To optimize population available for STIRAP, we developed a new rotational cooling scheme, designed to maximize the population in the $|X, J = 0^+\rangle$ state (see Fig. 3.2.2), rather that in $|X, J = 1^-\rangle$, which was used in ACME I . The first step in this scheme is identical to ACME I, in which laser light at 690 nm optically pumps molecules from $|X, J = 2^+\rangle$ to $|X, J = 0^+\rangle$ via the $|C, J = 1^-\rangle$ state. To pump out all molecules, we use 5–7 passes of a laser beam resonant with the $|X, J = 2^+\rangle - |C, J = 1^-\rangle$ transition. Each pass has orthogonal polarization to the previous, addressing all M states in $|X, J = 2^+\rangle$. Due to parity and angular momentum selection rules, this results in optical

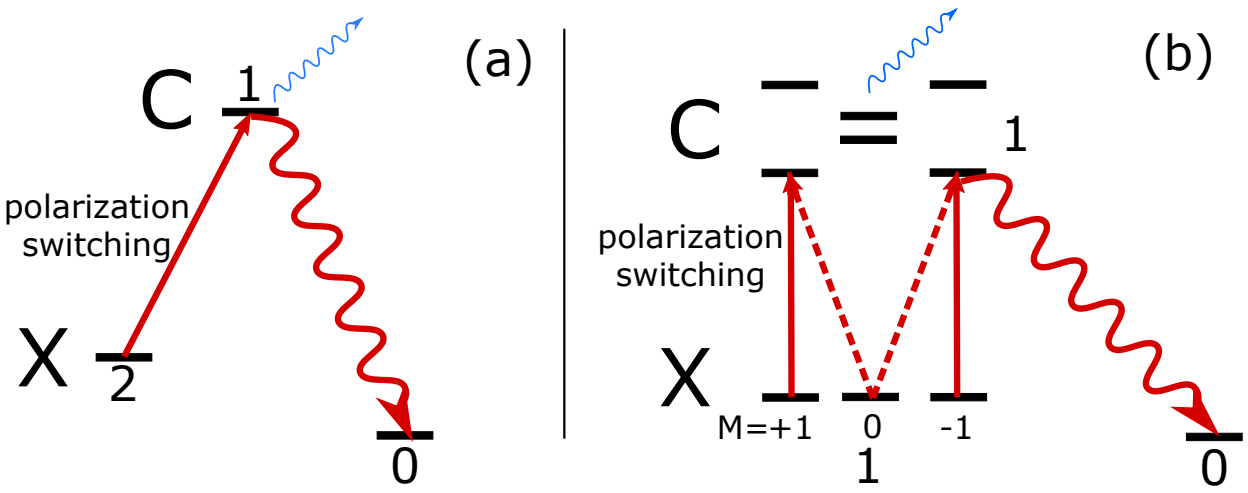

Figure 3.2.2: **The two ACME II rotational cooling steps. (a)** Population is transferred from $|X, J = 2^+\rangle$ to $|X, J = 0^+\rangle$ by optical pumping with 5–7 orthogonal polarization passes of a laser beam resonant with $|X, J = 2^+\rangle - |C, J = 1^-\rangle$. **(b)** An electric field mixes the parity of the $|C, J = 1^\pm, M = \pm 1\rangle$ levels allowing for population to be transferred from $|X, J = 1^-\rangle$ to $|X, J = 0^+\rangle$.

pumping of population from $|X, J = 2^+\rangle$ to $|X, J = 0^+\rangle$. The second stage is performed in an applied electric field of ≈ 100 V/cm, which weakly mixes the opposite-parity excited states $|C, J = 1^\pm, M = \pm 1\rangle$. A multipass, alternating polarization laser beam drives the $|X, J = 1^-\rangle \leftrightarrow |C, J = 1^{\text{mixed parity}}, M = \pm 1\rangle$ transition, partially transferring population from $|X, J = 1^-\rangle$ to $|X, J = 0^+\rangle$. The efficiency of population transfer in this scheme is limited by the branching ratio of the $X - C$ transition, which is 0.65-0.8%. These two combined rotational cooling steps increase the population in the $|X, J = 0^+\rangle$ state by a factor of 2-2.5.

While the rotational cooling gain in ACME II is larger than in ACME I, the initial population is lower, so they combine to give about the same amount of useful population. The gain in usable molecules due to STIRAP for the ACME II measurement compared to ACME I can then be parameterized as $G = g_{\text{RC}} \cdot g_{\text{ST}}$, with rotational cooling gain $g_{\text{RC}} \approx 1$. From here on, we refer only to the STIRAP improvement factor g_{ST}.

The laser radiation used for the two rotational cooling steps is derived from extended cavity diode (ECDL) lasers at 690 nm. The lasers are frequency-stabilized using a scanning

transfer cavity with computer-controlled servo [58]. The reference light at 1064 nm is derived from an Nd:YAG laser, which is frequency-doubled and stabilized to a molecular iodine line via modulation transfer spectroscopy [86].

A future improvement in rotational cooling efficiency in ACME III could come from replacing the 690 nm lasers resonant with the $X - C$ transition with 512 nm lasers resonant with the $X - I$ transition. The $X - I$ branching ratio was measured to be 0.91, significantly larger than for $X - C$, which is 0.65-0.8 [75]. The larger branching ratio reduces the rotational cooling loses to other electronic and vibrational states. This could further improve g_{RC} by a factor of 1.5–2. A laser at 512 nm is already in use for testing optical cycling and could also be implemented as part of rotational cooling.

3.2.3 STIRAP LASER SYSTEM

The STIRAP transfer is implemented with light derived from two systems of external cavity diode lasers (ECDLs) at 1090 nm (Stokes laser, near-resonant with the $C - H$ transition) and 690 nm (pump laser, near-resonant with the $X - C$ transition). The lasers are Toptica DL Pro with AR coated diodes (LD-1080-0300-1 and LD-0695-0040-AR-1). The lasers are actively frequency stabilized through simultaneous locking to a horizontal cylindrical ultra low expansion (ULE) glass cavity with a finesse of 30,000. The cavity is housed in a lab-built evacuated aluminum enclosure with two stages of temperature control. It is temperature regulated near the critical temperature of the ULE spacer of 27.8 °C with a long-term (usually days) stability better than 1 mK (Fig. 3.2.3a).

The lasers are locked to the ULE resonator using a feedback system based on the Pound-Drever-Hall (PDH) locking scheme [87] (Fig. 3.2.3b). The feedback is provided by a commercial digital proportional-integral-derivative (PID) regulator (Digilock 110), with a fast component to the current (bandwidth up to 5 MHz), and a slow component to the grating piezo (bandwidth up to 100 Hz). A resonant EOM at 10 MHz creates the

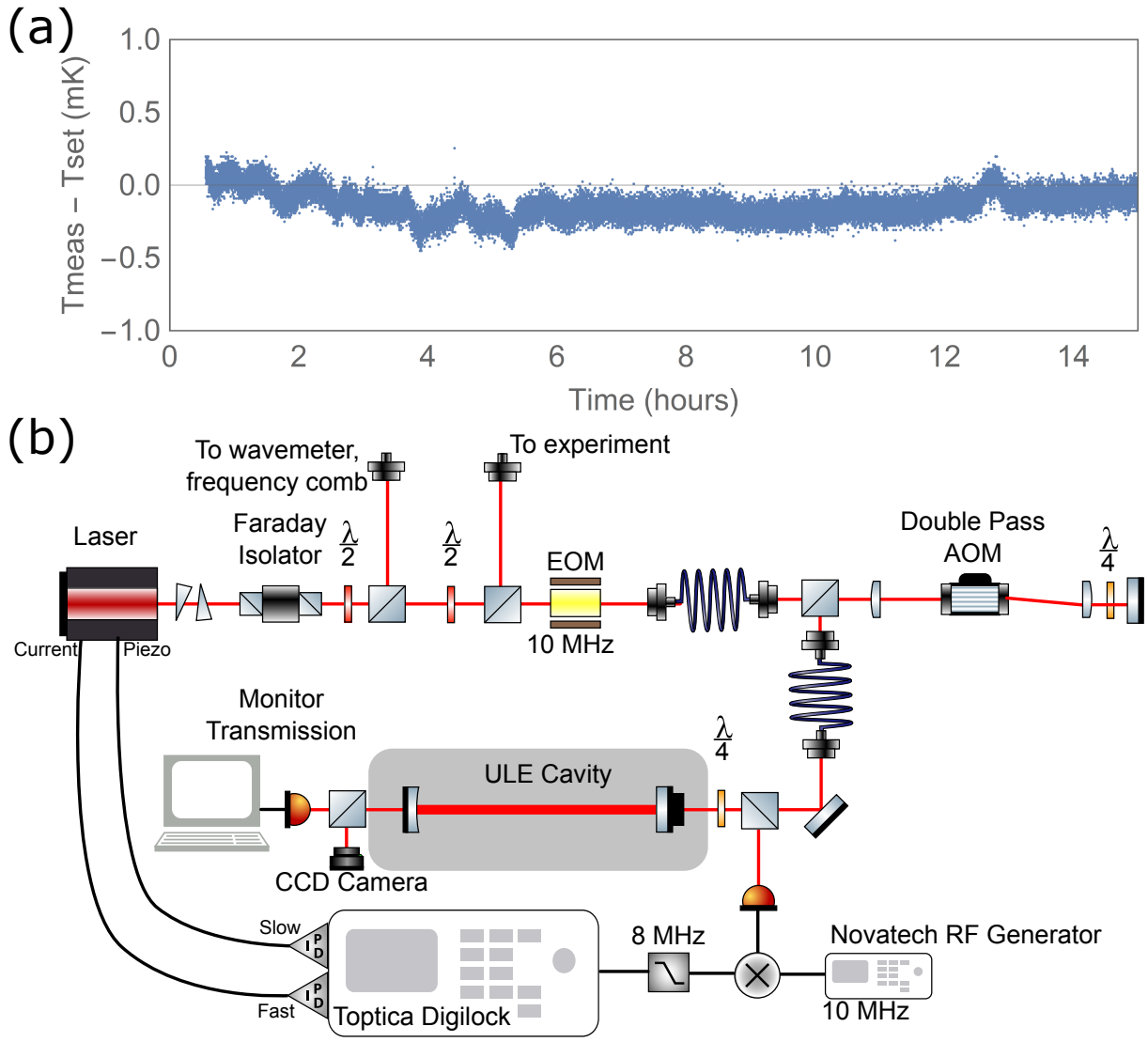

Figure 3.2.3: **ECDL laser lock to a ULE cavity system.** **(a)** Stability of temperature of the ULE cavity, measured with a free sensor, which is not used for temperature feedback. **(b)** Pound Drever Hall locking scheme of the ECDLs to the ULE cavity. The double pass AOM allows us to tune the frequency of the laser from resonance. Optical signals are in red and electronic signals are in black.

modulation sidebands necessary for the PDH lock, and an AOM allows for freely tuning the laser frequency away from the resonances of the cavity. A commercial fiber frequency comb (Menlo Systems) locked to a GPS-stabilized RF reference allows for monitoring and long term correction of the absolute laser frequencies. The largest correction is a linear drift of ∼7 kHz/day, due to the mechanical relaxation of the ULE spacer. The short term linewidth of the lasers was verified through a beat note measurement between two identically built systems locked to separate ULE cavities to be below 150 Hz.

The 690 nm laser light is amplified by a commercial tapered amplifier (TA-0690-0500-1) to ∼300 mW. The output of the TA is then coupled through a single-mode fiber that also acts as a spatial filter for light delivered to the experiment. The 1090 nm laser is amplified by a commercial fiber amplifier (Nufern PSFA-1084-01-10W-1-3) to 10 W.

1090 nm Stokes laser $\tilde{\mathcal{N}}$ switch implementation

The 1090 Stokes laser beam sets the spin orientation of the ACME II spin precession measurement. One of the main advantages of the $H^3\Delta_1$ state structure is that we are able to reverse the direction of the internal electric field $\vec{\mathcal{E}}_{\text{eff}}$ without reversing the laboratory electric field $\tilde{\mathcal{E}}$. We do so by switching the spectrocopic levels that the lasers address, which we denote by $\tilde{\mathcal{N}} = \pm 1$. This reversal is a powerful tool for rejection of systematic errors (see Section 2.1). The $\tilde{\mathcal{N}}$ switch requires that STIRAP populate either the $\tilde{\mathcal{N}} = +1$ or $\tilde{\mathcal{N}} = -1$ states, which are spectroscopically resolvable. To change the target level for population transfer, we tune the frequency of the 1090 nm Stokes laser to be on resonance with either the $\tilde{\mathcal{N}} = +1$ or $\tilde{\mathcal{N}} = -1$ states.

The frequency difference between the $\tilde{\mathcal{N}} = +1$ and $\tilde{\mathcal{N}} = -1$ states is given by the Stark shift at the chosen electric field value. The ACME II experiment was performed with two values of the electric field magnitude, $1\mathcal{E}$ ($\mathcal{E}_{\text{mag}} = 80$ V/cm), and $2\mathcal{E}$ ($\mathcal{E}_{\text{mag}} = 140$ V/cm). The criteria that we used for choosing these two optimal electric field values are described

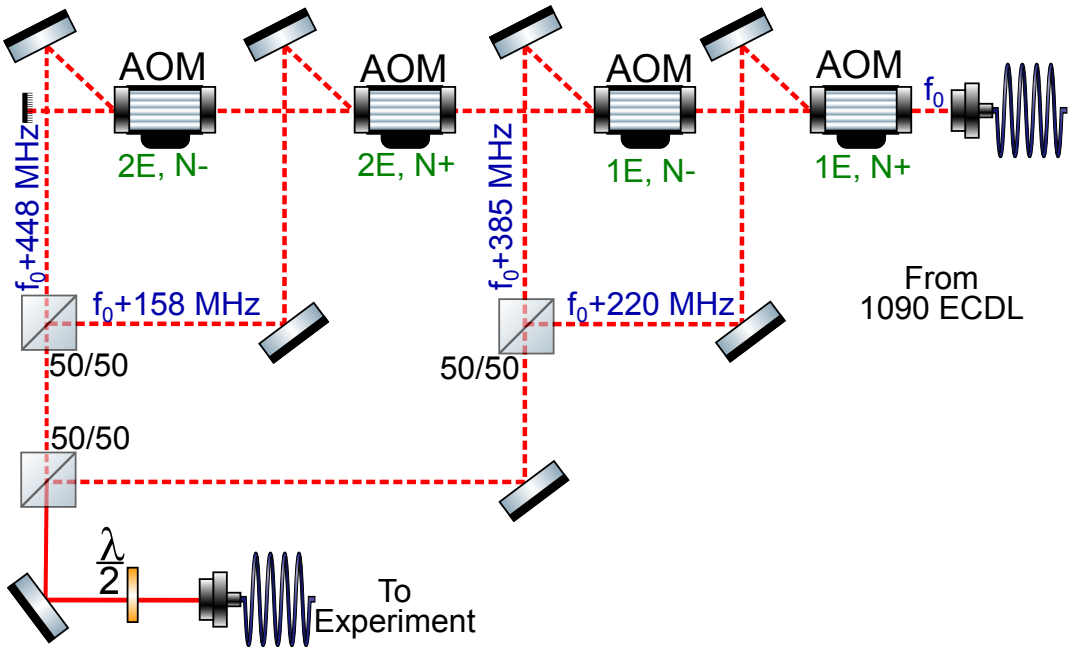

Figure 3.2.4: **1090 nm Stokes laser AOM optical setup for performing the $\tilde{\mathcal{N}}$ switch.** A set of four AOMs allow us to select the experiment $\tilde{\mathcal{N}}$, $|\mathcal{E}_{\text{mag}}|$ state ($\tilde{\mathcal{N}} = +1$ or $\tilde{\mathcal{N}} = -1$, $1\mathcal{E}$ or $2\mathcal{E}$) that STIRAP transfers population to. We switch between these states but sequentially turning one AOM on and the other three off. Each of the four AOMs are labeled with the state they address when turned on (green) and the beams of laser light (red) are labeled with the frequency shift added by the AOM to the frequency of the 1090 nm Stokes laser to ensure resonance with the selected Stark shifted state. All possible paths are recombined using 50/50 beamsplitters in the same fiber before being sent to the experiment.

in Section 3.3.2. To address either of the four configurations corresponding to $\tilde{\mathcal{N}} = \pm 1$ and $\mathcal{E}_{\text{mag}} \in \{1\mathcal{E}, 2\mathcal{E}\}$ configurations, there are four frequencies the STIRAP 1090 laser beam has to be resonant with. We implemented this capability on a separate breadboard with a set of four AOMs, as shown in Fig. 3.2.4. Turning one AOM on and the other three off shifts the frequency of the laser to be resonant with the selected $\tilde{\mathcal{N}} = \pm 1$ state for either $1\mathcal{E}$ or $2\mathcal{E}$ configuration. The power loss in this system was significant due to the need to recombine the laser beam on the same path using 50/50 beamsplitters. We used a separate Nufern fiber amplifier prior to the switching system to compensate for the factor of ~ 6 loss in power due to the $\tilde{\mathcal{N}}$ switching setup.

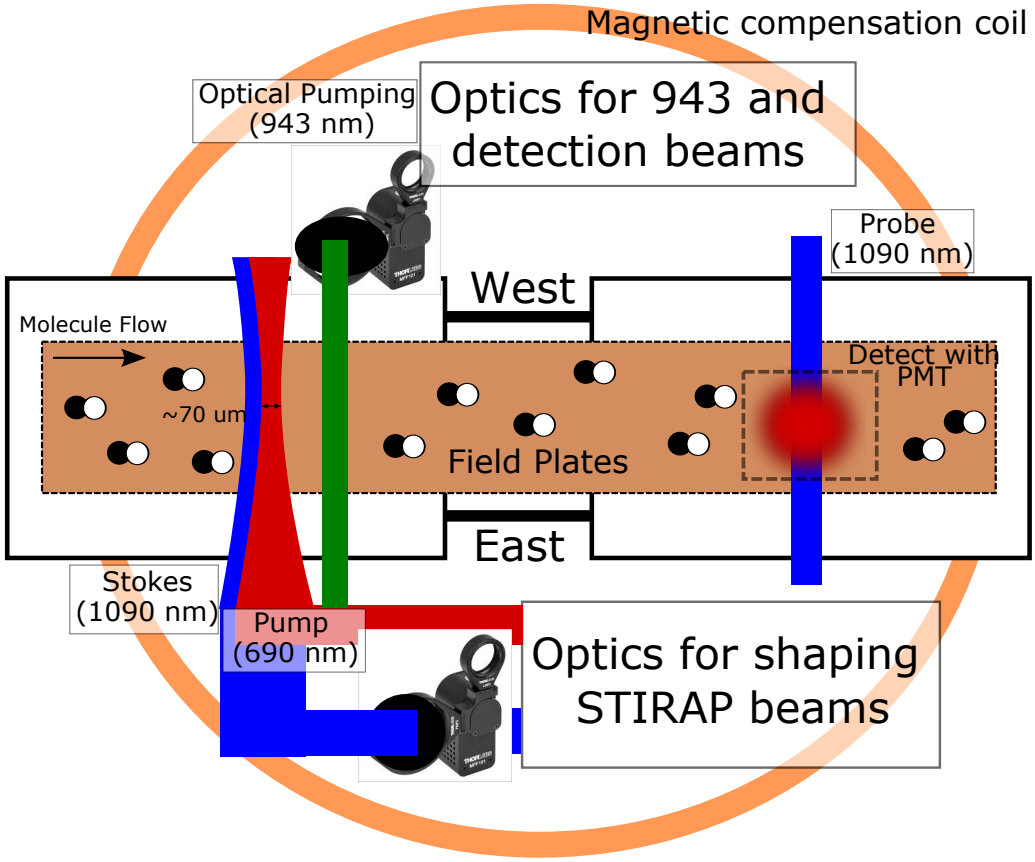

Figure 3.2.5: **Experimental system for initial tests of STIRAP in the stem region.** ThO molecules travel from left to right. A set of copper field plates apply the required electric field and a magnetic coil compensates the ambient magnetic field to first order. The molecules are transferred either by using overlapped 690-1090 nm STIRAP lasers or by optical pumping (943 nm). 690 fluorescence photons excited by a second optical pumping 1090 nm laser beam are detected with a PMT that is placed above the experiment vacuum chamber.

3.2.4 Initial STIRAP tests and phase noise

We initially set up preliminary tests of STIRAP efficiency in the stem region (Fig. 3.2.5). These tests were performed in a different geometry than that used in the ACME II apparatus, with electric and magnetic fields which were significantly worse controlled than in the typical ACME experiment. For applying the electric field, we used copper field plates with ITO coated glass inserts for optical access for photon collection. Due to the limited size of the field plates, there were significant (several percent level) amounts of fringing electric

field gradients. There was no magnetic shielding and a compensation coil was used to cancel the ambient magnetic field to first order. However, the laser optical access available in this system was much more extensive compared to that typically available in the ACME II apparatus. Large solid angle access was available through the side windows of the stem vacuum chamber.

To replicate the velocity distribution of the molecular beam in the ACME II apparatus, we used adjustable collimators to reduce the transverse velocity of the molecular beam to $\sigma_{\text{Doppler}} \sim 2$ MHz. Population was transferred from X to H either through STIRAP, with a set of overlapped pump and Stokes beams, or less efficiently using opticaly pumping on the $H - A$ transition (943 nm). The amount of population in H was detected by optical pumping with a second 1090 nm beam resonant with the $H - C$ transition. The red 690 nm fluorescence photons were collected with a large diameter (3") cylindrical lens and read out by a PMT (Hamamatsu R8900U-20) and DAQ device.

These initial tests allowed us to observe the first signs of coherence, although the efficiency achieved was far from unity, saturating as a function of power to a maximum level of the $30 - 40\%$. Investigations into the cause of the low efficiency revealed that the 690 Pump ECDLs which were set up with low-cost, high power diodes (Opnext HL6750MG) had a relatively high phase noise pedestal that reduced the STIRAP efficiency.

Phase noise

Population transfer with close to unity efficiency of the entire ensemble of ThO molecules is possible in STIRAP if the two-photon detuning of the laser fields is near zero, i.e. roughly within the two-photon population transfer linewidth, $\Delta\omega_{2\text{ph}}$ [88]. In the case of significant differential phase noise between the pump and the Stokes lasers outside of this two-photon resonance linewidth, but within the one-photon resonance linewidth, the dark state eigenvector can acquire a component of the intermediary state $|2\rangle$ and population can radiatively decay out of the three-level system. The two-photon lineshape is difficult to describe ana-

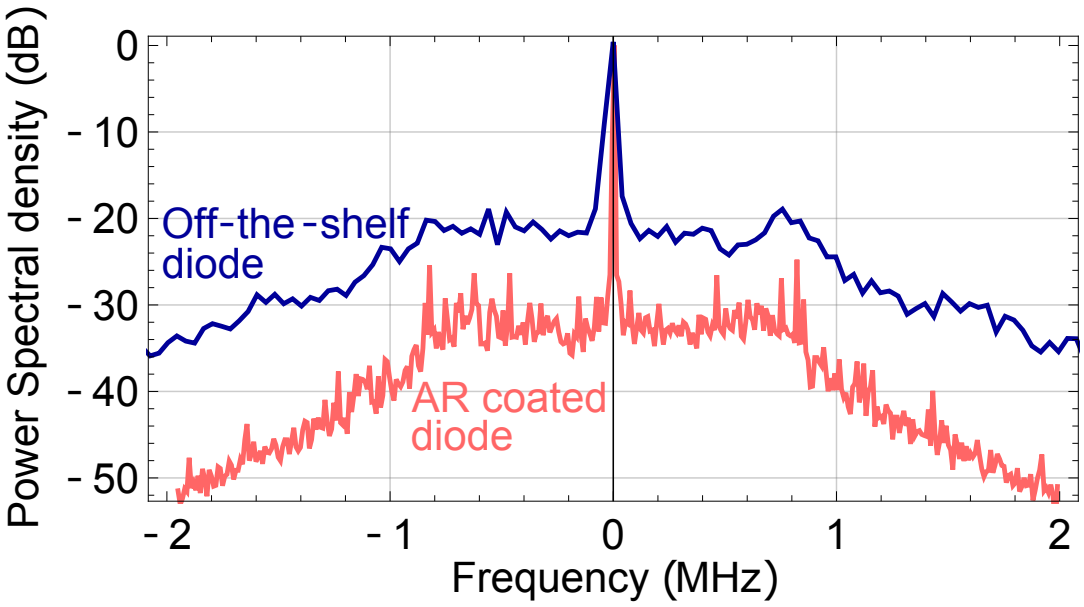

Figure 3.2.6: **Power spectral densities of the 690 nm STIRAP pump lasers.** The power spectral densities are typical of stabilized ECDLs with a very narrow central component on top of a much weaker broad pedestal. The AR-coated diodes provide a 10 dB reduction in the noise pedestal compared to the off-the-shelf diodes.

lytically and varies significantly with the specific properties of the system, such as molecule phase space distribution, Rabi frequencies, lifetime of the excited state, interaction time, and one-photon detuning. Nevertheless, in our system it is possible to crudely estimate $\Delta\omega_{2\text{ph}}$ as follows. Due to experimental constraints described below, we operate in a regime where the time when the STIRAP pulses overlap ΔT is on the order of $1/\gamma_C$, where γ_C is the decay rate of the intermediate excited state C. In this case, $\Delta\omega_{2\text{ph}}$ is within a factor of order unity of $\Omega_{\text{eff}}/2$, where $\Omega_{\text{eff}} = \sqrt{\Omega_P^2 + \Omega_S^2}$ is an effective two-photon Rabi frequency [88]. In our system, two-photon linewidths $\Delta\omega_{2\text{ph}}$ are typically in the range of $2\pi \times$ (2–4) MHz FWHM, and $\Omega_{\text{eff}} \approx 2\pi \times 14$ MHz, limited by the pump and Stokes laser beam intensities.

To characterize the phase noise present in our lasers, we measured their power spectral

densities using an optical beat note with a second laser system locked to a separate ULE cavity. Both systems were constructed to be as similar as possible. Figure 3.2.6 shows the power spectral density of a beat note between two identical 690 nm lasers (50 ms integration time). The power spectra show a narrow $\approx 2\pi\times150$ Hz FWHM peak on top of a much broader suppressed pedestal, typical of stabilized ECDLs. The width of the central peak was measured using a much smaller resolution bandwidth than shown in Fig. 3.2.6. The initial tests in the stem region were performed with a set of off-the-shelf diodes (Opnext HL6750MG) (blue in Fig. 3.2.6), which showed relatively high power in the spectral pedestal. Using these diodes, we observed that the STIRAP transfer efficiency saturated as a function of laser power, reaching a maximum level of only 30–40%. This behavior is consistent with recently reported detrimental effects on STIRAP transfer efficiency due to broad pedestals in the spectral lineshape that are common to stabilized ECDLs [89].

To reduce the laser phase noise in the pedestals, the off-the-shelf diodes were replaced with AR-coated diodes, which yield a narrower linewidth in an ECDL configuration before locking ($2\pi \times 200$ kHz compared to $2\pi \times 1.5$ MHz). The power spectrum of the beat note from locked ECDLs with the new diodes displays a much-suppressed pedestal (-30 dB instead of -20 dB) with approximately the same pedestal linewidth ($\sim 2\pi \times 2$ MHz FWHM), as shown in Fig. 3.2.6. Simulations using a phase noise model consistent with the improved power spectrum predict near-unity STIRAP efficiency. The 1090 nm laser power spectral densities, not shown here, exhibit similar pedestal suppression and pedestal linewidths to those of the 690 nm AR-coated diodes. Tests with the lower phase noise lasers are described in Section 3.2.6 and resulted in significantly higher transfer efficiency that before.

3.2.5 Considerations on the STIRAP spatial intensity profile

Although STIRAP has been performed in a number of atomic and molecular beam experiments [79–84], STIRAP within the ACME experiment is challenging for several reasons,

which mostly arise from the fact that we are operating with lasers with power outputs that are close to our minimum requirements for achieving efficient population transfer. In experiments such as ours, where entire molecular ensembles with large phase-space distributions are transferred via weak molecular transitions, the required laser powers and intensities are significant and can be challenging to achieve with current laser technology. To perform STIRAP with near-unity transfer efficiency, two-photon resonance must be maintained [78], which can place demanding constraints on the phase coherence of the lasers used [89]. Furthermore, it is important to apply smoothly-varying Stokes and pump pulses in such a manner that the adiabaticity criterion is fulfilled during the entirety of the transfer process [78, 90]. This is challenging due to the geometrical constraints of our apparatus.

In considering the spatial intensity profiles necessary for the laser beams, it is important to note that STIRAP relies on adiabaticity for obtaining high transfer efficiencies [78]. The "local" adiabaticity criterion,

$$\left| \frac{\dot{\Omega}_P \Omega_S - \Omega_P \dot{\Omega}_S}{\Omega_P^2 + \Omega_S^2} \right| \ll |\omega^{\pm} - \omega^0|, \tag{3.4}$$

where $|\omega^{\pm} - \omega^0|$ is the field-induced splitting in the dressed state energy eigenvalues [90], sets constraints on the spatial "smoothness" and overlap of the STIRAP laser beams. In the case when the laser profiles have smooth shapes, an integration of the above gives the "global" adiabaticity criterion $\Omega_{\text{eff}} \Delta T \gg 1$ [78].

Laser beamshaping is restricted by optical power availability and geometrical considerations. Along the $\hat{z}$ direction, the laser beams need to be significantly larger than the 25 mm diameter of the molecular beam in order to ensure that all molecules are addressed. The laser beam diameters necessary along the molecular beam forward velocity (along $\hat{x}$) are constrained by both the adiabaticity and two-photon resonance conditions. It can be shown that $\Omega_{\text{eff}} \Delta T \propto \sqrt{w_x}$, where w_x is the waist ($1/e^2$ intensity half-width) of the laser beam along $\hat{x}$ and the proportionality constant is a function of the transition dipole

moments, available laser power, laser beam diameter along $\hat{z}$, and molecular beam longitudinal velocity. The adiabaticity criterion, $\Omega_{\text{eff}}\Delta T \gg 1$, puts a lower limit on the waist at $w_x \gg 10$ μm.

The transverse velocity distribution of the ThO molecules in the STIRAP transfer region has a FWHM of 4.5 m/s. Since the two photons have a large relative wavelength difference (690 nm pump and 1090 nm Stokes), the different velocity classes will experience different Doppler shifts for the two STIRAP beams. This results in a distribution of two-photon detunings within the molecular beam with a width of $\Delta\omega_{\text{Doppler}} \approx 2\pi \times 1.2$ MHz FWHM. $\Delta\omega_{\text{Doppler}}$ must be smaller than the intrinsic two-photon linewidth of the STIRAP process $\Delta\omega_{2\text{ph}}$ to ensure near-unity transfer efficiency for all of the molecules in the ensemble. $\Delta\omega_{2\text{ph}}$ increases with increasing laser intensity [91], which we achieve by decreasing the laser beam waists along the molecular beam forward velocity, w_x. Simulations involving numerical integration of the Hamiltonian for the three-level system show that for close to unity transfer efficiency, we require $w_x < 300$ μm.

These limits are also set, in part, by the weak transition dipole moment of the Stokes transition. The $H - C$ dipole moment is estimated at 0.02 ea_0 [61]. Even with 10 W of power available for the Stokes transition, the typical peak Rabi frequencies accessed in our system, $\Omega_S \approx 2\pi\times 8$ MHz, are orders of magnitude smaller than available in the first demonstration of STIRAP [79]. For comparison, the transition dipole moment of the pump transition, $X - C$, is estimated at 0.3 ea_0 [60, 61], making the power requirements lower for that transition. With 50 mW of power, we are able to achieve pump peak Rabi frequencies of $\Omega_P \approx 2\pi \times 12$ MHz.

Laser launch geometry

The $|X, J = 0^+\rangle \equiv |1\rangle$ initial state and desired spin-aligned state $|\psi(t = 0), \tilde{\mathcal{N}}\rangle \equiv |3\rangle$ (from Eq. 3.2) are one unit of angular momentum projection apart ($\Delta M = \pm 1$). STIRAP between $|1\rangle$ and $|3\rangle$ requires one laser beam to have $\hat{z}$ polarization (corresponding to $\Delta M =$

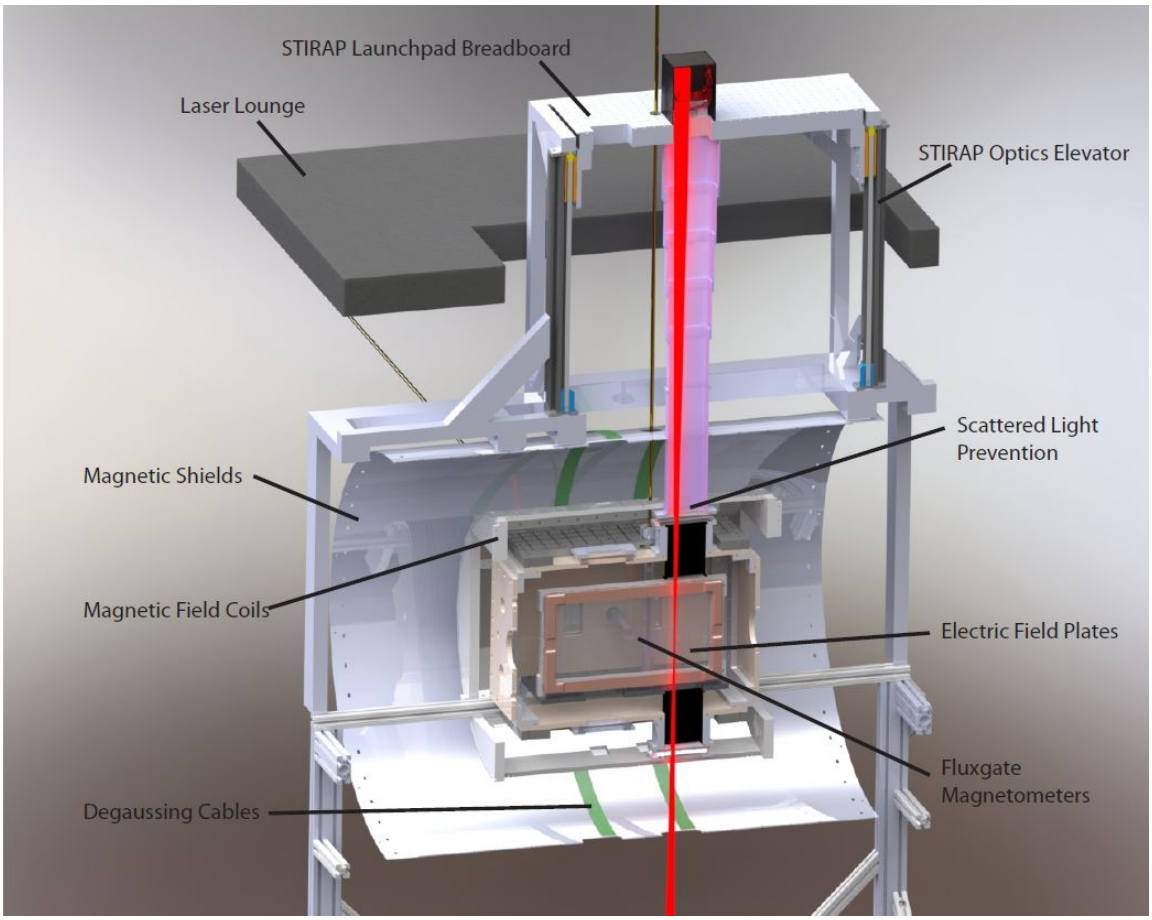

Figure 3.2.7: **Launching optics for the STIRAP lasers.** The optics are placed on a breadboard above the ACME II experimental apparatus. The STIRAP lasers are sent through the experiment vertically with a 45 degree mirror. A separately mounted platform (the "Laser Lounge") allows personnel access for optics set up and alignment.

0) and one $\hat{x}$ polarization (corresponding to $\Delta M = \pm 1$). Access to the $\hat{z}$ polarization in the molecular beam region requires that the laser beams be sent vertically (along the $\hat{y}$ axis), as shown in Fig. 3.2.7 and Fig. 3.2.10. Another very important advantage of this configuration is that the laser fields travel between the transparent glass electric field plates. This avoids potential optical damage to the electric field plates and prevents imperfect STIRAP laser intensity profiles due to reflections off the field plates.

The optics that allow for the alignment and launch of the STIRAP laser beams vertically through the experiment were mounted on a breadboard, which was fixed above the

experiment (Fig. 3.2.7). The breadboard was rigidly mounted on top of an 80/20 structure suported by the floor, which was built around the existing interaction region structure. A separate personnel support structure, which we named the "Laser Lounge", is supported by two aluminum I beams that are connected to supports in the walls of the lab. The three structures are mechanically isolated to prevent vibrations in one of the structures from propagating to the main experiment chamber.

Lasers spatial intensity profiles

To satisfy previously described constraints, the laser beams are expanded in $\hat{z}$ to waists of 20–25 mm and then collimated. Along $\hat{x}$, the optical beams are first expanded to diameters of 10–20 mm and then focused to the required small waists (w_x) of 150 μm (690 nm pump) and 160 μm (1090 nm Stokes), at the position of the molecular beam. The geometry of the STIRAP optical setup is shown in Figure 3.2.8. The Rayleigh lengths for the laser beams are 100 mm (pump) and 70 mm (Stokes), larger than the molecular beam diameter of 25 mm, ensuring small variations in the laser beam diameter and peak intensity across the molecular beam along the vertical direction $\hat{y}$. The resulting peak intensities are $I_S \approx 1000$ mW/mm^2 for the Stokes beam (1090 nm) and $I_P \approx 6$ mW/mm^2 for the pump beam (690 nm).

Due to experimental complexity associated with other components of the ACME experimental apparatus, such as large-volume mu-metal magnetic shields, experiment vacuum chamber, and magnetic field coils, the available optical access is limited. To allow for easy adjustability, the last optical element is placed outside of the magnetic shields, at a distance of 1.5 meters from the focal point. These constraints limit the achieved laser intensity profile quality. Figure 3.2.9 shows profiles of the laser beams along the molecules' forward velocity axis ($\hat{x}$), at the waist, measured with a CCD beam profiler. It is important to note that the quality of the beam shapes degrades at the vertical extremities of the molecular

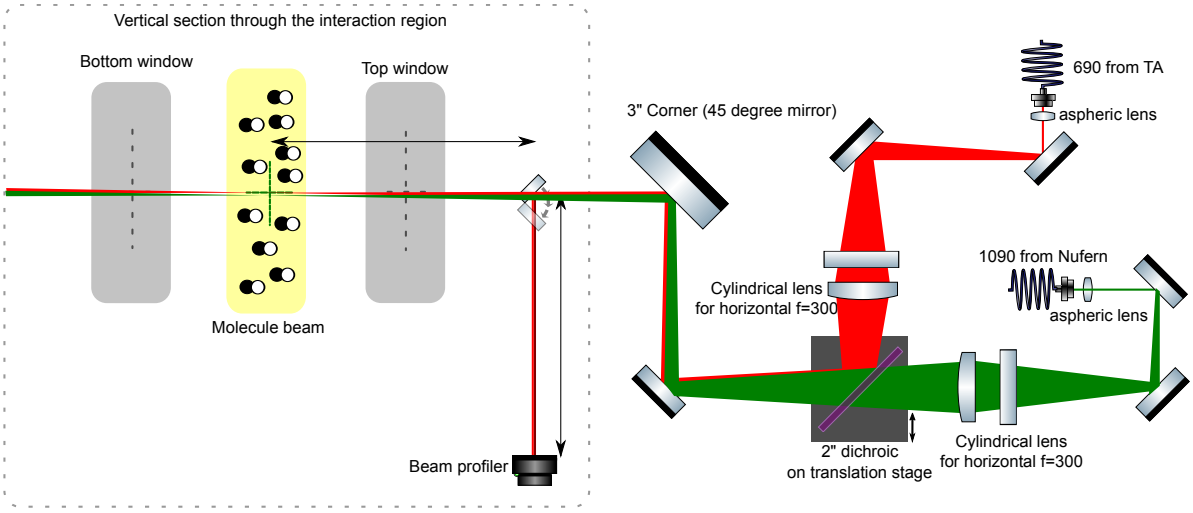

Figure 3.2.8: **Optics used for STIRAP beam shaping.** The 690 and 1090 nm lasers beams are separately expanded and then focused at the location of the molecular beam. They are later combined with a dichroic beamsplitter. The dichroic is mounted on a motorized translation stage that allows for fine tuning of the Pump-Stokes laser beams overlap. A 3″ mirror redirects the horizontal beam vertically through the experiment. We perform the shaping of the laser spatial intensity profiles and adjust their overlap by observing the beams on a CCD beam profiler at a distance equal to the distance to the molecular beam with a pick-off mirror.

beam, as one moves away from the focal point, with Airy-like lobes in the tails increasing in amplitude up to 10–20% of the maximum intensity.

Imperfect laser intensity profiles can either cause the local adiabaticity criterion (Eq. 3.4) to not be fulfilled, leading to non-adiabatic transfer of population to the intermediary lossy state $|2\rangle$, from which population decays out of the three level system, or can leave population in the initial state $|1\rangle$. Additionally, when on one-photon resonance, excess optical power in the tails of the laser beam profiles similar to an Airy pattern caused by clipping of the laser beams can drive optical pumping, depleting the population of the initial state $|1\rangle$ before the STIRAP process begins, or depleting the desired final state $|3\rangle$ after the two-photon process is complete. Careful alignment of the relative pointing of the Stokes and pump beams to better than a few milliradians is extremely important for maintaining optimal overlap over the vertical 25 mm spatial extent of the molecular beam.

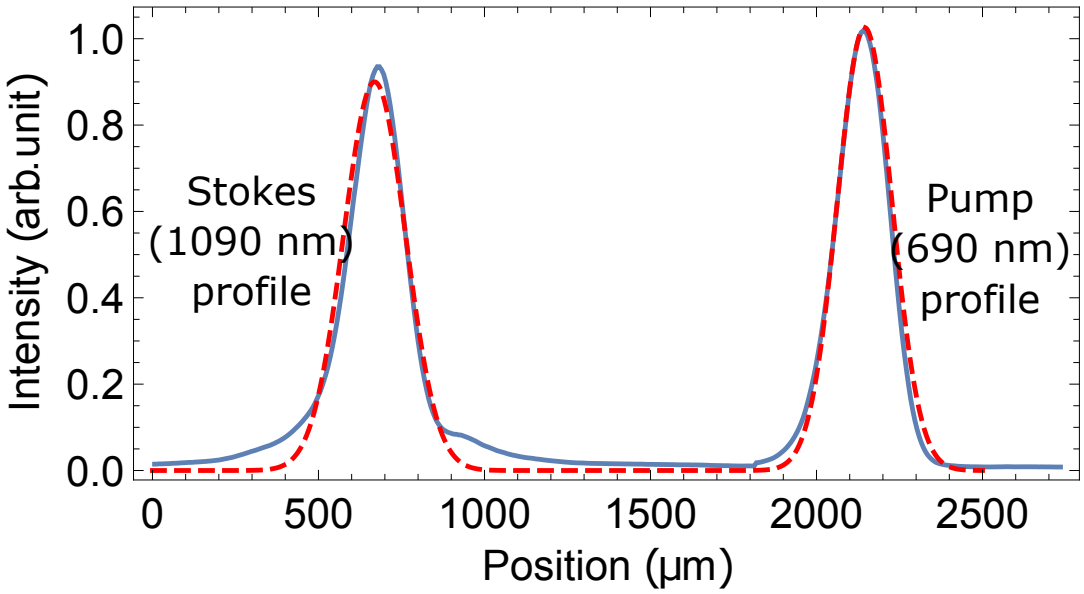

Figure 3.2.9: **STIRAP laser intensity profiles.** Typical normalized laser spatial intensity profiles (along the $\hat{x}$ axis) at the center of the molecular beam (integrated over a 5 mm range along $\hat{z}$ - blue line) and Gaussian fits (dashed red line). The beam profiles are greatly separated for clarity.

3.2.6 STIRAP implementation in ACME II apparatus

In the summer of 2014, we set up to test and implement STIRAP in the ACME II apparatus (Fig. 3.2.10). The beam source and stem region were the same as in the ACME II configuration. The ThO molecules are collimated 1.1 m downstream by a square aperture with dimensions of 25×25 mm. The molecules exit the aperture with a "flat-top" transverse velocity distribution with full width at half maximum (FWHM) of about 4.5 m/s. They travel into a region that has an uniform electric field $\vec{\mathcal{E}}$ that defines the $\hat{z}$ axis. The residual Earth's magnetic field has a component $\vec{\mathcal{B}}_z \sim 40$ mG along the $\hat{z}$ axis. The applied electric field magnitude $\mathcal{E} \approx 75$ V/cm fully polarizes the molecule in the lab frame [63].

After being prepared by either STIRAP or the ACME I method, electric and magnetic fields cause the spin-aligned state to accumulate a phase ϕ, resulting in

$$|\psi(\tau), \tilde{\mathcal{N}}\rangle = \frac{e^{-i\phi}|M=+1, \tilde{\mathcal{N}}\rangle - e^{+i\phi}|M=-1, \tilde{\mathcal{N}}\rangle}{\sqrt{2}}. \tag{3.5}$$

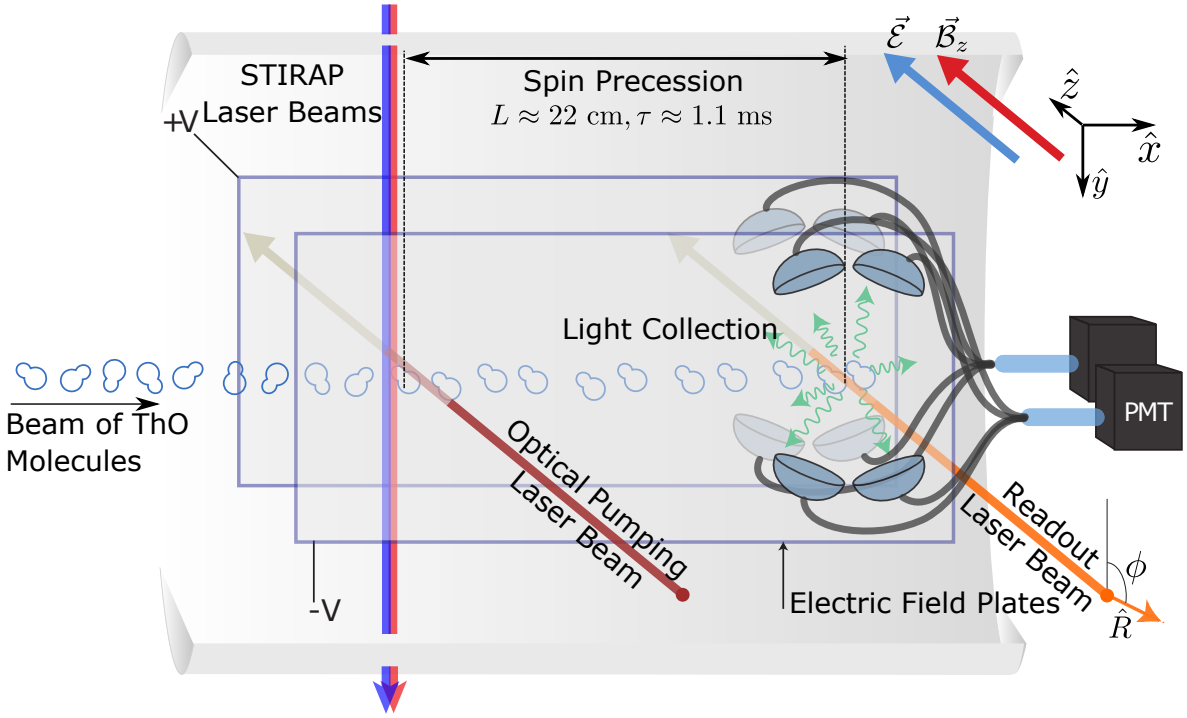

Figure 3.2.10: **Schematic of the experimental configuration used for implementing and testing STIRAP.** A collimated pulsed beam of ThO molecules enters the interaction region. The spin-aligned state is prepared, precesses in parallel electric and magnetic fields and is read out in the detection region by linearly polarized light, with resulting fluorescence collected and detected by photomultiplier tubes (PMTs).

The phase ϕ (see Eq. 2.5) is dominated by the effects of $|\mathcal{B}_z| = |\vec{\mathcal{B}} \cdot \hat{z}|$, and its $\tilde{\mathcal{B}} = \mathrm{sgn}(\vec{\mathcal{B}} \cdot \hat{z})$

$$\phi \approx \frac{-\mu_B g \tilde{\mathcal{B}} |\mathcal{B}_z| \tau}{\hbar}. \tag{3.6}$$

This phase also describes the angle by which the initial spin alignment rotates in the xy plane while in the interaction region.

After traveling through the interaction region for a distance $L \approx 22$ cm, corresponding to a time $\tau \approx 1.1$ ms, the phase of the spin-aligned state can be read out in the detection region using laser-induced fluorescence. The detection scheme relies on excitation of molecules with a linearly polarized readout laser to a short-lived state (the C state in ACME I, the I state in the current tests) that emits photons when decaying to the ground state X. These

photons are collected and detected by PMTs. In the typical ACME detection scheme, ϕ was determined by rapidly switching between polarizations. In the STIRAP experiments described here, we are primarily interested only in the total number of molecules, so the laser polarization direction is not switched, but rather kept constant. The laser's linear polarization direction $\hat{R}$ is chosen such that the detected fluorescence signal is maximized.

Care must be taken to minimize contamination of the detected signal with photons from other regions of the experiment, which would lead to additional noise in our eEDM data. The STIRAP scheme we describe in this paper uses pump coupling through the same $X - C$ transition that was used in ACME I for fluorescence detection (690 nm). We avoid the background from the STIRAP pump laser by using excitation at 703 nm from the H state to the I state instead of the C state [75]. The fluorescence accompanying the I state decay at 512 nm is easily separable from the 690 nm pump light background using interference optical filters.

Gain and efficiency measurements

In order to quantify the signal improvement over ACME I, we measure the STIRAP molecule gain factor g_{ST} by quickly switching between the STIRAP state preparation scheme and the ACME I optical pumping scheme by alternately blocking the relevant laser beams for these two schemes on a timescale of 5 seconds, faster than normal fluctuations in the molecule beam flux [72]. We detect the population in the prepared spin-aligned state by optically pumping on the $H - I$ transition with a linearly polarized laser and detecting laser induced fluorescence signals at 512 nm (S_{ST} and S_{OP}, respectively, for STIRAP and optical pumping) that are proportional to the transferred population.

Given that STIRAP state transfer is performed out of $|X, J = 0^+\rangle$, and the ACME I state transfer scheme was performed out of $|X, J = 1^-, M = \pm 1\rangle$, the gain factor g_{ST} can be expressed as

$$g_{\mathrm{ST}} = \frac{S_{\mathrm{ST}}}{S_{\mathrm{OP}}} \frac{\sum_{\pm} P(|X, J = 1^-, M = \pm 1\rangle)}{P(|X, J = 0^+\rangle)}, \tag{3.7}$$

where $P(|\psi\rangle)$ is the initial population in state $|\psi\rangle$. In the following measurements, rotational cooling schemes are not used. The initial populations are assumed to follow a Maxwell-Boltzmann distribution with a rotational temperature of 4 ± 1 K [2], as observed previously with our beam source [72].

The STIRAP transfer efficiency η_{ST} is calculated from the measured gain by $\eta_{\mathrm{ST}} = k \cdot g_{\mathrm{ST}}$, where the proportionality factor k is obtained from an auxiliary calibration measurement. This calibration was performed by measuring both gain and transfer efficiency under experimental conditions where efficiency can be extracted with ease. We performed STIRAP with a one-photon detuning of $\Delta = 2\pi \times 15$ MHz, much larger than the Doppler linewidths of the pump (690 nm) and Stokes (1090 nm) beams of $2\pi \times 3.2$ MHz HWHM and $2\pi \times 2.0$ MHz HWHM respectively. The detuning is also much larger than the one-photon natural linewidth of $2\pi \times 0.3$ MHz HWHM. This large one-photon detuning is chosen such that one-photon transitions are highly suppressed. Even in the case of non-adiabatic transfer, the population that is not transferred to the desired final state $|3\rangle$ remains in the initial state $|1\rangle$ rather than populating the lossy intermediary state $|2\rangle$ and decaying out of the three-level system. A second probe laser, at 690 nm, driving the $|1\rangle \rightarrow |2\rangle$ transition, produces laser-induced fluorescence proportional to the population in state $|1\rangle$. The resulting 690 nm fluorescence is detected with the same PMTs used to detect the 512 nm fluorescence from the I state, as discussed above.

Fluorescence signals proportional to the population in state $|1\rangle$ are recorded when performing STIRAP ($S_{\mathrm{ST}}^{|1\rangle}$) and normalized to the case when no excitation is present ($S_0^{|1\rangle}$). The fluorescence signal proportional to leftover population in state $|1\rangle$ after performing STIRAP is given by

$$S_{\mathrm{ST}}^{|1\rangle} = S_0^{|1\rangle}[1 - \eta_{\mathrm{ST}}(1 - \eta_{\mathrm{decay}})], \tag{3.8}$$

where the correction factor $(1 - \eta_{\mathrm{decay}})$ accounts for decay from the metastable state H

[2] A Neon buffer gas flow of 40 SCCM was used in these measurements.

back to state $|1\rangle$ during the time molecules travel between the population transfer and the readout regions. Vibrational and rotational branching ratios [3] along with the lifetime of the H state (~ 2 ms) [5] and the precession time ($\tau \approx 1.1$ ms) give an estimated $\eta_{\text{decay}} \approx 13\%$, which is the fraction of population in the H state that decays back to state $|1\rangle$. Under the same large one-photon detuning conditions corresponding to the calibration measurement, η_{ST} is extracted from Eq. 3.8, and the gain g_{ST} is measured using the same procedure described above. We then calculate the proportionality factor $k = \eta_{\text{ST}}/g_{\text{ST}} \simeq 6.2 \pm 0.3$, where the uncertainty is dominated by the error in the rotational Boltzmann factor. We then use k to infer the transfer efficiency η_{ST} from the measured gain g_{ST} for all other data, regardless of the laser detunings and other experimental parameters.

Experimental Results

The transfer efficiency measured under optimal conditions in our system is shown in Fig. 3.2.11a, as the spatial overlap of the pump and Stokes beams is varied, at a one-photon detuning $\Delta = 2\pi \times 8$ MHz. The two-photon resonance condition, $\delta = 0$, is maintained for molecules with zero transverse velocity. As one would expect from the underlying theory [78], optimal transfer efficiency is obtained for the Stokes pulse preceding the pump pulse, with a separation between the two comparable to the waist size (160 μm). The maximum observed transfer efficiency is $75 \pm 5\%$. We observe a second, lower efficiency, local maximum when the two laser beams overlap in the reverse order, with the pump pulse applied first. This feature is a consequence of a large one-photon detuning [79]. Unlike when on resonance, the initial state is not optically pumped by the STIRAP pump pulse arriving first. As the molecules pass through the laser beams, the overlap region allows a partially adiabatic two-photon process to drive a fraction of the population (40%) to the

[3] A vibrational branching from $(H, v = 0)$ to $(X, v = 0)$ of $\sim 94\%$ is calculated using the method of Ref. [92] and spectroscopic data from Ref. [93]. Rotational branching from $(H, J = 1, M = \pm 1)$ to $(X, J = 0)$ is 1/3.

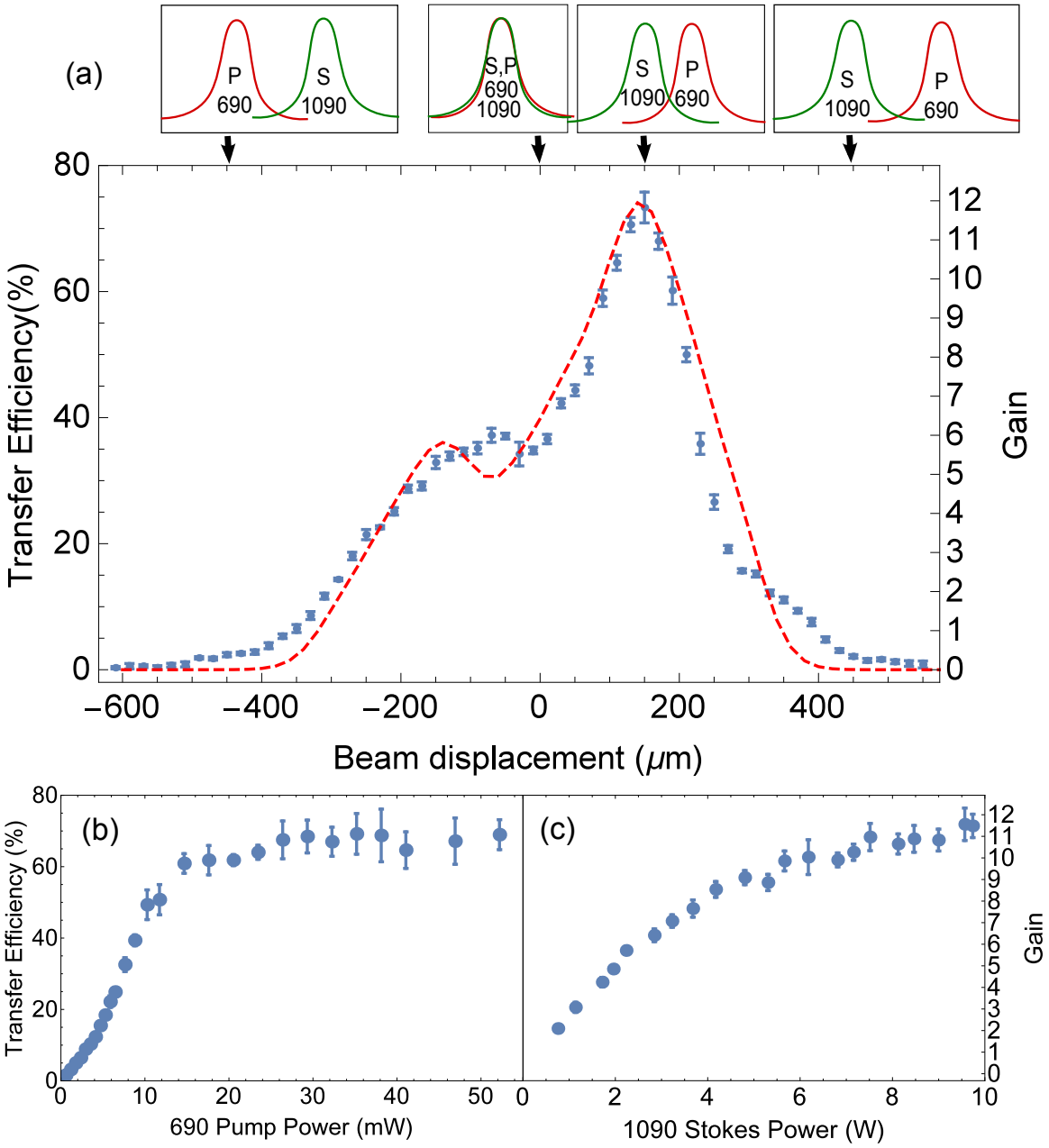

Figure 3.2.11: **STIRAP experimental results.** **(a)** Efficiency of population transfer from ground state $|X, J = 0\rangle$ to a spin-aligned state in the $|H, J = 1\rangle$ state, as a function of the spatial overlap of the pump and Stokes beams (laser beam widths $\approx$ 150 μm) for the experiment (blue) and simulation (red dashed line). Insets along the top show the relative positions of the optical field pulses, as they are encountered by the molecules, traveling from left to right. Power saturation behavior of the **(b)** pump 690 nm laser and **(c)** Stokes 1090 nm laser.

final state $|3\rangle$. We observe a dip in efficiency when the two pulses are completely overlapped and the transfer efficiency vanishes when the separation between the laser beams is large compared to the laser intensity widths, as the overlap between the Stokes and pump beams drops to zero. Simulations performed by integrating the Schroedinger equation with a three-level system Hamiltonian show qualitative agreement to the data (fits shown in Fig. 3.2.11a). The simulations were performed with molecular ensemble parameters consistent with the measured experimental values. In addition, a Stokes and pump relative laser beam pointing misalignment of $\sim$5 mrad was included in the simulation and partially accounts for the lower than unity efficiency.

Figures 3.2.11b and 3.2.11c show the dependence of transfer efficiency on the power of the Stokes and pump lasers. Each data set is taken with the other laser at full power, always at the same one-photon detuning $\Delta = 2\pi \times 8$ MHz and on two-photon resonance $\delta = 0$, for molecules with zero transverse velocity. The 690 nm pump transition $|1\rangle \rightarrow |2\rangle$ is driven well into the saturated regime. The STIRAP transfer efficiency vs. 1090 nm Stokes laser power data shows that higher transfer efficiency might be achievable with greater power (Fig. 3.2.11c).

Figure 3.2.12 shows the variation of the transfer efficiency with the detunings of the two lasers. This data is taken with both lasers at full power, with optimal overlap. As expected, STIRAP efficiency is very sensitive to two-photon detunings $\delta \neq 0$, but quite robust to one-photon detunings $\Delta \neq 0$. Unlike many other STIRAP systems, we obtain higher efficiency when running at one-photon detunings that are large compared to the Doppler linewidths of the pump and the Stokes beams. Transfer efficiency decreases substantially, to 10–20%, when on one-photon resonance. We believe that this is due to sharp changes in the spatial intensity profiles of the laser beams across the large spatial extent (25 mm) of the molecular beam. On resonance, any excess laser intensity in the wings of the spatial intensity profiles (due e.g. to scatter or diffraction from apertures in the laser beam paths) can drive optical pumping, depleting the population of the initial state. This effect is accentuated by the

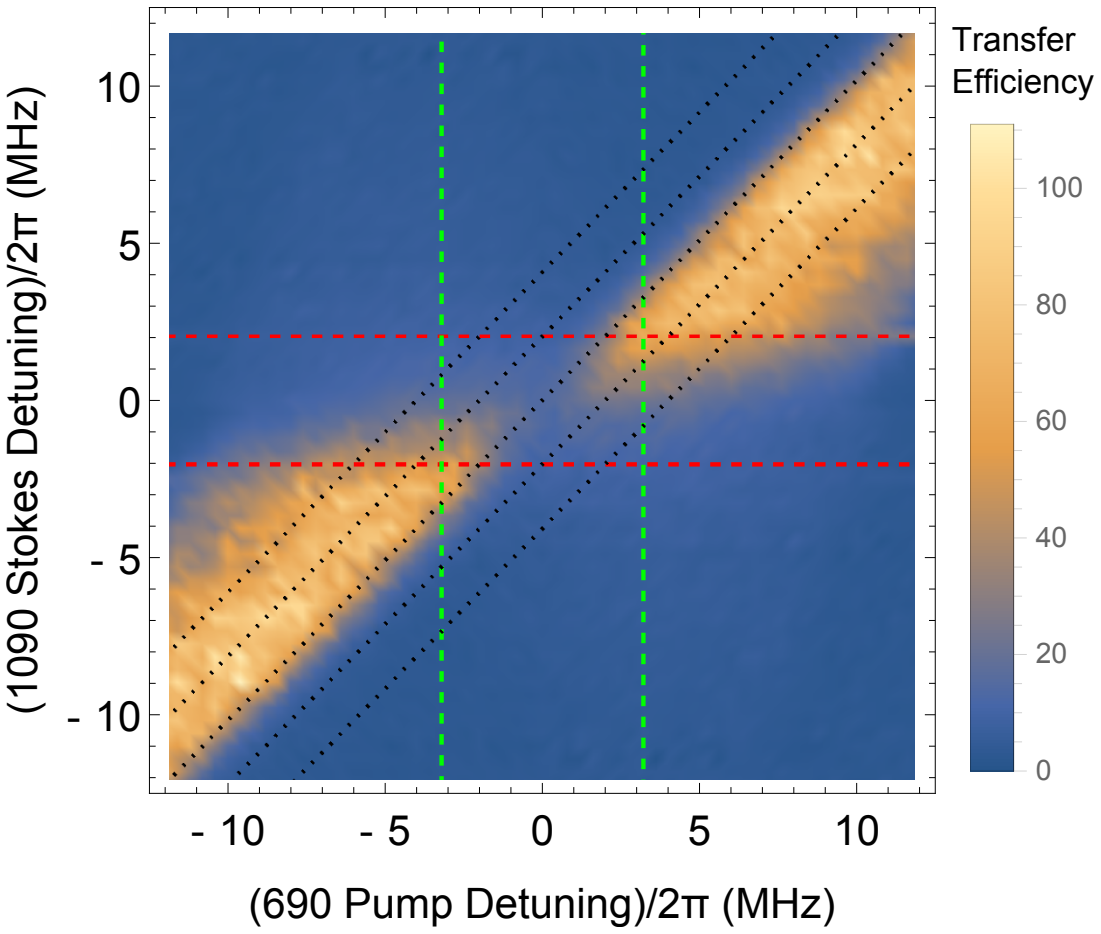

Figure 3.2.12: **Variation of STIRAP efficiency with detuning.** Density plot showing variation of the measured transfer efficiency with the detunings of the two lasers. Green (red) dashed lines are a guide to the eye, and indicate the extent of the pump (Stokes) one-photon resonance FWHM linewidth. Dotted black lines that indicate constant two-photon detunings are drawn at $\delta \in 2\pi \times \{-4, -2, 0, +2, +4\}$ MHz.

relatively small transition dipole moment of the $|2\rangle \rightarrow |3\rangle$ Stokes transition, since population in the intermediary $|2\rangle$ state decays to other non-resonant molecular states (mostly to other rotational levels of the ground state X) with a much larger probability than to the desired state $|3\rangle$. Simulations of the molecule ensemble, when integrating the Schroedinger equation of the three-level system, show similar behavior when including Airy-like wings in the spatial intensity profiles of the lasers with amplitudes at the level of 10–20% of the maximum intensity, comparable to the ones observed in our laser beams.

At one-photon detunings that are large compared to the one-photon Doppler linewidths of the pump and Stokes lasers, the two-photon profile is asymmetric (Fig. 3.2.12): the transfer efficiency drops at a faster rate as the two-photon detuning is tuned towards the pump one-photon resonance than when the two-photon detuning is tuned towards the Stokes one-photon resonance. This is general STIRAP behavior that occurs when at one-photon detunings that are large compared to Ω_{eff} and when the Rabi frequencies are not equal [94]. In our case $\Omega_P/\Omega_S \approx 1.5$. We later directly verified the dependence of the STIRAP lineshape on the Ω_P/Ω_S ratio by tuning the power of the 690 Pump laser, as shown in Figure 3.2.13. As expected, the STIRAP lineshape is symmetric when $\Omega_P/\Omega_S \approx 1$.

We verified that the STIRAP process directly populates a spin-aligned state $|3\rangle$ required for performing the spin precession measurement [66]. Figure 3.2.14 shows sinusoidal oscillations of the fluorescence signal characteristic of our spin analysis method, as the angle of the linear polarization of the readout beam is varied with a half-wave plate. The contrast of the spin analysis fringes is $93 \pm 2\%$, comparable to that observed with the ACME I preparation method, $94 \pm 2\%$ [5].

3.2.7 Requirement for a refinement laser

Due to the high power (10 Watts) of 1090 nm Stokes laser used and the difficulties of the geometry of the STIRAP optical setup, we expected imperfections in the STIRAP transfer process to lead to systematic errors or statistical noise. More details on our investigations into systematic effects caused by STIRAP performed in this geometry are given in Section 5.5. In order to suppress these type of effects, we implemented a second linearly polarized "refinement" laser beam that reprojects the STIRAP prepared spin onto the polarization axis of the "refinement" laser. This laser optically pumps away the unwanted spin component and leaves behind a dark superposition of the two resonant $M = \pm 1$ sublevels of H.

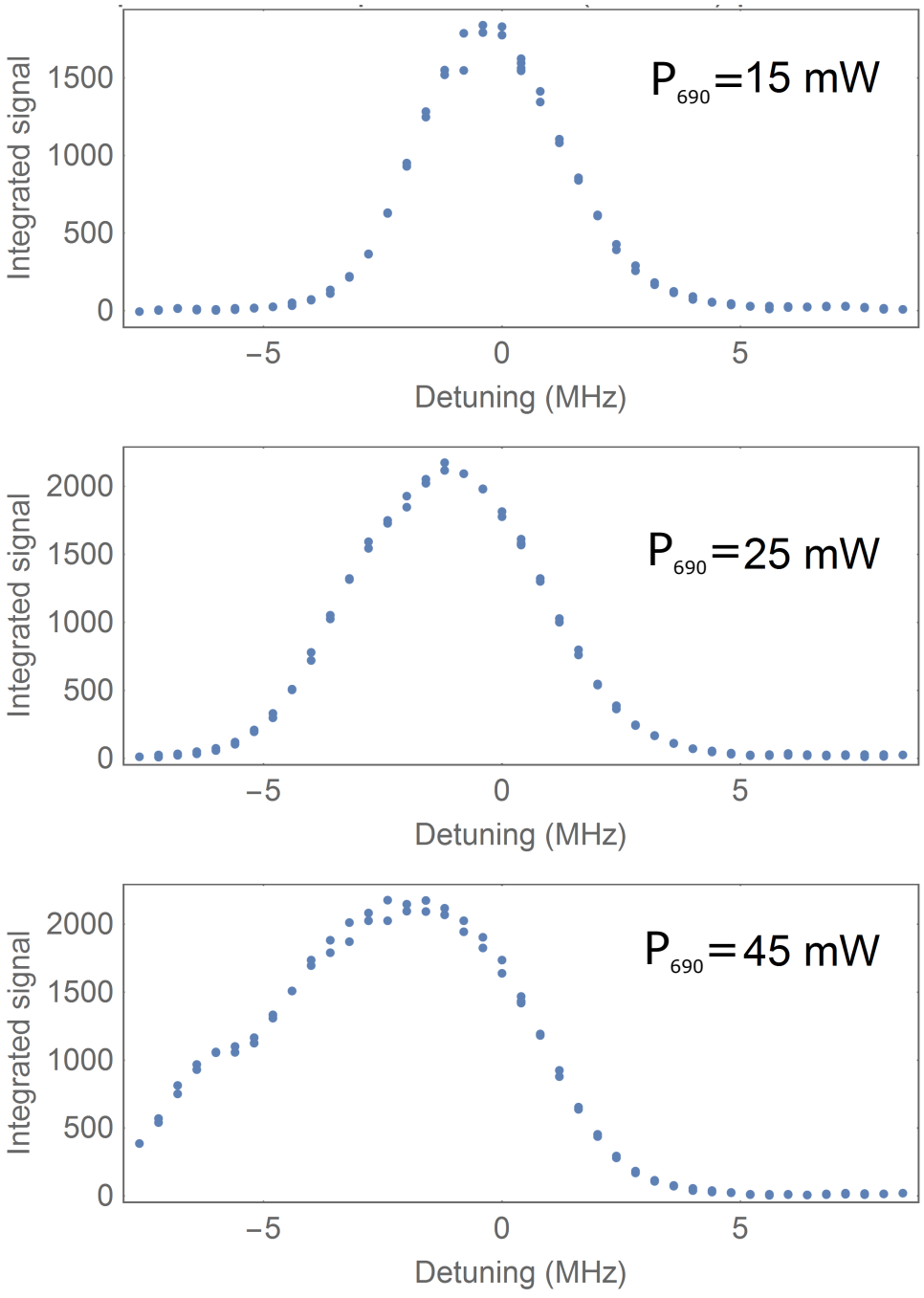

Figure 3.2.13: **Variation of STIRAP lineshape with 690 nm pump laser power.** As expected, the lineshape is symmetric when $\Omega_S = \Omega_P$ and becomes more and more asymmetric as $\Omega_P/\Omega_S \gg 1$.

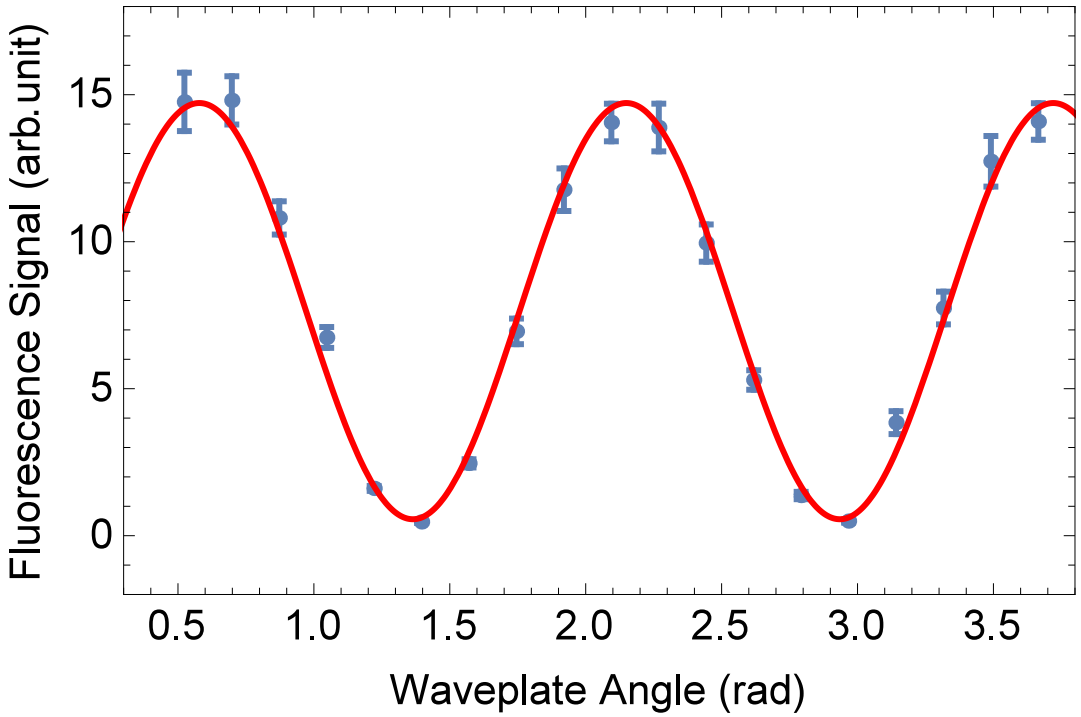

Figure 3.2.14: **STIRAP spin analysis fringes.** Spin analysis fringes showing coherent preparation of the aligned-spin electron state, data (blue) and sinusoidal fit (red line). Error bars correspond to 1σ (68%) confidence intervals.

The suppression factor is proportional to the achieved saturation, so we prefer to use transitions with higher transition dipole moments and higher available power for this purpose. While we could have used the same $H - C$ transition that was used as part of state preparation in ACME I, we instead decided to use the new detection transition $H - I$ instead. The new transition offers comparable levels of power $\sim$1 W, but with larger transition dipole moment, which makes saturation stronger for the same amount of laser intensity used. This decision was also made to reduce complexity in the experimental apparatus, by avoiding the installation of a second laser, and complexity in the experiment scheme, as using a different state with different transitions would mean different systematics in the refinement and probe beams. The laser setup and implementation in the ACME II experiment are described in detail Section 3.3.3.

3.2.8 Efficient rotational cooling STIRAP

In addition to the tests shown above, we have also demonstrated STIRAP in a rotational cooling configuration, in which population transfer is achieved between the ground rotational levels $|X, J = 0^+\rangle$ and $|X, J = 2^+, M = 0\rangle$. Such a scheme was initially planned for use with a quadrupole electrostatic lens, for transferring ThO population into and from the focusing, low field-seeking state, $|X, J = 2^+, M = 0\rangle$. As discussed before, we did not use the electrostatic lens in ACME II, but this demonstration could still prove useful in future ACME experiments.

Implementation of this rotational cooling STIRAP scheme required an initial step of optical pumping to clear the $|X, J = 2^+, M = 0\rangle$ level, which is thermally populated from the beam source (Fig. 3.2.15 (a)). We replaced the Stokes 1090 nm laser with a second 690 nm laser, polarized along $\hat{z}$ tuned on resonance with the $|X, J = 2^+, M = 0\rangle \rightarrow |C, J = 1^-, M = 0\rangle$ transition. The detection of the population in the final $|X, J = 2^+, M = 0\rangle$ state was performed using another 690 nm laser, with fluorescence at 690 nm being detected by a PMT. To avoid scatter, this laser was launched vertically through the detection region such that it travelled in between the transparent $\mathcal{E}-$field plates.

The conditions of this STIRAP transfer scheme are more favorable compared to the typical experiment configuration. Since the two STIRAP lasers have very similar frequencies, the distribution of 2-photon detunings corresponding to the 4.5 m/s FWHM transverse velocity spread is much smaller than in the $X-H$ STIRAP configuration, $\Delta\omega_{\text{Doppler}} \sim 2\pi\times 900$ Hz. This relatively small distribution ensures the detunings of all transverse velocity classes fall within the 2-photon population transfer linewidth $\Delta\omega_{2\text{ph}}$, even for reasonably low power levels. Furthermore, since the power available at 690 nm allows us to reach comparatively higher Rabi frequencies than at 1090 nm, near saturation inefficiencies are significantly reduced in this scheme.

Figure 3.2.15 shows the efficiency of population transfer from $|X, J = 2^+, M = 0\rangle$ to

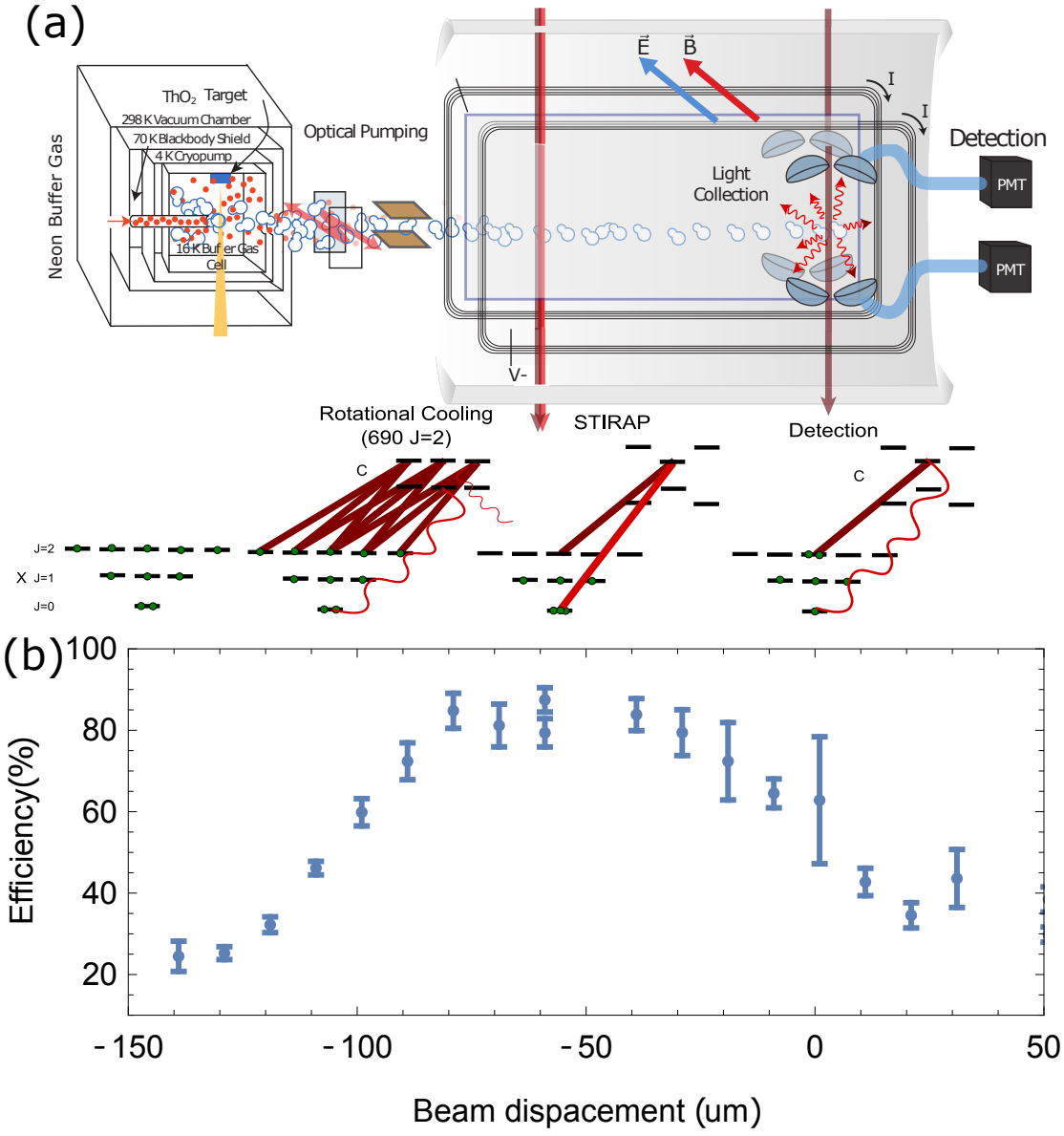

Figure 3.2.15: **Experimental setup for STIRAP population transfer between rotational levels in X.** (a) The $|X, J = 2^+\rangle$ state is first depleted via optical pumping. A pair of partially overlapped 690 nm laser beams; Stokes, resonant with $|X, J = 2^+, M = 0\rangle - |C, J = 1^-\rangle$ and Pump, resonant with $|X, J = 0^+\rangle - |C, J = 1^-\rangle$ perform the STIRAP transfer from $|X, J = 0^+\rangle$ to $|X, J = 2^+, M = 0\rangle$. Population in $|X, J = 2^+, M = 0\rangle$ is detected with fluorescence on a PMT from a probe optical pumping laser resonant with that state. All beam are sent vertically (along $\hat{y}$) to limit scattered photons. (b) Transfer efficiency as a function of overlap between the Pump and Stokes STIRAP laser beams.

$|C, J = 1^-, M = 0\rangle$ as a function of the displacement between the two laser beams. For optimal overlap, at full power, we are able to achieve efficiencies of up to 90%.

3.2.9 Conclusion, use and robustness

We have presented in detail the implementation of STIRAP in ACME II and contrasted it with the previously used optical pumping methods of preparing the desired spin-aligned state in ACME I. STIRAP can be applied with high transfer efficiency ($75 \pm 5\%$) in systems characterized by low transition dipole moments, large volume of excitation, and with limited optical access. The implementation of STIRAP increased the ACME II signal by a factor of 12.

Given the constraints of the STIRAP implementation in ACME II, the STIRAP setup proved to be extremely robust. We were routinely able to acquire eEDM data for multiple months within the couple of years of data acquisition without any maintenance. The only instances where realignment was necessary was when we needed to replace the 1090 Stokes lase launching fiber due to a failure of the fiber amplifier.

Even higher transfer efficiencies could be achieved in the future with a higher Stokes laser power. Higher power fiber amplifiers have been constructed in other laboratories [95, 96]. Such a system would need to be built and issues with polarization drift out of the fiber and long term robustness would have to be ironed out before it could be implemented in a future ACME iteration. Focusing of the laser beams to an even narrower waist to achieve higher intensities could be possible in the future. This would become significantly more feasible if the experiment geometry is modified to allow for placement of the STIRAP intensity profile shaping optics closer to the molecular beam. STIRAP could also be performed using a different intermediary state, with higher transition dipole moments, as described in Chapter 6.

3.3 Fluorescence detection optimization

There are two separate factors that increase our detection efficiency in ACME II by a combined factor of 5 compared to ACME I. The first factor results from optimized collection and transfer of photons from the fluorescing ThO molecular cloud to the PMTs. Secondly, important gains were obtained from the implementation of a new detection transition through the I state, with fluorescing photons in a range of the optical spectrum (512 nm) where PMTs have increased photon to photoelectron conversion efficiency (quantum efficiency).

3.3.1 Detection optics optimization and lightpipes

The goal of the collection optics is to gather and transfer the largest possible number of fluorescence photons to the PMTs, where they can be converted into photoelectrons. The ACME II collection optics use the same basic design as in ACME I, but with optimized geometry that increases the experiment photon collection efficiency. To maintain optimal electric field uniformity, all of the collection optics components are placed outside of the field plates (Fig. 3.3.1). They consist of 8 lens doublets, 4 on each side of the field plates. The 4 lens doublets are tiled compactly to optimize collection solid angle, but also allow for a small rhomboid area in the space between them that is used for the launching of the readout laser beam. Each lens doublet consists of a large 3" lens that effectively collimates the fluorescence light and a second 2" lens that focuses the light, creating an image which is roughly the size of the fluorescence cloud.

Lightpipes

In ACME I, each of the 8 lens doublets focused its light into a bundle of fiber with 9 mm diameter. The four bundles on each side of the experiment were combined into a larger,

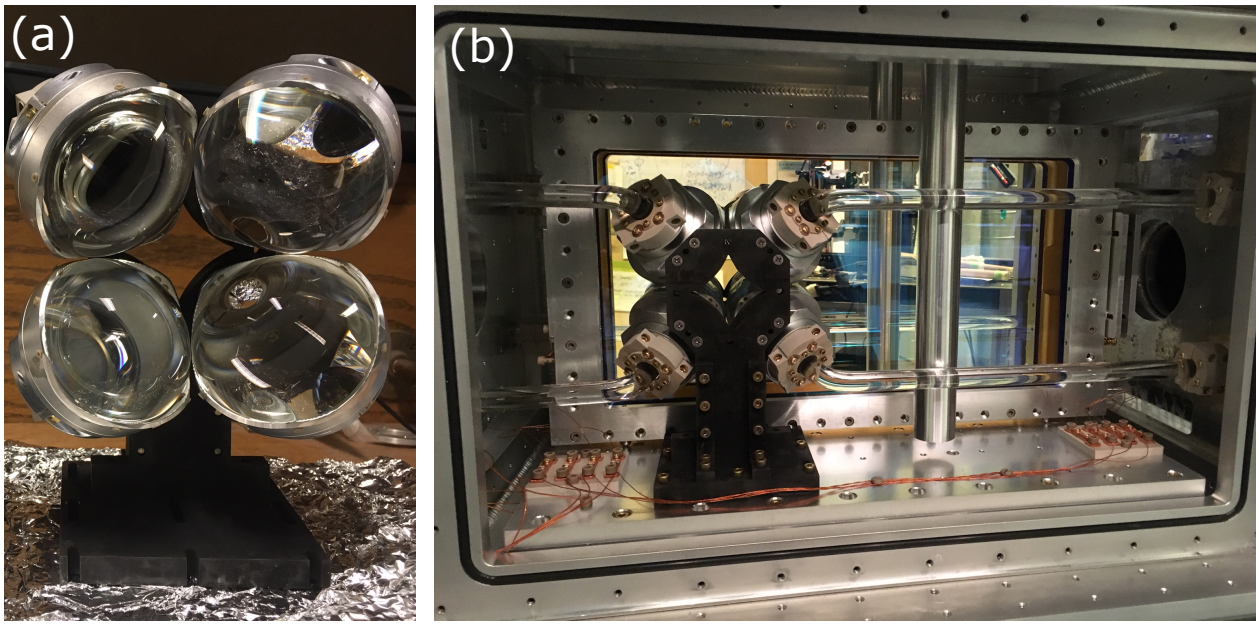

Figure 3.3.1: **ACME II collection optics. (a)** Front view of the 4 sets of lens doublets on one side of the experiment. They are mounted closely-packed on a rigid structure, such that the subtended fluorescence photon collection solid angle is maximized. **(b)** View of the inside of the interaction region, with collection optics installed. Glass lightpipes collect and transfer fluorescence light outside of the experiment chamber to the PMTs.

16 mm, bundle. While the mechanical flexibility of the fiber bundles offered superior robustness and ease of use, their transmission was limited by the fiber to fiber 65% packing fraction, loses due to fiber damage and lack of anti-reflection (AR) coating at the input and output sides. To recover this loss factor, we implemented lightpipes made out of fused silica to transfer the light, with optically contacted AR coating windows on both ends to minimize reflection loss.

The experiment geometry required that a bent section of the lightpipe be used. To allow for easier installation we decided to use two sections that are mated using PEEK collars. The first section is bent, taking the light from the lens doublets and bringing it into the plane perpendicular to the end-cap vacuum flanges. The second section of lightpipes were straight, guiding the fluorescence light through the vacuum chamber end-cap flange and magnetic shields to the PMTs. The lighpipe to lightpipe connection suffered from

$\sim$10% joint loses, but having this geometry allowed for much easier lightpipe fabrication and installation. To accommodate lightguides with a single bend, which were significantly easier to manufacture, we repositioned the location of the holes in the vacuum chamber and the μ-metal shielding end-caps. We used a water jet machine to modify the μ-metal end-caps, which ensures low stress and therefore low mechanical deformation of the annealed magnetic shielding material.

The fused silica bent lightguides were manufactured by molding straight fused silica rods on curved CNC machined graphite molds[4]. The ends were cut and repolished to obtain an optical quality finish. Glass flats with an AR coating at the detection wavelength (512 nm) on one side were glued to the lighpipe ends using an optical index matching adhesive[5] to reduce reflection loses at the input and output ends of the lightpipes.

Collection optics optimization

We used a ray tracing software[6] to design, benchmark and optimize the optical system. To simulate the angular distribution of emitted dipole fluorescence of the ThO molecules being read out by the probe laser beam, we recreated an accurate representation of the molecular fluorescence volumetric source. The ACME II collection simulations included the effects of the anisotropic angular fluorescence distribution of the dipole radiation, including dependence on the parity of the excited state used, $\tilde{\mathcal{P}}$ [66]. Together with an implementation of the optical components of the system, this computer model allowed us to optimize the geometry of the collection optics system, maximizing the proportion of collected photons as a function of system geometry.

As described in detail in Section 3.4.2, the field plate separation was increased from ACME I to ACME II from 2.5 cm to 4.5 cm. The aperture size of the fixed collimators was increased from 1 cm to 2.5 cm. These changes decreased our collection efficiency, mainly

[4]Fabrication performed by Norm Dreschsel at National Scientific Co. based on our molds.
[5]Norland 61
[6]Synopsis LightTools.

in two ways:

1. Increasing the aperture of the fixed collimators increases the size of the ThO molecule fluorescence cloud in the detection region. Since fluorescence is highly divergent and since the PMTs accept photons within a limited range of incident angles, geometric phase space conservation requires that the fluorescence cloud image is comparable in size to the fluorescence cloud volume. The larger image required larger transfer element (lighpipe) diameter and larger photosensitive area (larger total PMT area).

2. In order to maintain the best possible electric field uniformity, collection optics are only placed outside of the electric field plates. Since the separation between the field plates increased compared to ACME I, the collection lenses subtend a smaller solid angle than before.

To address the first loss factor and maintain a high photon collection efficiency, we increased the area of the light guiding elements proportionally, from 9 mm diameter in ACME I to 16 mm diameter in ACME II and increased the detection area of the PMTs. In ACME I, we combined the light from all four lens doublets into a single lightpipe, transferring the fluorescence from the lenses on corresponding to each field plate to its own PMT. In contrast, ACME II uses an individual lightpipe for each lens doublet with an individual PMT. This increased our number of PMTs from 2 to 8 and the photosensitive detection area by a factor of 4. Recovery of the maximal collection efficiency with larger lightpipe diameter and larger total PMT area is shown in Figure 3.3.2b.

The second factor decreased the size of the the solid angle captured by the ACME II collection optics by 30-40% compared to ACME I. A significant (20 %) fraction of this loss was recovered by simply increasing the lens packing fraction by tiling them closer together. The optics are now as closely tiled as possible, without overlapping or creating custom tiled optical elements and while still allowing for sufficient space for the readout laser beam to address all molecules.

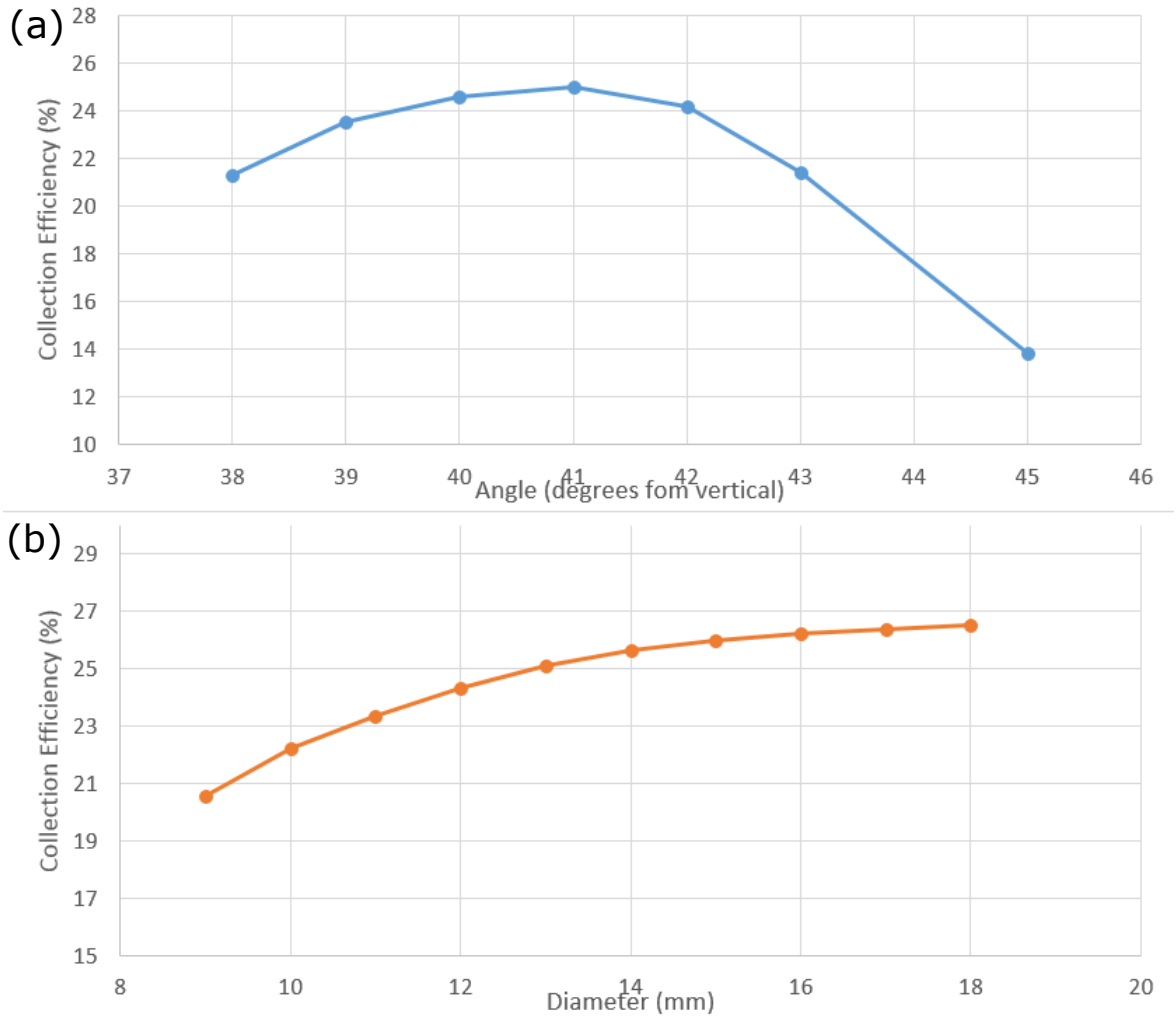

Figure 3.3.2: **Simulations of collection efficiency versus experiment geometry parameters. (a)** Efficiency versus angle of the collection lenses plane with respect to the vertical. An angle of 41 degrees is found to be optimal. **(b)** Recovery of collection efficiency with larger lightpipe diameters. Our lightpipe diameter (16 mm) recovers most of the gain loss when using the same diameter as was previously used in ACME I (9 mm) with the new geometry of our molecular beam.

Using ray tracing simulations, we optimized the angle of the lenses with respect to the vertical axis. An angle of 41 degrees was found optimal, compared to the 45 degrees in ACME I (Fig. 3.3.2b). In addition, the mechanical mounting of the collection optics was improved, making the system more robust to vibrations. The collection optics mounts were blackened to absorb diffracted probe laser beams photons and therefore reduce scatter.

A loss factor in the ACME II collection efficiency occurs in the field plates, which were measured to only transmit 70% of the light at 512 nm. This was partly because their AR coatings were not optimized for the 512 nm fluorescence wavelength, since we ordered the ACME II field plates before considering the $H - I$ transition for detection.

To verify the collection efficiency numbers given by the LightTools simulations, we set up a test system outside of the experiment vacuum chamber. We used a Delrin sphere with light from a 512 nm ECDL laser as the isotropic diffuse light source and measured the lightpipe light output using a large area (1 inch) photodiode. The measured collection efficiency was $\sim$ 20%, for an improvement over ACME I, where it was $\sim$ 15% . This gain was achieved due to the implementation of lightpipes and increased optimization of the collection geometry, and in spite of the increased field plate separation and larger fluorescence volume. The increase in molecule fluorescence volume gave us gains in the number of useful molecules that offset the loses in fluorescence collection efficiency, as described in Section 3.4.2.

3.3.2 I state and new readout transition

In ACME I, we detected fluorescence photons at the wavelength of 690 nm, resulting from decay from state C to the ground state X. Molecules were excited to the C state through optical pumping on the $H - C$ transition (1090 nm). The main drive towards switching to a new transition was our decision to use the $X - C$ transition (690 nm wavelength) as the pump STIRAP transition (see Section 3.2). To avoid same wavelength scatter from entering our PMTs and reducing signal to noise, we decided to look into an alternative for

the detection transition. New spectroscopy of the ThO molecule revealed the I state as a possibly better candidate for detection [75, 76].

There are a number of requirements for an optimal detection transition. We present them below along with comments on how the I state satisfies these conditions:

1. The excited state should have a **large branching ratio to a single other quantum level**, typically the ground state, such that the detected photons can be easily separated from the background using optical filters with a single pass band.

   - the I state has a branching ratio of $\sim 91\%$ to the ground state X [75]. This is larger than the $\sim 75\%$ branching from C to X, and translates to a small signal gain of a factor of 1.2.

2. The excited state should have a **small branching ratio to the $H\ ^3\Delta_1$ experiment state**, since this type of decay populates the dark superposition, reducing contrast and the sensitivity of the phase measurement.

   - the I state has a branching of only 5% to the H state. This reduces contrast by only a few percent and is comparable to the branching from C to H in ACME I.

3. The fluorescence photons should have a **wavelength that is easily collected** using regular optical materials and converted into electronic signal with high quantum efficiency. As mentioned above, the wavelength should be far enough for the wavelengths of other laser used in the experiment to ensure efficient filtration of contaminating scatted light using interference filters.

   - the $I - X$ fluorescence wavelength is 512 nm, which is shorter than the $C - X$ wavelength of 690 nm. By using photomultiplier tubes (PMTs) that are optimized for the 512 nm detection wavelength[7], we were able to obtain an increased detection quantum efficiency of 25% compared to 10% in ACME I. The 512 nm wavelength

[7] Hamamatsu R7600U-300.

is far away from the other 703 nm, 690 nm, 1090 nm lasers in the experiment and custom interference filters[8] block these wavelengths with at least 60 dB of attenuation. We typically use two stacked filters for reducing the background scatter noise to far below fluorescence rates.

4. The excited state **lifetime should be short compared to the characteristic transit time of the molecules through the laser beams**, which is on the order of (2 mm)/(180 m/s) $\approx$ 10 μs. This ensures that the experiment state is completely pumped out within the readout region.

   - the I state lifetime of 115 ns [75] is significantly shorter than the 500 ns lifetime of the C state in ACME I [60]. Both are sufficiently short to ensure the molecules are pumped within the probe laser beam. This shorter lifetime gave us access to faster molecular dynamics and allowed us to increase the polarization switching rate by a factor of 2. To accommodate the faster molecular dynamics, we also increased the experiment bandwidth, as described in Section 3.3.5.

5. The **transition dipole moment should be large enough** so that the Rabi frequencies that we can achieve with the available laser technology are large enough to fully pump out the population in H.

   - the transition dipole moment in the molecule frame can be calculated from the lifetime and branching ratio measurement to be $d_{HI}^{\mathrm{mol}} = 0.27\ ea_0$ [75]. For the transition we need to drive, $|H, J = 1, M = \pm 1\rangle - |C, J = 1, M = 0\rangle$, the transition dipole moment is $d_{HI} = \frac{1}{\sqrt{8}} d_{HI}^{\mathrm{mol}} = 0.095\ ea_0$. We can then estimate the required power for transferring the entire molecular beam to 100 mW.

   To verify the previous spectroscopy measurements [76] and quantify precisely the amount of power that we require, we decided to find the transition and measure the

[8] Semrock FF01-520/70-25.

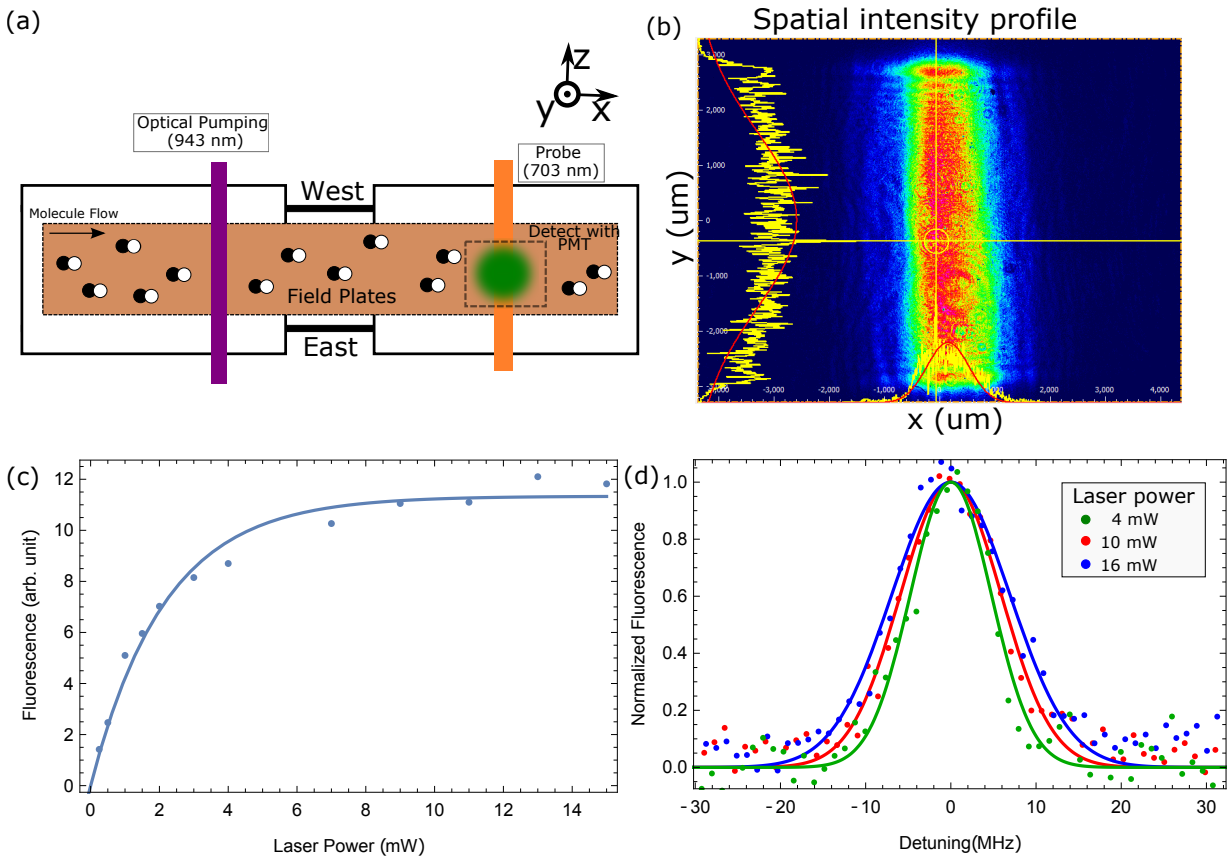

Figure 3.3.3: **Measurement of the saturation power required in the ACME II apparatus for the $I - H$ detection transition.** **(a)** Experiment setup in the stem region of the ACME apparatus. Molecules flow from left to right in the applied quantizing electric field. The H state is populated by exciting $X - A$ with a 943 nm laser (purple). A probe laser at 703 nm excites the $H - I$ transition. The 512 nm fluorescence (green) from the decay of I to X is measured on a PMT. **(b)** Spatial intensity profile of the laser used for the measurement. The laser is clipped vertically to maintain an homogeneous intensity profile. **(c)** Fluorescence versus laser power showing saturation for the used geometry at around 10 mW. **(d)** Broadening of the spectral lines for higher laser power, consistent with saturation behavior.

required saturation power directly in the ACME II experiment. We used a 703 nm diode[9] in an ECDL, locked to the computer controlled scanning cavity system. We were able to find the $|H, J = 1\rangle - |I, J = 1\rangle$ transition frequency at 14222.455 cm^{-1}, first with in-cell absorption (1% absorption) and then in fluorescence.

We set up a saturation measurement in the stem region (Fig. 3.3.3a). The transverse velocity distribution was set using adjustable molecular beam collimators to a FWHM of 4.5 m/s, the same value as in the ACME II interaction region. The electric field was set to 158 V/cm, sufficient to fully mix the parities in the H and I states. The H state was populated by decay from the A state by pumping with $X - A$ at 943 nm. A probe laser at 703 nm excited the $H - I$ transition and the 512 nm fluorescence was detected with a PMT placed above the STEM region. We shaped the intensity of the probe laser beam using a pair of cylindrical lenses to obtain a vertically elongated spatial profile. It was clipped vertically using razor blades to obtain a $\sim$ 6 mm height approximately flat topped intensity profile along y and Gaussian along x (Fig. 3.3.3b). We measured fluorescence, which is proportional to the number of molecules pumped, on resonance, at various power levels (Fig 3.3.3c)). The data is fit with an exponential saturation curve.

For this geometry, where we only saturate 6 mm tall molecular distributions, the power required for 95 (99) percent saturation is 6 (8) mW. Extrapolating for the 30 mm spread of the molecular beam, we would require 40 mW to saturate 99% of molecules. In addition, we verified that the laser lineshapes showed lineshape broadening behavior typical of saturation (Fig. 3.3.3d).

6. The excited state should be a **good parity state**, which is well resolved from other transitions at electric fields that are comparable to ones in the typical experiment running configuration, at $\sim$10-200 V/cm. This allows us to project the spin orientation

[9] HL7001MG.

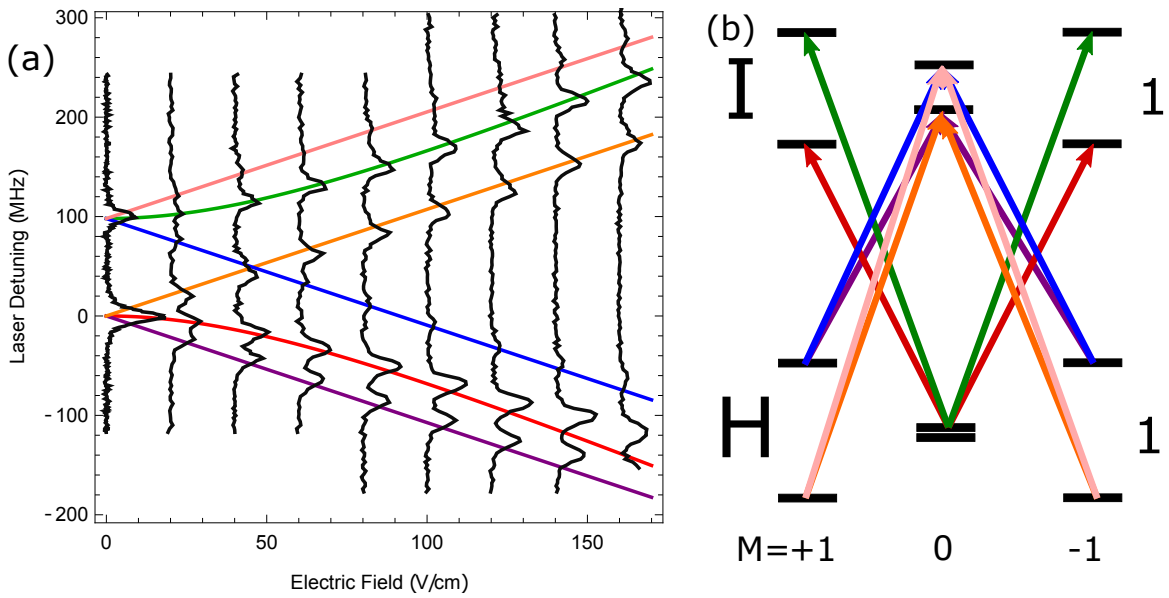

Figure 3.3.4: **Measurement of the electric dipole moment of the I state. (a)** Molecular resonances corresponding to σ^+ and σ^- transitions, shown as a function of electric field magnitude. **(b)** Identified transitions in the $|H, J = 1\rangle - |I, J = 1\rangle$ manifold. Transitions in plots **(a)** and **(b)** are labeled using the same color coding. The electric dipole moment of both H and I, D_H and D_I, states can be extracted from the dependence of the Stark shift on applied electric field $\mathcal{E}$.

axis to the polarization axis of the probe laser. The excited state should be reasonably well-separated from other electronic states to prevent off-resonant pumping that could create interference with other experimental states.

- to verify that the Ω doublet states of the excited state I parities are sufficiently far from each other to be spectroscopically resolved and that the electric dipole of the I state allows for optimal selection of the electric field magnitude, we used the same setup described above to measure the Ω doublet spitting and the electric dipole moment of the I state, D_I. With the probe laser polarization aligned along $\hat{x}$, driving σ^+ and σ^- transitions, the probe laser was scanned over a large enough range to measure all allowed transitions between $|H, J = 1\rangle$ and $|I, J = 1\rangle$. The results of these measurements are shown in Fig. 3.3.4. The $\Delta_\Omega = 91$ MHz splitting between the Ω doublets is sufficient to allow us to spectroscopically resolve the $\tilde{\mathcal{P}} = \pm 1$

states. The electric dipole moment is extracted from $\Delta_{\text{Stark}} = \sqrt{{\Delta_\Omega}^2 + (D_I \mathcal{E})^2}$. The measured value $D_I = 2.1\ ea_0$ resolves the levels of the used transitions for the two selected ACME II electric field magnitudes ($1\mathcal{E}$ and $2\mathcal{E}$), as described in detail in Section 3.5.2.

3.3.3 703 nm readout and refinement Ti:S laser configuration

At 703 nm, available laser diodes can only access up to 40 mW of power[10], which is insufficient to saturate the entire spatial and velocity distribution of ThO molecules in our experiment. We instead used a Titanium Sapphire (Ti:S) laser for obtaining sufficient amounts of probe light power. The commercial system[11] has an output of up to 5 Watts of power at 703 nm. The laser is pumped by an 18 Watts pump at 532 nm[12].

The Ti:S laser is referenced using a delay-line lock to a second narrow line, stable laser. The 703 reference ECDL is locked to the same ULE cavity described in Section 3.2.3, using the same PDH technique. The ECDL has very similar characteristics to the 690 nm laser described there, since it uses the same AR-coated diode tuned to 703 nm instead of 690 nm.

Two of the switches that are characteristic of the ACME II experiment sequence require tuning of the refinement or readout laser frequencies. The $\tilde{\mathcal{N}}$ switch requires tuning of both refinement and readout laser beams together, by a frequency that corresponds to the Stark shift of the selected electric field magnitude, typically in the 150-400 MHz range. We therefore designed the lock system to allow for tuning the laser on the fly, by up to 500 MHz, in a time which is short compared to the timescale of the $\tilde{\mathcal{N}}$ switch (which is performed every 600 ms).

To achieve this type of performance we actively stabilize the Ti:S frequency to the frequency of the 703 reference ECDL with an offset delay line lock [97] (Fig. 3.3.5a). A

[10] HL7001MG.
[11] MSquared SolsTiS 4000.
[12] Lighthouse Photonics Sprout

small proportion of the Ti:S laser light is combined with the 703 reference ECDL light on a fast photodiode[13]. The differential beat-note signal is extracted from the higher order components using a low pass filter and amplified. The signal is then mixed down with a custom-build RF chirp generator[14] which is capable of performing RF frequency sweeps with rates of up to 2 GHz/ms. Half of the signal is sent through a delay line and then recombined with the other half using a frequency mixer. The high frequency components of the signal are filtered out and the error signal is sent to the Ti:S, where an internal 2 stage PID applies feedback to the fast and slow piezos that position one of the mirrors of the Ti:S cavity with a bandwidth of up to 100 kHz.

The sinusoidal shape of the offset delay line lock error signal means that the lock capture range is set by the length of the delay line. For a 1 m coax cable, the capture range is ±100 MHz. This is sufficient so that the Ti:S lock can reliably follow a frequency chirp of $\sim$ 400 MHz in 5 ms, as shown in Figure 3.3.5b. During initial tests, the lock was robust enough to be able to switch more than 500,000 times every 0.5 seconds over the course of 4 days. This robustness was later confirmed during the ACME II experiment data runs. The linewidths observed were approximately 20 kHz (10 ms integration time), with $\sim$ 400 kHz jumps over 100-1000 ms timescale and a long term stability of 200 kHz within 24 hours. We believe that most of this noise is due to acoustic noise in the experiment room that is not suppressed by the locking setup.

We use 703 nm light in two places in the ACME II experiment: for refinement and for readout. The ACME II experiment requires $\sim$ 100 mW of power in the readout beam to ensure more than 99% of molecules are read out (see Sec. 3.3.2). Even higher powers, up to 800 mW, are required in the refinement beam to ensure full attenuation of possible imperfect STIRAP phase components.

The 4 W of 703 nm power available after the isolator are split using a half-waveplate

[13]MenloSystems APD210

[14]The device was designed and build by Jim McArthur and is based on an the AD9954 DDS chip.

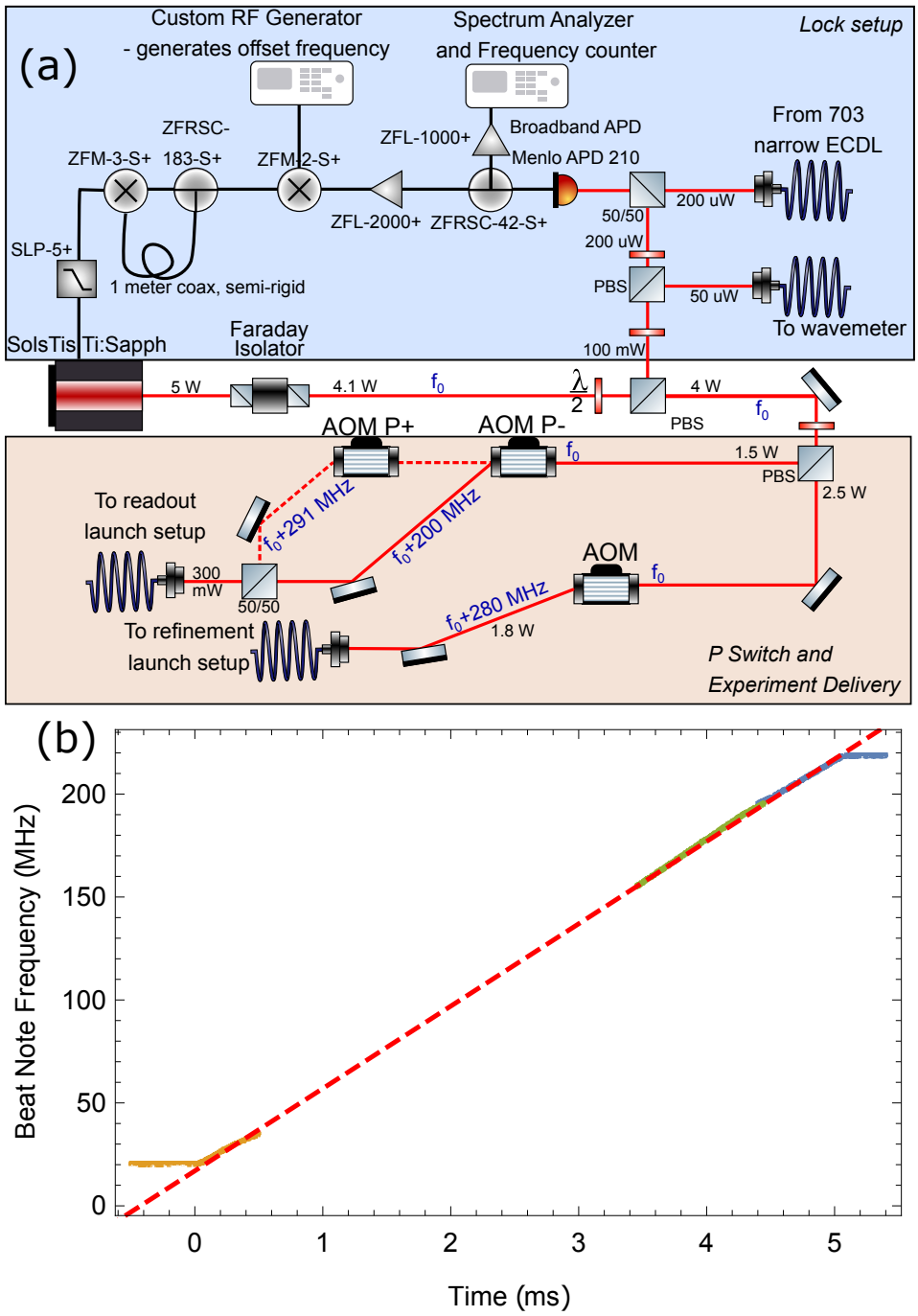

Figure 3.3.5: **Ti:S laser setup and fast frequency scanning.** **(a)** Optics for the Ti:S laser are used for locking (light blue background) or for performing the $\tilde{\mathcal{P}}$ switch and experiment delivery (light orange background). **(b)** Beat note measurement showing a Ti:S frequency chirp of 200 MHz in 5 ms, faster than that required for performing the $\tilde{\mathcal{N}}$ switch, which occurs every 0.6 ms.

and polarizing beam splitter (PBS) system into two paths (Fig. 3.3.5a). About 2.5 W are sent into a single-pass AOM, which is typically at 280 MHz. The frequency of the AOM can be tuned to 280 MHz+Δ_{ref} to only tune the refinement beam off resonance, without affecting the power of the readout beam. About 1.5 W of power are directed to the path used for the readout light. A set of 2 single pass AOMs allow us to set the readout light to be resonant with either the lower or the higher frequency parity state, $\tilde{\mathcal{P}} = \pm 1$, of the $|I, J = 1, M = 0\rangle$ state. When AOM P+ is on (off) and AOM P- is off (on), the frequency of the readout laser is detuned by 200 MHz (291 MHz), such that it is resonant with the $\tilde{\mathcal{P}}$=+1 ($\tilde{\mathcal{P}}$=-1) parity Ω doublet of the electronic state $|I, J = 1, M = 0\rangle$. The 80 MHz frequency difference between the refinement and readout beams is corrected for later in the polarization switching setup, which is described in Section 3.3.5.

3.3.4 Experiment laser delivery

The 703 nm light is delivered to the molecules through a set of optics that are mounted on a 2×3 feet optics table that is placed next to the interaction region. The optics configuration is similar to the ACME I setup, but streamlined to minimize the number of optical elements used and increase robustness (Fig. 3.3.6).

Both refinement and readout light intensity profiles are controlled in a similar way. They are launched from a fiber port. The aspheric lens in the fiber port is selected such that the Gaussian spatial profile of the collimated laser light beams has a 2 sigma diameter of ~ 1.5 mm. To address molecules across the entire spatial distribution of the molecular beam, the laser beams are expanded vertically to a 2 sigma diameter of 4 cm with a pair of cylindrical lenses. Any imperfections in the polarization coming out of the fiber are cleaned by a high extinction laser Glan-Laser PBS. A half-waveplate mounted on a precision rotation stage (Newport URS50BCC) allows us to rotate the refinement and readout axis of linear polarization.

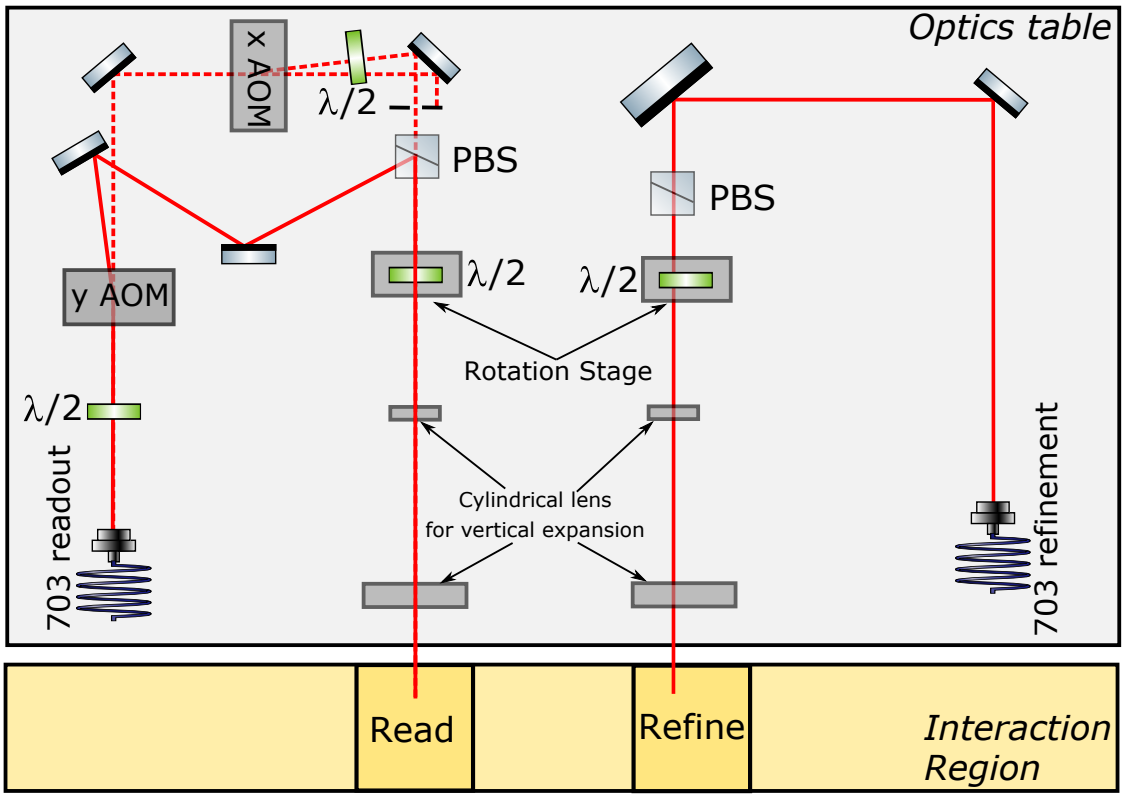

Figure 3.3.6: **Optical elements that deliver the 703 nm Ti:S light to the ACME II experiment.** Optics performing shaping of the laser beam spatial intensity profile, shown for both refinement of the readout laser beams. In addition, we use AOMs to quickly switch the polarization of the readout beam between orthogonal orientations, $\hat{X}$ and $\hat{Y}$. The two beams are recombined on a high extinction ratio PBS before entering the interaction region vacuum chamber.

3.3.5 Polarization switching

The polarization of the readout laser is switched between orthogonal $\hat{X}$ and $\hat{Y}$ by a set of two AOMs. When the $\hat{Y}$ AOM is off (on), and the $\hat{X}$ AOM is on (off), the light travels through the dotted (solid) path and the experiment polarization is vertical (horizontal). Both AOMs are set to 80 MHz, which matches the frequency offset implemented in the Ti:S optical delivery setup. This ensures that both readout and refinement beams address the ThO molecules with the same frequency.

In order to pump out both $\hat{X}$ and $\hat{Y}$ spin-projection quadratures in the time the molecules travel through the readout laser beam, the polarization switching period has to be less

than the molecule fly through time $\tau_{XY} < 10$ μs. In addition, the polarization switching period has to be much longer than the lifetime of the readout excited state, I in ACME II, $\tau_{XY} \gg \tau_I = 115$ ns such that there are sufficient decay cycles for the signal in each polarization bin to not contaminate the signal in the following bin. Furthermore, τ_{XY} needs to be longer than the finite switching time of the used AOMs, typically in the range of $100-200$ ns, given by the travel time of the acoustic waveform through the laser intensity profile.

Given the shorter lifetime of the I state used in ACME II for detection, $\tau_I \sim 115$ns [75] in ACME I, compared to $\tau_C \sim 500$ns [60], we decided to increase the rate of polarization switching, from 100 kHz to 200 kHz. This allowed us to decrease the diameter of the readout laser beam along $\hat{x}$, which streamlines the readout beamshaping optics configuration by eliminating the need to further expand horizontally the readout laser beam using cylindrical lenses after initial collimation with aspheres out of the fiber. The smaller diameter also increases laser intensity, improving saturation and decreases the size of the fluorescence source along $\hat{x}$, facilitating better photon collection efficiency.

3.3.6 Characterization of the detection PMTs

The PMTs used in ACME I were replaced for ACME II with a model which was significantly more sensitive at the 512 nm ACME II wavelength, with quantum efficiency of 25%[15]. This is a factor of 2.5 higher than the quantum efficiency of the ACME I PMTs at 690 nm and 1.25 times the quantum efficiency of those PMTs at 512 nm.

In the ACME II detection scheme, we extract the number of photons in each asymmetry bin by dividing the integrated fluorescence signal by the integral under one photon pulse. As is typically the case, there is significant variation between the gain of each PMT due to variation in the PMT industrial production process. To correctly scale for the variation in

[15] Hamamatsu R7600U-300.

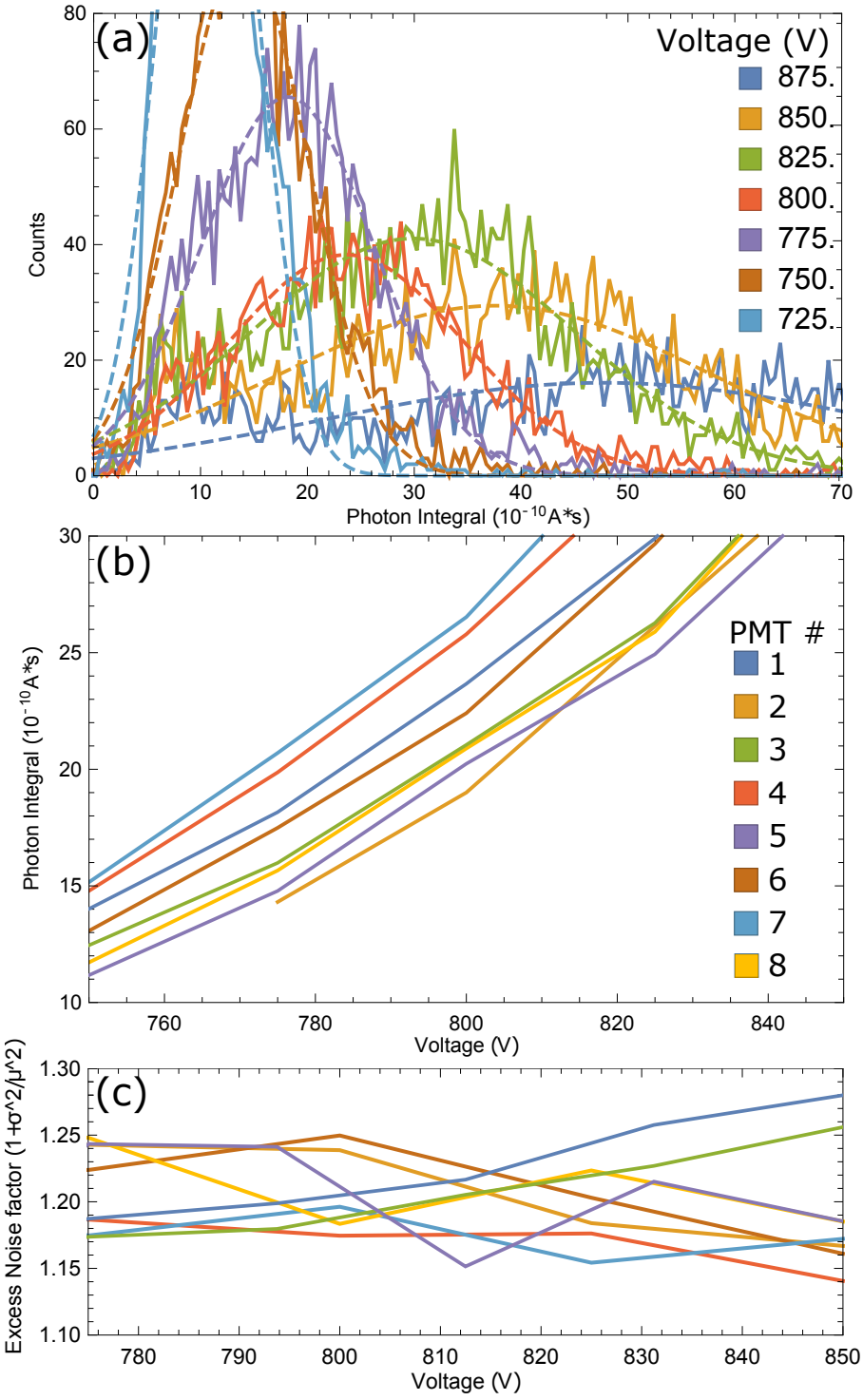

Figure 3.3.7: **Measurement of the PMT amplification factor.** **(a)** For a single PMT, histograms of the distribtuion of the integral below single photon pulses, for a number of applied bias voltages. For each of the eight PMTs, **(b)** variation of photon integral with applied bias voltage and **(c)** variation of the excess noise factor with voltage. The shown legend is common to plots **(b)** and **(c)**.

the photoelectron amplification factor, we individually measured the gain of each one of the 8 PMTs used in ACME II. To do so, we recorded traces of the PMTs running in conditions of low light, such that individual photon pulses can be easily identified. We integrated the area under a large number of photo-electron peaks and then plotted histograms of the integral area sizes. Such a histogram is shown in Figure 3.3.7a, for a number of applied PMT bias voltages. The distribution of photoelectron area is Poisonian, which is well approximated by a Gaussian for large N (typically $N > 1000$), so we fit the distribution to Gaussians. The value of the mean gives us the gain of the PMT, in units of the integral of a single photon, $\mathrm{A} \cdot \mathrm{s}$. The gain is non-linear and increases with increasing bias voltage (Fig. 3.3.7b).

PMTs in general show reduced signal-to-noise compared to the best case scenario, when signal to noise is limited by shot-noise. This decrease is caused primarily by variations in the number of electrons emitted during each step of multiplication on the PMT dynodes, which adds additional noise to the detected signal [98]. We estimate the excess noise factor of our PMTs from the distribution of the detected single photon integrals:

$$\mathrm{ENF} = 1 + \frac{\bar{x}_{PI}^2}{\sigma_{PI}^2}, \tag{3.9}$$

where $\bar{x}_{PI}$ is the mean of the single photon integral and σ_{PI} is the 1 sigma width of the single photon distribution. ENF is shown as a function of voltage in Figure. 3.3.7c. The excess noise factor of ~ 1.2 is characteristic of good quality PMTs [98] and we expect that this factor decreases the sensitivity of the ACME II measurement by a factor of $\sqrt{\mathrm{ENF}} \approx 1.1$. A very similar excess noise factor was measured for the ACME I PMTs and therefore had a similar effect on the ACME I measurement sensitivity.

3.3.7 Upgrades to DAQ and experiment control

Since the lifetime of the I state (115 ns) is a factor of 3 shorter than the C state (500 ns) used in ACME I, it also gives us access to faster molecular dynamics. To accommodate this bandwidth change, we also increased the acquisition rate of our PMT data from 5 MSa/s in ACME I to 16 MSa/s in ACME II. In addition, in ACME II, data acquisition occurs on 8 different channels, each corresponding to one of the 8 PMTs used. These two factors increased the DAQ data rate by a factor of 12.4 and the PXI scope used in ACME I[16] proved to be incapable of performing the task when set up with the original software configuration. We purchased a second 8-channel FPGA device that was able to run with the required data rate[17]. Upon further work with optimizing the device software interface, both devices were proved capable of the required performance, but we used the FPGA device for the majority of ACME II measurements.

To provide a robust platform for the faster data transfer rate required in ACME II, data saving was performed on a separate computer than the computer that sets and controls the ACME experimental sequence states (see Section 2.5). We implemented a hardware-based communication system between the experiment state control computer and the computer saving FPGA scope data to ensure the experiment data was saved and labeled correctly. We used a handshake system, in which the computer setting the experimental state waited on a flag from the acquisition computer and vice-versa before proceeding with the experimental sequence.

A large number of acquisition, control and monitoring LabView VIs were modified and updated for ACME II. Brendon O'Leary [99] and later Adam West and Daniel Ang contributed immensely to this effort. This increased robustness of the ACME II apparatus and allowed us to encounter less software bugs and crashes along the way.

[16] NI PXI-5922
[17] NI PXI-5171R FPGA

3.4 Geometric optimization of the molecular beam

We achieved a signal gain factor of 8 over ACME I by optimizing the geometry of the ACME II apparatus to allow for a larger acceptance solid angle of the ThO molecules produced by the buffer gas beam source. After exiting the zone of collisional freezing, the ThO molecules travel balistically with a divergence of 0.35 sr FWHM [72]. In ACME I, the detection region subtended only 6×10^{-5} sr, so only about 1 in 5000 of the molecules produced by the buffer gas beam source was useful for the spin precession measurement. Early in the development of ACME II, we designed and built a quadrupole electrostatic lens for focusing molecules in the low-field seeking $|X, J = 1^-, M = 0\rangle$ or $|X, J = 2^+, M = 0\rangle$ states. The lens was expected to increase the flux of detected ThO molecules by a factor of ∼20-25 over ACME I, but we found that the 30 kV voltages required to focus the ThO molecules also produced 60 keV Bremsstrahlung x-rays [100]. Furthermore, we learned that a significant fraction of the possible lens gains could be achieved in a much simpler configuration, by increasing the acceptance cross section of the produced molecules in the experiment measurement region.

We were able to increase the solid angle of detected molecules by optimizing two experiment geometry parameters. We reduced the length of the beamline between the beamsource cell aperture and spin-precession region; and we increased the size of the fixed collimator aperture and the separation between the two field plates.

3.4.1 Redesigned stem for reduced beam length

In ACME II, the distance between the beamsource conical aperture and the interaction region fixed collimator was reduced to 1.1 m compared to 1.3 m in ACME I, corresponding to an increase of a factor of 1.4 in solid angle. This was achieved by optimizing the geometry of the intermediary region between the beam source and the interaction region ("stem" region) in a number of small, cumulative ways. The purpose of this region is two-fold: (1) to allow for a flexible connection between the beamsource and interaction

region, through bellows, that allow for precise alignment of the beamsource and interaction region field plates, and (2) to provide space for the implementation of rotational cooling (described in section 3.2.2).

In addition, ACME I included a module containing adjustable collimators that enabled us to search for systematic errors that varied spatially or with the velocity of the molecular beam. Since we typically performed such tests infrequently, we decided to replace this module in ACME II with collimators mounted on the centering ring of the stem-interaction region gate valve, eliminating the need for additional space. To further reduce the length of the stem, the gate valves used for separating the stem and beam source and stem and interaction region were chosen to be of a shorter thickness and the formed bellows in ACME I were replaced with shorter length, more flexible, edge-welded bellows. In addition, to increase conductivity and reduce collisions between ThO mollecules and the background gas, we increased the diameter of the stem region from the KF50 to the ISO100 standard. The rotational cooling region was reduced in length, but preserved in the same location.

3.4.2 Optimized fixed size of collimator aperture and field plate separation

The precise reasons for the choice of 1 cm for the fixed collimator aperture size and 2.5 cm field plate separation in ACME I are lost to history. While this choice accomplishes one of the main purposes of the fixed collimators, which is to prevent ThO molecules from colliding and accumulating on the ThO surface, further optimization of these parameters was possible for ACME II.

The geometry of the molecular beamsource, fixed collimators and field plates is shown in Figure 3.4.1. Given a choice for the dimensions of the fixed collimators aperture, d_{c}, the minimum field plate separation, d_{fp}, is given by

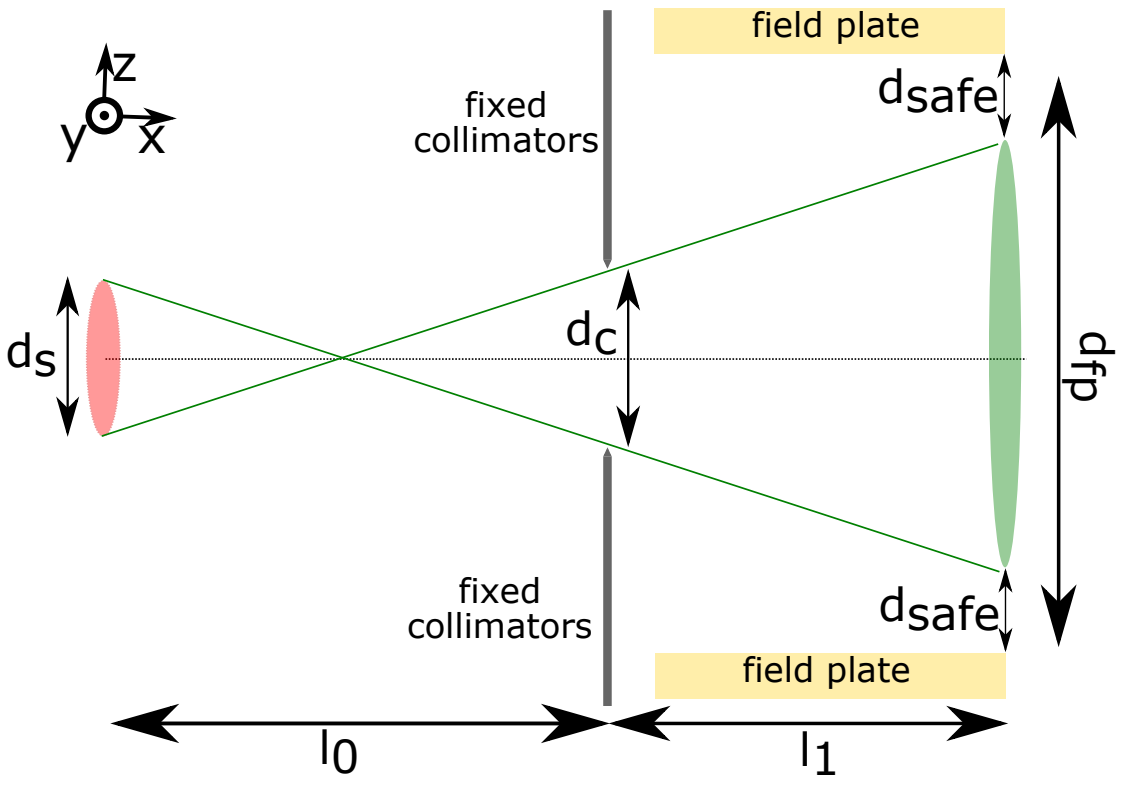

Figure 3.4.1: **Geometry of the ThO molecular beam.** The geometry is chosen such that there is no line of sight between molecules leaving the ThO molecular source of size d_s and the field plates. The size of the fixed collimators, d_c, is set by the separation between the electric field plates d_{fp}. An additional safety distance of d_{safe} accounts for missalignement in the system. Scales exaggerated for clarity.

$$d_{\mathrm{fp}} = 2d_{\mathrm{safe}} + d_{\mathrm{s}}\frac{l_1}{l_0} + d_{\mathrm{c}}\left(1 + \frac{l_1}{l_0}\right), \tag{3.10}$$

where $d_{\mathrm{s}} = 7$ mm is the size of the effective molecular size, $l_0 = 1.1$ m is the separation between the molecular source and the fixed collimator and $l_1 = 48$ cm is the separation between the fixed collimator and the detection region. $d_{\mathrm{safe}} = 3$ mm is a safety margin that accounts for the unavoidable imperfections between the alignment of the various mechanical components of the setup.

Since our molecular beam is well described by a flat topped angular distribution of ThO molecules, the number of useful molecules increases quadratically with the size of

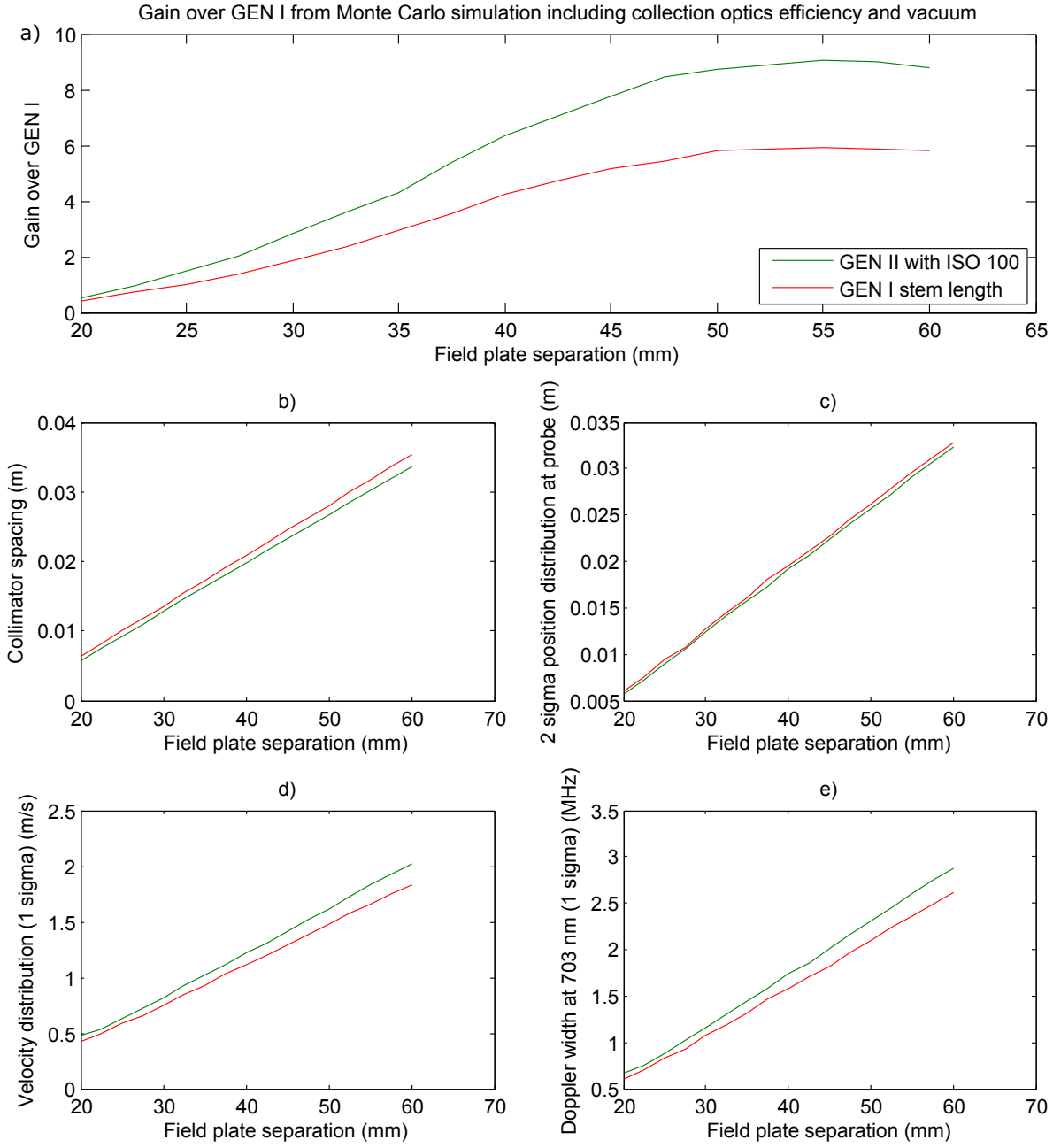

Figure 3.4.2: **Simulation data showing effects of increasing field plate separation on ThO beam properties.** All plots are shown for two different ThO beamline lengths: ACME I (red), and ACME II (green). The plots show: **(a)** signal gain over ACME I, **(b)** optimal collimator spacing, **(c)** size of the molecular cloud at the probe region, **(d)** the width of the velocity distribution and **(e)** its corresponding Doppler with at the probe wavelength of 703 nm.

the fixed collimators. However, these gains are tempered by losses in the efficiency of the collection optics setup. As described in Section 3.3.1, some of these losses were recovered by increasing the size of the photosensitive area and further maximizing the collected solid angle in ACME II compared to ACME I. Increasing these parameters even further would require a larger experiment vacuum chamber, with larger magnetic shields, which come with a prohibitive cost in resources, time and complexity. Without a complete redesign of the system, the photon collection efficiency efficiency begins to diminish at around 4 cm. This efficiency drop becomes a lot faster than the quadratic molecular size gain and the combined gain, shown in Figure 3.4.2 decreases as the field plate separation is larger than 5 cm.

An additional complication of increasing the fixed collimators aperture is that the molecule ensemble that enters the spin precession region has a larger distribution of positions and velocity. This larger phase phase distribution requires more STIRAP, refinement and read-out lasers power to achieve the same level of transfer saturation. In addition, larger spatial dependence of the molecular cloud makes the spin precession measurement increasingly susceptible to systematic effects coupling to imperfections in the laboratory fields, such as electric or magnetic field gradients (a systematic effect due to magnetic field gradients is discussed in Section 5.4). Although these factors did not limit ACME II, they could become significant in a future ACME experiment.

One advantage of the increased field plate separation is that imperfection on the surface of the ITO coated glass field plates, such as patch potentials, are further away from the ThO molecules. Consequently, we have observed in ACME II a reduction in the non-reversing electric field component, $\mathcal{E}^{\mathrm{nr}}$, which was responsible for a number of systematic effects (see Section 5.3).

Given all these factors, we increased the separation of the field plates to 4.5 cm, with a fixed collimator separation of 2.5 cm, which gives an increase in signal by a factor of 8.

3.4.3 Measurement of saturation power and Doppler width in ACME II

Figure 3.5.1 shows measurements of readout fluorescence signal and linewidth as a function of power. The saturation power for 99% of molecules at 30 mW of 703 power is consistent with initial measurements described in Section 3.3.2. The value of the linewidth at low power, before being increased by power broadening, is consistent with the ACME II experimental geometry, as described in Section 3.4.2. The 2.7 MHz linewidth results from a combination of the lineshape expected from Doppler broadening (2.1 MHz) combined with the laser linewidth (∼0.5 MHz).

3.5 Electric and magnetic fields

The ACME II electric and magnetic field generating apparatus have been modified to allow for better control and monitoring of these important experiment parameters.

3.5.1 Field plates with improved birefringence and coating properties

In ACME I, the leading source of systematic error came from an AC Stark shift effect, associated with an ellipticity gradient across the area of a laser beam, and coupling to the non-reversing component of the electric field ($\mathcal{E}^{\mathrm{nr}}$). A thermal stress-induced birefringence gradient, caused by absorption of the laser power by the glass electric field plates and vacuum chamber windows, was responsible for the large ellipticity gradient ($\sim$ 10%/mm circular polarization fraction) [5]. ACME II uses redesigned field plates and vacuum windows, with Corning 7980 fused silica instead of Schott Borofloat glass, for an order of magnitude lower thermal expansion and reduced bulk laser absorption. The field plates are coated with a thinner layer of conductive ITO (20 nm compared to 200 nm in ACME I), which further reduces thermal absorption. We tested the properties of small test pieces of glass that were coated with ITO in the same run and under the same conditions as the

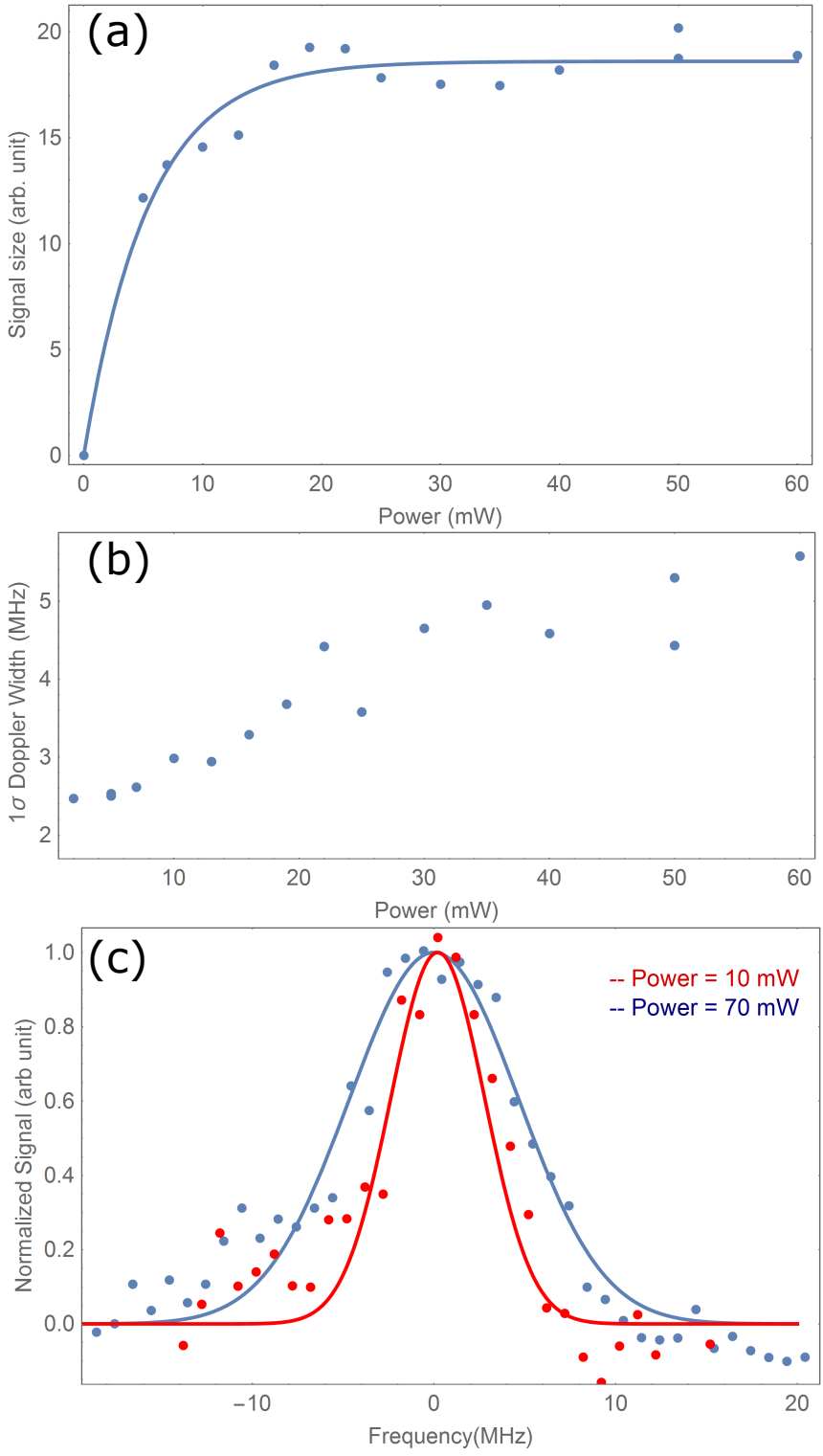

Figure 3.5.1: **Power saturation of the ACME II molecular beam.** **(a)** Signal size as a function of readout laser power. **(b)** Linewidth as a function of readout laser power. **(c)** Power broadened lineshape shown at 10 mW and 70 mW of power.

ACME II field plates. To measure the resistivity of the ITO coating, we used a ResMat 4 point probe measurement device, located in the Harvard Center For Nanoscale (CNS) facilities (Fig. 3.5.2a). The device accepts small wafers (up to 8 inches in diameter and at most 2 mm thick) and can generate a map of the resistivity of the sample with a set number of points. For our sample, the sheet resistance is in the 2000 - 4000 Ω/sq range, which is sufficient to ensure the entire field plate can charge much faster than the timescale of the $\tilde{\mathcal{E}}$ switch, which is ~ 2 s.

To ensure that the thinner ITO coating and improved glass properties reduced the thermal stress induced birefringence, Vitaly Andreev inherited and improved the polarimeter built in ACME I by Paul Hess and Ben Spaun [60, 61, 101]. Using this setup, we verified through direct polarimetry that the thermal stress induced ellipticity gradients within the ACME II laser beams were reduced to below 0.1%/mm, consistent with zero within the sensitivity of the polarimetry measurement (Fig. 3.5.2b).

3.5.2 ACME II electric field magnitude selection

As described in Section 3.3.2, ACME II uses a different state than ACME I, I, for detection and refinement. To accommodate for the properties of this state, we reconsidered the electric field magnitude that is optimal for running the experiment. The requirements for an optimal electric field value are:

1. We would like for the transitions used for both STIRAP ($H - C$) and the refinement/detection transition ($H - I$) to be as **far away in frequency from other transitions** that we do not use as possible. This includes transitions with polarization which is different to the desired applied laser polarization, since such polarization components might occur due to imperfections in the optics system. Any population driven on such transitions that were nearly resonant with the experiment lasers reduce the experiment contrast and could increase our susceptibility to noise or systematic

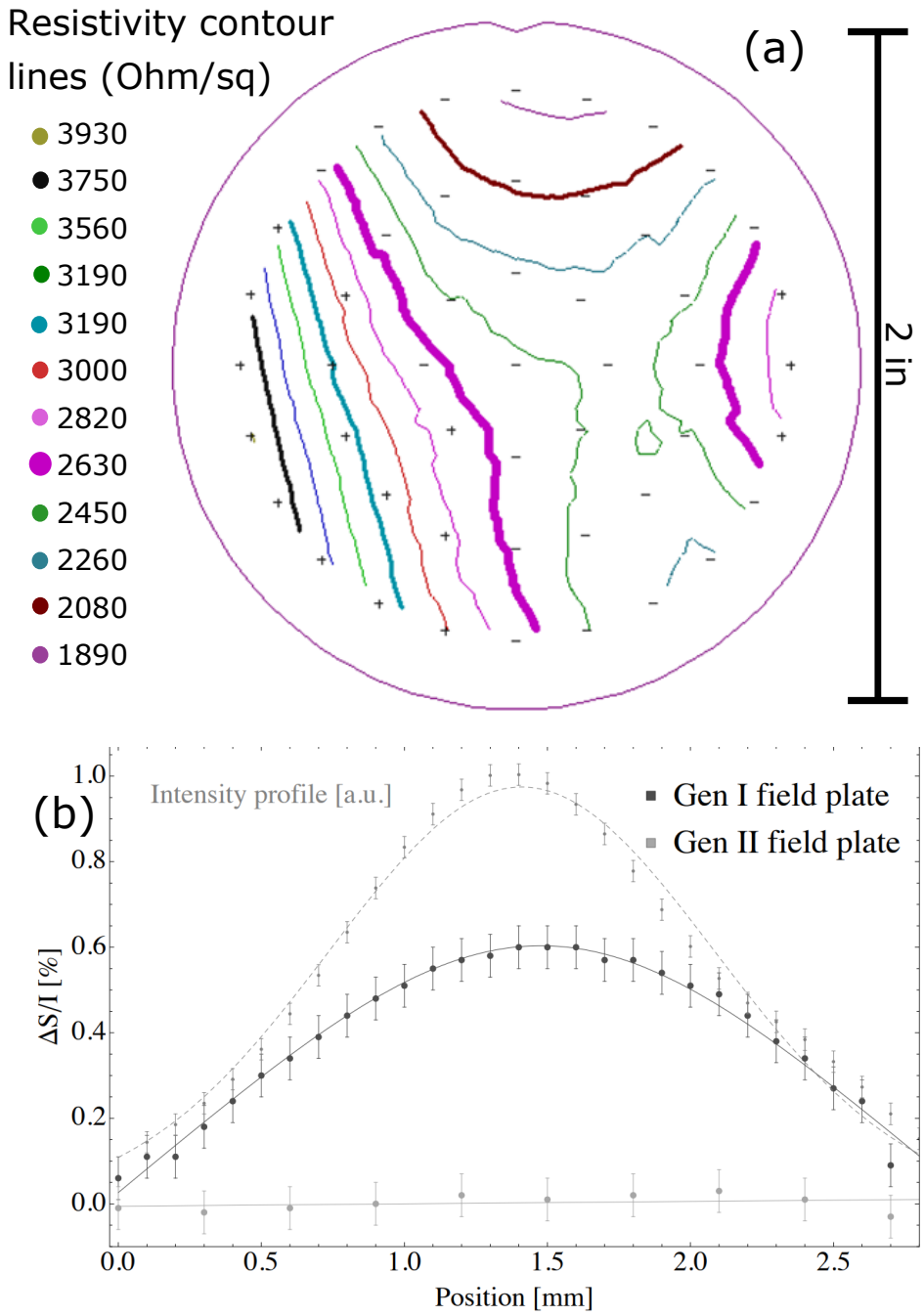

Figure 3.5.2: **Characterization of the ACME II field plates.** **(a)** Measured spatial variation in sheet resistivity of test glass pieces coated with a 20 nm thin layer of ITO. **(b)** Polarimeter measurement of the ellipticity gradient ($\Delta S/I$) of the laser beam, after passing through the field plates. The light passing through the ACME II field plates shows significantly reduced birefringence gradient compared to ACME I.

error.

2. The **molecular polarization** (alignment of the molecule with the applied electric field) in the prepared spin state should be as good (close to unity) as possible.

3. In general, we would prefer to choose **electric field magnitudes that are small**, such that they require small values of applied voltages to the two field plates which are 4.5 cm away. This limits leakage currents and reduces the technical challenges of supplying the required voltage.

Given these conditions, we would like to choose at least two running electric field magnitudes that are significantly different. Performing the experiment at both values allows us to look for systematic effects that depend on the magnitude of the electric field. Fig. 3.5.3a,b shows the energies of the levels for the $H-C$ and $H-I$ transitions. Figure 3.5.3c shows the purity of the $|H, J=1, M=\pm 1\rangle$ levels that we use for the spin precession measurement. After optimizing under these conditions, we chose two ACME II electric field magnitude values, $|\mathcal{E}| = 80$ V/cm ($1\mathcal{E}$ configuration) and $|\mathcal{E}| = 140$ V/cm ($2\mathcal{E}$ configuration).

Given the 4.5 cm field plate spacing, the voltages required to apply both of these electric field values were ± 180 V and ± 315 V. The Apex PA98 supplies used in ACME I were not sufficient to achieve these higher voltages. We therefore upgraded our supplies to a higher voltage (± 600 V)[18] powered by Acopian supplies and controlled with a BiasDAC.

3.5.3 Measurements of the electric field using microwaves

In ACME II, we used a microwave scheme to directly measure the electric field in the precession region and its correlated components. The experimental scheme and apparatus design used for the microwave measurements are similar to those used in ACME I [6].

In brief, microwaves that are linearly polarized along $\hat{y}$ are sent into the precession region between the two field plates from the downstream region, traveling along the $-\hat{x}$ direction.

[18] Apex PA89a.

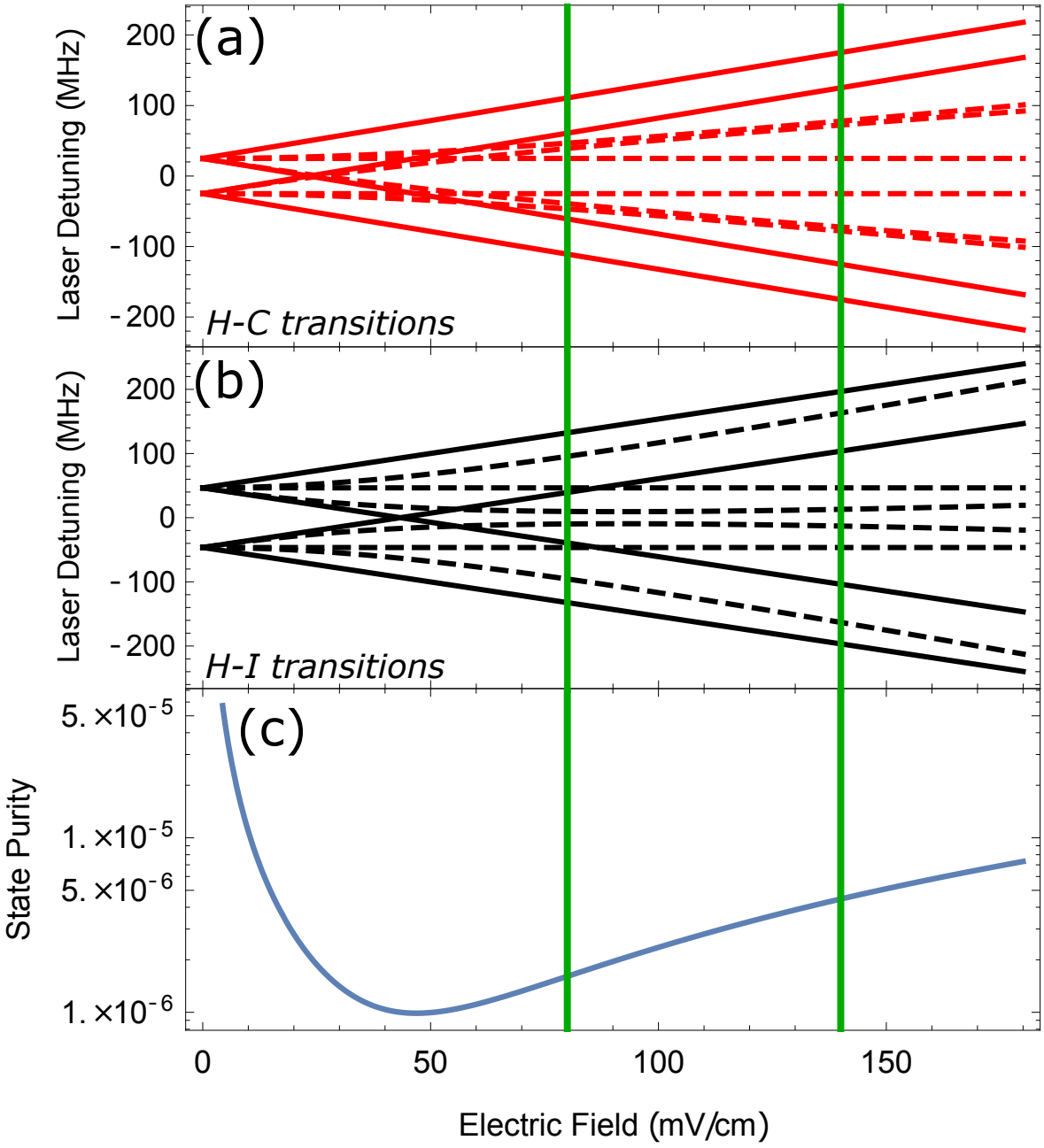

Figure 3.5.3: **Factors contributing to the electric field magnitude selection.** **(a)** Frequencies for the $H - C$ transitions, used in the experiment (solid lines) and undesired (dashed lines). **(b)** Frequencies for the $H - I$ transitions, used in the experiment (solid lines) and undesired (dashed lines). **(c)** The state purity of $|H, J = 1, M = \pm 1\rangle$ as a function of electric field magnitude. The green lines show the two electric field magnitude values ($1\mathcal{E}$(80 V/cm) and $2\mathcal{E}$(140 V/cm)) used in the ACME II measurement.

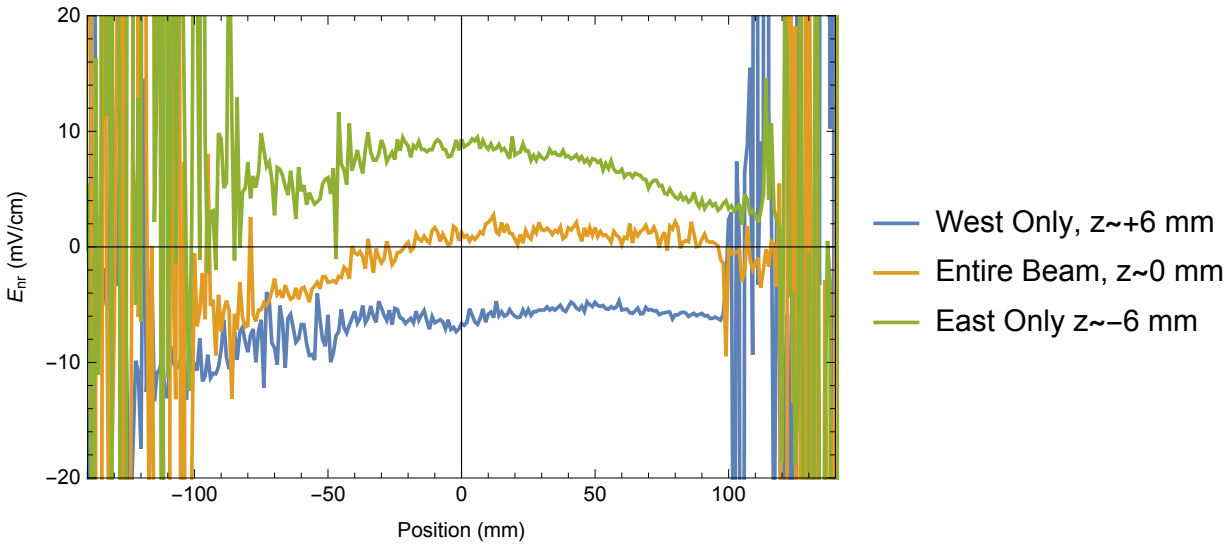

Figure 3.5.4: **Microwave measurement of $\mathcal{E}^{\mathrm{nr}}$.** We measure the component of the electric field which does not reverse, $\mathcal{E}^{\mathrm{nr}}$, at three different positions in the molecular beam along $\hat{z}$. This allows us to extract the gradients $\partial\mathcal{E}^{\mathrm{nr}}/\partial z$ and $\partial\mathcal{E}^{\mathrm{nr}}/\partial x$.

In ACME II, STIRAP necessarily prepares a spin-aligned state along $\hat{x}$ (see Section 3.2). Since the microwaves are traveling along $\hat{x}$ and are polarized along $\hat{y}$, we first need to prepare a spin aligned state with a component along this direction. To do so, we rotate the polarization of the refinement beam by $\pi/4$, re-preparing a state in the $x-y$ plane which has its spin aligned at an angle of $\pi/4$ with respect to the STIRAP-prepared $\hat{x}$ spin alignment, with equal components along $\hat{x}$ and $\hat{y}$. The microwaves then deplete the component of the state that is aligned with $\hat{y}$. We compute the asymmetry in population between the $\hat{x}$ and $\hat{y}$ population components using our usual polarization switching scheme (see Section 3.3.5). We fit the microwave asymmetry lineshape to obtain the resonant microwave frequency. We measure the resonant microwave frequency for states in all $\tilde{\mathcal{N}} = \pm 1$, $\tilde{\mathcal{E}} = \pm 1$, $\tilde{\mathcal{L}} = \pm 1$ switch configurations. By performing parity sums on those states (Eq. 2.7), we extract correlated components of the electric field. $\mathcal{E}^{\mathrm{nr}}$, the non-reversing component of the electric

field, is given by the $\tilde{\mathcal{N}}$, $\tilde{\mathcal{E}}$ correlated detuning component

$$\mathcal{E}^{\mathrm{nr}} = \Delta^{\mathcal{N}\mathcal{E}}/D_H, \tag{3.11}$$

where D_H is the electric dipole moment of the H state. As described in detail in Section 5.3, $\mathcal{E}^{\mathrm{nr}}$ is of great interest to us as it is one of the parameters leading to the various systematic effects in ACME I and ACME II.

Gradients in $\mathcal{E}^{\mathrm{nr}}$, particularly those in the $\hat{y}$ and $\hat{z}$ directions, can also contribute to systematic effects (section 5.4.1). We measure them by performing the microwave measurement with only half of the molecular beam. We measure $\partial\mathcal{E}^{\mathrm{nr}}/\partial z$ by blocking half of the STIRAP state preparation laser beams using razor blade collimators, along $\hat{z}$ (Fig. 3.5.4). We also measure $\partial\mathcal{E}^{\mathrm{nr}}/\partial y$ by using razor blade light collimators to either block the top or bottom of the readout beam, along $\hat{y}$.

3.5.4 Magnetic field control and monitoring upgrades

The ACME II magnetic field generation and monitoring system is based on that used in the ACME I measurement, but with important upgrades. To allow for better monitoring and *in situ* measurement of the magnetic fields, we modified the flanges of the vacuum chamber by adding insert pockets that allow for placement of the field monitoring flux gate magnetometers in regions $20 - 30$ cm away from the location of the molecules. The magnetometers were mounted on long rods that were connected to rotation stages outside of the vacuum chamber. We could rotate the magnetometers *in situ* by rotating these rods. We subtract the slowly drifting electronic offset which is common to flux gate magnetometers by rotating the magnetometers by 180 degrees and taking the difference between the two configurations.

There are four magnetic field monitoring magnetometers, two that extend in the $\hat{y}$ direction and two that extend in the $\pm\hat{z}$ direction on either side of the electric field plates. The

$\hat{y}$ magnetometers are connected to a translation stage that allows us to map the magnetic field and therefore extract magnetic field gradients along the $\hat{y}$ direction. In addition to this monitoring, we mapped the magnetic fields and their gradients before and after the eEDM dataset by sliding a 3-axis fluxgate magnetometer down the beamline, along $\hat{x}$, at the position of the ThO molecules in the apparatus. We also perfomed this magnetometer measurement at a few vertical $\hat{y}$ positions to measure magnetic field gradients in $\hat{y}$. While a translation along $\hat{z}$ was not possible due to the geometry of the field plates, we could extract these field components by measuring the others and using Maxwell's equations.

The geometry of the magnetic field coils was modified to allow space for the magnetometers and better optical access through larger windows in ACME II. The main magnetic field coils perform the same role as in ACME I, to apply the uniform precession magnetic field along the $\hat{z}$ direction, $\mathcal{B}_z$. Additional coils allow us to apply $\mathcal{B}$-field offsets in the transverse directions ($\mathcal{B}_x$ and $\mathcal{B}_y$), as well as all possible first-order gradients ($\partial\mathcal{B}_z/\partial z$, $\partial\mathcal{B}_z/\partial y$, $\partial\mathcal{B}_x/\partial x$, $\partial\mathcal{B}_y/\partial y$, $\partial\mathcal{B}_y/\partial x$, $\partial\mathcal{B}_z/\partial x$), which we use for systematic error checks.

The magnetic shields were modified by cutting more holes for increased optical access, magnetometer pockets and lightpipe access. We changed the degaussing geometry and increased the degaussing current to better be able to remove residual magnetization in the $\mu-$metal shields. Increasing the degaussing frequency to 100 Hz, which better penetrates the thickness of the mu-metal shields, also helped with improved degaussing strength.

3.5.5 Interaction region assembly and vacuum

All components of the ACME II apparatus were constructed from materials that we carefully selected. To minimize the residual magnetic field and its gradients, all parts that are installed inside the magnetic field shielding were chosen to be non-ferrous and non-magnetic. Examples of materials with magnetism that we can tolerate are: aluminum 6061, titanium, copper, brass, plastics, ceramics, glass, phosphor bronze, berylium copper. All parts that were installed within the magnetic shields were tested for magnetization by passing them

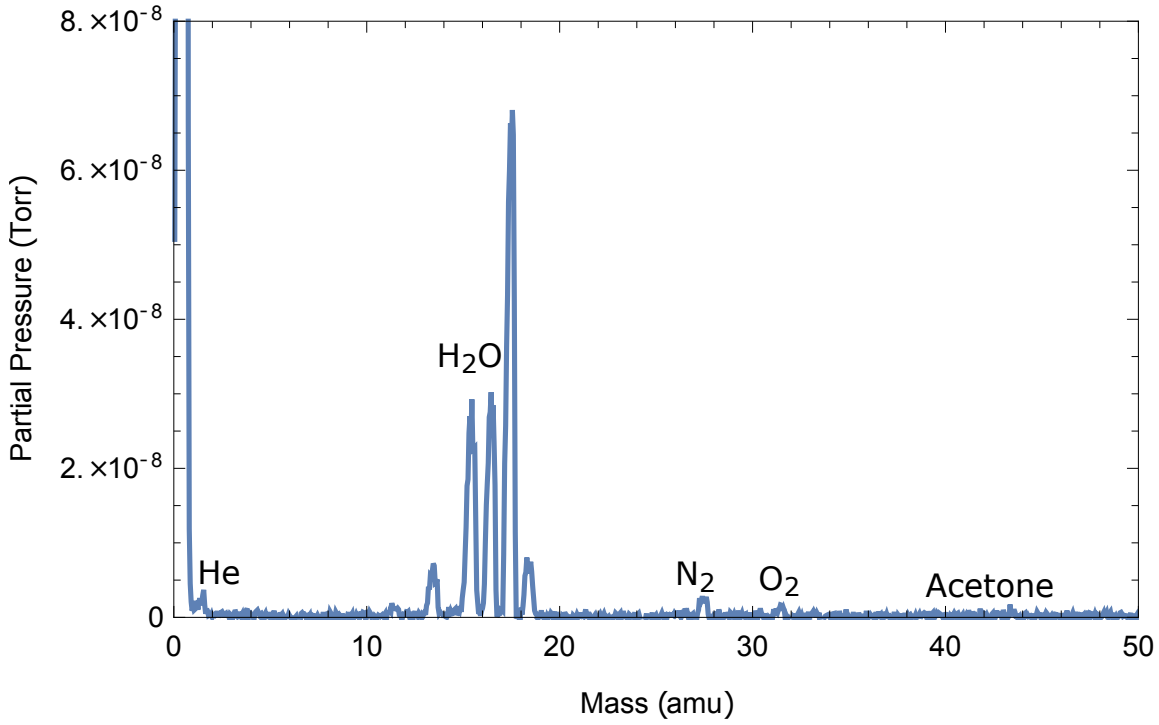

Figure 3.5.5: **Composition of the interaction region vacuum.** The composition of the interaction region vacuum after baking was measured with an residual gas analyzer (RGA). The largest peaks are due to water.

over a fluxgate magnetometer and looking for magnetic fields with a sensitivity of better than 1 μG.

We were careful about the outgassing properties of the materials that compose the parts installed inside the vacuum chamber, with preference for metals. Low outgassing rates are a requirement for reaching a low enough vacuum regime such that the collision rate between ThO molecules and background gas is neglijible and minimally reduces the number of ThO molecules in the beam. In addition, we need to ensure outgassed materials do not deposit on the electric field plates, causing patch potentials, or on the optics, reducing laser intensity profile uniformity. In the cases where we needed formable materials, such as for mounting the collection optics of field plates, we used PEEK or Viton, and tested the material composition of each part carefully in a separate setup by measuring their outgassing properties. To remove water and other solvent contaminants, we baked the

vacuum chamber at $\sim$ 100 °C for several days. After bake out, the pressure stabilized at $\sim 1 \times 10^{-7}$ torr, with a composition of mainly water and atmospheric gases (Fig. 3.5.5).

A famous explorer once said, that the extraordinary is in what we do, not who we are. I'd finally set out to make my mark; to find adventure. But instead adventure found me. In our darkest moments, when life flashes before us, we find something; Something that keeps us going. Something that pushes us.

Lara Croft, *Tomb Raider*

4

Data Analysis

This chapter describes the data analysis techniques used to extract the eEDM value from the ACME II dataset. The analysis is heavily interlaced with the measurement scheme and is designed to optimize eEDM sensitivity and minimize the effects of unwanted systematic effects.

4.1 Signal Asymmetry

As described in Section 2.4, we read out the precession phase Φ by addressing the $H - I$ transition with linearly polarized light and monitoring the resulting fluorescence. There

were eight separate acquisition channels, one corresponding to each of the eight PMTs and light collection lens doublets (see Section 3.3.1). To take full advantage of the digitization range of our data acquisition (DAQ) digitizer[1] ([-2,+2] V; see Section 3.3.7), the signal corresponding to each one of the eight PMTs is multiplied by a factor of 25 using low loise preamplifiers[2]. An LC low-pass filter with a cut-off frequency of $2\pi \times 5$ MHz removes any short timescale dynamics from the signal and prevents aliasing of frequency components higher than the Nyquist frequency corresponding to the 16 MSa/s digitization rate.

Each of the eight signal paths have identical amplification and filtering electronics, but variation of the photoelectron avalanche multiplication factor of each of the 8 PMTs makes it so that the photoelectron signals are produced with varying gain. The procedure for measuring the PMT gain factors is described in Section 3.3.6. We correct for this variation by dividing each signal by the measured PMT gain. We collect 10 ms of data per pulse of ThO molecules (one pulse is produced every 20 ms). From the 10 ms of data, ~ 3 ms are high signal, where the fluorescence signal is much larger than the background scatter (Fig. 4.1.1c).

To normalize against changing molecule number, we alternate the readout laser polarization fast enough so that each molecule is reliably projected onto one of the two orthogonal spin alignment directions, $\hat{X}$ and $\hat{Y}$, with a probability determined by the orientation of its spin, during the time $\approx 10\mu$s it flies through the laser beam [66]. To do so, we overlap two laser beams with orthogonal $\hat{X}$ and $\hat{Y}$ polarizations, which we switch on and off rapidly (200 kHz) using AOMs. The $\hat{X}$ and $\hat{Y}$ pulses each have a duration of 1.9 μs, with a 0.6 μs delay between them to minimize the overlap of signal due to the finite lifetime of the I state (115 ns) [76] between successive pulses (Fig. 4.1.1a). This timing structure ensures that approximately one fluorescence photon is emitted by each molecule by projecting the molecule spin aligned state onto the two orthogonal spin states corresponding to the two

[1] NI PXI-5171R FPGA
[2] SRS SR445A

orthogonal polarizations, $\hat{X}$ and $\hat{Y}$, of the linearly polarized probe laser beam.

The switching of the laser polarization results in a time varying PMT signal, $S(t)$, as shown in Figure 4.1.1a. The shape of the time modulated signal is given by the molecular dynamics resulting from the properties of the readout molecular states H, I and the laser beam intensity spatial and time profile. Immediately after the laser is switched on, there is a rapid increase in fluorescence as molecules in the laser beam are quickly excited. When $\Omega_r t \ll 1$, where $\Omega_r \sim 2\pi \times 3$ MHz is the Rabi frequency of the readout $H - I$ transition, the fluorescence magnitude increases as $S(t) \propto \Omega_r^2 t^2$. Later, when $\Omega_r t \geq 1$, population is evenly mixed between the H and I states, causing $S(t)$ to decay exponentially with a time constant of $2\tau_I \approx 230$ μs, where $\tau_I \approx 115$ ns is the lifetime of the I state. During this time, molecules continue to enter the laser beam, such that the exponential decay approaches a constant fluorescence rate in the steady state. After the laser turns off, the signal decays exponentially to zero with time constant τ_I.

During data acquisition, we average 25 molecular pulses together to form a "trace" (Fig. 4.1.1c) and record individual traces corresponding to each of the eight PMTs. We typically sum the photoelectron signal in the eight PMTs but also frequently check the spatial dependence of the fluorescence as a diagnostic.

We use the time range of [0.5,2.5] ms of each trace, where there are no molecules produced, to determine the time-dependent background, $B(t)$. We do not use the first 0.5 ms to reduce potential noise due to leakage of the signal triggering the DAQ digitizer into the measurement channels. $B(t)$ consists of an offset caused by the DC electronic offset intrinsic to the PMTs and amplifiers and a time-varying component caused by turning on and off the probe lasers and other light sources in the experiment (see Figure 4.1.1b). To reduce the uncertainty in the background, we use the fact that $B(t)$ is modulated at the polarization switching frequency and assume that $B(t)$ is otherwise constant over the duration of each trace. We average together the 2 ms background data in each trace, corresponding to 400

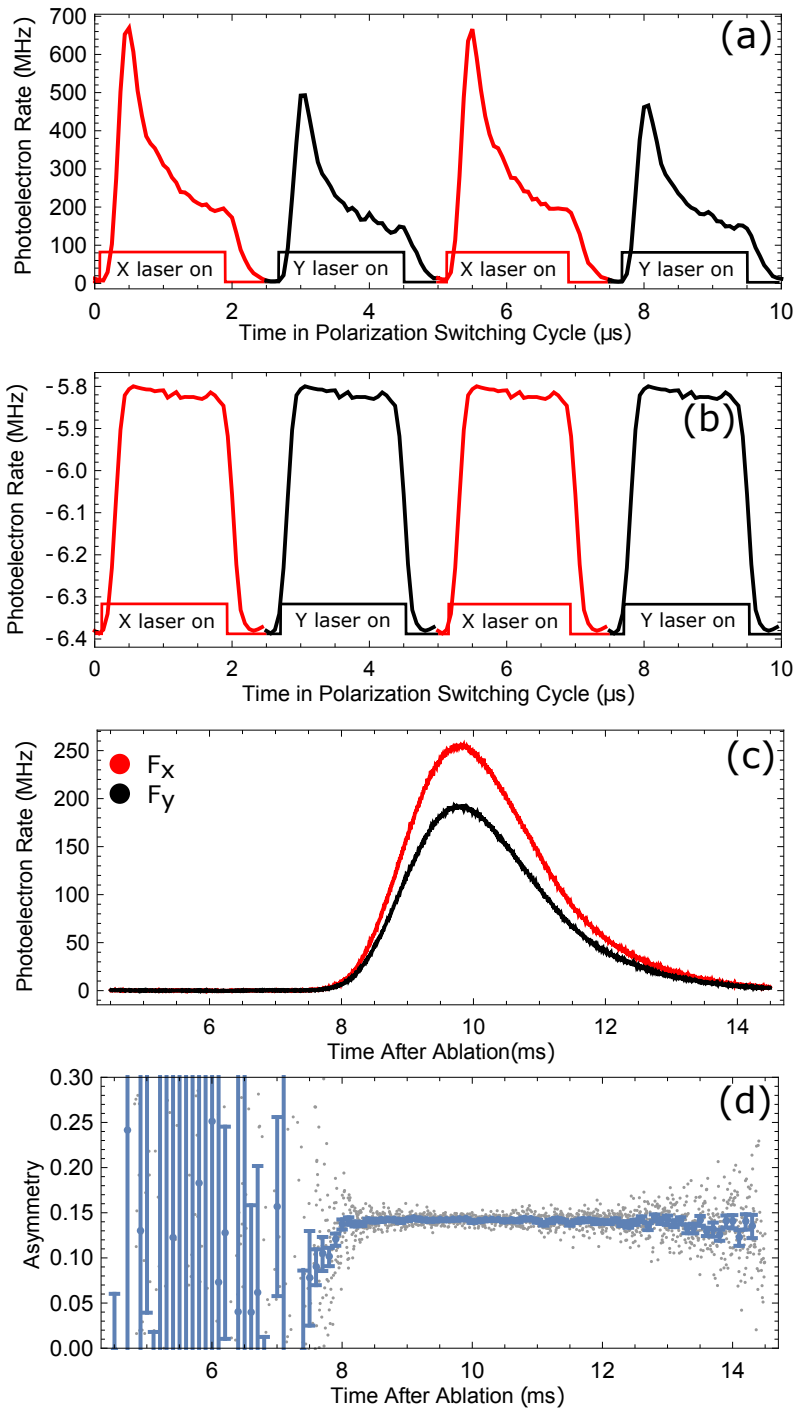

Figure 4.1.1: **Trace data analysis.** **(a)** Molecular fluorescence signal $F(t)$ for the $\hat{X}$ (red) and $\hat{Y}$ (black) orthogonal polarizations. **(b)** Background signal $B(t')$ obtained from data acquired before the arrival of the molecules in the readout region. The data is averaged over 2 ms (400 polarization cycles). **(c)** Integrated fluorescence signals F_X and F_Y for the entire molecular pulse. **(d)** Asymmetry computed for each pair of consecutive $\hat{X}$-$\hat{Y}$ polarization pulses (gray points). The blue points with error bars are constructed from a linear regression of 20 adjacent gray asymmetry points.

polarization cycles, to compute the trace background per polarization cycle, $B(t')$. We then compute the fluorescence $F(t)$ produced by each polarization state by subtracting the signal from the background $F(t) = S(t) - B(t')$.

We integrate $F(t)$ over times associated with pairs of orthogonality polarized ($\hat{X}$ and $\hat{Y}$) laser pulses to compute F_X, F_Y. Integration is performed over a specific time window that we denote polarization "integration sub-bin". To ensure that the choice of sub-bin did not affect our result, we examine and show that the mean value of $\omega^{\mathcal{NE}}$ is independent of the choice of sub-bin in Section 4.6. After binning, the amplitude of both F_X and F_Y pulses follows the envelope of the molecular pulse (Fig. 4.1.1c). We normalize against this slow-evolving amplitude by computing the asymmetry, $\mathcal{A}$. The asymmetry, shown in Figure 4.1.1d, is computed for each polarization cycle (corresponding to 5 μs)

$$\mathcal{A} = \frac{F_X - F_Y}{F_X + F_Y} \tag{4.1}$$

The asymmetry has a linear dependence on time after ablation because the molecules precess in the magnetic field over a fixed distance. Slower molecules, which arrive later, precess more than faster molecules, which arrive earlier. The slope of linear dependence is given by the magnitude of the magnetic field.

We determine the uncertainty in $\mathcal{A}$ by grouping together $n \approx 20-30$ adjacent asymmetry points. For each group, we perform a linear regression to account for the linear dependence of asymmetry on time within the molecular pulse. After correcting for the linear slope, we calculate the group mean asymmetry, $\bar{\mathcal{A}}_j$, and uncertainty in the mean, $\delta\bar{\mathcal{A}}_j$, which are shown as points and error bars in Figure 4.1.1d.

The previous operation gives us asymmetry points in time after ablation for each of the 64 traces in one block. However, each block contains 4 switches $\tilde{\mathcal{N}}, \tilde{\mathcal{E}}, \tilde{\mathcal{B}}, \tilde{\theta}$, which corresponds to $2^4 = 16$ states. We use standard error propagation to perform a weighted average over the four degenerate traces corresponding to each of the 16 states.

4.2 Contrast and Phase

To compute the phase Φ, we need to divide $\mathcal{A}$ by the contrast $\mathcal{C}$ (see Eq. 2.5). Ideally, $\mathcal{C} = 1$, but experimental imperfections such as velocity dispersion and population decay into the opposite $\hat{X}, \hat{Y}$ polarization quadrature typically limit $\mathcal{C} < 1$. As described in Section 2.4, the orthogonality of the polarizations of the $\hat{X}$ and $\hat{Y}$ readout laser beams is set by a polarization beam splitter (PBS). A half-waveplate placed after the PBS in the optical path of the readout laser beam allows us to change the global angle θ between the $\hat{X}$ and $\hat{Y}$ axes and the laboratory frame. The contrast, which is given by the sensitivity of the asymmetry to phase, can be computed either from $2\mathcal{C} = -\partial\mathcal{A}/\partial\theta$ or $2\mathcal{C} = -\partial\mathcal{A}/\partial\phi$. We could therefore measure contrast either by dithering the accumulated phase ϕ (by varying $\mathcal{B}_z$) or the relative laser polarization angle θ. We use the later since it can be performed in a fast manner (<1 s) by rotating the half-waveplate with a computer-controlled rotation stage.

The spin precession measurement asymmetry is shown as a function of θ in Figure 4.2.1. To optimize the eEDM sensitivity, we ran the experiment on the steepest part of the asymmetry fringe, $\theta = \theta^{\mathrm{nr}}$. We measured the contrast for each asymmetry group, $\mathcal{C}_j$, by switching θ between two angles, $\theta = \theta^{\mathrm{nr}} + \Delta\theta\tilde{\theta}$, where $\tilde{\theta} = \pm 1$ and $\Delta\theta = 0.1$ rad. For each block experimental state, we calculate the contrast as

$$\mathcal{C}_j(\tilde{\mathcal{N}}, \tilde{\mathcal{E}}, \tilde{\mathcal{B}}) = -\frac{\bar{\mathcal{A}}_j(\tilde{\theta} = +1, \tilde{\mathcal{N}}, \tilde{\mathcal{E}}, \tilde{\mathcal{B}}) - \bar{\mathcal{A}}_j(\tilde{\theta} = -1, \tilde{\mathcal{N}}, \tilde{\mathcal{E}}, \tilde{\mathcal{B}})}{4\Delta\theta}. \tag{4.2}$$

Given that the measurement was performed on the slopes of the spin-precession fringes, where the asymmetry is near zero, we calculate the total accumulated phase for each of the 2^3 block experimental states from

$$\Phi_j(\tilde{\mathcal{N}}, \tilde{\mathcal{E}}, \tilde{\mathcal{B}}) = \frac{\bar{\mathcal{A}}_j(\tilde{\theta} = +1, \tilde{\mathcal{N}}, \tilde{\mathcal{E}}, \tilde{\mathcal{B}}) + \bar{\mathcal{A}}_j(\tilde{\theta} = -1, \tilde{\mathcal{N}}, \tilde{\mathcal{E}}, \tilde{\mathcal{B}})}{4\tilde{\mathcal{C}}_j(\tilde{\mathcal{N}}, \tilde{\mathcal{E}}, \tilde{\mathcal{B}})} + q\frac{\pi}{4}. \tag{4.3}$$

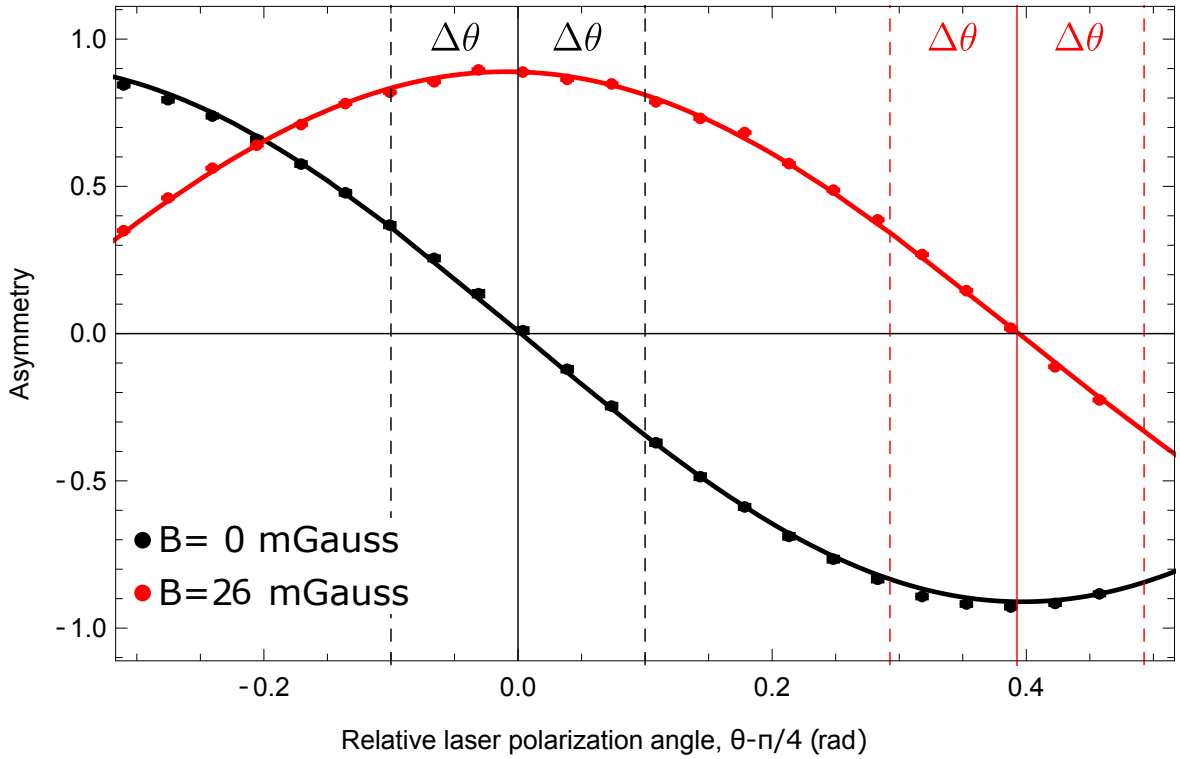

Figure 4.2.1: **ACME II spin analysis fringes.** The fringes are shown as a function of readout laser linear polarization angle, θ. The fringes are shown with no magnetic field ($\mathcal{B}_z = 0$ mG) and when the magnetic field is tuned to cause Zeeman spin precession of $\pi/4$ ($\mathcal{B}_z = 26$ mG). The dashed vertical lines show the typical values of the waveplate dither, $\Delta\theta$, used to extract the contrast, $\mathcal{C}$.

The Zeeman precession angles of $\{0, \pi/4\}$, corresponding to $q \in \{0, \pm 1\}$ are set by applying magnetic field magnitudes of $\mathcal{B}_z \in \{\pm 1, \pm 26\}$ mGauss. We apply small magnetic field values, rather than turn the magnetic field off completely so that we can still measure the precession time, τ, from the Zeeman precession phase. Since we compute phase for each state individually, correlations between the contrast and experimental switches are suppressed. However, we still monitor and limit possible contributions due to these correlations, as described in Sections 5.7 and 5.16.

Both contrast and phase calculations were performed for each of the points and error bars corresponding to asymmetry groups (Figure 4.3.1). Error bars are propagated using standard Gaussian statistics. Figure 4.3.1a shows a typical contrast trace when the applied magnetic field is low $\mathcal{B}_z \approx 1$ mGauss (corresponding to ≈ 0 Zeeman precession angle),

where the contrast magnitude $|\mathcal{C}| \sim 96\%$ is independent of time within the molecular pulse. As shown in Figure 4.3.1b, contrast is reduced to $|\mathcal{C}| \sim 94\%$ when $\mathcal{B}_z \approx 26$ mGauss (corresponding to $\approx \pi/4$ Zeeman precession angle). We believe the reduction in contrast at higher $\mathcal{B}_z$ is due to velocity dispersion in the molecular beam. The contrast is lower at the beginning and end of the molecular pulse, due to increased velocity dispersion in the velocity classes corresponding to those arrival times.

The sign of the contrast can be reversed by performing the measurement on the slope of opposite sign, which corresponds to an interchange of the roles of the $\hat{X}$ and $\hat{Y}$ polarization laser beams. Two superblock switches perform such a reversal: $\tilde{\mathcal{R}}$ and $\tilde{\mathcal{P}}$. The $\tilde{\mathcal{R}}$ switch physically rotates the $\hat{X}-\hat{Y}$ probe polarization basis by $\pi/2$ through the use of the readout waveplate. The $\tilde{\mathcal{P}}$ switch tunes the readout laser to address opposite parity sub-levels of the readout I state. In addition, for the special case when $|q| = 1$, the $\tilde{\mathcal{B}}$ switch also corresponds to a $\pi/2$ rotation of the readout laser basis on the lab frame.

The $\tilde{\mathcal{P}}$ and $\tilde{\mathcal{R}}$ switches allow us to reverse the sign of the contrast and offer important suppression of effects that might shift the asymmetry but not occur due to a true phase, such as coming from relative imperfections in the readout $\hat{X}$ and $\hat{Y}$ laser beams. Examples of mechanisms causing such effects are described in Section 5.15. Since a true phase need not depend on the sign of $\mathcal{C}$, performing these switches as part of the experimental sequence rejects such "asymmetry" effects. For example, $\Phi^{\mathcal{N}\mathcal{E}}$ will only change sign with the $\tilde{\mathcal{N}}$ and $\tilde{\mathcal{E}}$ switches, but $\mathcal{A}^{\mathcal{N}\mathcal{E}}$ also changes sign with $\tilde{\mathcal{P}}$, $\tilde{\mathcal{R}}$ and $\tilde{\mathcal{B}}$ (when $q = 1$). Performing these switches and computing the parity sum that is even with respect to them suppresses such offsets from contaminating the phase measurement channels.

4.3 Computing correlated phase and frequency

After computing the phase for each of the 2^3 $(\tilde{\mathcal{N}}, \tilde{\mathcal{E}}, \tilde{\mathcal{B}})$ experimental states, $\Phi_j(\tilde{\mathcal{N}}, \tilde{\mathcal{E}}, \tilde{\mathcal{B}})$, we use Eq. 2.7 to convert quantities from the state basis to the experiment switch-parity

basis. We denote phase in the experiment switch parity basis as Φ_j^u, where u is the selected combination of switches under which Φ_j^u is odd. Φ_j^u is even under all other switches over which the base transformation was performed. We use the superscript "nr" to denote the component of the phase that is even under all considered switches.

To extract the precession frequency, we measure the precession time, τ_j, from the Zeeman precession phase component (Figure 4.3.1c),

$$\Phi_j^B = -\mu_{\mathcal{B}} g_{\mathcal{N}} \mathcal{B}_z \tau_j. \tag{4.4}$$

The measurement of Φ^B once per block (period 1 minute) was sufficient to correct for the slow drift in τ of up to 20% over a 10-20 minute period. The uncertainty of B_z and $g_{\mathcal{N}}$ is less than 1%, so it does not contribute significantly to the measurement of τ. We then compute the spin precession frequencies from

$$\omega_j^u = \Phi_j^u / \tau_j. \tag{4.5}$$

We compute the correlated frequency by dividing Φ_j^u by τ_j by performing point by point division, since the uncertainty in τ_j is sufficiently smaller than that in Φ_u and therefore does not significantly increase the ω_j^u error bar. Figure 4.3.1d shows the computed eEDM correlated frequency $\omega_j^{\mathcal{NE}}$ for one block of data.

So far, we have kept the subscript j for all of our measured quantities. This allowed us to look and correct for variations of the measured quantities with time after ablation, such as was the case for the ablation time τ_j. However, as discussed in detail in Section 4.6. such effects are not present in the channels of interest. Thus, we typically drop this superscript and average all data in time after ablation in the selected signal cut region, for all parity sum channels in each block, obtaining ω^u. The choice of signal cut is discussed in Section 4.6.

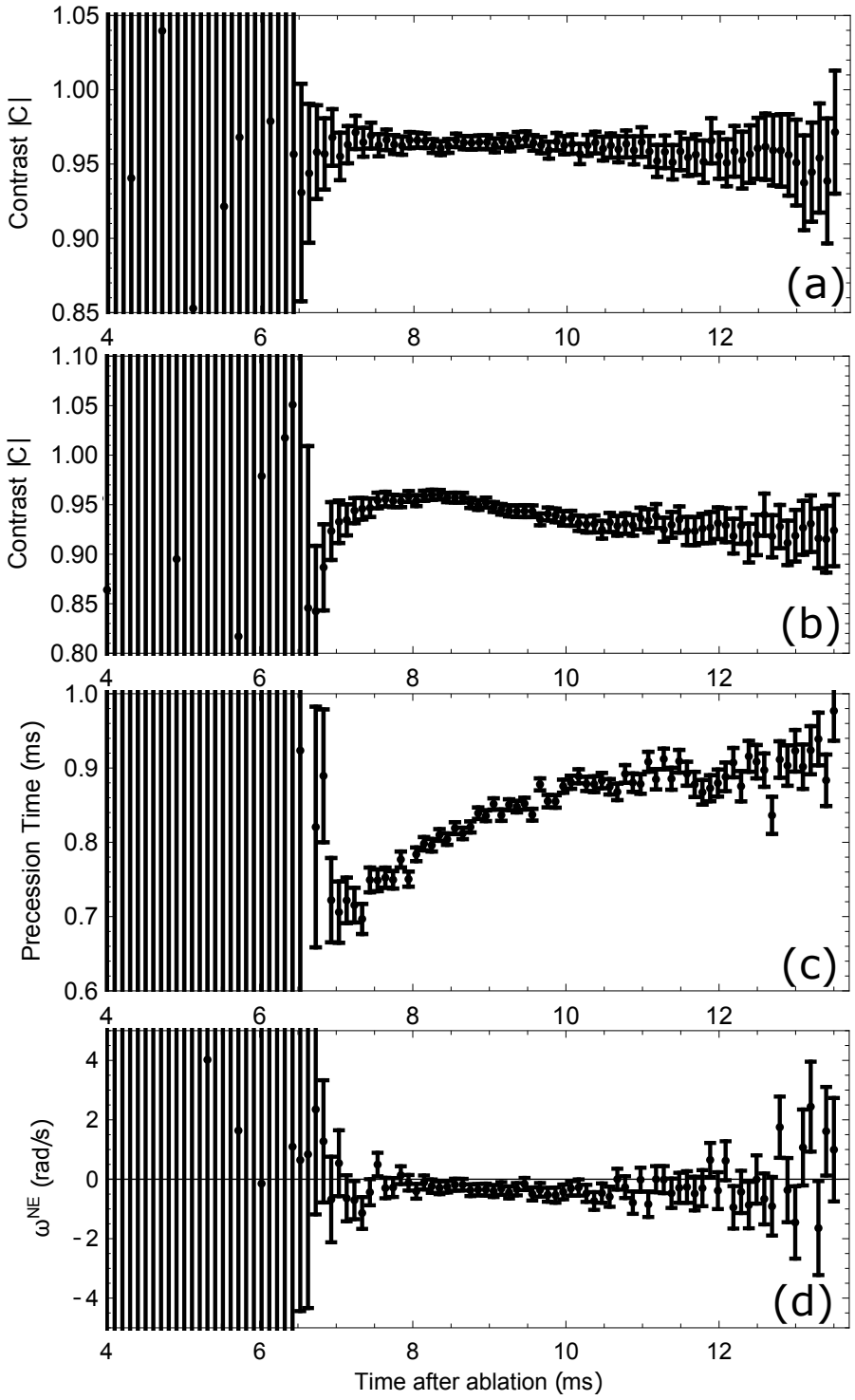

Figure 4.3.1: **ACME II block data.** Block contrast, as a function of time after ablation, when data is acquired with **(a)** a small Zeeman phase ~ 0 (corresponding to low $|\mathcal{B}_z| = 1$ mGauss) or **(b)** Zeeman phase $\sim \pi/4$ (corresponding to $|\mathcal{B}_z| = 24$ mGauss). **(c)** Precession time as a function of arrival time. Molecules that arrive earlier in time traveled faster and therefore have a smaller precession time. **(d)** $\omega^{\mathcal{NE}}$, the eEDM correlated precession frequency calculated for one block. Error bars correspond to 1σ (68%) confidence intervals.

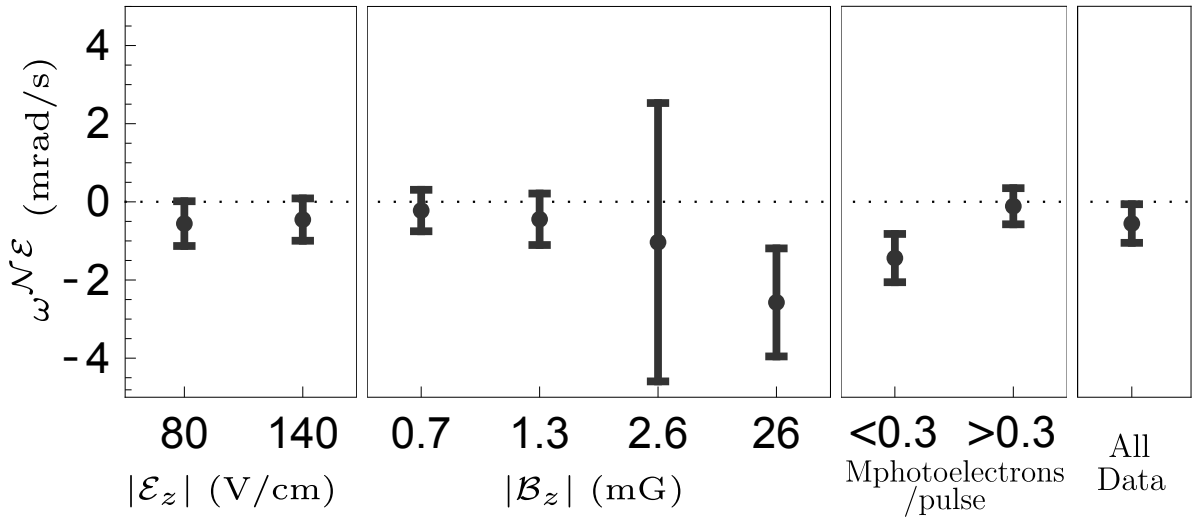

Figure 4.3.2: **Variation of $\omega^{\mathcal{NE}}$ with experiment parameters.** Values of $\omega^{\mathcal{NE}}$ grouped by the magnitudes of $|\mathcal{E}_z|$, $|\mathcal{B}_z|$, block-averaged number of photoelectrons per pulse, and combined for all states. Error bars correspond to 1σ (68%) confidence intervals.

Each superblock contains 16 blocks, but only 2^3 states, corresponding to the $\tilde{\mathcal{P}}, \tilde{\mathcal{L}}, \tilde{\mathcal{R}}$ switches of a superblock (see Fig. 2.5.1). We average together the block quantities corresponding to the two degenerate states using Gaussian weighted averages. We next perform the same base transformation described in Eq. 2.7 for the superblock switches and obtain the precession frequency in the superblock switch parity basis.

The eEDM is extracted from $\omega^{\mathcal{NE}}$, the superblock parity sum that is only correlated with the two switches that reverse the sign of $\vec{\mathcal{E}}_{\text{eff}}$, $\tilde{\mathcal{N}}$ and $\tilde{\mathcal{E}}$, but none of the other performed switches. In the absence of systematic errors the eEDM is given by $d_e = -\omega^{\mathcal{NE}}/\mathcal{E}_{\text{eff}}$.

In addition to the 7 switches described above, we also varied the $\mathcal{B}$-field magnitude, $|\mathcal{B}_z| = 0.7,\ 1.3,\ 2.6,\ 26\,\text{mG}$ (corresponding to $|\phi| \approx \frac{\pi}{160}, \frac{2\pi}{160}, \frac{4\pi}{160}$, and $\frac{\pi}{4}$, respectively), and the $\mathcal{E}$-field magnitude, $|\mathcal{E}_z| = 80,\ 140\,\text{V/cm}$. 5% of data was taken with $|B_z| = 2.6$ mG; the rest was taken at $|B_z| = 0.7, 1.3, 26$ mG in approximately equal amounts. Most data was taken with magnetic field magnitudes lower than $|B_z| < 2.6$ mG to minimize the amount of noise present in the measured frequency and contrast. Equal amounts of data were taken

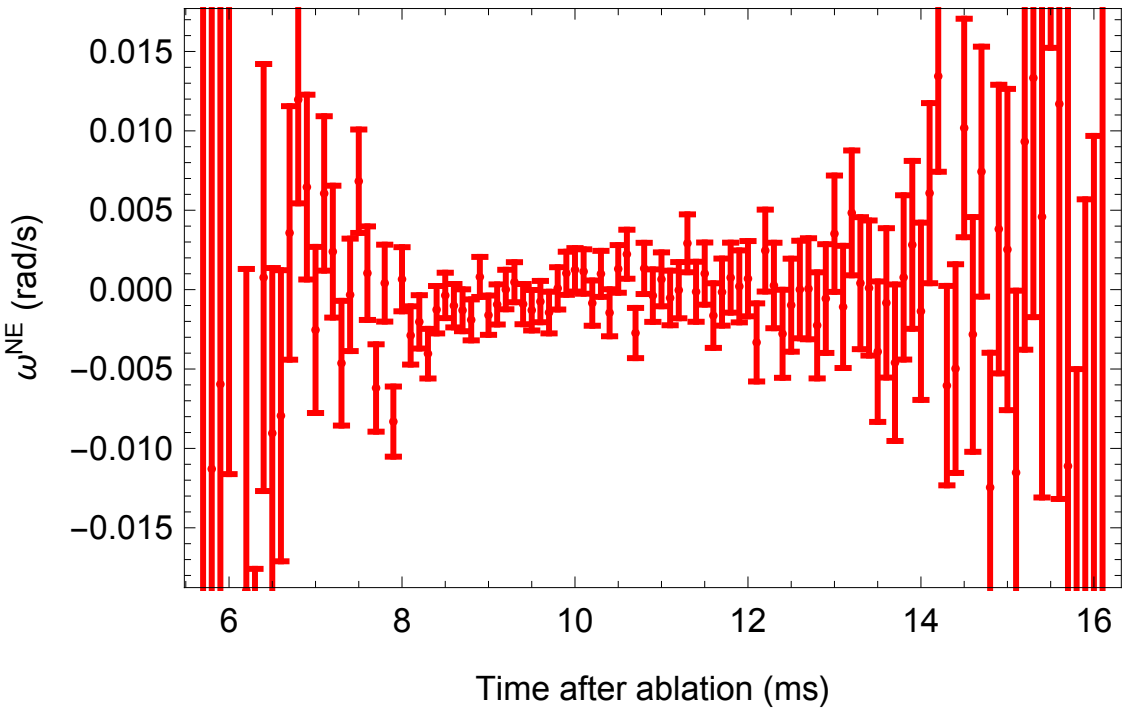

Figure 4.3.3: $\omega^{\mathcal{NE}}$ **showing no variation with time after ablation.** To obtain variation of $\omega^{\mathcal{NE}}$ vs. time after ablation, we perform a weighted average of the $\omega^{\mathcal{NE}}$ channel for all blocks in the EDM dataset, while preserving information of time within the molecular pulse. Error bars correspond to 1σ (68%) confidence intervals.

with each of the two electric field magnitudes. The $\omega^{\mathcal{NE}}$ values obtained from isolating the data under each of these parameter values are shown in Fig. 4.3.2.

In addition, we have analyzed our data by grouping it by other experiment parameters, which we do not switch and might vary continuously over the dataset. Figure 4.3.3 shows the variation of $\omega^{\mathcal{NE}}$ with time after ablation within the molecular pulse.

4.4 Nonzero channels and $\omega^{\mathcal{NB}}$

While we expect most other channels to be zero, there are some frequency channels that are non-zero due to known effects. We use these channels to verify that our understanding of the measurement is correct and to search for and monitor systematic errors. Such an example is $\omega^{\mathcal{NB}}$, which we can use to measure Δg, the difference in the magnetic moment

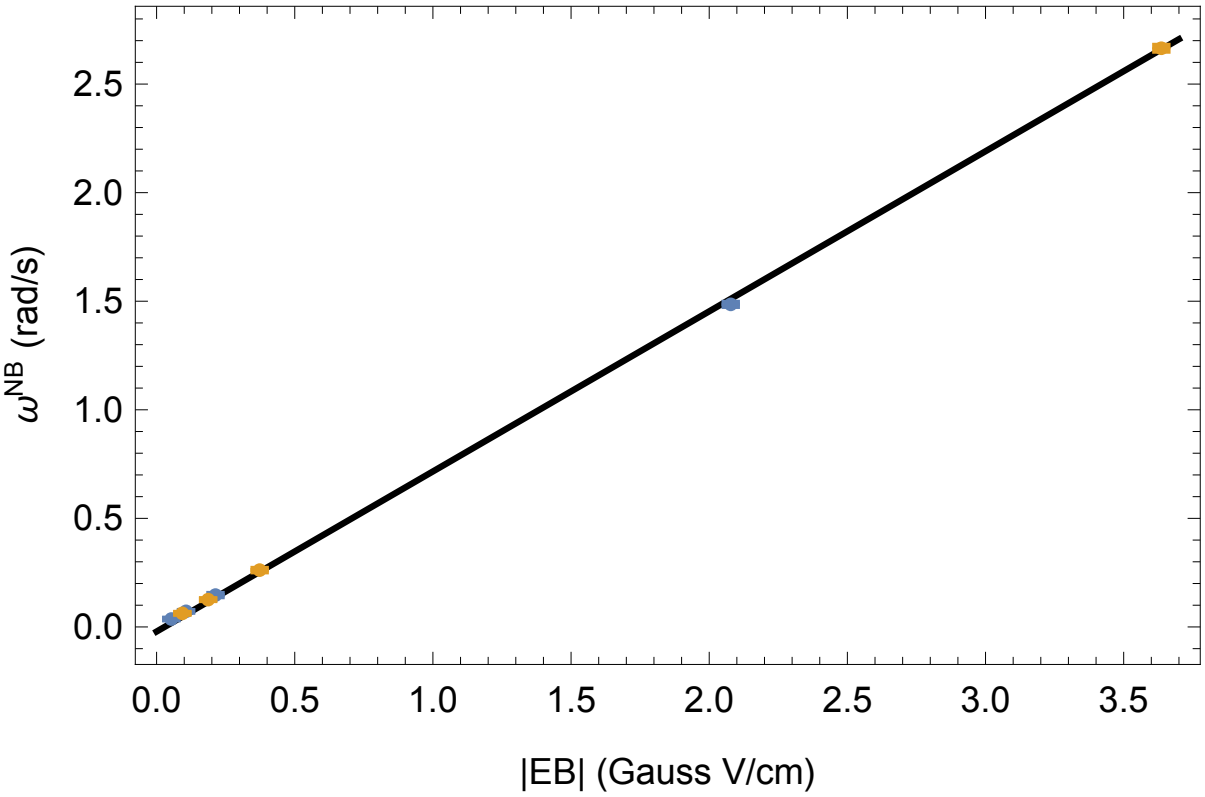

Figure 4.4.1: **Measurement of η.** $\omega^{\mathcal{NB}}$ shown as a function of $|\mathcal{EB}_z|$ for the $H, J = 1$. We use the slope of the linear fit $\omega^{\mathcal{NB}}/|\mathcal{EB}_z| = -\eta\mu_B/\hbar$ to extract $\eta = -0.82$. Error bars are smaller than the display markers.

magnitude between the upper and lower $\mathcal{N}$-levels, arising from perturbations due to other electronic and rotational states [68]. This difference is a general feature of measurements in Ω-doublet systems and limits the ability of the $\tilde{\mathcal{N}}$ switch to suppress specific systematic errors (see Section 5.8), so it is an important quantity to measure. As expected, we observe a linear dependence of the $\omega^{\mathcal{NB}}$ frequency with $\mathcal{E}$ and $\mathcal{B}_z$:

$$\omega^{\mathcal{NB}} = -\frac{\eta\mu_B\mathcal{EB}_z}{\hbar}. \tag{4.6}$$

Since we have measured $\mathcal{E}$, $\mathcal{B}_z$ and μ_B precisely from auxiliary data, we can extract $\eta = -0.82$ nm/V (Figure 4.4.1). This value is consistent with that predicted by molecular theory, and it arises as primarily due to mixing from other electronic and rotational states

that are near the $H^3\Delta_1, J = 1$ manifold [59, 68].

4.5 Blind addition

In order to remove experimenter bias from contaminating our results, we performed the entire eEDM data analysis with a blind offset on the $\omega^{\mathcal{NE}}$ frequency channel such that the mean of that channel was not known until all of the data was acquired and the systematic error of the measurement was determined. There were no changes in the data analysis procedure or data that were included in the result after the blind was removed.

We used the same blind value during the entire data taking campaign and preliminary systematic searches. The blind, ω_{blind}, is a random number extracted from a Gaussian distribution with mean zero and distribution width of $\sigma = 10^{-28}\ e \cdot \mathrm{cm}$, a factor of two larger than the uncertainty of the previous best eEDM result, obtained in ACME I [5].

The blinding was performed on all quantities related to the eEDM value, $\omega^{\mathcal{NE}}$, $\Phi^{\mathcal{NE}}$ and $\mathcal{A}^{\mathcal{NE}}$ as follows:

$$\omega^{\mathcal{NE}}_{\text{blinded}} = \omega^{\mathcal{NE}} + \omega_{blind} \tag{4.7}$$

$$\Phi^{\mathcal{NE}}_{\text{blinded}} = \Phi^{\mathcal{NE}} + \omega_{blind}\tau_j \tag{4.8}$$

$$\mathcal{A}^{\mathcal{NE}}_{\text{blinded}} = \mathcal{A}^{\mathcal{NE}} + 2\mathcal{C}\omega_{blind}\tau_j. \tag{4.9}$$

4.6 Data cuts

We apply two cuts on the magnitude of the molecular pulse signal. Firstly, to remove data with low signal-to-noise, we apply a threshold cut on the magnitude of the molecular fluorescence signal, for the groups of each individual trace $F_j^{\text{tot}} = (F_X + F_Y)$. The statistics of the count rates of fluorescence photoelectrons are Poisonian, which are well-aproximated as Gaussian, for large number of photoelectrons. However, since the asymmetry (Eq. 4.1)

is the ratio of two normally distributed random variables, $(F_X - F_Y)$ and $(F_X + F_Y)$, its distribution is not strictly Gaussian. This distribution has Lorentzian tails in the limit in which the mean of the denominator is small or comparable in size to its uncertainty $\bar{F}_j^{\mathrm{tot}} \leq \sigma_{F_j^{\mathrm{tot}}}$ [59]. These Lorentzian tails increase measurement noise and increase the difficulty of assigning an accurate error bar, since proper treatment of such data requires non-Gaussian statistics. Since the frequency and phase are computed from asymmetry, they follow similar statistics, so would also show non-Gaussian tails. However, when $\bar{F}_j^{\mathrm{tot}} \gg \sigma_{F_{\mathrm{tot}}}$, the distribution of $\mathcal{A}$ approaches a Gaussian distribution. We therefore apply a signal size cut of $F_{\mathrm{cut}} = 10$ MS/s to remove the data points corresponding to groups where $\bar{F}_j^{\mathrm{tot}} \ll \sigma(F_X + F_Y)$, where the distribution would deviate from Gaussian and increase the overall measurement uncertainty. We perform this cut for each trace in a block.

The second signal size cut was motivated by an observed decrease in the contrast at earlier and later times in the ablation pulse (Figure 4.3.1a,b). We believe such lower contrast is caused by an increase in velocity dispersion of the molecular beam at the points at early and late time in the ablation process. Out of an abundance of caution, we remove such low contrast data by applying a percent threshold cut of the maximum signal in the pulse, which was typically set to 15% of the amplitude of the molecular pulse. For the signal sizes typical in ACME II, the percent threshold cut was typically more stringent than the signal offset cut, removing a larger fraction of the low signal data.

A filtering step was implemented on each set of 4 degenerate traces in a block. Rarely, with a frequency of a few events per day, the FPGA acquisition would be spuriously triggered, which typically caused the traces to be significantly delayed in time from optimal (by a few ms), which would cause the asymmetry to change by an amount that was significantly larger than that given by statistics. Attempts to remove the physical source of such spurious triggers were unsuccessful. We instead check each 4 sets of nominally degenerate traces in a block and remove either one or two traces where the asymmetry was significantly different (> 10 sigma). This procedure removed less than 0.5% of the data.

In order for a block of data to be included in the final measurement, we also required that each of the 8 $(\tilde{\mathcal{N}}, \tilde{\mathcal{E}}, \tilde{\mathcal{B}})$ experiment states have a measured fringe contrast $\mathcal{C}$ that was physical, between $70 - 100\%$. Such low contrast is usually caused by a laser coming unlocked during the measurement sequence. This cut resulted in less than 0.1% of blocks being discarded. Variations in the magnitude of this cut resulted in smaller than 1% variation in the measured eEDM value.

4.7 Variation of $\omega^{\mathcal{NE}}$ with choice of analysis parameters

To ensure no unexpected effect in our data analysis, we have varied the free parameters in our analysis and looked for a change in the $\omega^{\mathcal{NE}}$ and other measurement channels. These parameters include the size of the signal cut threshold, the number of points included in an asymmetry bin and the choice of the integration sub-bin. We have not observed significant variation of $\omega^{\mathcal{NE}}$ with any of these parameters (Figure 4.8.1).

4.8 Variation of $\omega^{\mathcal{NE}}$ with time

We have also investigated the variation of the $\omega^{\mathcal{NE}}$, the eEDM correlated frequency, with time. Such analyses, searching for an oscillating eEDM component can be used to search and constrain the parameters of axion-like dark matter and its coupling to the ThO molecule [102]. In addition, lack of time variation in our measurement channel further ensures no time-varying systematic errors exist in the ACME experiment, such as caused by environmental parameters that might have a natural time period. Such period might be, for example, daily (beam source de-ice, rotation of the earth), weekly (change in fields due to experimental weekly processes in the other experiments in the LISE building, scheduling of city transit), monthly (target change, motion of the moon). We do not believe any of these effects to be anywhere close to current ACME sensitivity, but we checked anyway.

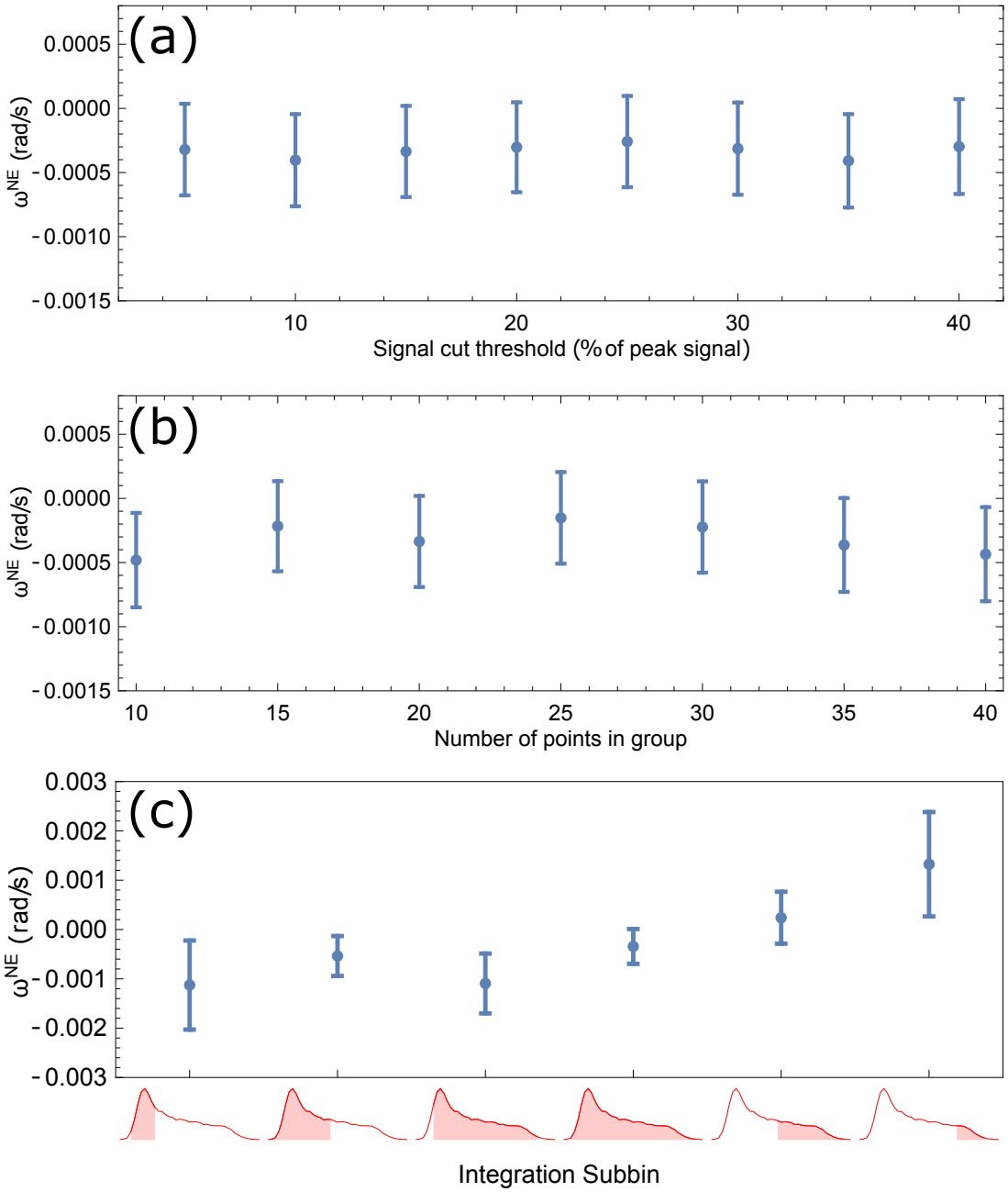

Figure 4.8.1: **Variation of $\omega^{\mathcal{NE}}$ with choice of analysis parameters.** $\omega^{\mathcal{NE}}$ shown as a function of: **(a)** signal cut threshold, **(b)** number of points in an asymmetry group, and **(c)** choice of integration subbin. Data is integrated over the entire eEDM dataset. Error bars correspond to 1σ (68% confidence interval).

We perform this analysis on the ACME II dataset. Each eEDM datapoint corresponds to a superblock which was acquired over a 20 minute period and is time-stamped with a precision that is much better than the acquisition timescale. Figure 4.8.2a shows the time series of all of the ACME II final set superblock datapoints, where time 0 corresponds to the time-stamp of the first acquired superblock, on 1/7/2018, at 3:20 PM.

We look at slow time variation in our eEDM data by performing least squares spectral analysis using the Lomb-Scargle periodgram formalism [103–105]. The Lomb-Scargle is a Fourier analysis method that allows us to compute the periodgram of a time-series where the data points need not be collected at regular time intervals. The method performs least-squares fits of the data with the chosen frequency components. We choose 10,000 frequency steps between 5×10^{-8} Hz and 5×10^{-4} Hz with a step size of 5×10^{-8} Hz. We compute the Lomb-Scargle periodgram from

$$PN(\omega) = \frac{1}{2\sigma}\left\{\frac{\left[\sum_j (Y_j - \bar{Y})\cos\omega(t_j-\tau)\right]^2}{\sum_j \cos^2\omega(t_j-\tau)} + \frac{\left[\sum_j (Y_j - \bar{Y})\sin\omega(t_j-\tau)\right]^2}{\sum_j \sin^2\omega(t_j-\tau)}\right\}, \quad (4.10)$$

where:

$$\tau = \frac{1}{\omega}\tan^{-1}\left[\frac{\sum_j \sin 2\omega t_j}{\sum_j \cos 2\omega t_j}\right]. \quad (4.11)$$

The levels which a peak must exceed to reach statistical significance at $\{1,2,3,4,5\}\sigma$ are determined by

$$\Lambda = -\ln\left[1-(1-\alpha)^{1/M}\right], \quad (4.12)$$

where α is the probability of detection and M is an effective number that typically depends on the number of points, their actual spacing and the number of frequency tested distance. We use here M as equal to the number of data points, which is a simple, conservative choice [104]. A more accurate value for M could be better estimated by performing a Monte Carlo analysis of our data [106].

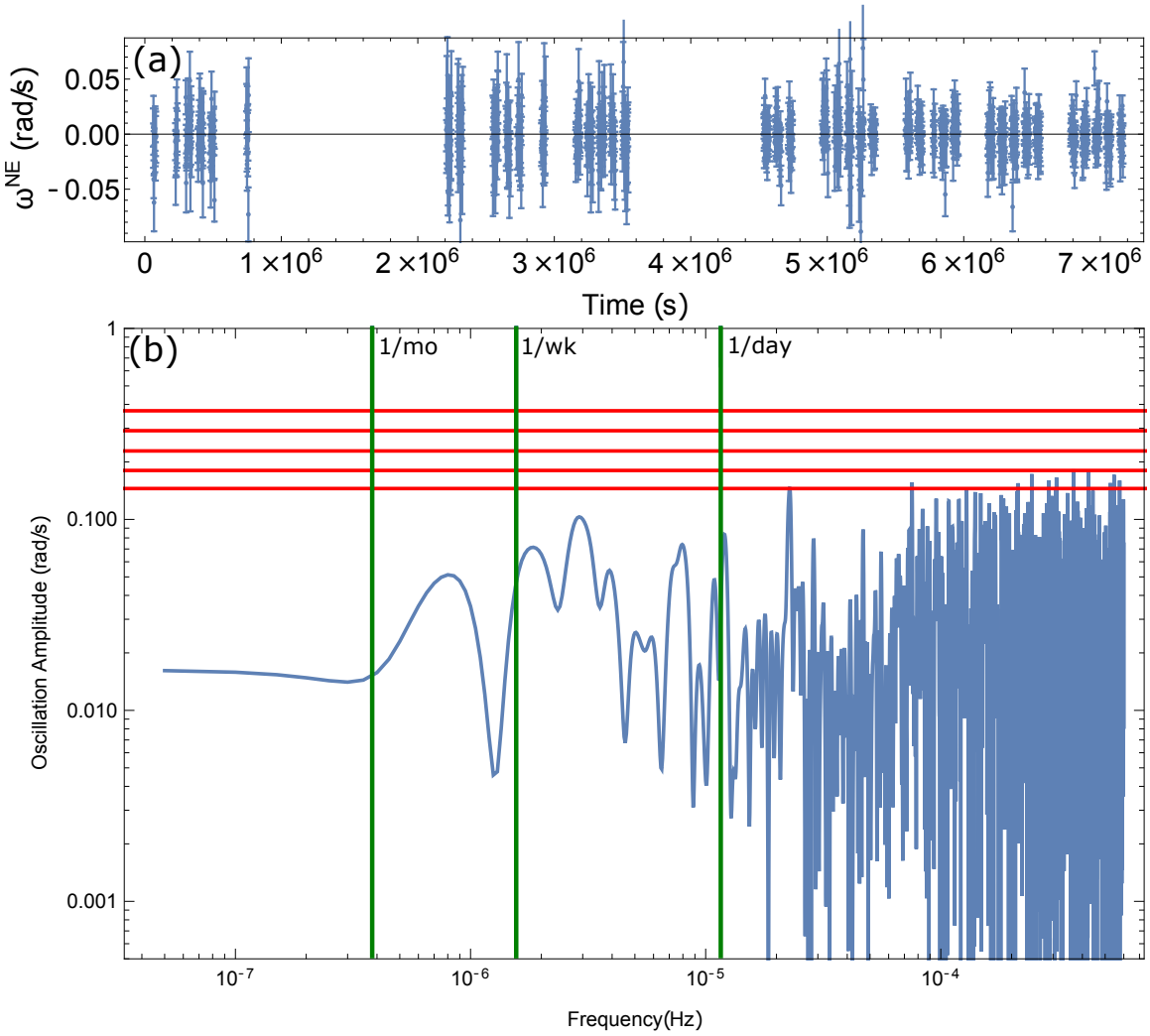

Figure 4.8.2: **Variation of $\omega^{\mathcal{NE}}$ with time. (a)** Time series showing superblocks taken for the ACME eEDM dataset. Time 0 corresponds to the time-stamp of the first acquired superblock, on 1/7/2018, at 3:20 PM. Error bars correspond to 1σ (68% confidence intervals). **(b)** Periodgram of the time series data, showing no significant oscillation peaks. False alarm thresholds are marked with red for $1, 2, 3, 4, 5\sigma$ confidence intervals. The green lines show frequencies corresponding to one day, one week and one month.

The results of this analysis is shown in Figure 4.8.2b, which shows the frequency spectral components of the data, with no peak reaching the significance threshold. We therefore conclude that no unknown time varying component of $\omega^{\mathcal{NE}}$ is present in ACME II.

4.9 Statistics of the eEDM dataset

The data discussed in this section was recorded over a 2 month run period (Figure 2.5.1). The total run time for the eEDM dataset was ~ 500 hours, ~ 350 of which produced data used to compute the eEDM and ~ 150 of which were used for the interleaved systematic error checks (Figure 2.5.1). We also paused the experiment for ~ 8 hours each 24 hours (typically during the night) to thermally cycle the beam source to remove neon ice buildup.

Figure 4.9.1 shows time series for all of the superlock data acquired for the eEDM dataset. We show it grouped by magnetic field magnitude, since we have seen an increase of noise with higher magnetic field. The mechanism causing this source of noise is described in Section 4.10.

Figure 4.9.2a,b shows the distribution of the $\omega^{\mathcal{NE}}$ superblock data. The majority of the data is consistent with a Gaussian distribution, but with more points in the tails. We perform a robust M-estimator analysis [107] on bootstrapped [108, 109] sets of data to extract confidence intervals corresponding to 1σ (68%). Since the noise arising from fluctuations in the mean longitudinal velocity is $|\mathcal{B}_z|$ dependent, we perform separate M-estimator analyses on subsets of data with different $\mathcal{B}_z$ magnitudes, then combine the sets using standard Gaussian uncertainty propagation.

4.9.1 M-estimator analysis

The M-estimator analysis is an extension of the standard least-squares regression technique. There, the residuals of the fit are weighted by the square of their errors, consistent with

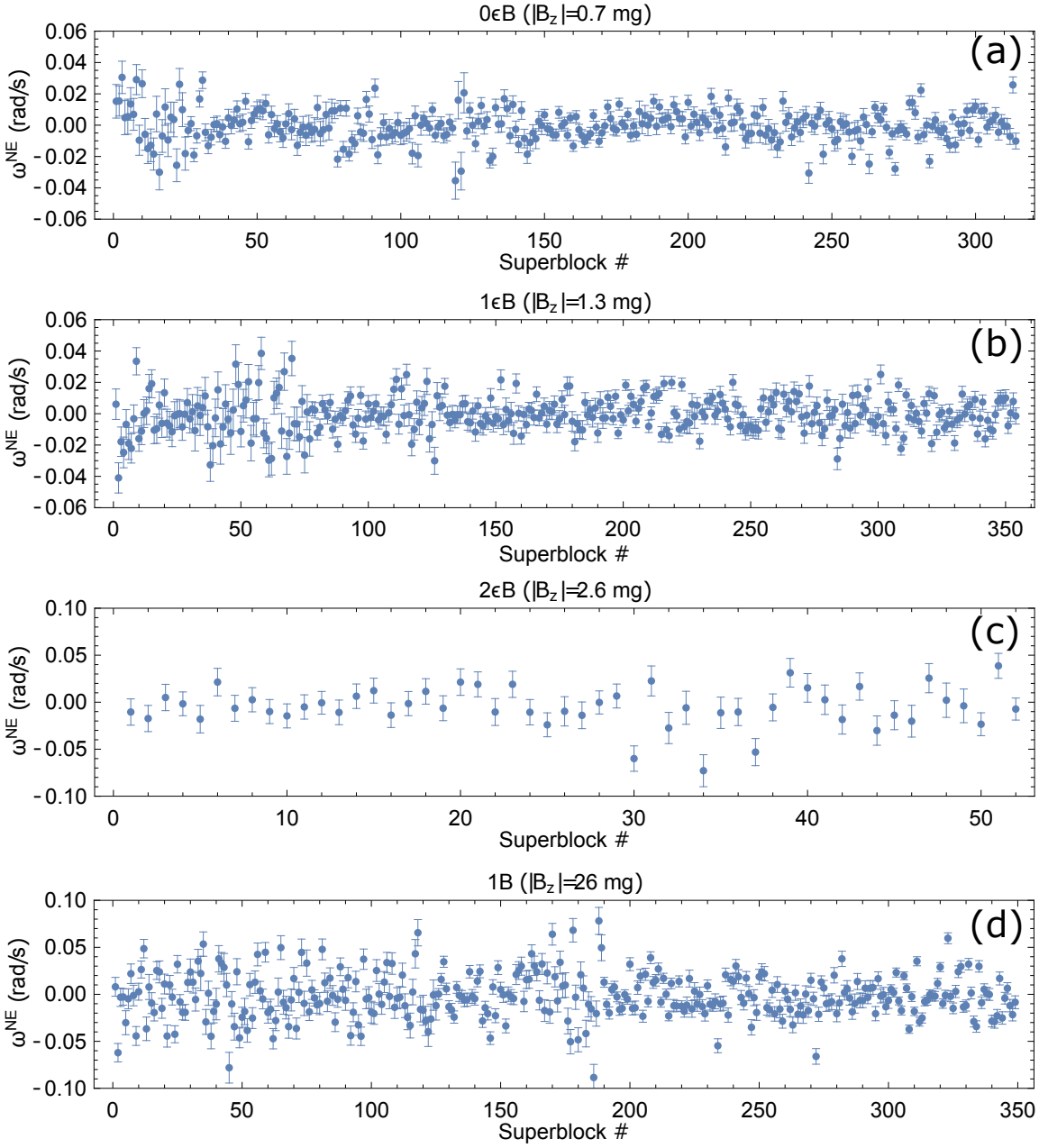

Figure 4.9.1: **The ACME II dataset, grouped by $|\mathcal{B}_z|$ magnitude.** $\omega^{\mathcal{NE}}$ corresponding to each superblock in ACME II is shown, for each value of magnetic field: **(a)** $0\epsilon\mathcal{B}$ (0.7 mG), **(b)** $1\epsilon\mathcal{B}$ (1.3 mG), **(c)** $2\epsilon\mathcal{B}$ (2.6 mG), **(d)** $1\mathcal{B}$ (26 mG).

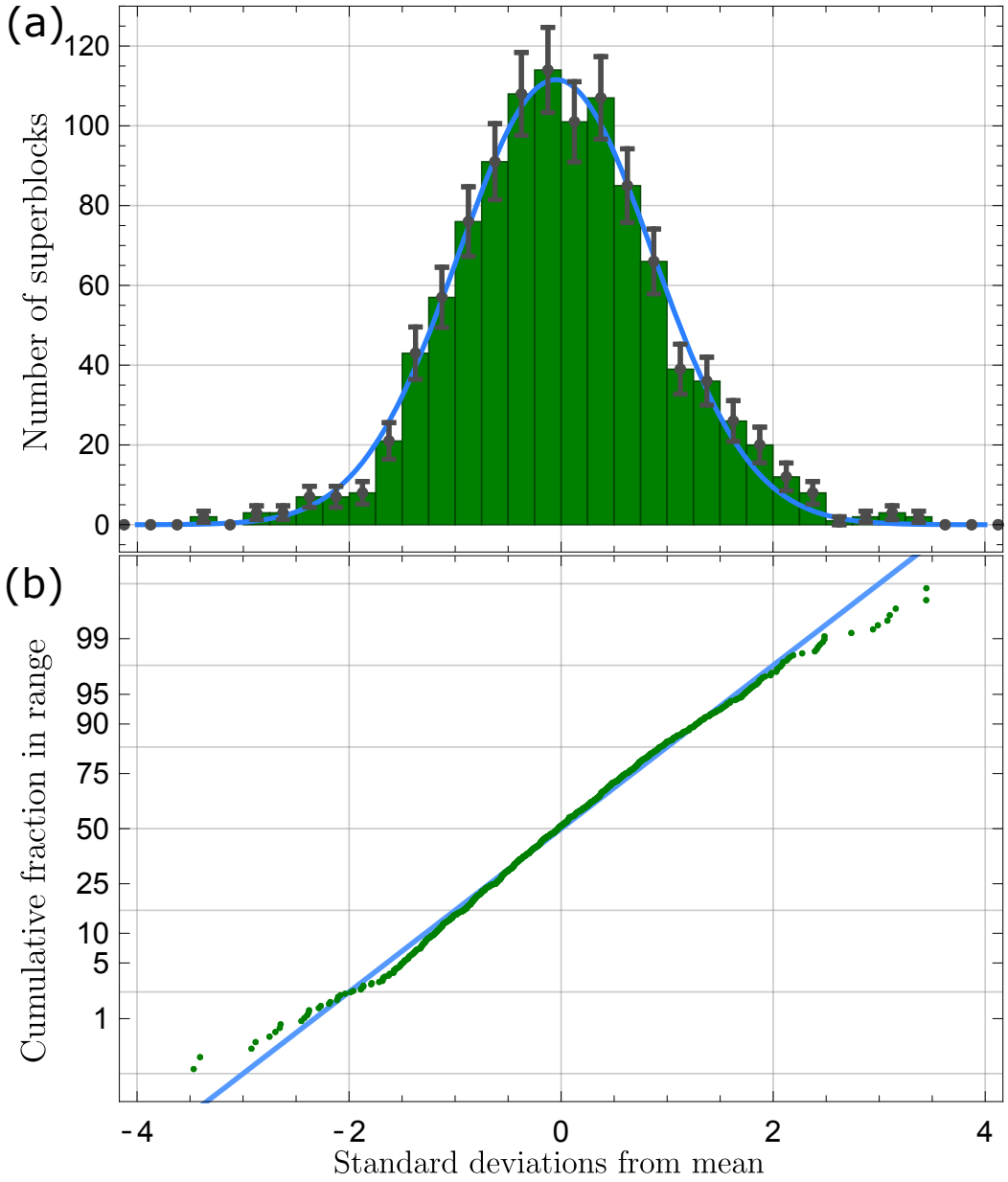

Figure 4.9.2: **Statistics of the EDM dataset. a.** Histogram of centered and normalized $\omega^{\mathcal{NE}}$ superblock values, i.e. $(\omega^{\mathcal{NE}} - \langle\omega^{\mathcal{NE}}\rangle)/\sigma_{\omega^{\mathcal{NE}}}$. Here, $\langle\omega^{\mathcal{NE}}\rangle$ is the mean of $\omega^{\mathcal{NE}}$ over the dataset, $\sigma_{\omega^{\mathcal{NE}}} = \sigma^{\text{s-n}}_{\omega^{\mathcal{NE}}}\sqrt{\chi^2_r(\mathcal{B})}$, where $\sigma^{\text{s-n}}_{\omega^{\mathcal{NE}}}$ is the superblock uncertainty propagated from "groups" (consistent with shot noise), and $\chi^2_r(\mathcal{B})$ is the reduced chi-squared value for the sets of superblocks with a given $\mathcal{B}$-field magnitude. Error bars indicate the standard deviation in the bin value expected from a Poisson distribution. Gaussian histogram fit shown with blue line. **b.** Normal probability plot (points) and comparison to a normal distribution (blue line). Deviations from the line outside of $\pm 1.5\sigma$ indicate more data points in the tails than expected from a normal distribution.

the Gaussian statistics that are being assumed. The disadvantages of this approach is that it doesn't perform well for distributions with long tails, where the Gaussian statistics assumption is violated. There, few data points far away from the mean ("outliers") can move the weighted mean by a significant amount. M-estimators allow for these outliers to be significantly down-weighted in comparison to least squares, by assuming another distribution of the weighting function [110].

Our procedure for computing the M-estimator mean is based on the Iteratively Reweighted Least Squares (IRLS) technique [110] applied to the set of superblock points, with means x_i and errors σ_i:

1. Set the iteration counter to $i = 0$ and use weighted mean to compute the initial guess of the mean of the data, $\langle x \rangle^{(0)} = \text{wmean}[x_i, \sigma_i]$.

2. Find the initial residuals from $r_i = x_i - \langle x \rangle^{(0)}$.

3. To preserve scale equivariance, the residuals are scaled by the median absolute deviation (MAD), which is calculated from $s^{(0)} = 1.4826 \cdot \text{Median}[\text{Abs}[r_i/\sigma_i]]$.

4. Compute the initial standardized residuals, $u_i^{(0)} = \frac{r_i^{(0)}}{s^{(0)}}$.

5. Compute the weights for the next iteration by using the chosen weighting function, wfun[], (Huber, Tukey, Hampel, etc.) $w_i^{(0)} = \text{wfun}[u_i^{(0)}]/\sigma_i^2$.

6. Iterate i=1. Use weighted averages to compute the new estimate of the mean, where the errors are now given by the inverse of the weights $\langle x \rangle^{(1)} = \text{wmean}[x_i, 1/w_i]$.

7. Find the new residuals from $r_i = x - \langle x_i \rangle^{(1)}$.

8. To preserve scale equivariance, the residuals are scaled by the median absolute deviation (MAD), which is calculated from $s^{(1)} = 1.4826 \cdot \text{Median}[\text{Abs}[r_i/\sigma_i]]$.

9. Compute the initial standardized residuals, $u_i^{(1)} = \frac{r_i^{(1)}}{s^{(1)}}$.

10. Compute the weights for the next iteration by using the chosen weighting function, wfun[], (Huber, Tukey, Hampel, etc.) $w_i^{(1)} = \text{wfun}[u_i^{(1)}]/\sigma_i^2$.

11. Compute the fractional difference between the mean of this iteration and the previous mean, Abs $\left[\frac{\langle \text{x} \rangle^{(1)} - \langle \text{x} \rangle^{(0)}}{\langle \text{x} \rangle^{(1)}}\right]$. If the fractional difference is larger than 10^{-6} go back to step 6.

12. Iterate steps 6-11 until the mean has converged.

This procedure typically converges within 3-5 iterations. We run the M-estimator algorithm on bootstrapped sets of the ACME II superblock data. We typically use $10,000$ sets. Each bootstrapped set contains the same number of elements as the initial set, but where the elements have been randomly resampled from the initial data set. We use the resulting distribution of M-estimator means to compute confidence intervals. 1σ corresponds to a 68% confidence interval.

For the ACME II dataset, we perform our robust M-estimator analysis [107, 109] using different weighting functions, such as Huber, Hampel, or Tukey. For the quoted numbers, we use the Huber weighting function for its simplicity and wide use; other choices change the mean and its uncertainty by only a few percent. This procedure also yields results consistent with those found using alternate methods such as directly scaling the error bars by χ_r^2 or performing a 5% trimmed mean on bootstrapped data [111].

4.10 Frequency noise

The scatter in the superblock data is found to be larger than expected from group-level uncertainties. This noise is present equally in all switch parity components of the frequency. Furthermore, the noise does not vary as a function of time after ablation. The excess noise in the precession frequency has one contribution that is proportional to, and another that is independent of the $\mathcal{B}$-field magnitude. We will discuss the two separately.

The first component of the excess noise increases the scatter of our superblock data to $\chi^2_r \sim 7$, but only for data acquired at the largest applied $\mathcal{B}$-field, $|\mathcal{B}_z| = 26$ mG. It also increased the noise proportionally when we took diagnosis data at $|\mathcal{B}_z| = 52$ mG, corresponding to a Zeeman precession phase of π. We verified through simulations and a direct measurement (see Section 4.12) that this is consistent with $\sim 0.05\%$ shot-to-shot fluctuations in the mean longitudinal molecular velocity ($\langle v \rangle \sim 200$ m/s). Since the refinement and readout laser beams are fixed in space, variations in $\langle v \rangle$ change the precession time τ; this causes variations in phase ϕ proportional to $|\mathcal{B}_z|$ (for $d_e = 0$), as shown in Eq. 2.5. To reduce its effect, we acquire most data at lower magnetic field magnitudes, where the associated increase in χ^2_r is negligible.

The $\mathcal{B}$-independent component results in an uncertainty that is ~ 1.7 times larger than the shot-noise limit, corresponding to a reduced chi-squared statistic of $\chi^2_r \sim 3$. Since our fastest switch, $\tilde{\mathcal{N}}$, does not remove such noise, it enters the measurement at timescales faster than 0.6 s. As described in detail below, the mechanism causing the frequency noise is general to the ACME fast polarization switching scheme used for the measurement of $\mathcal{A}$. It is independent of the switches performed and therefore has no effect on the offset of the $\omega^{\mathcal{NE}}$ or any of the other odd measurement channels.

4.11 Mechanism causing asymmetry noise

Since the noise is general to all experiment switch parity channels, it is not related to any one of the experiment parameter reversals, and in particular to the EDM switches, $\tilde{\mathcal{N}}$, $\tilde{\mathcal{E}}$. We therefore perform most of the asymmetry noise diagnosis described here in an experimental configuration that is similar to ACME II, but without performing any of the 7 switches. Furthermore, we perform our analysis on single molecular pulses, rather than averaging 25 consecutive pulses in a "trace", as was done in ACME II. This allows us to observe the properties of our measurement of $\mathcal{A}$ directly, before underlying effects specific

to our measurement scheme are hidden by the switches performed and further averaging.

As described in Section 4.3, the frequency is calculated from asymmetry, $\mathcal{A}$, contrast, $\mathcal{C}$, and precession time, τ,

$$\omega = \frac{\mathcal{A}}{2\mathcal{C}\tau}, \tag{4.13}$$

so *a priori*, noise in any of these quantities could be responsible for the noise in the frequency. Initial investigations revealed that the noise was present in the measurement of the asymmetry and propagated from there into the frequency measurement, so we refer to this source of excess noise as "asymmetry noise".

We observed that noise at timescales that are shorter than one molecular pulse (< 3 ms) was significantly reduced ($\chi^2_r \approx 1$). Since our fastest switch, $\tilde{\mathcal{N}}$, does not remove such noise, it enters the measurement at timescales faster than 0.6 s. Observing the noise in the asymmetry at various timescales within this range revealed that, while it had no dependence on the time within the molecular pulse (shot), there was a dependence of the magnitude of the noise as a function of time within the polarization switching bin (Figure 4.11.3). In particular, the noise increased in magnitude near the beginning and the end of the polarization bin, when the laser light is switched on and off, and was nearly consistent with $\chi^2_r \approx 1$ in between. We understand the mechanism producing this noise as described below.

4.11.1 Polarization switching timing configuration

The polarization switching system used for normalizing against changing molecule number is described in detail in Section 3.3.5. It allows us to detect the phase of the spin-precession signal by projecting the molecule spin alignment onto two orthogonal $\hat{X}, \hat{Y}$ quadratures. The timing structure used for acquiring data used for these asymmetry investigations is shown in Figure 4.11.1 and has slightly modified timing parameters than those used for the ACME II dataset (described in Section 3.3.5). Most of these changes were prompted by

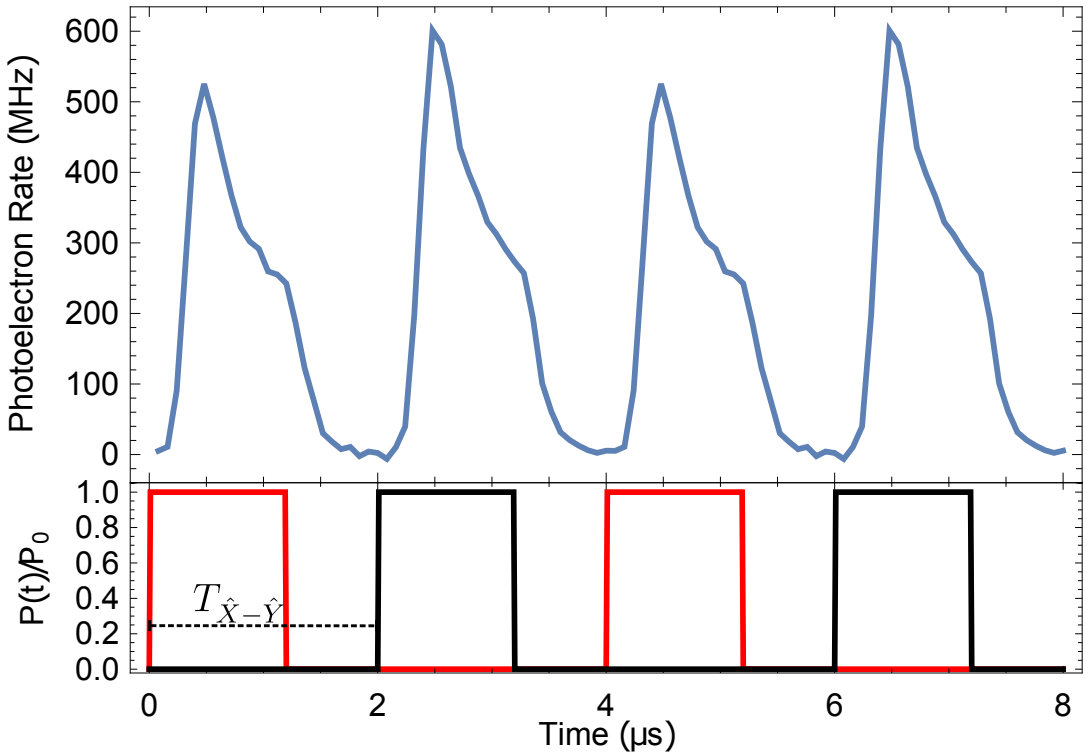

Figure 4.11.1: **Timing of polarization switching for noise tests.** The upper blue trace shows the detected photoelectron signal as a function of time. This signal structure reflects the laser power modulating timing structure shown below, in black and red, corresponding the the orthogonal polarization $\hat{X}$ and $\hat{Y}$ laser powers, respectively. The time delay between the $\hat{X}$, $\hat{Y}$ polarization laser waveforms, $T_{\hat{X}-\hat{Y}}$ is ideally equal to half of the period, $\mathcal{T}/2$.

the timing synchronization requirements of the data acquisition system used.

In ACME II, a common high precision timing box[3] provided timing through TTL pulses to the laser that triggers ablation, the RF switches that modulated the AOM on and off and the data acquisition (DAQ) digitizer[4]. The three trigger signals are phase locked, which greatly suppresses timing jitter in the acquired data ($<$ 25 ps jitter).

However, the quality of the DAQ timing is impacted because the DAQ digitizer uses an internal clock to set the timing of the sampling and digitization process. If no external clock signals are used to synchronize the timing box and DAQ digitizer, we have observed an additional acquisition trigger delay that causes subsequent acquired molecular pulses to be

[3]SRS DG 645.
[4]NI PXI-5171R FPGA.

recorded with varying time axis offsets, of up to $\sim$ 100 ns. Each subsequent molecular pulse (acquired at a rate of 50 Hz) is offset from the previous by $\sim$ 10 ns. When the delay reaches $\sim$ 100 ns (every 10 molecular pulses), it resets to 0, creating a periodic sawtooth pattern. The trigger delay sawtooth period is $\sim$ 200 ms with a linear drift rate of $\sim$ 500 ps/ms.

We eliminate this varying acquisition timing delay by using an external clock (10 MHz from a Rubidium reference clock[5]) to synchronize both the timing box and DAQ digitizer. Proper synchronization of the DAQ digitizer to an external clock is only possible when the sampling rate is set to be an integer divisor of the 250 MSa/s internal clock rate. This requires us to use a slightly modified timing structure from that used in ACME II. We chose to use a 12.5 MSa/s acquisition rate (compared to 16 MSa/s in ACME II) in these tests, limited by the data transfer rate performance of the computer system performing the acquisition and to avoid recording large amounts of data (Figure 4.11.1). At this sampling rate, each acquired sample contains signal integrated over 80 ns (compared to 62.5 ns in ACME II). To ensure an even number of points in a polarization switching cycle, we set the polarization switching frequency to 250 kHz (compared to 200 kHz in ACME II), such that each polarization cycle contains 50 points, 25 corresponding to the $\hat{X}$ and $\hat{Y}$ bins, respectively. The time between the $\hat{X}$ and $\hat{Y}$ polarization cycles, when both laser polarizations are off (dead-time) is set to 0.8 μs (0.6 μs in ACME II).

One important parameter in the polarization switching timing structure is the typical time delay between the $\hat{X}$ and $\hat{Y}$ laser pulses, $T_{\hat{X}-\hat{Y}}$ (Fig. 4.11.1). Ideally, $T_{\hat{X}-\hat{Y}} = \mathcal{T}/2$, where $\mathcal{T}$ is the polarization switching period. However, the modulation of the $\hat{X}$, $\hat{Y}$ laser powers is performed by AOMs, which introduces additional delay in the timing of the polarization cycles. This delay can be up to 200 ns and is sensitive to the geometrical parameters and alignment of the specific AOM used and varies significantly from model to model. We typically correct for this additional delay by manually adding an offset between the timing pulses modulating the AOMs that shutter the $\hat{X}, \hat{Y}$ polarization lasers beams.

[5]SRS FS 725.

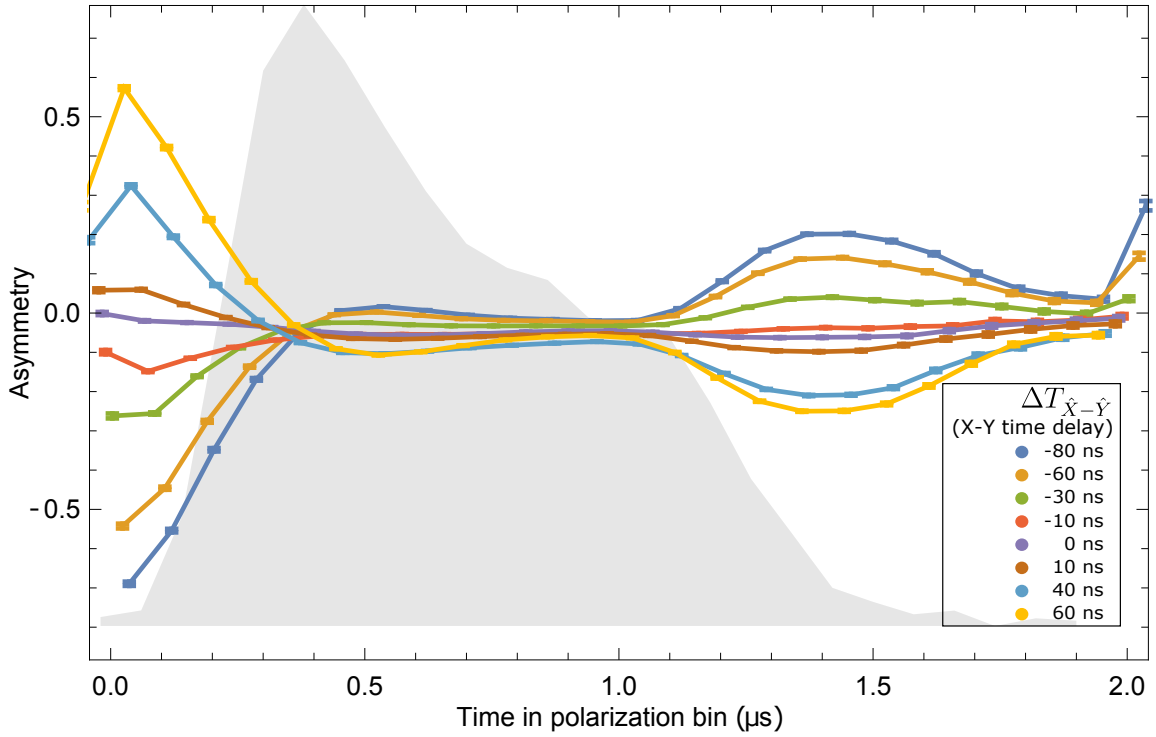

Figure 4.11.2: **Variation of asymmetry within the polarization bin.** Measured assymmetry is shown as a function of time within the polarization bin. The shape and magnitude of the dependence is heavily dependent on $\Delta T_{\hat{X}-\hat{Y}}$, the $\hat{X}-\hat{Y}$ pulse delay parameter and reflects the curvature of the fluorescence signal in the polarization bin (shown in light gray). The asymmetry is calculated by averaging 200 consecutive shots (4 seconds averaging time).

4.11.2 Noise Mechanism

As described in Section 4.1, we use Eq. 4.1 on the modulated polarization switching signal to compute the asymmetry between adjacent $\hat{X}$, $\hat{Y}$ orthogonal polarization bins (Fig. 4.11.1). We typically compute the asymmetry by averaging a number of consecutive samples within the polarization bins, common to both $\hat{X}$ and $\hat{Y}$ fluorescence pulses. We refer to this chosen time region as an integration "sub-bin". In contrast, we analyze the data used for the noise tests described here by performing the asymmetry calculation directly on acquired samples in the $\hat{X}$ and $\hat{Y}$ bins one by one, without previous summing over adjacent points. We use this procedure to better illustrate the dependence of the noise and

asymmetry offset on the time within polarization bin.

Figure 4.11.2 shows the shape of the asymmetry as a function of time within the polarization bin, averaged over 200 consecutive shots (corresponding to 4 s). We observe that the difference in the phase delay between the fluorescence signals corresponding to the orthogonal $\hat{X}$ and $\hat{Y}$ polarization orientations, $\Delta T_{\hat{X}-\hat{Y}} = T_{\hat{X}-\hat{Y}} - \mathcal{T}/2$, has a large effect on the shape and magnitude of the resulting asymmetry and its depedence on time within the integration sub-bin. This occurs because when $\Delta T_{\hat{X}-\hat{Y}} \neq 0$, the $\hat{X}$, $\hat{Y}$ bins are subtracted with a time offset. This causes a variation of the computed asymmetry within the polarization bin, which is proportional to the first order derivative of the modulated fluorescence signal.

We note that any of the experiment switches performed routinely as a part of the ACME II superblock data acquisition structure remove the dependence of the asymmetry on the polarization bin. In particular, as described in Section 4.8, we have searched for and not observed a variation of the eEDM frequency, $\omega^{\mathcal{NE}}$, or any of the other correlated frequency channels on time within the polarization bin. In addition, the $\tilde{\mathcal{P}}$ and $\tilde{\mathcal{R}}$ switches each interchange the roles of the $\hat{X}$ and $\hat{Y}$ readout laser beams. Any asymmetry effects such as these are removed by these switches, such that they don't contaminate the measurement of ϕ and ω. Therefore, such offset appears in the $\omega^{\mathcal{PR}}$ channel when performing the experiment with the 7 switches typical to the ACME II superblock configuration.

While the performed switches prevent the dependence of asymmetry on time within the polarization bin from causing a phase offset, it can still cause noise in the asymmetry, when combined with a variation in the timing of the shot on timescales that are shorter than the fastest experiment switch, $\tilde{\mathcal{N}}$ (0.6 s). This is shown in Figures 4.11.3a and 4.11.3b, when there is a large amount of timing noise or with reduced timing noise, respectively. We achieve the two configurations by either synchronizing or not synchronizing the clock of the data acquisition to the external clock, as described in Section 4.11.1. In the presence of large

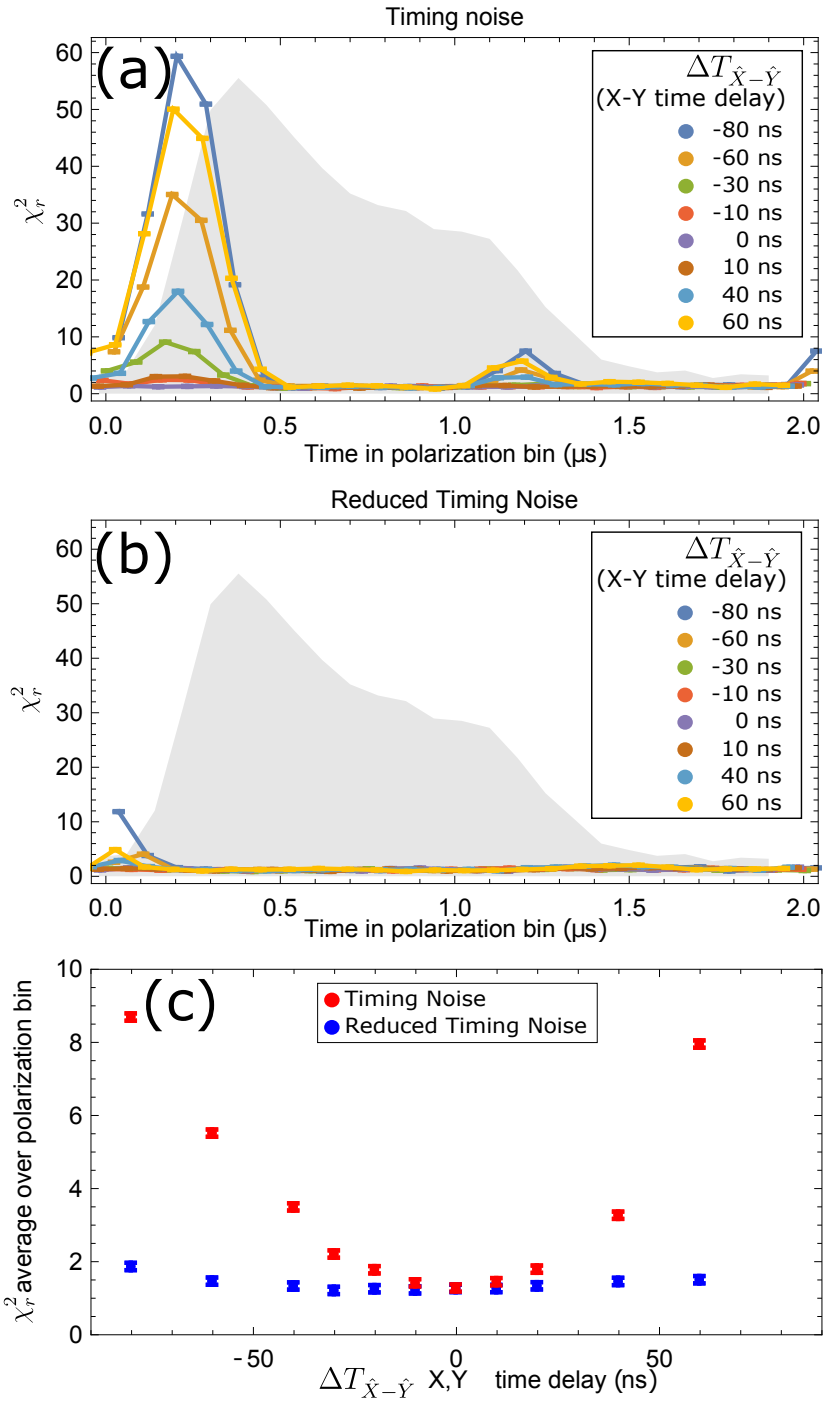

Figure 4.11.3: **Variation of asymmetry noise within the polarization bin with $\Delta T_{\hat{X}-\hat{Y}}$.** Measured magnitude of excess noise, parameterized by χ_r^2, is shown as a function of time within the polarization bin, for various values of $\Delta T_{\hat{X}-\hat{Y}}$, with large timing noise **(a)**, and when timing noise is reduced **(b)**. The noise is larger where the curvature of the fluorescence signal (shown in light gray) is more pronounced. χ_r^2 is averaged over the time in polarization bin in figure **(c)**, which displays the time-averaged χ_r^2 as a function of $\Delta T_{\hat{X}-\hat{Y}}$, for large timing noise and when timing noise is reduced. All χ_r^2 values calculated for 200 consecutive shots, acquired over 4s.

timing noise, the computed χ_r^2 for the set of 200 traces is larger at the beginning and end of the polarization switching pulse, where the curvature of the fluorescence signal is larger. Consistent with our model, the noise is proportional to the shape of the asymmetry curves shown in Figure 4.11.2, and therefore increases when the $\hat{X} - \hat{Y}$ time delay parameter, $\Delta T_{\hat{X}-\hat{Y}}$, is non-zero. Figure 4.11.3c shows the χ_r^2 averaged over the entire polarization bin as a function of the $\Delta T_{\hat{X}-\hat{Y}}$ parameter, in the presence of timing noise and with timing noise reduced, illustrating the reduced magnitude of noise with lower timing jitter and when $\Delta T_{\hat{X}-\hat{Y}} = 0$.

4.11.3 Control and suppression of noise

With the noise mechanism understood, we can reduce the magnitude of the excess noise by suppressing the experiment imperfections that contribute to it. As shown in Figure 4.11.3c, we can reduce the noise by suppressing timing noise and/or setting $\Delta T_{\hat{X}-\hat{Y}}$ to zero. Each of these parameters reduces the noise by orders of magnitude compared to that present in ACME II.

A third method can also be used to further suppress this noise source. Since the cause is noise in the timing of the molecular pulse acquisition, fluorescence signal magnitude is transferred between adjacent acquisition points within the polarization bin. The asymmetry noise is caused by computing the asymmetry for data samples with improper time-varying timing labeling. However, the total number of fluorescence photons is the same for each $\hat{X}$, $\hat{Y}$ polarization bin, given by the number of molecules that are addressed by the readout laser beam. We can therefore suppress the asymmetry noise by integrating over a larger sub-bin. The larger integration sub-bin suppresses variations in the signal of the individual samples, significantly reducing noise even in the presence of large timing noise, as shown in Figure 4.11.4.

We verified the suppression of the asymmetry noise when using the three methods de-

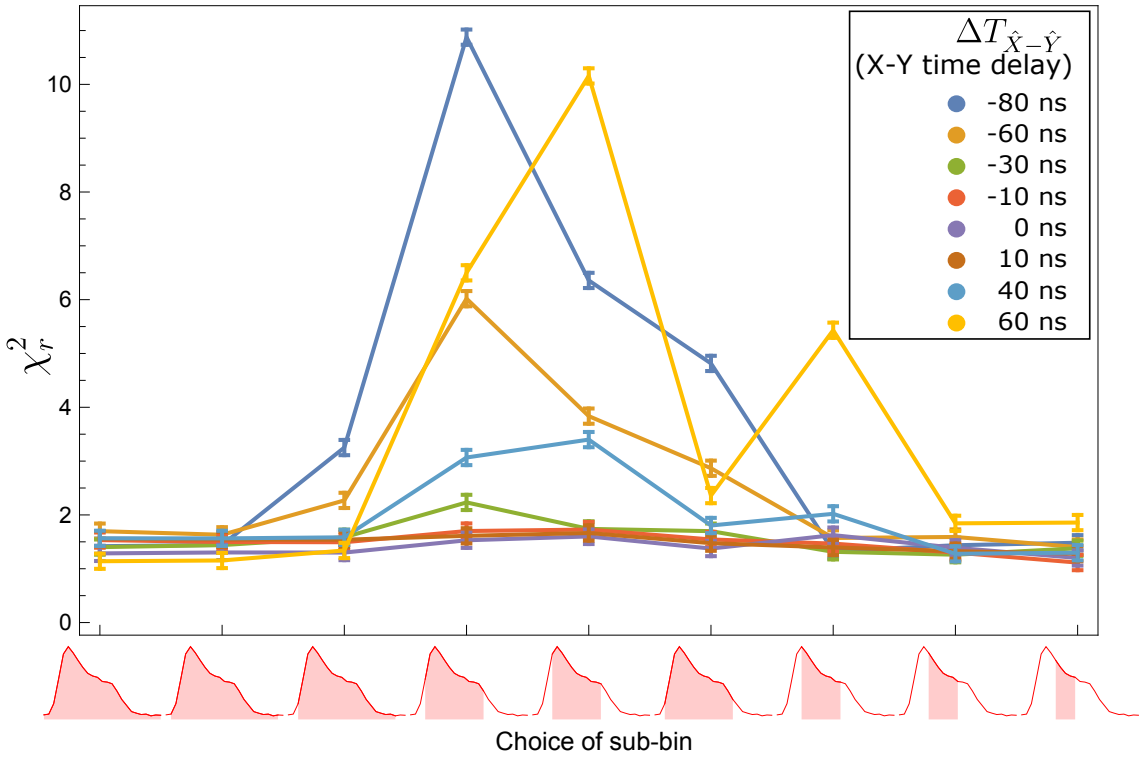

Figure 4.11.4: **Dependence of excess noise on choice of integration sub-bin.** The noise (χ_r^2) is reduced when the integration sub-bin averages out the samples with largest amount of excess noise, at the beginning and the end of the polarization bin. This behavior is consistent for all values of the $\hat{X}-\hat{Y}$ delay parameter, $\Delta T_{\hat{X}-\hat{Y}}$. The shown data is acquired in the "large timing noise" configuration, where the clocks of the timing box and DAQ digitizer and not synchronized. All χ_r^2 values calculated for 200 consecutive shots, acquired over 4s.

scribed above by acquiring 12 superblocks of data with the same sets of switches as in the ACME II experiment, which produced data consistent with a Gaussian distribution with $\chi_r^2 = 0.87 \pm 0.40$, consistent with 1. This confirmed the suppression of sources of excess noise to significantly below the ACME II sensitivity.

An alternative method of suppressing such noise in the future is by performing one of the experimental switches at a timescale that is faster than that of the noise. Removing noise in the asymmetry can be achieved by performing the $\tilde{\mathcal{P}}$ switch, which is currently implemented using AOMs and could be easily performed at a faster timescale. Performing the $\tilde{\mathcal{N}}$ switch at faster timescales removes both sources of asymmetry and phase noise,

although its implementation could prove more challenging in a future ACME apparatus, as described in Chapter 6.

4.12 Noise in the precesion time τ

As mentioned above, the magnitude of the excess noise was significantly higher when running at larger magnitudes of magnetic field, such as when $|\mathcal{B}_z| = 26$ mG ($1\mathcal{B}$ configuration). The noise increased to $\chi_r^2 \sim 7$ in this configuration. We believe that the phase noise occurs due to noise in the precession time τ that is due to changes in the mean velocity of the molecular beam, as explained below.

The angle of Zeeman phase precession is larger at $1\mathcal{B}$ ($\Phi = \pi/4$) by at least a factor of 10 than at the other magnetic field magnitudes ($0\epsilon\mathcal{B}$, $1\epsilon\mathcal{B}$, $2\epsilon\mathcal{B}$). As shown by Eq. 2.5, variation in the precession time τ is amplified by the larger magnetic field magnitude to create noise in the phase.

We performed a direct measurement of τ by implementing a notch in the STIRAP 690 nm pump beam and measuring the transit times of those molecules. To do so, we added an AOM in the path of the STIRAP pump beam, which acts as a switch and allows us to modulate the laser power between 0 and typical power. Using a fast RF switch, we turned off the STIRAP pump beam for a short period of 100 μs, which caused state preparation to be quenched, reducing the signal to 0. The timing of the TTL signal performing the turn off is synchronized to the trace trigger, such that the notch timing is synchronized between traces. This produces a dip in the molecule fluorescence signal (Fig. 4.12.1). The local velocity dispersion of the molecular beam causes molecules in the same x spatial location but with different velocities to precess by different phases, which causes the shape of the dip to "broaden", such that it is not a square and instead resembles a Gaussian. The amount of broadening observed is consistent with the 10% velocity dispersion of the beam of ThO molecules [59].

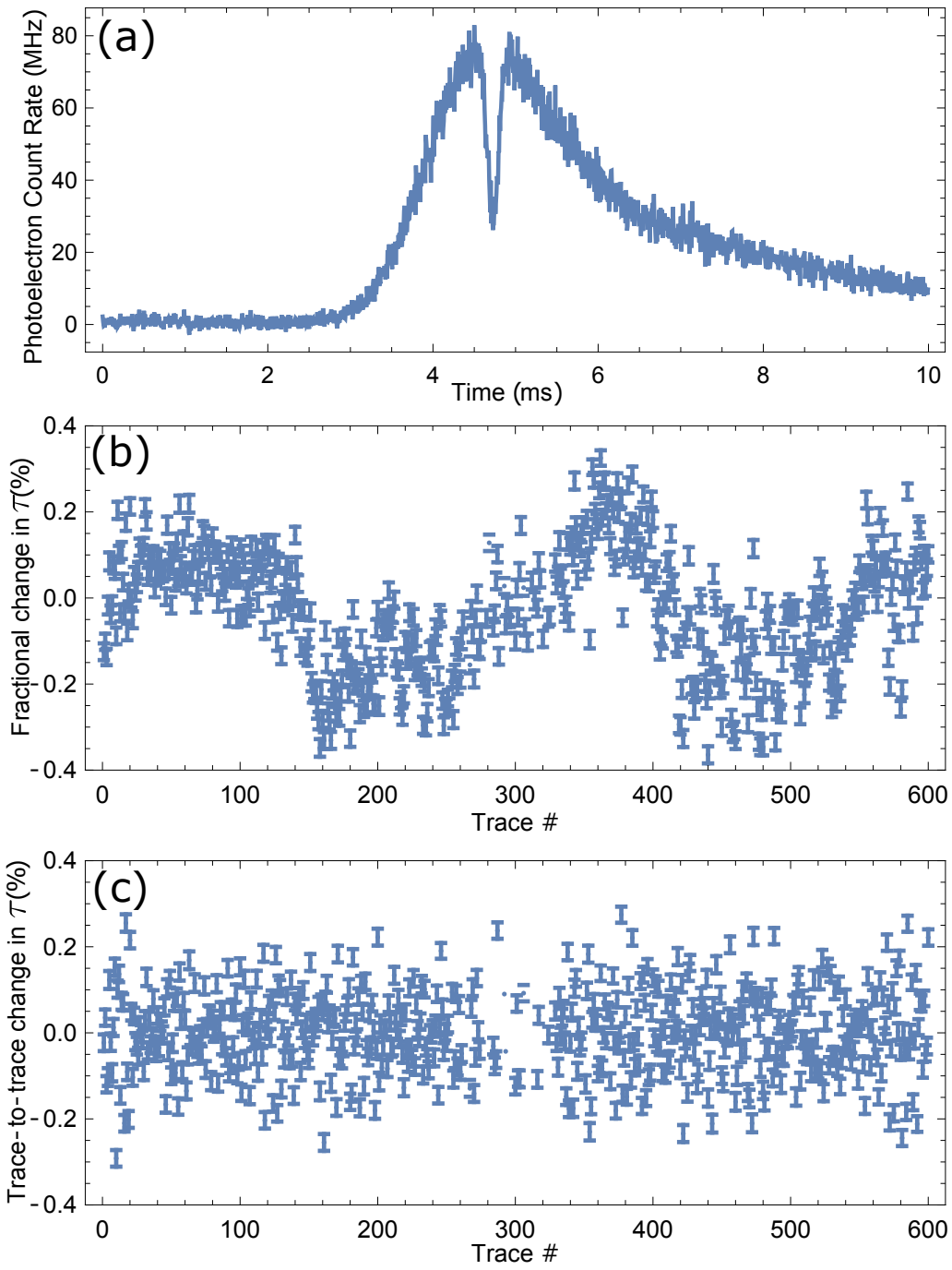

Figure 4.12.1: **Direct measurement of the precession time τ. (a)** Molecular fluorescence pulse with notch, which is implemented by the turning off the 690 nm STIRAP pump laser for 100 μs. We use the position of the notch in time to extract τ. Polarization switching is turned off for these measurements. **(b)** Fractional change in τ over a period of 360 seconds corresponding to 600 traces. **(c)** Fractional change in τ from trace to trace, on the timescale of the $\tilde{\mathcal{N}}$ switch. This plot is obtained by taking the the differences of time corresponding to consecutive traces in **(b)**. Since this noise is on the timescale of the $\tilde{\mathcal{N}}$ switch, it will contribute to all of the the experiment channels which are odd in the switch.

By fitting a Gaussian function to the dip and measuring the position of the peak over time, we can measure the change in the precession time, τ, from trace to trace (Fig. 4.12.1b,c). These fluctuations have a typical magnitude of 0.1% rms, sufficient to explain the excess noise for the $1\mathcal{B}$ configuration in comparison with the low magnetic field running configurations. We believe these fluctuations come from varying longitudinal velocity of the molecular beam, on the shot-to-shot timescale. The change in velocity is known to be correlated with changes in the properties of the ablation process, such as the position of the ablation laser on the ceramic ThO target, although we have not carefully investigated each ablation parameter individually.

Another contribution to the variation in τ could come from a variation in the precession distance between the refinement and readout laser beams. Such displacement could be caused by pointing variation in the two lasers beams. However, pointing fluctuations of 20-50 μm/m cause a change in τ that is a factor of a few smaller than that observed above, so we believe that the dominant effect comes from velocity variations instead.

We could have used this technique to measure τ in real time and correct for it in the calculation of the phase. In practice, the uncertainty of the τ measurement, limited by the velocity dispersion of the molecular beam, is comparable to the uncertainty of the phase measurement, so not entirely sufficient to remove the noise. In addition, since we have measured reduced contrast in at the beginning and end of the molecular pulse described in Section 4.2, we believe that the precession time is not necessarily uniform within each shot and might vary based on the time within the shot. This effect could further decrease the effectiveness of the technique of reducing noise through direct measurement of τ. Furthermore, implementing this technique reduces the signal, since the region where the notch is performed becomes unusable for extracting eEDM data.

Instead, we decided to acquire most data at lower magnetic fields, where the magnitude of the $\mathcal{B}-$correlated noise is reduced. The technique of measuring τ using the notch could prove useful, when the velocity noise is a larger proportion to the experiment shot noise,

in a future ACME experiment with higher signal-to-noise.

Well, we do get $1.35 a day, right? Best job I ever had!

Grady 'Coon-Ass' Travis, *Fury*

5

Systematic errors

The experiment was designed to be resilient to systematic errors that affected past eEDM measurements. This chapter describes our search for unforeseen systematic errors and the procedures we used to develop models that explain the observed systematic effects. We typically quantify the contribution of systematic effects to the eEDM measurement by directly measuring the dependence of the eEDM frequency channel, $\omega^{\mathcal{NE}}$, on the exaggerated experimental imperfection and by performing auxiliary measurements to measure the typical magnitude of the imperfections. To perform these checks with high sensitivity, we have implemented systems that allow us to apply imperfections which are

typically much larger than those present in the experiment under normal running conditions. We limit the size of the systematic effects to much below the statistical sensitivity by reducing and controlling these experimental imperfections.

As shown in Section 2.1, a true contribution of the eEDM to the spin precession frequency should reverse sign with the reversal of internal the electric field, $\vec{\mathcal{E}}_{\text{eff}}$, which can be achieved either by reversing it spectroscopically through the $\tilde{\mathcal{N}}$ switch or by reversing the electric field in the laboratory by changing the sign of the voltages on the field plates, $\tilde{\mathcal{E}}$. We call this term the $\omega^{\mathcal{N}\mathcal{E}}$ correlated frequency. If $\omega^{\mathcal{N}\mathcal{E}}$ is due to a true eEDM, it cannot vary with any other experimental parameter.

To search for possible unforeseen systematic errors, we varied a large number of experiment parameters and looked at their effect on $\omega^{\mathcal{N}\mathcal{E}}$. If $\omega^{\mathcal{N}\mathcal{E}}$ changes, there must be a systematic error that is correlated with the varied parameter. All ACME II systematic effects occurred due to a combination of two or more experimental imperfections, $P_1, P_2, P_3 ... P_N$, acting in concert to create an effect. Typically, one of the parameters was correlated with the $\tilde{\mathcal{N}}, \tilde{\mathcal{E}}$ switches:

$$\omega_P^{\mathcal{N}\mathcal{E}} = P_1 P_2 ... P_N^{\mathcal{N}\mathcal{E}}. \tag{5.1}$$

It is also possible to observe systematic effects due to the coupling of parameters which are independently correlated with $\tilde{\mathcal{N}}$ or $\tilde{\mathcal{E}}$, such as $P_1^{\mathcal{N}}$ and $P_2^{\mathcal{E}}$. An example of such an effect is a frequency component which is $\tilde{\mathcal{E}}$ correlated, $\omega^{\mathcal{E}}$ that can contribute to $\omega^{\mathcal{N}\mathcal{E}}$ due to the small difference in the g-factors of the two $\tilde{\mathcal{N}}$ states and is described in Section 5.8.

When we find a systematic imperfection parameter P_1 that moves $\omega^{\mathcal{N}\mathcal{E}}$, we attempt to find at least another controllable parameter P_2 and the physical mechanism connecting the two to $\omega^{\mathcal{N}\mathcal{E}}$. We can then exaggerate P_1 and use P_2 to minimize the effect of P_1 on $\omega^{\mathcal{N}\mathcal{E}}$. We can also perform the vice-versa experiment, where we exaggerate P_2 and use P_1 to minimize the effect of P_2 on $\omega^{\mathcal{N}\mathcal{E}}$. This process ensures that the systematic effect $\omega_P^{\mathcal{N}\mathcal{E}}$ is suppressed to at least second order.

In addition to $\omega^{\mathcal{NE}}$, we monitored all other correlated frequency channels ω^{u}, contrast, fluorescence signal, and a large number of additional experiment parameters, such as laser power, pointing, vacuum pressure, room temperature and humidity. We looked for correlations between these auxiliary measurement parameters and experiment switches to determine any effect that might not be consistent with our understanding of the experiment.

5.1 Determining systematic errors and uncertainties

To search for possible sources of systematic error, we varied over 40 separate experimental parameters over a larger range than typically present in the experiment (Table 5.1.1) and measured their effect on $\omega^{\mathcal{NE}}$ and the other parity components of both ω and $\mathcal{C}$. We separate these parameters in two categories. Category I contains parameters which have a typical ideal experimental value under normal running conditions. Deviations from this value correspond to experimental imperfections. Category II contains parameters for which there is no clear optimum value and for which the spin precession measurement is nominally insensitive to. Although direct limits on systematic errors cannot be derived, these served as checks for the presence of unanticipated systematic errors.

For each Category I parameter, P, we exaggerate the size of the imperfection by a large factor, if possible larger than 10, relative to the maximum size of the imperfection under typical running conditions, $\bar{P}$, where $\bar{P}$ is obtained from auxiliary measurements. Assuming a linear dependence of $\omega^{\mathcal{NE}}$ on P [6, 44, 112], we extract the sensitivity of $\omega^{\mathcal{NE}}$ to P by computing the slope

$$S_P = \partial\omega^{\mathcal{NE}}/\partial P. \tag{5.2}$$

Such data, taken with intentionally applied parameter imperfections (i.e., when P is set to a nonzero value although its ideal value is zero), is used only for determination of systematic shifts and uncertainties and is not averaged into the EDM dataset.

Table 5.1.1: **Parameters varied during our systematic search.** Left: Category I Parameters — These were varied far from their values under normal conditions of the experiment. For each of these parameters direct measurements or limits were placed on possible systematic errors. Right: Category II Parameters — These had no single ideal value. Although direct limits on systematic errors cannot be derived, these served as checks for the presence of unanticipated systematic errors. See the main text for more details on all the systematics referenced.

Category I Parameters
Magnetic fields
- $\mathcal{B}$-field gradients: $\frac{\partial \mathcal{B}_z}{\partial z}$, $\frac{\partial \mathcal{B}_z}{\partial y}$, $\frac{\partial \mathcal{B}_x}{\partial x}$, $\frac{\partial \mathcal{B}_y}{\partial y}$, $\frac{\partial \mathcal{B}_y}{\partial x}$, $\frac{\partial \mathcal{B}_z}{\partial x}$ (even and odd under $\tilde{\mathcal{B}}$)
- Non-reversing $\mathcal{B}$-field: $\mathcal{B}_z^{\mathrm{nr}}$
- Transverse $\mathcal{B}$-fields: $\mathcal{B}_x, \mathcal{B}_y$ (even and odd under $\tilde{\mathcal{B}}$)
- $\tilde{\mathcal{E}}$-correlated $\mathcal{B}$-field: $\mathcal{B}_z^{\mathcal{E}}$ (to measure suppression of possible $\phi^{\mathcal{E}}$ effects by the $\tilde{\mathcal{N}}$ switch)
Electric fields
- Non-reversing $\mathcal{E}$-field: $\mathcal{E}^{\mathrm{nr}}$
- Field plate ground voltage offset
Laser detunings
- Detuning of refinement/readout lasers: Δ_{ref}, Δ_{read}
- 1-photon, 2-photon detuning of STIRAP lasers
- $\tilde{\mathcal{P}}$-correlated detuning: $\Delta^{\mathcal{P}}$
- $\tilde{\mathcal{N}}$-correlated detuning: $\Delta^{\mathcal{N}}$
- Detuning of rotational cooling lasers
Laser powers
- $\tilde{\mathcal{N}}\tilde{\mathcal{E}}$-correlated power, $P^{\mathcal{N}\mathcal{E}}$
- Power of refinement/readout lasers: $P_{\mathrm{prep}}, P_{\mathrm{read}}$
- $\tilde{\mathcal{N}}$-correlated power, $P^{\mathcal{N}}$
- $\tilde{\mathcal{P}}$-correlated power, $P^{\mathcal{P}}$
- Readout $\hat{X}$-,$\hat{Y}$-dependent laser power
Laser pointings/position along $\hat{x}$
- Pointing change of the refinement/readout lasers
- Readout $\hat{X}$-,$\hat{Y}$-dependent laser pointing
- Position of refinement beam along $\hat{x}$
Laser polarization
- Polarization rotation of readout laser
- Readout polarization dither angle, θ
- Refinement/readout laser ellipticity
Molecular beam clipping
- Clipping of the molecular beam along $\hat{y}$ and $\hat{z}$ (changes transverse velocity and position of the ensemble)

Category II Parameters
Experiment Timing
- Readout $\hat{X}, \hat{Y}$ polarization switching rate
- Allowed settling time between block switches
Analysis
- Signal size cuts, asymmetry magnitude cuts, contrast cuts
- Spatial dependence of fluorescence recorded by the eight PMTs
- Variation with time within the molecular pulse
- Variation with time within the $\hat{X}$,$\hat{Y}$ polarization cycle
- Search for correlations with all ω, C switch-parity components
- Search for correlations with auxiliary monitored parameters ($\mathcal{B}$-fields, laser powers and frequencies, vacuum pressure, environment and beam source pressures and temperatures)
- 4 analyses of the data

We use these measured slopes to compute systematic shifts and uncertainties. If S_P was either expected or observed to be nonzero, we compute an associated systematic shift

$$\omega_P^{\mathcal{NE}} = S_P \bar{P}. \tag{5.3}$$

The uncertainty in $\omega_P^{\mathcal{NE}}$ is calculated using standard error propagation of uncorrelated variables,

$$\delta\omega_P^{\mathcal{NE}} = \sqrt{\left(S_P \delta\bar{P}\right)^2 + \left(\bar{P}\delta S_P\right)^2}, \tag{5.4}$$

where $\delta\bar{P}$ is the uncertainty in P and δS_P is the uncertainty in S_P. The systematic means and uncertainties are included in the final systematic error budget given in Table 5.1.2. All shifts of this type are subtracted to compute a systematic free eEDM frequency,

$$\omega_T^{\mathcal{NE}} = \omega^{\mathcal{NE}} - \sum_P \omega_P^{\mathcal{NE}}. \tag{5.5}$$

For these types of parameters, we monitored the size of the systematic error throughout the EDM dataset by performing "Intentional Parameter Variations" (see Section 2.5).

The large majority of Category I parameters were not observed to cause significant systematic slopes. When S_P was expected and observed to be consistent with zero, we do not apply a systematic correction associated with parameter P but still compute an upper limit on the associated uncertainty:

$$\delta\omega_p^{\mathcal{NE}} = \bar{P}\sqrt{(S_P)^2 + (\delta S_P)^2}, \tag{5.6}$$

where we have made the estimate that $\delta P \approx \bar{P}$. We include uncertainties of this type in the final systematic error budget in certain cases described in the sections below.

For parameters which were observed to cause a statistically significant shift in $\omega^{\mathcal{NE}}$, we verified the assumed linear dependence of $\omega^{\mathcal{NE}}$ on P by taking data at a few values of P.

Class	Parameter	Shift	Uncertainty
A	$\partial\mathcal{B}_z/\partial z$ and $\partial\mathcal{B}_z/\partial y$	7	59
A	$\omega_{\mathrm{ST}}^{\mathcal{NE}}$(via $\theta_{\mathrm{ST}}^{H-C}$)	0	1
A	$P_{\mathrm{ref}}^{\mathcal{NE}}$	-	109
A	$\mathcal{E}^{\mathrm{nr}}$	-56	140
A	$\lvert\mathcal{C}\rvert^{\mathcal{NE}}$ and $\lvert\mathcal{C}\rvert^{\mathcal{NEB}}$	77	125
A	$\omega^{\mathcal{E}}$(via $\mathcal{B}_z^{\mathcal{E}}$)	1	1
C	Other $\mathcal{B}$-field gradients total (4)	-	134
C	Non-Reversing $\mathcal{B}$-field ($\mathcal{B}_z^{\mathrm{nr}}$)	-	106
C	Transverse $\mathcal{B}$-fields ($\mathcal{B}_x^{\mathrm{nr}}, \mathcal{B}_y^{\mathrm{nr}}$)	-	92
C	Refinement/readout laser detunings	-	76
C	$\tilde{\mathcal{N}}$-correlated laser detuning ($\Delta^{\mathcal{N}}$)	-	48
	Total Systematic	29	310
	Statistical		373
	Total Uncertainty		486

Table 5.1.2: **Systematic shifts and their statistical uncertainties.** Units of μrad/s. All uncertainties are added in quadrature. For $\mathcal{E}_{\mathrm{eff}} = 78$ GV/cm, $d_e = 10^{-30}$ e·cm corresponds to $|\omega^{\mathcal{NE}}| = \mathcal{E}_{\mathrm{eff}} d_e/\hbar = 119$ μrad/s.

We check for nonlinear dependence by also fitting higher order polynomial functions to the $\omega^{\mathcal{NE}}$ vs P functional form. We note that it is still possible for non-linear dependence to be present between the specific parameter values at which we took data. To ensure such behavior was not expected, we created physical quantitative models for systematic effects corresponding to each P which caused a significant shift. Since we did not observe non-linear dependence and our models were consistent with linear dependence in the parameter P range of interest, we believe our procedure produced accurate estimates of the systematic errors.

5.2 Systematic error bar

The criteria for inclusion of a systematic effect in the error bar is similar to the ACME I measurement [6]. We include a measured effect in the $\omega^{\mathcal{NE}}$ channel in the systematic uncertainty if it belongs to one of the following three classes in order of decreasing importance

of inclusion:

- (A) If we measured a nonzero correlation between $\omega^{\mathcal{NE}}$ and some parameter which had an ideal value in the experiment, we performed auxiliary measurements to evaluate the corresponding systematic shift and the uncertainty in the shift. We subtract the shift from $\omega^{\mathcal{NE}}$ to obtain $\omega_T^{\mathcal{NE}}$ and add the statistical uncertainty in the $\omega^{\mathcal{NE}}$ shift in quadrature to the systematic error budget.

- (B) If we observed a signal in a channel that we deemed important to understand, and it was not understood, but was not observed to be correlated with $\omega^{\mathcal{NE}}$, we set an upper limit on the shift in $\omega^{\mathcal{NE}}$ due to a possible correlation between the two channels. Since such a signal represented a gap in our understanding of the experiment, we added this upper limit as a contribution to the systematic uncertainty.

- (C) We included a contribution to the systematic error bar from parameters which are closely related to parameters we have observed cause an $\omega^{\mathcal{NE}}$ shift or if similar experiments saw a nonzero, not understood correlation between their measurement channel and some parameter with an ideal experimental value. Since a systematic contribution could arise just below the statistical uncertainty of the systematic measurement, we added this upper limit as a contribution to the systematic uncertainty.

The systematics shifts and uncertainties that comprise the ACME II measurement error bar are shown in Table 5.1.2 and are grouped by inclusion class. There are 6 class A parameters which, when at a value that is far from ideal, cause shifts in $\omega^{\mathcal{NE}}$. The mechanisms that allow each of these groups of parameters to cause an associated shift in $\omega^{\mathcal{NE}}$ is described below: $\mathcal{B}_z$ magnetic field gradients ($\partial\mathcal{B}_z/\partial z$, $\partial\mathcal{B}_z/\partial y$) in Section 5.4; STIRAP $\mathcal{NE}$-correlated frequency ($\omega_{\mathrm{ST}}^{\mathcal{NE}}$) in Section 5.5; non-reversing electric field ($\mathcal{E}^{\mathrm{nr}}$) in Section 5.3; contrast correlations in Section 5.7; and $\omega^{\mathcal{E}}$ effects in Section 5.8.

We subtract systematic contributions associated with each one of these parameters. This corresponds to redefining the eEDM channel to be $\omega_T^{\mathcal{NE}} = \omega^{\mathcal{NE}} - \sum_{P\in\{\mathrm{Cl.\ A}\}} \omega_P^{\mathcal{NE}}$ free of

these systematics. We do not subtract a contribution for the $P^{\mathcal{NE}}$ effect, where we do not have a direct measurement of the normal experiment conditions $P^{\mathcal{NE}}$ value, but still include the extracted upper limit.

Class C contains a number of parameters that are similar to parameters that caused systematic shifts in the ACME I, ACME II, YbF or PbO experiments [6, 44, 65]. We do not subtract a systematic shift, but instead include an upper limit systematic error uncertainty due to possible dependence of $\omega^{\mathcal{NE}}$ on these parameters that is below the current statistical uncertainty of the systematic effect. The systematic error bar is extracted directly from the measured slopes S_P, obtained from systematic checks where we exaggerate P, and the measured non-ideal value of the parameters, $\bar{P}$ (Eq. 5.6). We discuss the reasons behind not including excess noise in the $\omega^{\mathcal{N}}$ channel as part of the ACME II systematic error bar, as was done in ACME I, in Section 5.14. None of the observed ACME II effects was compatible with the class B of systematic inclusion.

All systematic errors due to parameters presented in Table 5.1.2 are added in quadrature, as uncorrelated parameters, to compute a combined systematic uncertainty contribution of $\sigma_{\text{syst}} = 310$ μrad/s.

5.3 Systematic errors due to $\mathcal{E}^{\text{nr}}$

Performing the measurement in a differential manner, in which the eEDM frequency $\omega^{\mathcal{NE}}$ is correlated with the reversal of $\vec{\mathcal{E}}_{\text{eff}}$, rejects a large number of systematic and sources of noise in the ACME measurement. There are many parameters that can change the non-reversing precession frequency, ω^{nr}. However, since they are not correlated with the $\tilde{\mathcal{N}}$ and $\tilde{\mathcal{E}}$ switches, there is no contribution to $\omega^{\mathcal{NE}}$.

We are especially suspicious of parameters which are $\tilde{\mathcal{N}}, \tilde{\mathcal{E}}$-correlated. These correlated parameters can use multiple mechanisms to cause systematic effects in the measurement of $\omega^{\mathcal{NE}}$. We therefore carefully monitor the size of such correlated parameters and the

dependence of $\omega^{\mathcal{NE}}$ on them. In ACME I, we investigated effects related to two $\tilde{\mathcal{N}}, \tilde{\mathcal{E}}$-correlated laser parameters: detuning, $\Delta^{\mathcal{NE}}$, and power, $P^{\mathcal{NE}}$. As described later in this section, $\Delta^{\mathcal{NE}}$ arises directly from the presence of a non-reversing component of the electric field, $\mathcal{E}^{\mathrm{nr}}$. ACME I observed a dependence of $\omega^{\mathcal{NE}}$ on $\mathcal{E}^{\mathrm{nr}}$, which we briefly describe in Section 5.3.1 [5, 6]. While effects believed to be due to $P^{\mathcal{NE}}$-like parameters were measured indirectly, we did not find mechanisms that would lead to a $P^{\mathcal{NE}}$ in the laser beams used in the ACME experiment and create an $\omega^{\mathcal{NE}}$ effect at current sensitivity. Although we have never directly measured a $P^{\mathcal{NE}}$ component through an auxiliary measurement, we monitor the dependence of $\omega^{\mathcal{NE}}$ on $P^{\mathcal{NE}}$ and the value of $P^{\mathcal{NE}}$ under typical experimental conditions and include a limit on the possible magnitude of the resulting systematic error in the ACME II systematic error budget (see Section 5.6).

A non-reversing electric field, $\mathcal{E}^{\mathrm{nr}}$, is a component of the electric field that does not change sign with the reversal of the applied electric field. Such an imperfection might be caused by e.g. variations in the ITO coating, which could produce patch potentials [113]. In the presence of an $\mathcal{E}^{\mathrm{nr}}$, we can write the electric field in our precession region as

$$\vec{\mathcal{E}} \cdot \hat{z} = \mathcal{E}^{\mathrm{rev}} \tilde{\mathcal{E}} + \mathcal{E}^{\mathrm{nr}}. \tag{5.7}$$

For both electric field magnitudes used in ACME II ($1\mathcal{E}$ and $2\mathcal{E}$), the Ω-doublet states are fully mixed and the Stark shift is linear in the electric field $\Delta^{\mathcal{N}}_{\mathrm{Stark}} = -D_H|\mathcal{E}|\tilde{\mathcal{N}}$. In the presence of an $\mathcal{E}^{\mathrm{nr}}$ component, this becomes

$$\Delta^{\mathcal{N}}_{\mathrm{Stark}} = -D_H(|\mathcal{E}^{\mathrm{rev}}| + \mathcal{E}^{\mathrm{nr}}\tilde{\mathcal{E}})\tilde{\mathcal{N}} = -D_H|\mathcal{E}^{\mathrm{rev}}|\tilde{\mathcal{N}} - D_H\mathcal{E}^{\mathrm{nr}}\tilde{\mathcal{N}}\tilde{\mathcal{E}}. \tag{5.8}$$

To keep the lasers on resonance, we match the laser frequencies corresponding to the two $\tilde{\mathcal{N}}$ states to the $\mathcal{N}-$correlated Stark shift using the experimental scheme described in Section

3.2.3. The laser frequency is therefore given by

$$f^{\mathcal{N}} = f_0 + f^{\mathcal{N}}\tilde{\mathcal{N}}, \tag{5.9}$$

where f_0 which is the average frequency difference between the H state and the excited state (I in the case of optical pumping and C for the STIRAP beam) and $f^{\mathcal{N}}$ is the frequency difference between the two $\tilde{\mathcal{N}}$ experimental states. Therefore, the laser detunings in the ACME experiment are given by

$$\begin{aligned}
\Delta &= f^{N} - \Delta^{\mathcal{N}}_{\text{Stark}} && (5.10)\\
&= \Delta_0 + (D_H|\mathcal{E}_0| - f^{\mathcal{N}})\tilde{\mathcal{N}} + D_H\mathcal{E}^{\text{nr}}\tilde{\mathcal{N}}\tilde{\mathcal{E}} && (5.11)\\
&= \Delta_0 + \Delta^{\mathcal{N}}\tilde{\mathcal{N}} + \Delta^{\mathcal{N}\mathcal{E}}\tilde{\mathcal{N}}\tilde{\mathcal{E}}, && (5.12)
\end{aligned}$$

where we have grouped the detunings according to their correlations with $\tilde{\mathcal{N}}$ and $\tilde{\mathcal{E}}$. The $\tilde{\mathcal{N}}$ correlated detuning arises from a mismatch between the frequency of the laser and the frequencies of the two Stark-shifted $\tilde{\mathcal{N}}$ states. More importantly, the presence of the non-reversing electric field $\mathcal{E}^{\text{nr}}$ leads to an $\tilde{\mathcal{N}}\tilde{\mathcal{E}}$-correlated detuning, $\Delta^{\mathcal{N}\mathcal{E}}$ (Fig. 5.3.1).

The presence of $\mathcal{E}^{\text{nr}}$ causes $\tilde{\mathcal{N}}\tilde{\mathcal{E}}$-correlated detuning components for all 4 experimental lasers that are present in the interaction region: STIRAP pump, STIRAP Stokes, refinement and readout. To cause a shift in $\omega^{\mathcal{N}\mathcal{E}}$, $\mathcal{E}^{\text{nr}}$ can then couple to a dependence of precession frequency on detuning $\alpha^{\text{nr}}_{\Delta} = \partial\omega/\partial\Delta$ such that

$$\omega^{\mathcal{N}\mathcal{E}} = \alpha^{\text{nr}}_{\Delta} \cdot \Delta^{\mathcal{N}\mathcal{E}}. \tag{5.13}$$

As we discuss in detail in the following sections, there are a number of mechanisms that can cause such slopes to occur in each of the laser beams.

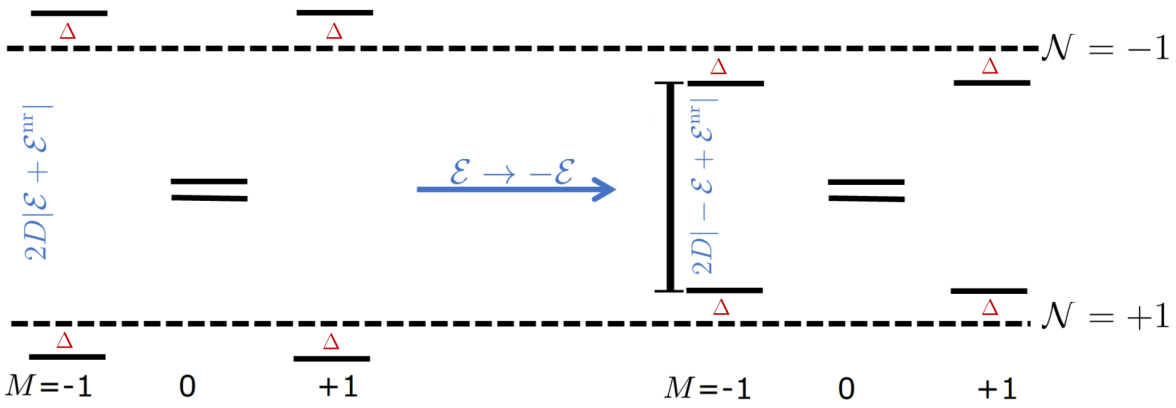

Figure 5.3.1: **Mechanism through which $\mathcal{E}^{\rm nr}$ causes a $\Delta^{\mathcal{N}\mathcal{E}}$ laser correlated detuning.** When a non-reversing component of the electric field, $\mathcal{E}^{\rm nr}$, is present, the H state acquires an additional Stark shift. This shift causes a differential detuning between the laser frequency and the molecular state. As shown in the figure, this detuning component reverses sign with either $\tilde{\mathcal{N}}$ or $\tilde{\mathcal{E}}$ switches, $\Delta^{\mathcal{N}\mathcal{E}}$.

5.3.1 AC Stark shift-birefringence systematic

We discovered one of the mechanisms leading from $\Delta^{\mathcal{N}\mathcal{E}}$ to $\omega^{\mathcal{N}\mathcal{E}}$ in ACME I. The largest ACME I systematic error came from a dependence of frequency on detuning that occurs due to imperfections in the ellipticity gradients of the refinement and readout lasers in combination with AC Stark shifts and $\mathcal{E}^{\rm nr}$. A nonzero phase vs detuning slope, $\alpha_\Delta^{\text{AC Stark shift}}$, occurred due to a combination of ellipticity gradients in the preparation and readout lasers and an AC Stark shift effect. This mechanism is carefully described in previous publications [5, 6].

A thermal stress-induced birefringence gradient, caused by absorption of the laser power by the glass electric field plates and vacuum chamber windows, was responsible for the large ellipticity gradient ($\sim 10\%$/mm circular polarization fraction) [5, 6]. As described in detail in Section 3.5.1, this term is greatly reduced in ACME II by using a type of glass for the field plates with reduced thermal expansion and bulk absorption coefficients and a transition that requires lower laser power. Running at lower laser power was possible by using a refinement and readout transition with a stronger transition dipole moment (see Section 3.3.2).

For the typical experiment configuration, when the refinement and readout lasers travel through the experiment along $\hat{z}$, ($\hat{k} \cdot \hat{z} = 1$), we did not observe a significant $\alpha_{\Delta}^{\mathrm{ACStark}}$. However, given the importance of this systematic effect in ACME I, we monitored and placed a direct systematic error on this effect. By applying a large value of $\mathcal{E}^{\mathrm{nr}}$ that is typically 15 times the measured residual $\mathcal{E}^{\mathrm{nr}}$, we measure $S_{\mathcal{E}^{\mathrm{nr}}} = \partial\omega^{\mathcal{NE}}/\partial\mathcal{E}^{\mathrm{nr}}$ regularly throughout the EDM dataset (Fig. 2.5.1e). $\mathcal{E}^{\mathrm{nr}}$ and its gradients in the precession region, $\partial\mathcal{E}^{\mathrm{nr}}/\partial z$ and $\partial\mathcal{E}^{\mathrm{nr}}/\partial y$, were measured every two weeks during the EDM dataset through a mapping method based on microwave spectroscopy [6]. We include in the systematic error budget (Table I) a contribution based on $S_{\mathcal{E}^{\mathrm{nr}}}$ and the measured ambient $\mathcal{E}^{\mathrm{nr}}$.

However, when $\hat{k} \cdot \hat{z} = -1$ (but not when $\hat{k} \cdot \hat{z} = +1$), we found a nonzero value of $\partial\omega^{\mathcal{NE}}/\partial\mathcal{E}^{\mathrm{nr}}$. This slope could be explained [6] by the presence of small ($\sim 1\%$/mm) ellipticity gradients, caused by mechanical stress birefringence from mounting of the electric field plates and/or vacuum chamber windows, on one side of the apparatus but not the other. Unlike in ACME I, we were not able to minimize this effect by aligning the polarization of the lasers with the birefringence axis of the optics, since the spin alignment is fixed by the STIRAP beams to be along $\hat{x}$. While the systematic-free $\omega_T^{\mathcal{NE}}$ value was consistent for both $\hat{k} \cdot \hat{z} = \pm 1$ configurations, the larger $\partial\omega^{\mathcal{NE}}/\partial\mathcal{E}^{\mathrm{nr}}$ slope significantly increases (factor of ~ 5) the $\mathcal{E}^{\mathrm{nr}}$ systematic uncertainty for $\hat{k} \cdot \hat{z} = -1$. Hence, in ACME II, we treat $\hat{k} \cdot \hat{z} = -1$ as a parameter variation consistency check and acquire the final EDM dataset only with $\hat{k} \cdot \hat{z} = +1$. Methods that could allow us to reduce the value of this ellipticity gradient imperfection parameter in the future are described in Chapter 6.

5.4 Magnetic field gradients coupled to correlated detunings

Another contribution to systematic shifts arises from gradients of $\mathcal{B}_z$ along the z and y axes, $(\partial\mathcal{B}_z/\partial z)^{\mathrm{nr}}$ and $(\partial\mathcal{B}_z/\partial y)^{\mathrm{nr}}$. When applying large values of $(\partial\mathcal{B}_z/\partial z(y))^{\mathrm{nr}}$ magnetic

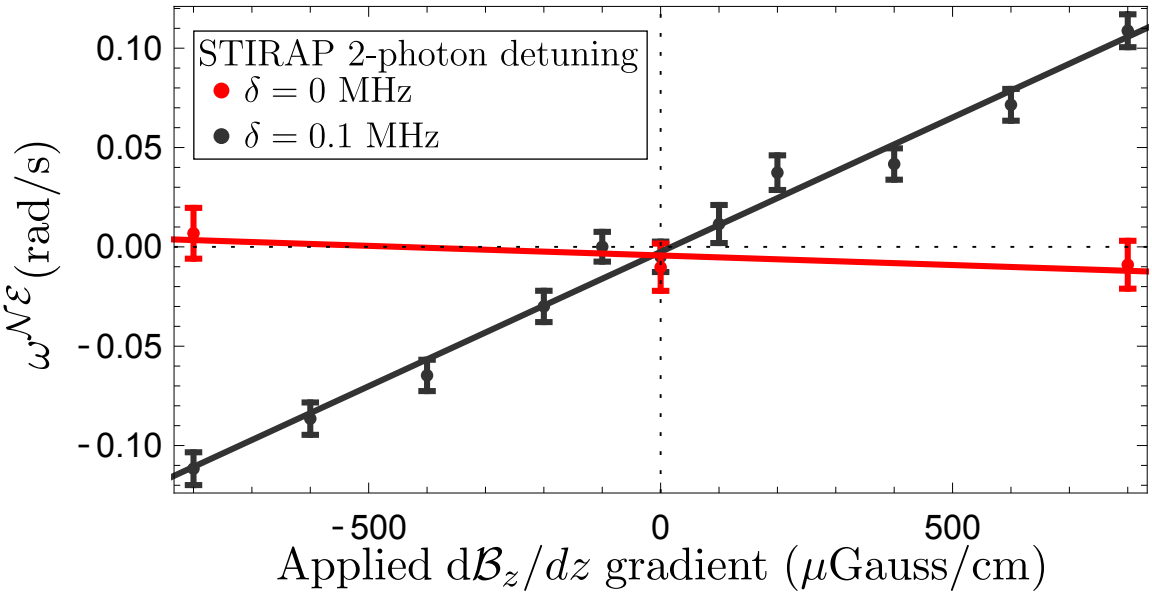

Figure 5.4.1: $\omega^{\mathcal{NE}}$ **dependence on an applied** $\partial\mathcal{B}_z/\partial z$**, which is the result of a systematic effect.** We observed systematic dependence of $\omega^{\mathcal{NE}}$ on a larger applied $\partial\mathcal{B}_z/\partial z$ (black). The slope $\partial\omega^{\mathcal{NE}}/\partial(\partial\mathcal{B}_z/\partial z)$ is consistent with zero when δ is set to zero (red).

field gradients, we observed statistically significant shifts of up to $S_\partial\mathcal{B}_z/\partial z, S_\partial\mathcal{B}_z/\partial y \approx 200$ (μrad/s)/(mGauss/cm) (Fig. 5.4.1). The dependence is linear in the applied range of gradients. Since these applied field gradients are much larger than the typical residual values under typical running conditions, the systematic contribution was a factor of 2-3 lower than the eventual statistical uncertainty of the measurement. However, we still made the effort to understand and suppress this term.

We understand the nonzero slopes associated with parameters $S_{\partial\mathcal{B}_z/\partial z} = \partial\omega^{\mathcal{NE}}/\partial(\partial\mathcal{B}_z/\partial z)$ and $S_{\partial\mathcal{B}_z/\partial y} = \partial\omega^{\mathcal{NE}}/\partial(\partial\mathcal{B}_z/\partial y)$, as follows. The largest component of the spin precession frequency, ω, comes from the Zeeman term which is proportional to $\mathcal{B}_z$, $\omega_B = -\mu_H\tilde{\mathcal{B}}|\mathcal{B}_z|/\hbar$, (Eq. 2.5). A gradient $\partial\mathcal{B}_z/\partial z$ ($\partial\mathcal{B}_z/\partial y$), together with a translation of the center of mass of the detected molecular beam along the direction of the gradient, dz_{CM} (dy_{CM}), can create

a shift in the measured precession frequency,

$$\mathrm{d}\omega = -\mu_H \partial \mathcal{B}_z/\partial z \cdot \mathrm{d}z_{\mathrm{CM}}/\hbar \tag{5.14}$$

$$\mathrm{d}\omega = -\mu_H \partial \mathcal{B}_z/\partial y \cdot \mathrm{d}y_{\mathrm{CM}}/\hbar. \tag{5.15}$$

We identified two separate effects that can cause such translations in our system: one that arises from a non-reversing electric field, $\mathcal{E}^{\mathrm{nr}}$, and one that arises from gradients in such a field, $\partial\mathcal{E}^{\mathrm{nr}}/\partial z$ and $\partial\mathcal{E}^{\mathrm{nr}}/\partial y$. Both effects are associated with incomplete laser excitation, and each can occur in both the STIRAP and readout laser beams.

5.4.1 First effect: coupling with $\mathcal{E}^{\mathrm{nr}}$ gradients

We first describe the shifts related to gradients in the non-reversing electric field, $\partial\mathcal{E}^{\mathrm{nr}}/\partial z$ and $\partial\mathcal{E}^{\mathrm{nr}}/\partial y$. For clarity, we describe the systematic shift due to $\partial\mathcal{B}_z/\partial z$, although the systematic effect is entirely analogous for both $\partial\mathcal{B}_z/\partial z$ and $\partial\mathcal{B}_z/\partial y$ gradients. The systematic effect occurs in both the STIRAP and readout laser regions, but we discuss the part associated with a translation of the center of mass of the molecules that are successfully prepared by STIRAP, which is the dominant contribution.

Mechanism

We nominally tune the STIRAP 2-photon detuning, δ, to resonance ($\delta = 0$), where the STIRAP transfer efficiency, η, is maximal ($\eta(\delta = 0) = \eta_0 \approx 75\%$) [73]. When $\delta = 0$, by definition the derivative of the transfer efficiency vs. detuning is $\partial\eta/\partial\delta = 0$. However, if slightly off resonance, $\partial\eta/\partial\delta$ will be nonzero: $\partial\eta/\partial\delta \propto \delta$ (for small δ). A small change in the 2-photon detuning, $\mathrm{d}\delta$, can thus lead to a change in the transfer efficiency given by

$$\mathrm{d}\eta = \frac{\partial\eta}{\partial\delta} \cdot \mathrm{d}\delta. \tag{5.16}$$

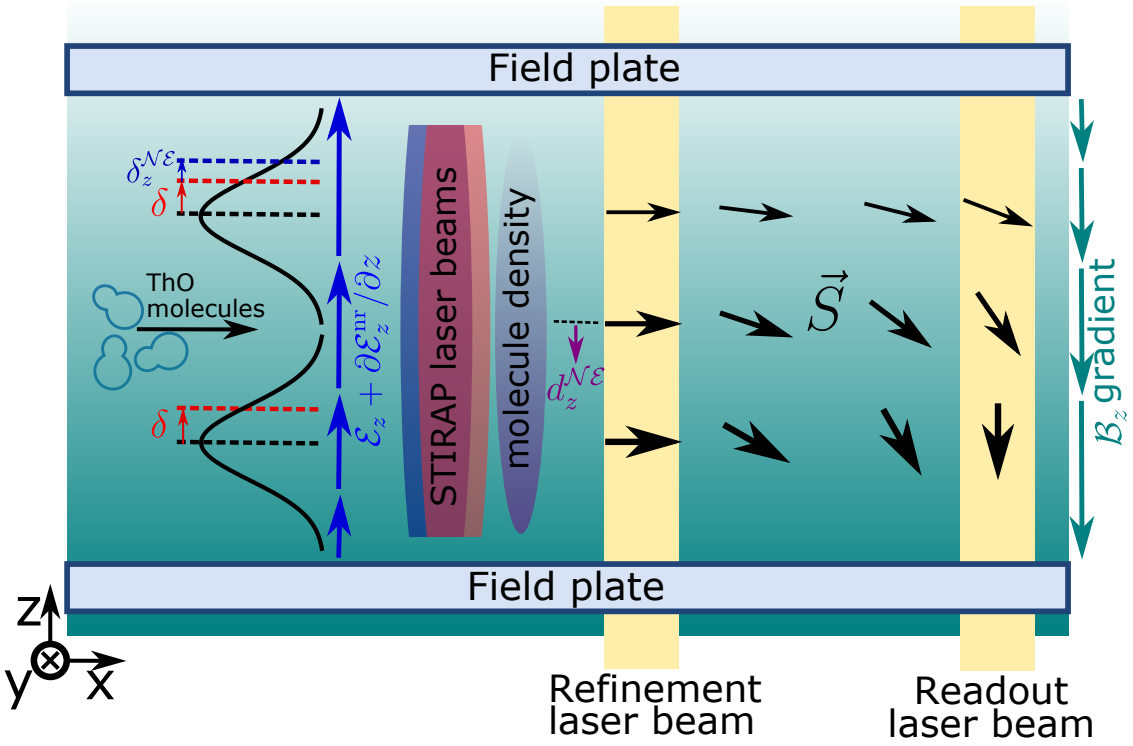

Figure 5.4.2: **Mechanism leading to a systematic shift due to $\partial\mathcal{B}_z/\partial z \times \delta \times \partial\mathcal{E}^{\rm nr}/\partial z$.** A $\partial\mathcal{E}_z^{\rm nr}/\partial z$ gradient (blue arrows) causes a z-dependent 2-photon detuning correlated with $\tilde{\mathcal{N}}\tilde{\mathcal{E}}$ ($\delta_z^{\mathcal{N}\mathcal{E}}$), due to the Stark shift $D\mathcal{E}$. When $\delta \neq 0$, the combination of a nonzero $\delta_z^{\mathcal{N}\mathcal{E}}$ and a dependence of the STIRAP efficiency on 2-photon detuning, $\partial\eta/\partial\delta$ (shown as black lineshapes) acts to translate the detected molecular cloud (purple gradient ellipse) position by $\mathrm{d}z_{\rm CM}^{\mathcal{N}\mathcal{E}}$ (purple arrow). A nonzero $\partial\mathcal{B}_z/\partial z$ (teal color gradient) causes molecules to accumulate more (less) precession phase if their position has a smaller (larger) z coordinate. The effects combine to create the dependence of $\omega^{\mathcal{N}\mathcal{E}}$ on $\partial\mathcal{B}_z/\partial z$. Scales exaggerated for clarity.

Spatial dependence of δ on z, $\partial\delta/\partial z$, will then cause a z-dependence of η, described by

$$\eta(z) = \frac{\partial\eta}{\partial\delta}\frac{\partial\delta}{\partial z}z + \eta_0. \tag{5.17}$$

Such a dependence of δ on z can arise from different sources, including, for example, spatially inhomogeneous $\mathcal{E}$-fields that Stark shift the molecular resonance.

We estimate the size of this effect by building a simple model, with a constant molecular

density along z. When integrating the molecular density along z, this effect shifts the center of mass of the molecules that are successfully prepared by the STIRAP lasers along z by

$$\mathrm{d}z_{\mathrm{CM}} = \frac{\int_{-a}^{a} z\eta(z)\mathrm{d}z}{\int_{-a}^{a} \eta(z)\mathrm{d}z} \tag{5.18}$$

$$= \frac{a^2}{3\eta_0}\frac{\partial\eta}{\partial\delta}\frac{\partial\delta}{\partial z}, \tag{5.19}$$

where a is the half-width of the molecular beam in z.

Such translations in molecular beam position, in the presence of a $\mathcal{B}$-field gradient, cause a shift in the precession frequency

$$\mathrm{d}\omega = -\frac{\mu_H \partial\mathcal{B}_z/\partial z \cdot \mathrm{d}z_{\mathrm{CM}}}{\hbar}. \tag{5.20}$$

If $\partial\delta/\partial z$ has a component correlated with $\tilde{\mathcal{N}}\tilde{\mathcal{E}}$, then $\partial\delta^{\mathcal{N}\mathcal{E}}/\partial z$ can lead to a systematic error in the measurement of $\omega^{\mathcal{N}\mathcal{E}}$. In the ACME II measurement, a nonzero $\partial\delta^{\mathcal{N}\mathcal{E}}/\partial z$ is caused by a gradient in the non-reversing $\mathcal{E}$-field component along z, $\partial\mathcal{E}^{\mathrm{nr}}/\partial z$ (see Section 5.3).

When all terms in our model are accounted for (Fig. 5.4.2), we obtain a systematic error contribution given by:

$$\omega^{\mathcal{N}\mathcal{E}}_{\partial\mathcal{B}_z/\partial z - \partial\mathcal{E}^{\mathrm{nr}}/\partial z} = -\left(\mu_B \frac{\partial\mathcal{B}_z}{\partial z}\right)\left(\frac{a^2}{3\eta_0}\frac{\partial\eta}{\partial\delta}\right)\left(D_H \frac{\partial\mathcal{E}^{\mathrm{nr}}}{\partial z}\right)/\hbar. \tag{5.21}$$

While we can exaggerate $\mathcal{E}^{\mathrm{nr}}$ by applying an asymmetric voltage on the $\mathcal{E}$-field plates, we have no experimental means to apply $\mathcal{E}^{\mathrm{nr}}$ gradients. However, since this systematic depends on three imperfections ($\partial\mathcal{E}^{\mathrm{nr}}/\partial z$, δ through $\partial\eta/\partial\delta$, and $\partial\mathcal{B}_z/\partial z$), amplifying any one of these individually allows us to accurately find settings that null the product of the other two imperfection-related parameters. Then, under ordinary run conditions (when all controllable parameters are nulled), the product of the residual imperfections is at least second-order small.

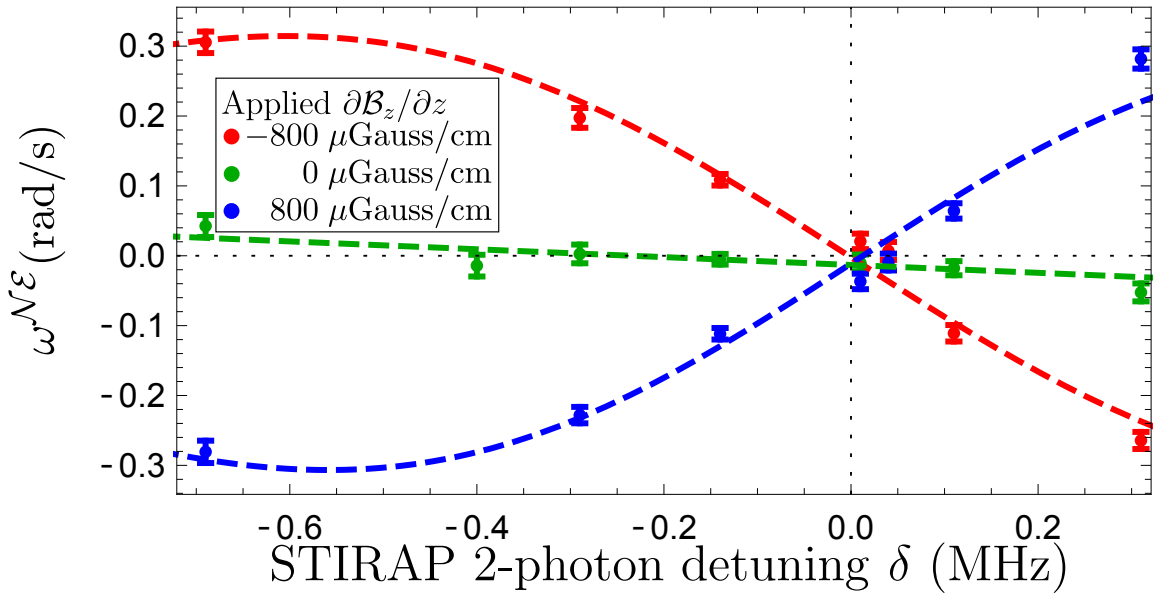

Figure 5.4.3: **Dependence of $\omega^{\mathcal{NE}}$ on both δ and $\partial\mathcal{B}_z/\partial z$.** Fits (dashed curves) to a simple lineshape model show good agreement with the data. $\delta = 0$ is defined as where all curves cross. The error bars represent 1σ statistical uncertainties.

As described above, this specific systematic model has 4 separate contributions, due to the combinations of $\partial\mathcal{B}_z/\partial z - \partial\mathcal{E}^{\rm nr}/\partial z$ and $\partial\mathcal{B}_z/\partial y - \partial\mathcal{E}^{\rm nr}/\partial y$, which both occur in both the STIRAP and readout laser beams. However, the STIRAP contributions are under normal running conditions the most significant, due to the narrower linewidth of the STIRAP resonance, $\sigma_{\rm ST} \approx 2\pi \times 1.5$ MHz than for the readout, $\sigma_{\rm read} \approx 2\pi \times 3$ MHz. In addition, the $\partial\mathcal{B}_z/\partial z - \partial\mathcal{E}^{\rm nr}/\partial z$ contribution is larger due to the larger $\partial\mathcal{E}^{\rm nr}/\partial z$ in that direction.

Confirmation of model

By intentionally varying δ and deliberately applying a nonzero $\partial\mathcal{B}_z/\partial z$, we verified our model for how these parameters cause a false shift in $\omega^{\mathcal{NE}}$ (Fig. 5.4.2). Under typical run parameters, the Rabi frequencies of the Pump and Stokes lasers are kept equal and the STIRAP 2-photon resonance lineshape is reasonably well approximated by a Gaussian

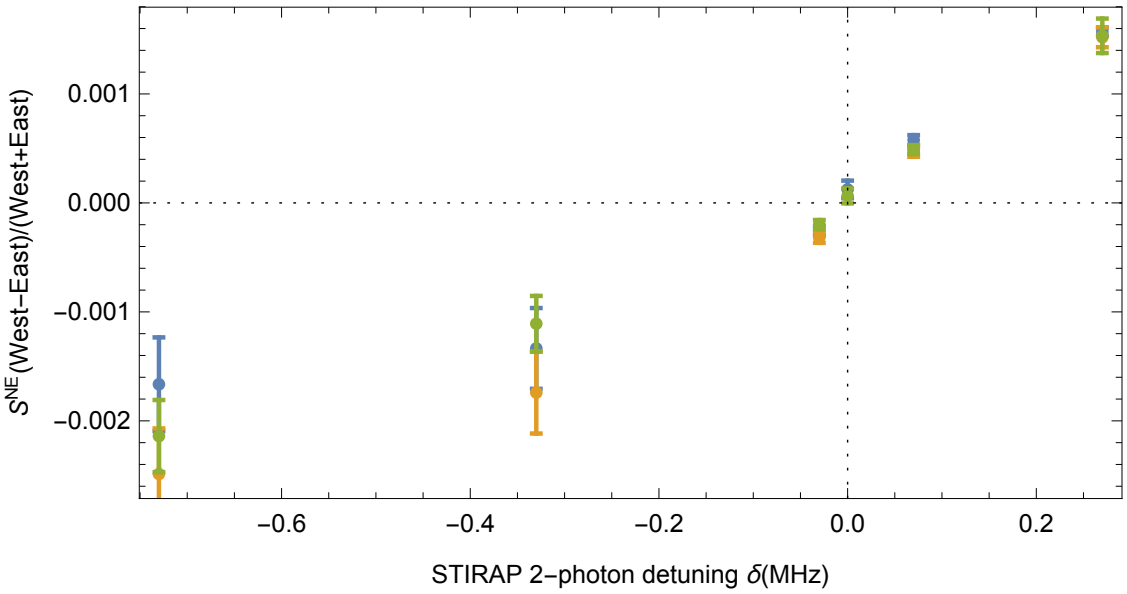

Figure 5.4.4: **West-east PMT fluorescence asymmetry.** The asymmetry in west-east fluorescence scales with the STIRAP 2-photon detuning, δ, when a large $\partial\mathcal{B}_z/\partial z$ magnetic field gradient is applied. This is consistent with a translation in the center of mass of the molecules along z due to the $\tilde{\mathcal{N}}, \tilde{\mathcal{E}}$-correlated detuning, $\delta^{\mathcal{N}\mathcal{E}}$, caused by a gradient $\partial\mathcal{E}^{\mathrm{nr}}/\partial z$. The extracted values for $\partial\mathcal{E}^{\mathrm{nr}}/\partial z$ from this data are consistent with those measured directly in Section 3.5.3.

[73]. The resonance lineshape is then given by

$$\eta(\delta) = \eta_0 e^{-\delta^2/(2\sigma_{\mathrm{ST}}^2)}. \tag{5.22}$$

Using this equation, we fit the $\omega^{\mathcal{N}\mathcal{E}}$ vs. δ data (Figure. 5.4.3) to the function

$$L(\delta) \equiv \frac{\partial\omega^{\mathcal{N}\mathcal{E}}}{\partial\delta} = -c\cdot\delta\cdot e^{-\delta^2/(2\sigma_{\mathrm{ST}}^2)}, \tag{5.23}$$

where the free fit parameters are σ_{ST} and the scaling factor

$$c = \frac{1}{\sigma_{\mathrm{ST}}^2}\frac{a^2}{3\eta_0}(\mu_B\frac{\partial\mathcal{B}_z}{\partial z})(D_H\cdot\frac{\partial\mathcal{E}^{\mathrm{nr}}}{\partial z})/\hbar. \tag{5.24}$$

We measured $\partial\mathcal{E}^{\mathrm{nr}}/\partial z$ and $\partial\mathcal{E}^{\mathrm{nr}}/\partial y$ in an auxiliary measurement using microwaves, as

described in Section 3.5.3. The measured magnitudes were consisted with the size of the observed systematic slopes.

Furthermore, we investigated the spatial dependence of the fluorescence signal, F, by grouping the PMT signal by the spatial location of the PMTs ($+z$ or $-z$, $+y$ or $-y$, $+x$ or $-x$). As expected, we observed an $\tilde{\mathcal{N}}\tilde{\mathcal{E}}$-correlated z-dependent fraction of the fluorescence signal, $\partial F^{\mathcal{N}\mathcal{E}}/\partial z$ (Figure 5.4.4). This independently confirmed the $\tilde{\mathcal{N}}\tilde{\mathcal{E}}$-correlated translation in z, $\mathrm{d}z_{\mathrm{CM}}^{\mathcal{N}\mathcal{E}}$, when we amplify the effect by applying deliberate nonzero values of δ. The magnitude of $\mathcal{E}^{\mathrm{nr}}$ gradients extracted from this data is consistent with the direct measurement described in Section 3.5.3.

5.4.2 Second Contribution

The second contribution to the $\mathcal{B}$-field gradients class of systematic errors comes from a coupling of the $\mathcal{B}$-field gradients to an $\tilde{\mathcal{N}}\tilde{\mathcal{E}}$-correlated translation of the detected molecular population that is related to an $\mathcal{E}^{\mathrm{nr}}$ offset, rather than a gradient in $\mathcal{E}^{\mathrm{nr}}$. We focus our discussion on the effect in the readout beam, which comes from a translation of the molecular beam in z, the propagation direction of the readout laser, therefore coupling to a $\partial\mathcal{B}_z/\partial z$ gradient only. The effect is analogous for $\partial\mathcal{B}_z/\partial y$ in the STIRAP laser beams, which propagate along $\hat{y}$. This contribution it typically a factor of three to five smaller than the first contribution.

Mechanism

To describe the mechanism leading to the systematic effect, we use a simple numerical simulation that models the behavior of the ACME II molecular beam. After leaving the beam source, molecules travel ballistically through the precession region. We start with a source (effective width $\sim$6 mm), from which molecules leave with a longitudinal velocity of 180 m/s. The transverse velocity at the source is a Gaussian with a width (1σ) of 15 m/s.

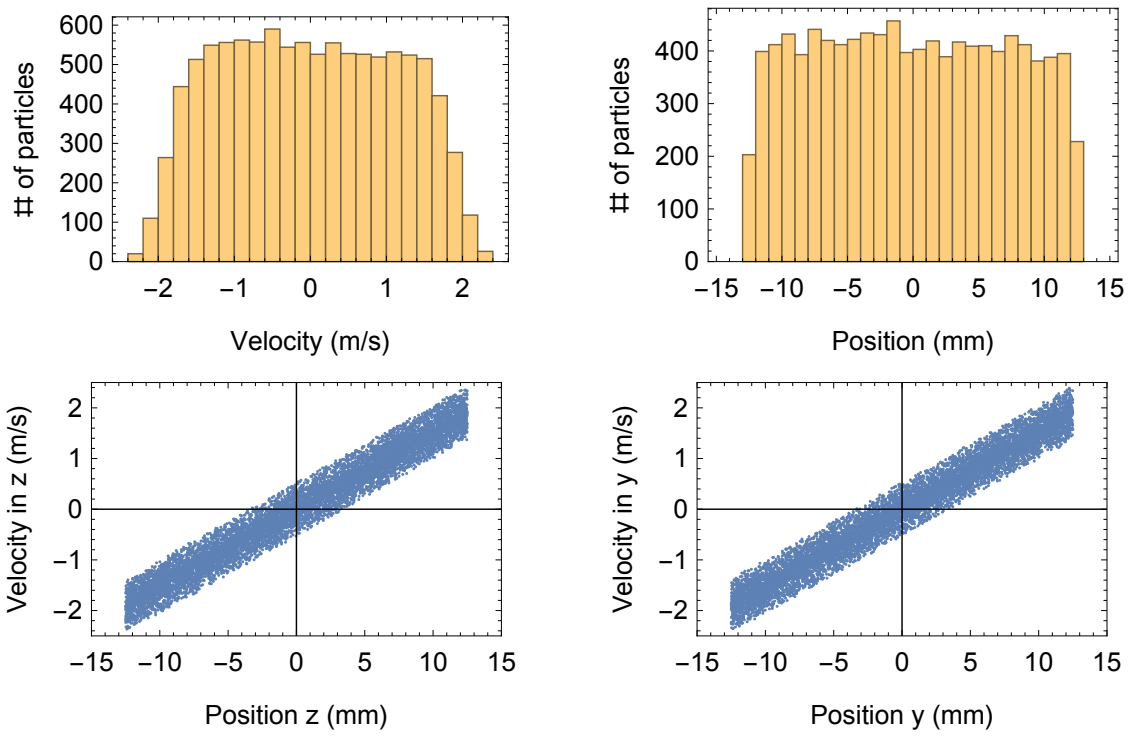

Figure 5.4.5: **Numerical simulation showing the transverse distribution of molecules in position and velocity space.** Top figures show histograms of the transverse (along y and z) spatial and velocity distribution of molecules in the precession region. The distributions are nearly flat-topped, as set by the fixed collimators. The lower figures show the strong correlations (> 0.9 correlation coefficient) between the velocity and position of molecules along the transverse z and y directions.

Since the beam of ThO molecules diverges from the source (effective width ∼6 mm) to the size of the molecular beam in the precession region (where collimators define the beam width to be ∼25 mm) over a distance of 1.1 m, there is a strong correlation (> 0.9 correlation coefficient) between the z position of the molecules and their transverse velocity, $v_z \propto z$ (see Fig. 5.4.5).

Finite transverse velocity causes a Doppler shift for the readout laser $\Delta_z^{\mathrm{Dopp}} = k_{\mathrm{read}} v_z$. This leads to a correlation between the detuning experienced by a molecule and its position:

$$\frac{\partial \Delta_z^{\mathrm{Dopp}}}{\partial z} = \frac{\partial \Delta_z^{\mathrm{Dopp}}}{\partial v_z} \frac{\partial v_z}{\partial z}. \tag{5.25}$$

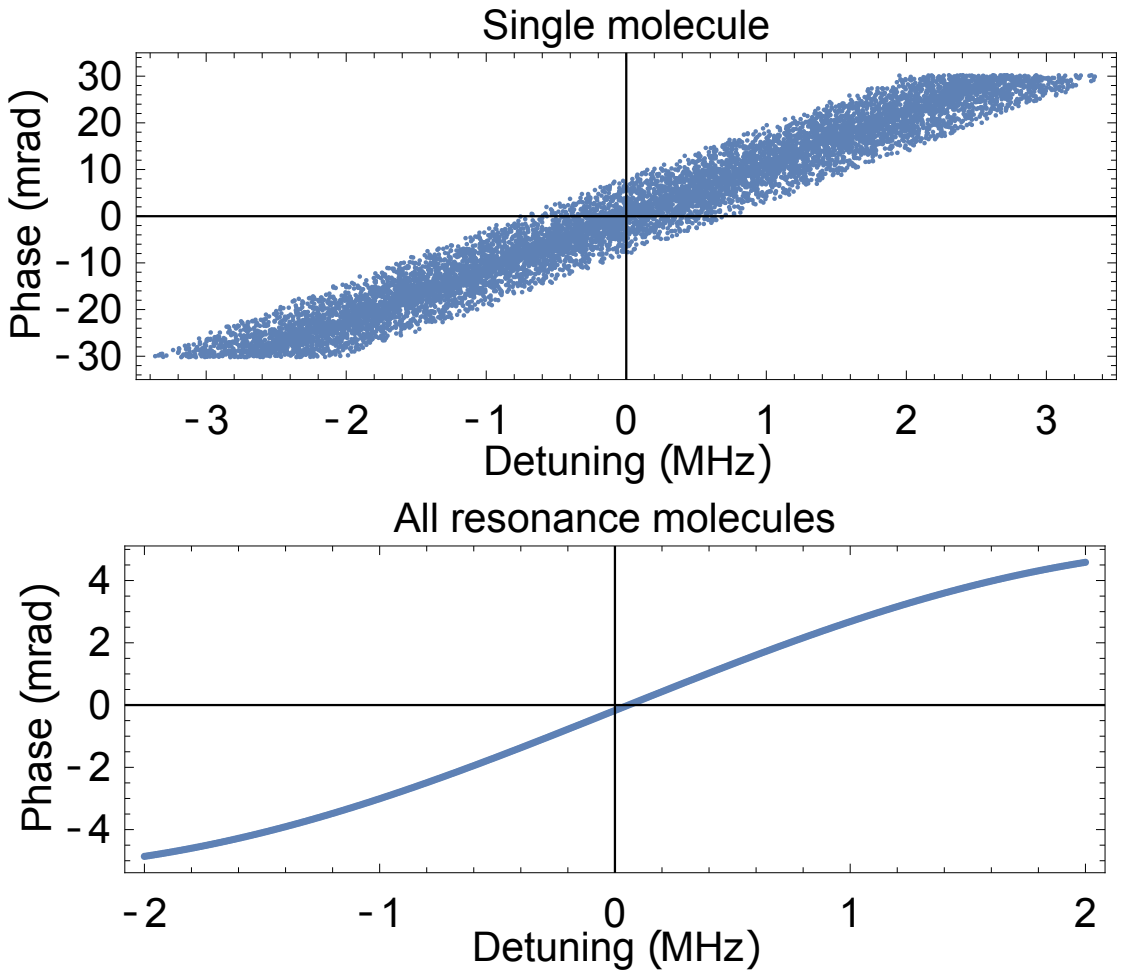

Figure 5.4.6: **Phase dependence on detuning for the $\partial\mathcal{B}_z/\partial z - \mathcal{E}^{\mathrm{nr}}$ systematic.** Numerical data showing the dependence of phase vs detuning when a large $\partial\mathcal{B}_z/\partial z$ gradient is applied. The plots are shown **(a)** for each molecule in the interaction region, and **(b)** when integrated over the detuning range of the entire molecular ensemble addressed by the readout laser beam.

This in turn means that a change in laser detuning, $\mathrm{d}\Delta$, leads to a translation of the detected molecular beam in z, given by

$$\mathrm{d}z_{\mathrm{CM}} = \frac{\partial z}{\partial \Delta_z^{\mathrm{Dopp}}}\mathrm{d}\Delta. \tag{5.26}$$

Such a translation, in concert with a nonzero $\partial\mathcal{B}_z/\partial z$, causes a shift in the precession frequency,

$$\mathrm{d}\omega = -\mu(\partial\mathcal{B}_z/\partial z)\mathrm{d}z_{\mathrm{CM}}/\hbar. \tag{5.27}$$

In the context of our simulation, the phase accumulated by each molecule is shown as a function of its detuning for the entire molecular cloud in Figure 5.4.6a. To calculate the phase dependence on detuning for the entire molecular beam, we integrate over the typical Doppler and power broadened nearly-Gaussian line-shape of the readout laser beam with a 1σ width of $2\pi \times 2.5$ MHz (Figure 5.4.6b).

Finally, this can lead to a systematic shift in the eEDM frequency, $\omega^{\mathcal{NE}}$, if there is a mechanism that leads to an $\tilde{\mathcal{N}}\tilde{\mathcal{E}}$-correlated detuning, $\Delta^{\mathcal{NE}}$. As shown in Section 5.3, this type of correlated detuning is caused in our measurement by $\mathcal{E}^{\mathrm{nr}}$, $\Delta^{\mathcal{NE}} = D_H \mathcal{E}^{\mathrm{nr}}$. The complete systematic shift is then given by

$$\omega^{\mathcal{NE}}_{\partial \mathcal{B}_z/\partial \mathrm{z}-\mathcal{E}^{\mathrm{nr}}} = -\mu d \frac{\partial \mathcal{B}_z}{\partial z} \frac{1}{k_{\mathrm{read}}} \frac{\partial z}{\partial v_z} \frac{D_H \mathcal{E}^{\mathrm{nr}}}{\hbar}, \tag{5.28}$$

where d is a scaling term obtained when integrating over the entire readout beam distribution of detunings, rather than for a single velocity class.

Confirmation

We verified that there is a slope of phase vs detuning that is correlated with the size of the applied magnetic field gradient $\partial \mathcal{B}_z/\partial z$ and that is linear on detuning, as shown in Figure 5.4.7. Its magnitude is consistent with that expected from simulations.

In addition, we intentionally exaggerated $\mathcal{E}^{\mathrm{nr}}$ and verified that it couples to a deliberately applied $\partial \mathcal{B}_z/\partial z$ to cause a shift in the $\omega^{\mathcal{NE}}$ channel, as just described.

5.4.3 Reduction and monitoring

For the eEDM data set, we minimized the magnitudes of both slopes, $S_{\partial \mathcal{B}_z/\partial z}$ and $S_{\partial \mathcal{B}_z/\partial y}$. We reduced both contributions to the systematic, from coupling to $\mathcal{E}^{\mathrm{nr}}$ and gradients $\partial \mathcal{E}^{\mathrm{nr}}/\partial z(y)$ by tuning the readout laser such that $\Delta = 0$, and the STIRAP lasers such that $\delta = 0$ (Fig. 5.4.1), respectively. The size of the residual slopes under these optimized

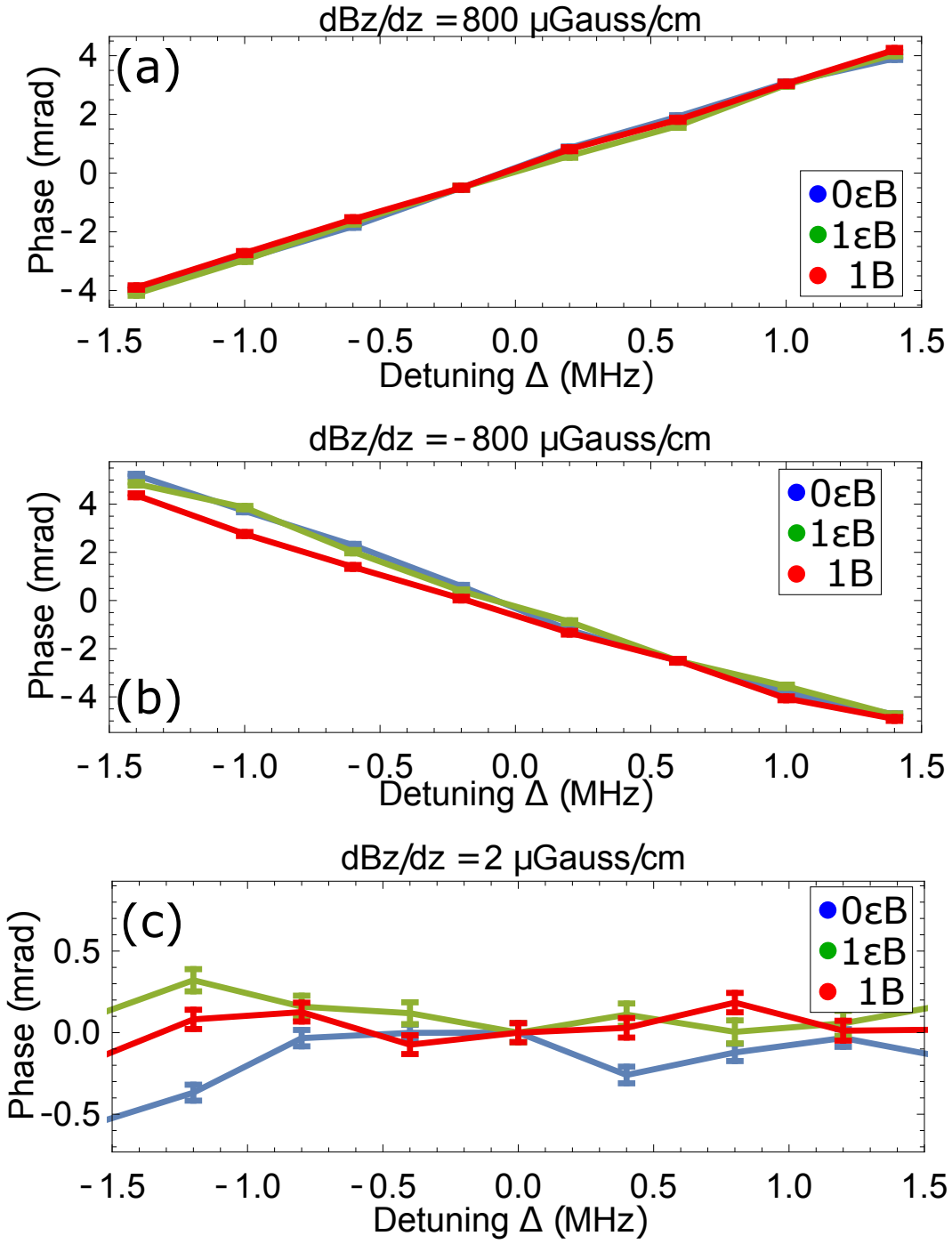

Figure 5.4.7: **Phase dependence on readout detuning in the presence of magnetic field gradients.** Experimentally measured slopes for phase dependence on readout laser detuning in the presence of magnetic field gradients. The slope is linear in the magnetic field gradient value, and is shown here for three values of applied $\partial\mathcal{B}_z/\partial z$ gradient: **(a)** $\partial\mathcal{B}_z/\partial z = 800$ μGauss/cm, **(b)** $\partial\mathcal{B}_z/\partial z = -800$ μGauss/cm, and **(c)** with only the residual $\partial\mathcal{B}_z/\partial z = 2$ μGauss/cm. The slope is independent of the value of applied $\mathcal{B}_z$, shown here in three configurations ($0\epsilon\mathcal{B}$, $1\epsilon\mathcal{B}$, $1\mathcal{B}$). Error bars correspond to 1σ (68%) confidence intervals.

conditions was then measured by deliberately applying large values of $\partial\mathcal{B}_z/\partial z$ and $\partial\mathcal{B}_z/\partial y$, and found consistent with zero. To ensure that the imperfections leading to nonzero values of these slopes (namely, a combination of δ, Δ, $\mathcal{E}^{\mathrm{nr}}$, and/or $\partial\mathcal{E}^{\mathrm{nr}}/\partial z(y)$) did not drift to large values, these slopes were monitored at regular intervals throughout eEDM data collection, every three hours (Fig. 2.5.1).

Finally, the ambient values of $\partial\mathcal{B}_z/\partial z(y)$ during the eEDM data set were minimized to below 1μG/cm using the experiment $\mathcal{B}$-field coils (Fig. 3.1.1). These field gradients were monitored twice daily using *in situ* magnetometers near the molecular beam; additional offline measurements were made before and after the eEDM data set by translating magnetometers along the molecular beam path.

We include in the systematic error budget (Table 5.1.2) a contribution calculated from the values of the measured systematic slope $S_{\partial\mathcal{B}_z/\partial z(y)}$ and the measured ambient $\partial\mathcal{B}_z/\partial z(y)$.

5.5 STIRAP $\tilde{\mathcal{N}}\tilde{\mathcal{E}}$-correlated phase

Another parameter that contributes to systematic shifts is associated with an ellipticity gradient across the spatial profile of the STIRAP $H-C$ laser beam. In practice, we control the size of the ellipticity gradient by using a half-waveplate to change the angle, $\theta_{\mathrm{ST}}^{H-C}$, between the original polarization of the $H-C$ laser and the average birefringence axis.

5.5.1 Mechanism

The systematic shift in the precession frequency, $\omega_{\mathrm{ST}}^{\mathcal{NE}}$, is associated with a rotation of the STIRAP prepared spin-aligned state. The effect is analogous to that observed in ACME I, which occured due to a combination of a birefringence gradient and residual $\mathcal{E}^{\mathrm{nr}}$. In ACME II, the systematic effect occurs in the STIRAP $H-C$ 1090 nm Stokes laser beam, rather than in the pump beam in ACME I. The detailed mechanism leading to the source

systematic error in ACME I is described above in Section 5.3.1 and previous publications [5, 6].

The $H - C$ STIRAP laser beam can acquire an ellipticity component if this beam's original polarization axis does not lie along the axis of undesired birefringence of optical elements in the path of the laser beam (e.g., vacuum chamber windows or beam shaping optics), i.e. $\theta_{\mathrm{ST}}^{H-C} \neq 0$. Spatial non-uniformity across the area of the laser beam of this birefringence leads to an ellipticity gradient in the laser beam.

This ellipticity gradient causes a shift in the precession frequency, ω_{ST}, which is linear in $\theta_{\mathrm{ST}}^{H-C}$ for small angles, due to AC Stark shift effects [5, 6]. This frequency shift, in turn, is proportional to the STIRAP 2-photon detuning, δ. If δ has an $\mathcal{N}\mathcal{E}$-correlated component, $\delta^{\mathcal{N}\mathcal{E}}$, this effect will cause a STIRAP-prepared $\tilde{\mathcal{N}}\tilde{\mathcal{E}}$-correlated spin precession frequency component,

$$\omega_{\mathrm{ST}}^{\mathcal{N}\mathcal{E}} = \frac{\partial \omega_{ST}^{\mathcal{N}\mathcal{E}}}{\partial \theta_{\mathrm{ST}}^{H-C}} \theta_{\mathrm{ST}}^{H-C}. \tag{5.29}$$

The $\tilde{\mathcal{N}}\tilde{\mathcal{E}}$-correlated detuning component, $\delta^{\mathcal{N}\mathcal{E}}$ can arise from $\mathcal{E}^{\mathrm{nr}}$, which causes $\tilde{\mathcal{N}}\tilde{\mathcal{E}}$-correlated Stark shifts with associated laser detunings $\delta^{\mathcal{N}\mathcal{E}} = D_H \mathcal{E}^{\mathrm{nr}}$ (see Section 5.3).

The refinement laser minimizes the slope $S_{\theta_{\mathrm{ST}}^{H-C}} = \partial \omega^{\mathcal{N}\mathcal{E}} / \partial \theta_{\mathrm{ST}}^{H-C}$ by reprojecting the STIRAP-prepared spin alignment, $\vec{S}_{\mathrm{ST}}$, along the polarization axis of the refinement beam, $\vec{\epsilon}_{\mathrm{ref}}$. The slope is given by

$$S_{\theta_{\mathrm{ST}}^{H-C}} = \frac{\partial \omega_{\mathrm{ST}}^{\mathcal{N}\mathcal{E}} / \partial \theta_{\mathrm{ST}}^{H-C}}{A_{\mathrm{ref}}}, \tag{5.30}$$

where

$$A_{\mathrm{ref}} = \frac{1}{\partial \omega^{\mathcal{N}\mathcal{E}} / \partial \omega_{\mathrm{ST}}^{\mathcal{N}\mathcal{E}}} \tag{5.31}$$

is a factor we refer to as the refinement attenuation. Its value depends on the properties of the refinement laser beam (power, spatial profile, and detuning).

5.5.2 Attenuation factor

The attenuation factor provided by the refinement laser beam can be increased by using higher laser power. A simple integration of the Schrodinger equation can give us an idea about the functional form of the dependence of attenuation on laser power. We use a coordinate system in which the refinement laser polarization is aligned along $\hat{x}$, $\vec{\epsilon}_{\rm ref} = \hat{x}$. If the STIRAP $H-C$ laser is linearly polarized at an angle $\theta_{\rm ST}^{\rm ref}$ with respect to the refinement laser polarization, the state prepared by the STIRAP laser beam is given by

$$|\psi_{\rm ST}\rangle = |X\rangle + \theta_{\rm ST}^{\rm ref}|Y\rangle. \tag{5.32}$$

The interaction between the ThO molecule $H-I$ transition and the refinement beam is desribed by the two level Hamiltonian

$$\mathrm{H} = \begin{pmatrix} \Delta - i\frac{\gamma_I}{2} & \Omega_2 & 0 \\ \Omega/2 & 0 & 0 \\ 0 & 0 & 0 \end{pmatrix} \begin{bmatrix} |I\rangle \\ |Y\rangle \\ |X\rangle \end{bmatrix} \tag{5.33}$$

After the optical pumping performed by the refinement laser, the initial state $|\psi_{\rm ST}\rangle$ has evolved under H to

$$|\psi_{\rm ref}\rangle = |X\rangle + \theta_{\rm ref}|Y\rangle, \tag{5.34}$$

where $\theta_{\rm ref}$ is given by the initial refinement- STIRAP polarization misalignment angle, $\theta_{\rm ST}^{\rm ref}$, reduced by the attenuation factor $A_{\rm ref}$,

$$\theta_{\rm ref} = \theta_{\rm ST}^{\rm ref}/A_{\rm ref}. \tag{5.35}$$

We can solve the Schrodinger equation analytically if we make the assumption that the laser beams are flat topped (such that H is time-invariant). This choice captures qualitatively

the dynamics that we observed in our experiment. If required, numerical integration over a Gaussian intensity profile can give a more accurate model of our current experimental system. For interaction time δt, we can calculate

$$A_{\text{ref}} \equiv \frac{\theta_{\text{ref}}}{\theta_{\text{ST}}^{\text{ref}}} = \frac{Re[\langle Y|\psi_{\text{ref}}\rangle]}{\theta_{\text{ST}}^{\text{ref}}} \tag{5.36}$$

$$= \text{Re}\left[e^{-\Delta_e \delta t/2}\left\{\cosh\left(\frac{\Omega_e \delta t}{2}\right) + \frac{\Delta_e}{\Omega_e}\sinh\left(\frac{\Omega_e \delta t}{2}\right)\right\}\right], \tag{5.37}$$

where

$$\Delta_e = \gamma_I/2 + i\Delta, \tag{5.38}$$

$$\Omega_e = \sqrt{\Delta_e^2 - \Omega^2}. \tag{5.39}$$

This leads to a dependence of attenuation on power that has two components: one oscillatory and one exponential. The frequency of the oscillatory component is given by the Rabi frequency and detuning used in the experimental system. Due to the oscillatory component, the attenuation can reach a negative value at specific values of laser power.

To measure attenuation, we apply a large component of $\omega_{\text{ST}}^{\mathcal{NE}}$ by using a larger value of θ_{ST}^{H-C} and measure the attenuated frequency component, $\omega^{\mathcal{NE}} = \omega_{\text{ST}}^{\mathcal{NE}}/A_{\text{ref}}$. We measure attenuation as a function of refinement beam laser power and observe a strong exponential component overlapped with an oscillatory component (see Figure 5.5.1), consistent with the analytical model described above.

5.5.3 Reduction and monitoring

At regular intervals throughout the eEDM dataset (Fig. 2.5.1), we measured the slope $S_{\theta_{\text{ST}}^{H-C}}$ by applying a large θ_{ST}^{H-C} (which leads to a large value of $\omega_{\text{ST}}^{\mathcal{NE}}$) and measuring the value of $\omega^{\mathcal{NE}}$ that survives refinement, as shown in Figure 5.5.2. This value is consistent

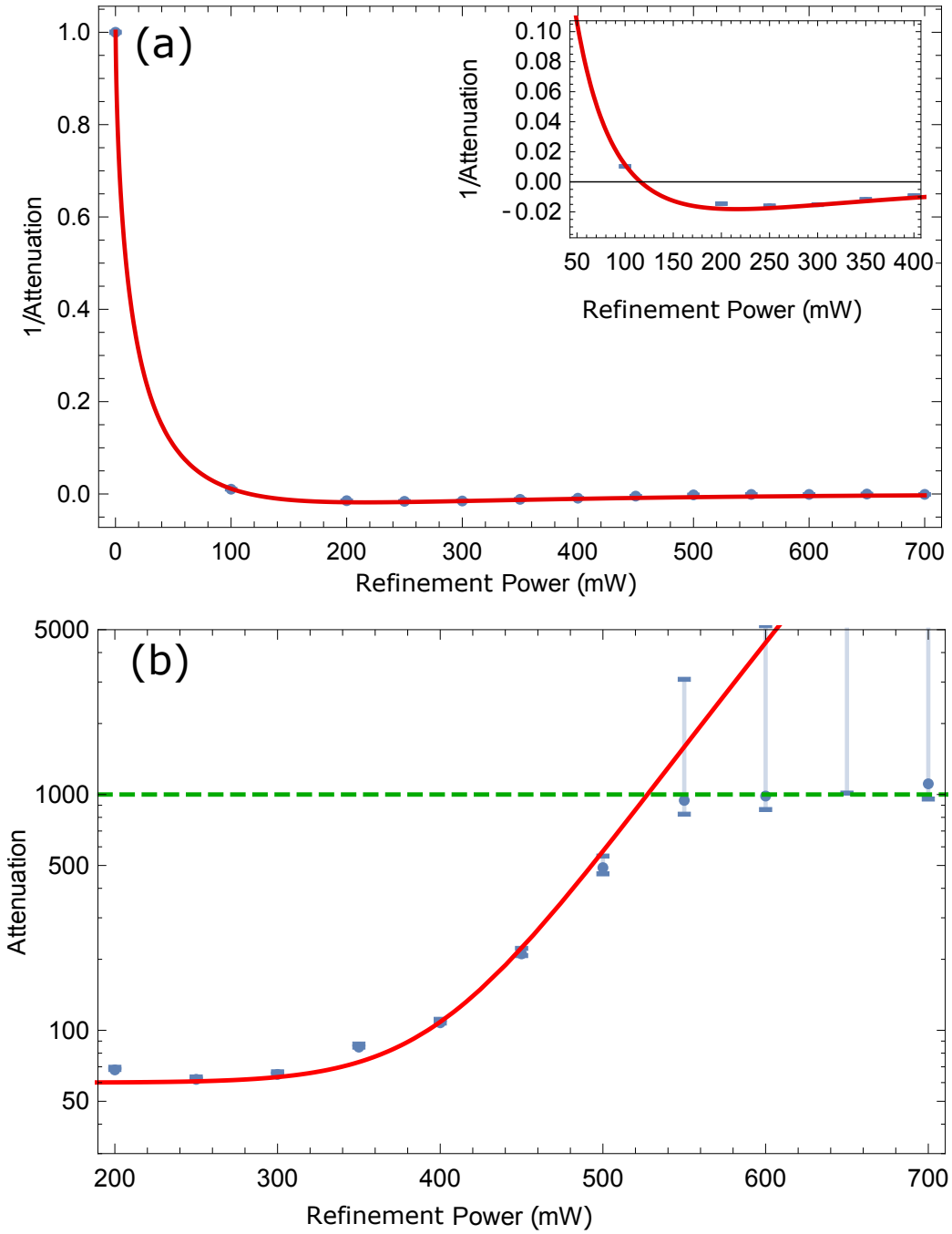

Figure 5.5.1: **Measured dependence of A_{ref} on refinement laser power.** Dependence of **(a)** $1/A_{\text{ref}}$ and **(b)** A_{ref} as a function of laser power in the refinement beam. The inset in **(a)** shows the same data, focusing on the oscillatory component of the attenuation, which can cause the attenuation to become negative. The green dashed lines in **(b)** show the level of uncertainty of our phase precession measurement which limits our possibility of measuring uncertainties in excess of $A_{\text{ref}} \sim 1000$.

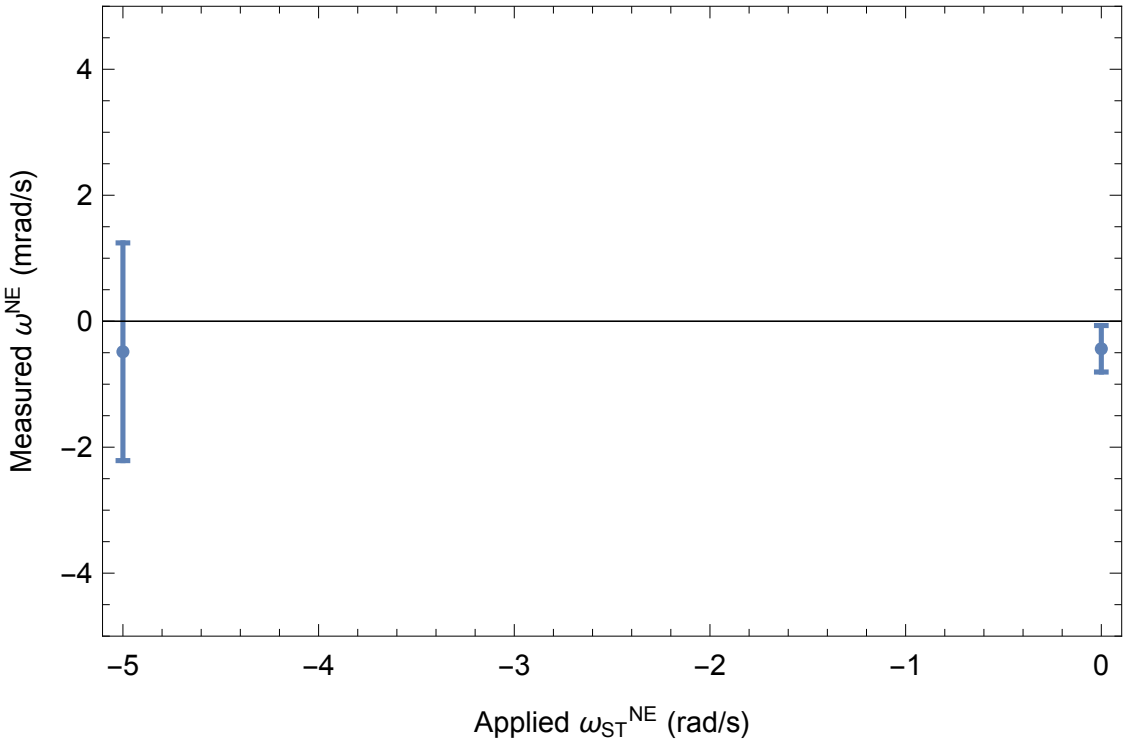

Figure 5.5.2: **Measurement limiting the contribution to $\omega^{\mathcal{NE}}$ due to $\omega_{\mathrm{ST}}^{\mathcal{NE}}$.** Data showing no significant difference between when there is no applied $\omega_{\mathrm{ST}}^{\mathcal{NE}}$ and when we a apply a large imperfection, $\omega_{\mathrm{ST}}^{\mathcal{NE}} = -5$ rad/s. This allows us to place a limit on the contribution of this systematic error to $\omega^{\mathcal{NE}}$ for typical experiment values of $\omega_{\mathrm{ST}}^{\mathcal{NE}}$. Error bars correspond to 1σ (68%) confidence intervals.

with 0, directly bounding the attenuation under ordinary conditions to $A_{\mathrm{ref}} > 10^4$.

By tuning the power of the refinement laser, P_{ref}, to zero such that $A_{\mathrm{ref}} = 1$, we observed a contribution to the precession frequency associated with the STIRAP state preparation laser beams, ω_{ST}. Consistent with the ellipticity gradient model described above, under these conditions we also observed an $\tilde{\mathcal{N}}\tilde{\mathcal{E}}$-correlated component, $\omega_{\mathrm{ST}}^{\mathcal{NE}}$, resulting from the combination of the AC Stark shift effects and a nonzero $\delta^{\mathcal{NE}}$ (caused by the residual, ambient $\mathcal{E}^{\mathrm{nr}}$). The slope $\partial\omega_{\mathrm{ST}}^{\mathcal{NE}}/\partial\theta_{\mathrm{ST}}^{H-C}$ was calibrated by setting $P_{\mathrm{ref}} = 0$ and measuring the dependence of $\omega_{\mathrm{ST}}^{\mathcal{NE}}$ on an exaggerated $\theta_{\mathrm{ST}}^{H-C}$ (Fig. 5.5.3).

We then measure the value of $\theta_{\mathrm{ST}}^{H-C}$ by using the relation

$$\theta_{\mathrm{ST}}^{H-C} = \frac{\omega_{\mathrm{ST}}^{\mathcal{NE}}}{\partial\omega_{\mathrm{ST}}^{\mathcal{NE}}/\partial\theta_{\mathrm{ST}}^{H-C}}. \tag{5.40}$$

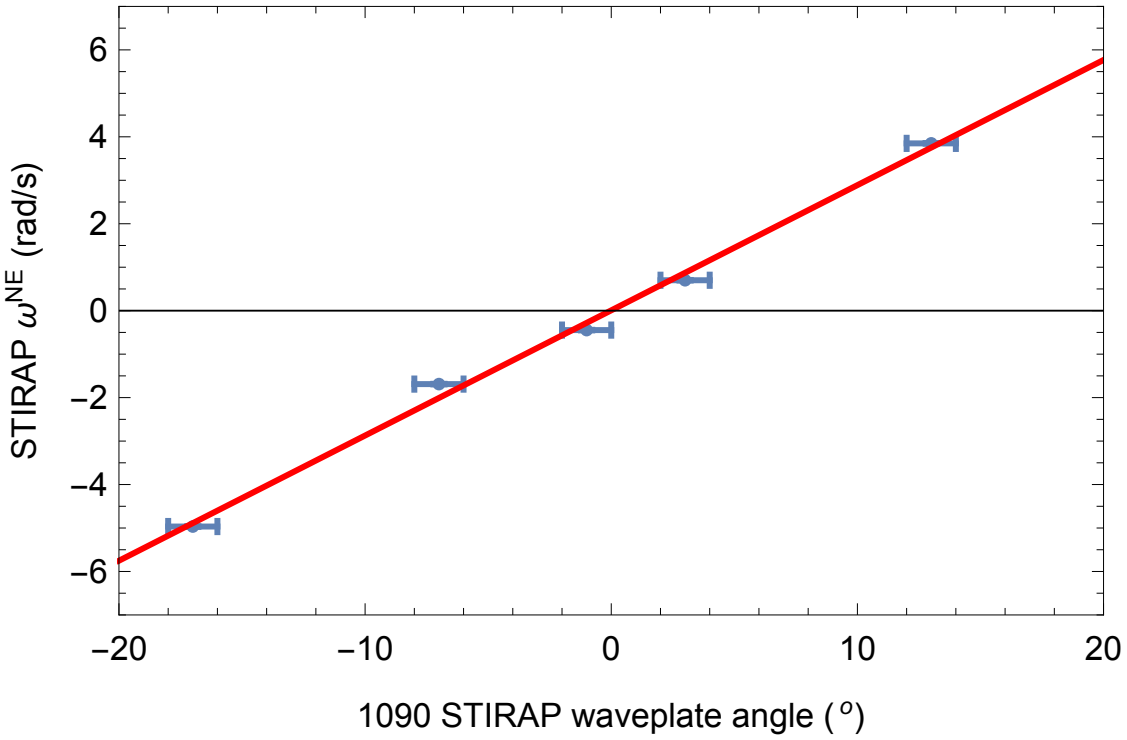

Figure 5.5.3: **Dependence of $\omega_{\rm ST}^{\mathcal{N}\mathcal{E}}$ on the 1090 STIRAP waveplate angle, $\theta_{\rm ST}^{H-C}$.** Dependence of $\omega_{\rm ST}^{\mathcal{N}\mathcal{E}}$ on $\theta_{\rm ST}^{H-C}$ with linear fit (red line). This measurement was performed with the refinement laser beam blocked, at zero power, $P_{\rm ref} = 0$. Error bars correspond to 1σ (68%) confidence interval. The vertical error bars are smaller than the markers.

To minimize the ellipticity gradient, we set $\theta_{\rm ST}^{H-C}$ to the value found to minimize $\omega_{\rm ST}^{\mathcal{N}\mathcal{E}}$ (Fig. 5.5.3). Both $\omega_{\rm ST}^{\mathcal{N}\mathcal{E}}$ and the slope $S_{\theta_{\rm ST}^{H-C}}$ were monitored at regular intervals throughout the eEDM dataset (Fig. 2.5.1). The measured values of the systematic slope $S_{\theta_{\rm ST}^{H-C}}$ and residual $\theta_{\rm ST}^{H-C}$ were used to compute the contribution to the systematic error budget (Table 5.1.2).

5.6 Correlated power, $P^{\mathcal{N}\mathcal{E}}$

Another parameter that contributes to a systematic shift is an $\tilde{\mathcal{N}}\tilde{\mathcal{E}}$-correlated component of the power of the refinement beam, defined by

$$P_{\rm ref} = P_{\rm ref}^{\rm nr} + \tilde{\mathcal{N}}\tilde{\mathcal{E}} P_{\rm ref}^{\mathcal{N}\mathcal{E}}. \tag{5.41}$$

In ACME I, we never directly observed the presence of a $P^{\mathcal{NE}}$ in the laser beams. However, there were indirect measurements that pointed towards the presence of such a correlated power component. Due to AC Stark shift effects [5, 6], the $\omega^{\mathcal{NEB}}$ channel has a strong linear dependence on $P^{\mathcal{NE}}_{\text{ref}}$. In ACME I, the $\omega^{\mathcal{NEB}}$ channel had a non-zero offset, which could be caused by a $P^{\mathcal{NE}}/P^{\text{nr}} \approx 0.017 \pm 0.002$, that changed sign with the direction of the lasers through the experiment, $\hat{k} \cdot \hat{z} = \pm 1$ [6].

In ACME II, we did not observe clear evidence of an $\tilde{\mathcal{N}}\tilde{\mathcal{E}}$-correlated power component, $P^{\mathcal{NE}}$. However, we observed a dependence of the $\omega^{\mathcal{NE}}$ channel on intentionally applied $P^{\mathcal{NE}}$ in the refinement beam, $P^{\mathcal{NE}}_{\text{ref}}$. As described below, a misalignment between the $\vec{\epsilon}_{\text{ref}}$ and $\vec{S}_{\text{ST}}$ polarization vectors, parametrized by misalignment angle $\theta^{\text{ref}}_{\text{ST}}$, leads to a nonzero value in the slope $S_{P^{\mathcal{NE}}_{\text{ref}}} = \partial\omega^{\mathcal{NE}}/\partial P^{\mathcal{NE}}_{\text{ref}}$.

5.6.1 Mechanism

The mechanism leading to the slope $S_{P^{\mathcal{NE}}_{\text{ref}}}$ is illustrated in Figure 5.6.1. We typically attempt to perfectly align $\vec{\epsilon}_{\text{ref}}$ with $\vec{S}_{\text{ST}}$. However, if the two vectors are misaligned by an angle $\theta^{\text{ref}}_{\text{ST}}$, the component of $\vec{S}_{\text{ST}}$ orthogonal to $\vec{\epsilon}_{\text{ref}}$ is reduced only by the factor A_{ref}; then the post-refinement spin alignment $\vec{S}$ will deviate from the ideal $\vec{\epsilon}_{\text{ref}}$ axis by an angle $\approx \theta^{\text{ref}}_{\text{ST}}/A_{\text{ref}}$.

As shown in Section 5.5.2, A_{ref} is dependent on the power of the refinement laser, P_{ref}. A small, perturbative, variation of the refinement power power, $\mathrm{d}P_{\text{ref}}$, causes a linear shift in the prepared phase

$$\mathrm{d}\omega_{\text{ref}} = -\frac{\theta^{\text{ref}}_{\text{ST}}}{A^2_{\text{ref}}}\frac{\partial A_{\text{ref}}}{\partial P_{\text{ref}}}\frac{\mathrm{d}P_{\text{ref}}}{\tau}. \tag{5.42}$$

Furthermore, if P_{ref} has an $\tilde{\mathcal{N}}\tilde{\mathcal{E}}$-correlated component, $P^{\mathcal{NE}}_{\text{ref}}$, this mechanism will cause a shift in $\omega^{\mathcal{NE}}$. To confirm this model, we verified that when deliberately applying a $P^{\mathcal{NE}}_{\text{ref}}$, in the presence of a large $\theta^{\text{ref}}_{\text{ST}}$, we observe the expected slope $S_{P^{\mathcal{NE}}_{\text{ref}}} = \partial\omega^{\mathcal{NE}}/\partial P^{\mathcal{NE}}_{\text{ref}}$.

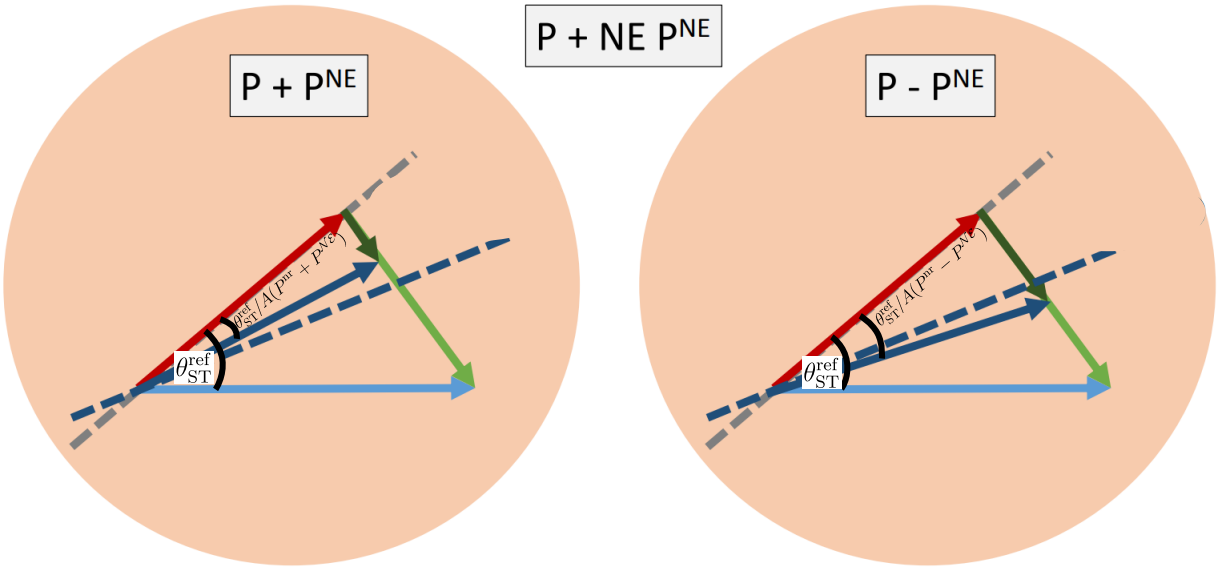

Figure 5.6.1: **Mechanism causing a dependence of $\omega^{\mathcal{NE}}$ on refinement laser $P^{\mathcal{NE}}$.** The systematic arises when the STIRAP prepared spin-aligned state (light blue arrows), $\vec{S}_{\mathrm{ST}}$, and the polarization of the refinement laser beam (red arrows), $\vec{\epsilon}_{\mathrm{ref}}$ are misaligned by an angle $\theta_{\mathrm{ST}}^{\mathrm{ref}}$. The component of $\vec{S}_{\mathrm{ST}}$ that is orthogonal to $\vec{\epsilon}_{\mathrm{ref}}$ (light green arrows) is reduced by the factor A_{ref}, such that the post-refinement spin alignment $\vec{S}$ (dark blue arrows) deviates from the ideal $\vec{\epsilon}_{\mathrm{ref}}$ axis by $\theta_{\mathrm{ST}}^{\mathrm{ref}}/A_{\mathrm{ref}}$. A_{ref} is dependent on the power of the refinement laser beam and an $\tilde{\mathcal{N}}\tilde{\mathcal{E}}$-correlated component of this laser power, $P^{\mathcal{NE}}$ leads to the systematic slope $S_{P_{\mathrm{ref}}^{\mathcal{NE}}}$. As shown above, the orientation of $\vec{S}$ (dark blue arrows) depends on the $\tilde{\mathcal{N}}\tilde{\mathcal{E}}$ state of the experiment.

5.6.2 Reduction and monitoring

For the eEDM dataset, we minimized the magnitude of $S_{P_{\mathrm{ref}}^{\mathcal{NE}}}$ by tuning $\theta_{\mathrm{ST}}^{\mathrm{ref}}$ to zero via a half-waveplate in the refinement laser beam. We did not observe clear evidence of a nonzero $P_{\mathrm{ref}}^{\mathcal{NE}}$ component in our eEDM dataset. However, we put a limit on its possible size throughout the eEDM dataset by placing bounds on the offset of $\omega^{\mathcal{NEB}}$, which has a strong linear dependence on $P_{\mathrm{ref}}^{\mathcal{NE}}$ due to AC Stark shift effects [5, 6]. The $\partial\omega^{\mathcal{NE}}/\partial P_{\mathrm{ref}}^{\mathcal{NE}}$ slope was monitored regularly throughout the eEDM dataset (Fig. 2.5.1e). We use the measured upper limit of $P_{\mathrm{ref}}^{\mathcal{NE}}$ and the value of $\partial\omega^{\mathcal{NE}}/\partial P_{\mathrm{ref}}^{\mathcal{NE}}$ to calculate a contribution to the systematic error budget (Table 5.1.2).

5.7 Correlated contrast: $\mathcal{C}^{\mathcal{NE}}$, $\mathcal{C}^{\mathcal{NEB}}$

The next contribution to systematic error arises from imperfections in the spin measurement contrast, $\mathcal{C}$. As part of the ACME II analysis, we checked for correlations between the $\omega^{\mathcal{NE}}$ channel and the other experimental channels and parameters, which are described in detail in Section 5.16. We observed correlations $S_{|\mathcal{C}|^u} = \partial\omega^{\mathcal{NE}}/\partial|\mathcal{C}|^u$ of $\omega^{\mathcal{NE}}$ with two contrast channels: $|\mathcal{C}|^{\mathcal{NE}}$ and $|\mathcal{C}|^{\mathcal{NEB}}$.

5.7.1 Mechanism

We calculate the eEDM frequency by extracting the $\tilde{\mathcal{N}}\tilde{\mathcal{E}}$-correlated component from the ratio of asymmetry to contrast, $\omega^{\mathcal{NE}} \approx [\mathcal{A}/(2\mathcal{C})]^{\mathcal{NE}}/\tau$. A first-order expansion of $\omega^{\mathcal{NE}}$ in terms of the individual parity components of all associated quantities results in

$$\omega^{\mathcal{NE}} \approx \frac{(\mathcal{A}\ \mathrm{sgn}(\mathcal{C}))^{\mathcal{NE}}}{2\tau|\mathcal{C}|^{\mathrm{nr}}} - \omega^{\mathcal{B}}\frac{|\mathcal{C}|^{\mathcal{NEB}}}{|\mathcal{C}|^{\mathrm{nr}}} - \omega^{\mathrm{nr}}\frac{|\mathcal{C}|^{\mathcal{NE}}}{|\mathcal{C}|^{\mathrm{nr}}} + ..., \tag{5.43}$$

where we used the fact that $|\mathcal{C}|^{\mathrm{nr}} \gg |\mathcal{C}|^u$ for any other parity component u. We looked for possible contributions from any other phase parity component channels, ω^u (not only those shown in Eq. 5.43), by searching the eEDM dataset for nonzero correlations between $\omega^{\mathcal{NE}}$ and $|\mathcal{C}|^u$, quantified by a nonzero value of the slope $S_{|\mathcal{C}|^u} = \partial\omega^{\mathcal{NE}}/\partial|\mathcal{C}|^u$ (see Section 5.16). We have observed such correlations only with two channels: $|\mathcal{C}|^{\mathcal{NE}}$ and $|\mathcal{C}|^{\mathcal{NEB}}$. This is consistent with the fact that only $\omega^{\mathcal{B}}$ and ω^{nr} have large values; these are due to $\mathcal{B}$-field precession and global offset phases, respectively.

5.7.2 Monitoring and contribution to systematic budget

The average values $\langle|\mathcal{C}|^{\mathcal{NE}}\rangle$ and $\langle|\mathcal{C}|^{\mathcal{NEB}}\rangle$ of the corresponding contrast channels are consistent with zero in the eEDM dataset. Furthermore, since we perform our analysis by dividing asymmetry by contrast state by state (see Section 4.2), contrast correlations are

removed to first order [6]. To be conservative, we still include in our error budget a limit on their possible contributions extracted from $S_{|\mathcal{C}|^{\mathcal{N}\mathcal{E}}}$ ($S_{|\mathcal{C}|^{\mathcal{N}\mathcal{E}\mathcal{B}}}$) and $\langle|\mathcal{C}|^{\mathcal{N}\mathcal{E}}\rangle$ ($\langle|\mathcal{C}|^{\mathcal{N}\mathcal{E}\mathcal{B}}\rangle$) (Table 5.1.2).

5.8 $\omega^{\mathcal{E}}$ CONTRIBUTIONS

Another contribution to the systematic error bar came from $\omega^{\mathcal{E}}$. Previous eEDM measurements have often been limited by a number of effects that would have produced an $\tilde{\mathcal{E}}$-correlated frequency in our measurement [28, 43, 50, 65]. These effects could be caused by leakage current, motional magnetic field ($\vec{v}\times\vec{\mathcal{E}}$), and geometric phase effects.

Such effects are suppressed in the ACME experiment by performing the additional $\tilde{\mathcal{N}}$ switch, which allows us to reverse the molecular orientation spectroscopically. The reversal of $\tilde{\mathcal{N}}$ does not, however, entirely eliminate a shft in the EDM-like phase due to $\omega^{\mathcal{E}}$. As discussed previously (see Section 4.4), there is a small and electric-field dependent difference between the $g-$factors of the two $\tilde{\mathcal{N}}$ levels, which means that a non-zero offset in the $\omega^{\mathcal{E}}$ channel also leaks into $\omega^{\mathcal{N}\mathcal{E}}$ at a lower level, with a contribution of

$$\omega^{\mathcal{N}\mathcal{E}}_{\omega^{\mathcal{E}}} = \frac{\eta\mathcal{E}}{g_H}\omega^{\mathcal{E}}. \tag{5.44}$$

To measure the slope $S_{\omega\mathcal{E}} = \partial\omega^{\mathcal{N}\mathcal{E}}/\partial\omega^{\mathcal{E}}$, we apply an $\tilde{\mathcal{E}}$-correlated component of the $\mathcal{B}$-field, $\mathcal{B}_z^{\mathcal{E}}$, which creates a large artificial $\omega^{\mathcal{E}}$. $S_{\omega\mathcal{E}}$ measures the suppression of any residual value of $\omega^{\mathcal{E}}$ by the $\tilde{\mathcal{N}}$ switch [64, 65]. As shown in Figure 5.8.1 the suppression factor of $\sim 660\pm65$ is consistent with that expected from the measurement of η of $\eta\mathcal{E}/g_H = 710\pm30$ (see Section 4.4).

The mean value of $\omega^{\mathcal{E}}$ in the eEDM dataset, $\langle\omega^{\mathcal{E}}\rangle$, was measured to be consistent with zero. Furthermore, none of the parameters varied as part of the systematic checks were observed to significantly shift $\omega^{\mathcal{E}}$. We place a limit on possible contributions to the sys-

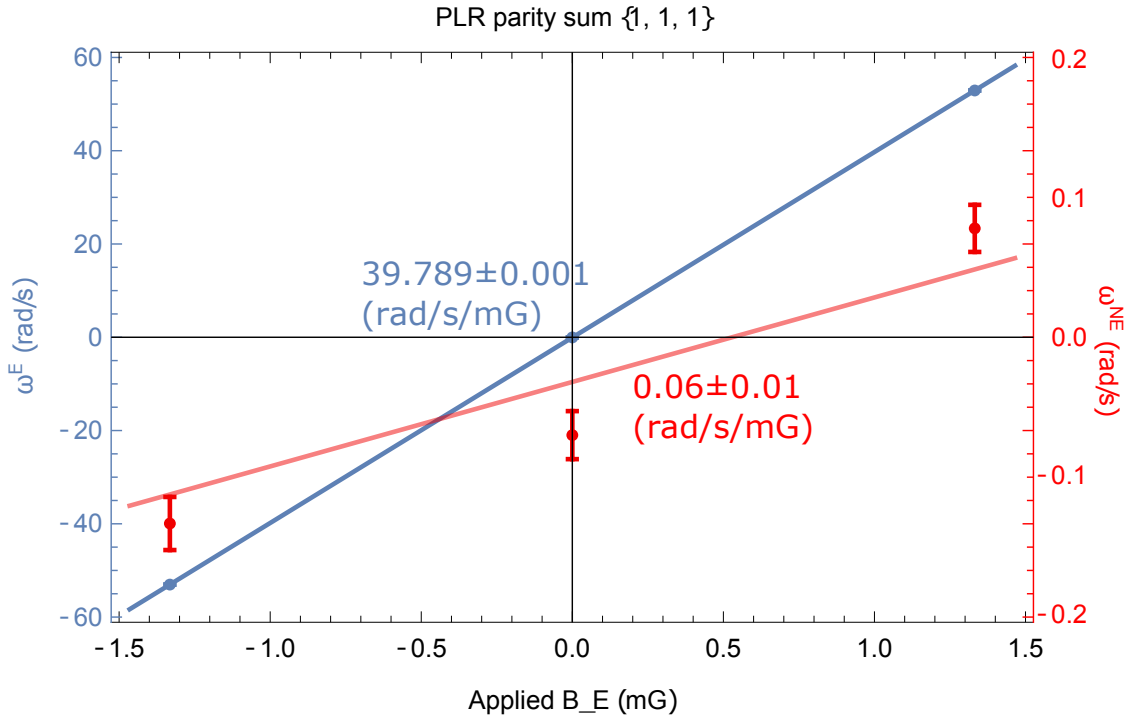

Figure 5.8.1: **Suppression of $\tilde{\mathcal{E}}$-correlated systematic effects by the $\tilde{\mathcal{N}}$ switch.** Blue data points and blue line show the large $\omega^{\mathcal{E}}$ frequency component intentionally created by applying a large $\tilde{\mathcal{E}}$-correlated component of the magnetic field, $\mathcal{B}_z^{\mathcal{E}}$. This large frequency $\omega^{\mathcal{E}}$ offse leads to a much smaller contribution to the $\omega^{\mathcal{N}\mathcal{E}}$ channel (red data points and red line), which is suppressed by a factor of 660 ± 65. This suppression factor is consistent with that expected from the difference in $g-$factors between the two $\tilde{\mathcal{N}}$ states, $\eta\mathcal{E}/g_H = 710 \pm 30$. Error bars correspond to 1σ (68%) confidence interval.

tematic errror budget from $\omega^{\mathcal{E}}$ effects from the measured values of $S_{\omega^{\mathcal{E}}}$ and $\langle\omega^{\mathcal{E}}\rangle$ (Table 5.1.2).

5.8.1 Leakage current measurement

A shift in $\omega^{\mathcal{E}}$ could occur due to leakage current. A leakage current flow creates a magnetic field. If the current flow is due to the voltage applied to create the electric field, it might change direction with a reversal of $\tilde{\mathcal{E}}$. This type of effects could lead to an $\tilde{\mathcal{E}}-$correlated magnetic field component, $\mathcal{B}^{\mathcal{E}}$. As discussed above, such effects cause offsets in the $\omega^{\mathcal{E}}$ frequency channel. This effect also leads to a heavily suppressed contribution to the $\omega^{\mathcal{N}\mathcal{E}}$

channel due to different values of the magnetic moment of the two $\tilde{\mathcal{N}}$ states.

We can measure the leakage current directly with the ThO molecules by measuring the Stark shift the molecules incur when in an electric field, $\Delta_{\text{Stark}} = D_H \mathcal{E}$. For a parallel plate capacitor, $\mathcal{E} = V/d$, where V is the applied voltage and $d = 4.5$ cm is the separation between the field plates. Voltage V is related to leakage charge through $C = Q/V$, where C is the field plate capacitance and Q is the electric charge. We compute the field plate capacitance from the geometry of the field plates (for area of 100 cm^2 and distance of 4.5 cm) of $C = 20$ pF. We can then extract the leakage current from:

$$I_{\text{leak}} = \frac{\partial Q}{\partial t} = C\frac{\partial V}{\partial t} \tag{5.45}$$

$$= C\frac{d}{D_H}\frac{\partial \Delta_{\text{Stark}}}{\partial t}. \tag{5.46}$$

We extract the Stark shift, Δ_{Stark}, by measuring the resonant frequency of the readout laser. We use the signal size as an indicator of the offset frequency from resonance. First, we calibrate the lineshape of signal as a function of electric field (Fig. 5.8.2a). We then disconnect the field plate supplies at the experiment (without grounding the field plates) and record the decrease in signal as a function of time. Using the previous calibration function and the distance between the electric field plates, we plot the potential drop as a function of time (Fig. 5.8.2b).

The sensitivity of this measurement drops fast when we are near the edges of the lineshape, but we can extract a linear slope in the center with a value of ~ 1.2 V/s. We then use Eq. 5.46 to compute the leakage current $I_{\text{leak}} \sim 25$ pA. At the $V = 360$ V potential, this I_{leak} corresponds to a leakage resistance of $R_{\text{leak}} \sim 10$ TΩ.

We can roughly estimate the magnitude of the magnetic field this current could create in a particularly bad current flow geometry. For example, in a Helmholz coil configuration with one turn and radius of 0.2 meters, the magnetic field at the center is approx-

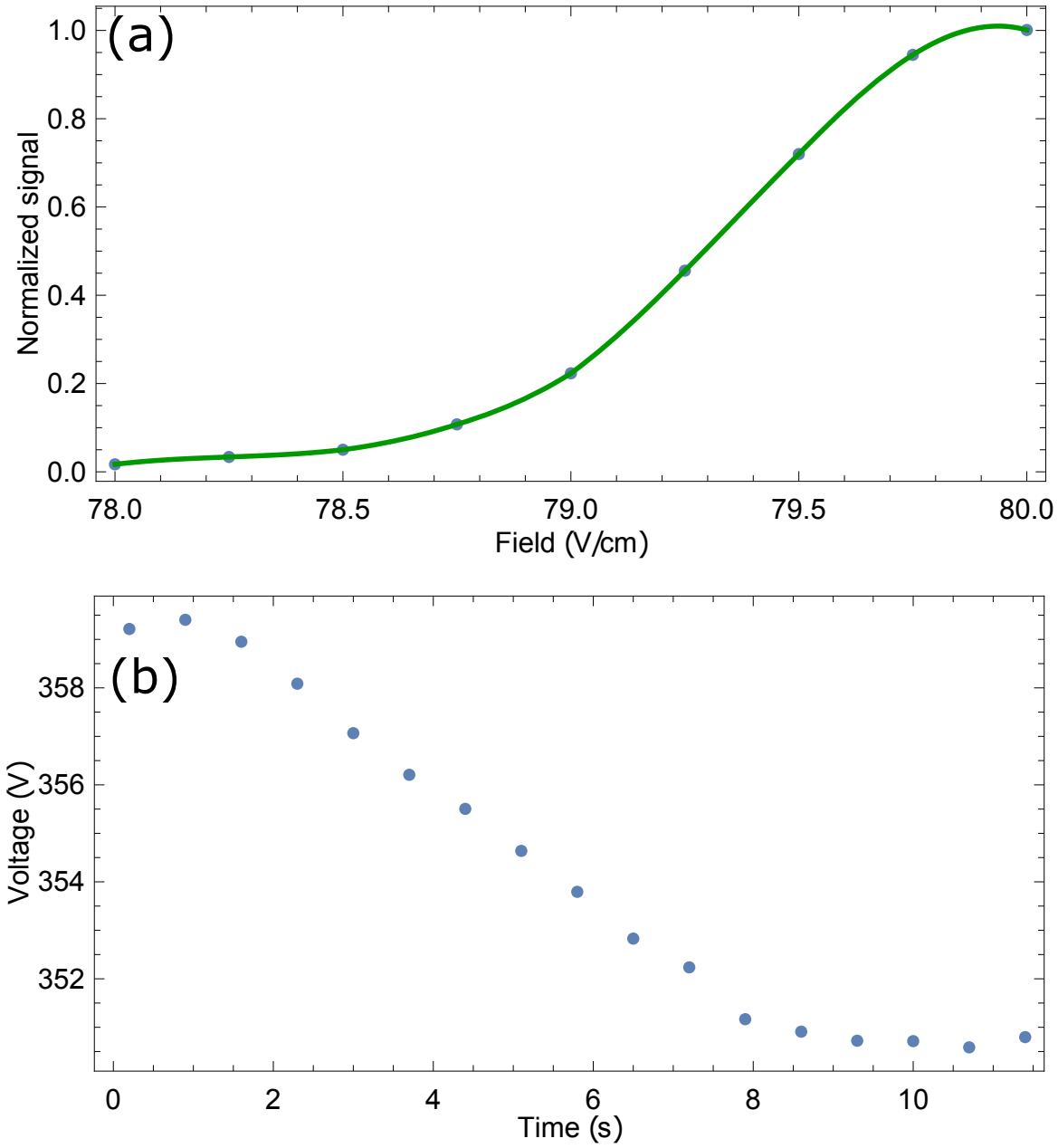

Figure 5.8.2: **Measurement of the leakage current.** **(a)** Calibration of the measurement lineshape, showing normalized molecular signal as a function of detuning due to the Stark shift caused by the electric field being away from the nominal 80 V/cm value. **(b)** Measurement of leakage current performed by measuring the decrease in signal over time, recalibrated using **(a)** to show decrease in voltage over time.

imately 1 pGauss. Such a field would create a magnetic precession in the experiment of $\sim 5 \cdot 10^{-8}$ rad/s, which is many orders of magnitude smaller than the ACME II statistical sensitivity of $\sim 5 \cdot 10^{-4}$ rad/s. We have not seen any indication of a shift in the $\omega^{\mathcal{E}}$ frequency channel due to leakage current or other effects.

5.9 Magnetic field imperfections

The ACME II measurement is build with a set of coils that allow us to apply magnetic fields in all three spatial dimensions and all 6 possible first order gradients (Section 3.5.4). The coils are constructed in a geometry that allows us to apply all field components independently of one another. This capability makes identifying systematic errors due to one specific parameter much easier. The applied fields can typically be factors of 100-1000 times larger than the usual residual fields in the ACME II running experiment configuration. Being able to exaggerate these imperfections by large factors compared to the usual residual fields allowed us to limit their possible systematic error contributions to be smaller than the experiment statistical uncertainty.

To look for magnetic field related systematic effects, we apply both $\tilde{\mathcal{B}}$-correlated and $\tilde{\mathcal{B}}$-uncorrelated magnetic field offsets and gradients and measure their effect on $\omega^{\mathcal{N}\mathcal{E}}$. The applied imperfections are: residual (non-reversing) $\mathcal{B}$-fields (along all 3 directions), all additional possible first order $\mathcal{B}$-field gradients ($\partial\mathcal{B}_x/\partial x$, $\partial\mathcal{B}_y/\partial y$, $\partial\mathcal{B}_y/\partial x$, $\partial\mathcal{B}_z/\partial x$). Since we observed shifts in $\omega^{\mathcal{N}\mathcal{E}}$ with two magnetic field gradients, $\partial\mathcal{B}_z/\partial z, \partial\mathcal{B}_z/\partial y$, we compute error bar contributions due to all magnetic field parameters and include them in the systematic error bar (Table 5.1.2).

5.10 Electric field imperfections

Unlike for the magnetic field, we are not able to control electric field gradients and offsets with the exception of the $\mathcal{E}^{\mathrm{nr}}$ average value. However, we were able to carefully monitor

the electric field configuration using microwave spectroscopy [6] (see Section 3.5.3). In addition, to search for systematic errors related to the electric field, we acquired equal amounts of eEDM data with two different electric field magnitudes ($1\mathcal{E}, 2\mathcal{E}$) and did not observe variation between the two configurations (see Section 4.3).

In addition, we applied a voltage offset common to both field plates and looked for shifts in any of the experiment frequency channels. Despite being two orders of magnitude larger than that present in the experiment under typical running conditions, this parameter did not shift $\omega^{\mathcal{NE}}$. Since we did not have a good reason for how this parameter could cause a systematic shift in $\omega^{\mathcal{NE}}$, we did not include it in the systematic error bar.

5.11 Laser imperfections

The refinement and readout lasers prepare and read out the precession phase, so imperfections in their parameters can be sources of systematic error. Furthermore, changes in the parameters of the rotational cooling, STIRAP or ablation lasers can also affect the level of usable molecular flux. We therefore varied all possible experiment laser parameters and looked for effects in $\omega^{\mathcal{NE}}$.

5.11.1 Laser detuning

We typically control the experiment detunings by tuning the frequency of our lasers with AOMs and recording the resulting fluorescence signal. We then set the lasers "on resonance", where the resulting fluorescence is maximized. The lasers are locked to ULE cavities, which have linear, slow, mechanical drifts of 7 kHz/day which are calibrated with a frequency comb and subtracted using AOMs. The largest detuning variation is caused by pointing variations in the laser beams and variation in the separation between the electric field plates. We estimate such variations might cause detuning noise with an amplitude that is smaller than 100 kHz.

As described in detail in Section 5.4, both the detunings of the STIRAP lasers and readout laser can couple to applied $\partial\mathcal{B}_z/\partial z$ and $\partial\mathcal{B}_z/\partial y$ magnetic field gradients and gradients in $\mathcal{E}^{\mathrm{nr}}$ to cause significant shifts in $\omega^{\mathcal{NE}}$. However, this effect is only statistically significant when large magnetic field gradients are applied. To account for this systematic effect and other new possible ones, we exaggerate the detunings of the refinement, readout, both 1-photon and 2-photon detuning of the STIRAP lasers and detunings of the rotational cooling lasers. In addition, we apply detuning components that are correlated with experimental switches, $\Delta^{\mathcal{N}}$, $\Delta^{\mathcal{P}}$, and $\Delta^{\mathcal{NE}}$ (which simulates $\mathcal{E}^{\mathrm{nr}}$). Most of these detunings were modified in the range where the efficiency of state preparation and readout was high enough such that the experiment usable molecular flux was not modified by more than a factor of 2. We typically intentionally apply detuning offsets of up to $2\pi \times (2-3)$ MHz. Under typical running parameters, we observed no dependence of $\omega^{\mathcal{NE}}$ on any of these parameters. We include contributions to the systematic error bar due to additional possible systematic effects related to the refinement/readout laser detunings, and a differential detuning between the two experimental $\tilde{\mathcal{N}}$ states, $\Delta^{\mathcal{N}}$ (Table 5.1.2).

We observed shifts correlated with variation in the detuning of the readout laser corresponding to asymmetry effects which are understood and explained in Section 5.15. These only appear in the $\tilde{\mathcal{P}}$ and $\tilde{\mathcal{R}}$ odd frequency channels and have no observed or expected contributions to $\omega^{\mathcal{NE}}$.

5.11.2 Laser pointing and position

Ideally, the propagation direction of the refinement and readout laser, $\hat{k}$, is parallel to the direction of the applied electric field, $\vec{\mathcal{E}}$. We typically align the refinement and readout laser beams with this axis by using the reflection of the ITO conductive layer on field plates as a guide, with an estimated accuracy of ~ 200 urad. We search for errors related to imperfect pointing by intentionally misaligning the refinement and readout lasers pointing by ~ 2 mrad. In addition, we also vary the relative pointing of the $\hat{X}$ and $\hat{Y}$ readout beams. We

typically tune the lasers back on resonance after each pointing misalignment, to decouple pointing and detuning effects. We did not observe a shift in $\omega^{\mathcal{NE}}$ with variation in any pointing parameters.

In addition, we shifted the position of the refinement laser beam by 2 mm downstream (in the $+\hat{x}$ direction). This reduces the length of the precession distance and changes the properties of the glass that the refinement laser passes through. We did not observe a variation of $\omega^{\mathcal{NE}}$ with this change.

We observed shifts correlated with variation of the relative pointing between the $\hat{X}$ and $\hat{Y}$ readout laser beams, corresponding to asymmetry effects which are understood and explained in Section 5.15. These only appear in the $\tilde{\mathcal{P}}$ and $\tilde{\mathcal{R}}$ odd frequency channels and have no observed or expected contributions to $\omega^{\mathcal{NE}}$.

5.11.3 Laser polarization

As described above in Section 5.6, a possible $\tilde{\mathcal{N}}\tilde{\mathcal{E}}$-correlated component of the refinement laser power, $P_{\text{ref}}^{\mathcal{NE}}$, can combine with a misalignment between the STIRAP prepared spin alignment and refinement laser polarization to create a systematic shift. We tune the polarization of the refinement laser beam to minimize this effect. To look for other possible systematic errors related to laser polarization, we varied the linear polarization angle of the readout laser, the readout dither angle, $\mathrm{d}\theta$, used for measuring the contrast $\mathcal{C}$. We also intentionally applied large fractional ellipticities ($S/I \sim 0.1$) with a quarter waveplate in both the refinement and readout lasers. None of these parameters caused significant shifts in $\omega^{\mathcal{NE}}$.

5.11.4 Laser intensity

The laser intensity does not typically have an ideal value. In general, we choose intensities such that we drive the optical transfer processes to completion without depositing too much optical power on the field plates or being close to driving off-resonant transitions to

unwanted quantum states. To search for possible systematic effects related to the laser intensities, we varied the power of the refinement and readout lasers by more than a factor of 2. No dependence of $\omega^{\mathcal{NE}}$ on the power of refinement and readout lasers was observed. As described in detail in Section 5.6, we observed a correlation of $\omega^{\mathcal{NE}}$ with an intentionally applied $\tilde{\mathcal{N}}\tilde{\mathcal{E}}$-correlated power of the refinement laser, $P^{\mathcal{NE}}$. We therefore also applied power variations correlated with the $\tilde{\mathcal{N}}$ and $\tilde{\mathcal{P}}$ experimental states used. We did not observe shifts with any of these parameters.

We observed shifts correlated with variation of the relative power between the $\hat{X}$ and $\hat{Y}$ readout laser beams, corresponding to asymmetry effects which are understood and explained in Section 5.15. These only appear in the $\tilde{\mathcal{P}}$ and $\tilde{\mathcal{R}}$ odd frequency channels and have no observed or expected contributions to $\omega^{\mathcal{NE}}$.

5.12 Molecular beam parameters

The molecular beam ideally travels parallel to the electric field plates, is well centered between the field plates, and is horizontal with respect to gravity. We typically align the molecular beam to better than 1 mm from this axis using an optical alignment technique with a theodolite. To look for possible systematic effects related to the position or velocity of the molecular beam, we block half of the beam in the transverse $\pm\hat{x}$ and $\pm\hat{z}$ directions and look for changes in the precession frequency. We block the ThO molecular beam with mechanical collimators built from sharp razor blades that we insert in the molecular beam before the precession region. These blades are rigidly mounted in the stem region, which is intermediary between the beam source and the interaction region. The sensitivity of the spin precession measurement during these systematic checks is reduced, as the signal is reduced by a factor of two in any of these configurations. We did not observed shifts in $\omega^{\mathcal{NE}}$ with any of these changes in the parameters of the molecular beam.

5.13 Timing and analysis parameters

In addition to the above, we also varied parameters related to experiment timing to ensure the results didn't depend on our specific data acquisition choices. We typically set the deadtime allowed for the settling of each switched parameters to allow for ample settling time, typically 3-10 times longer than the switch time (time until the parameter reaches 95% of its setpoint value). We verified that increasing the setting time by a factor of two for all $\tilde{\mathcal{N}}, \tilde{\mathcal{E}}, \tilde{\mathcal{B}}$ block switches did not cause any difference in the measured quantities.

The polarization switching rate is high enough such that each molecule can be read out by both $\hat{X}$ and $\hat{Y}$ (see Section 3.3.5). By acquiring data with a lower polarization switching rate of 100 kHz instead of the typical 200 kHz, we verified that the chosen polarization switching frequency did not modify any of the measured experimental channels. In addition, we looked for variation in $\omega^{\mathcal{N}\mathcal{E}}$ and other measurement channels with the choice of analysis parameters, as discussed in detail in Section 4.8.

5.14 $\omega^{\mathcal{N}}$ noise

ACME II did not have any effects that correspond to class B of inclusion of systematic effects in the systematic error bar. In ACME I, we included in the systematic error budget a contribution from unexplained variations in the $\tilde{\mathcal{N}}$-correlated frequency channel, $\omega^{\mathcal{N}}$ [5, 6]. Such variations are reduced in magnitude in ACME II. Moreover, they are now understood to be caused by a time-varying relative detuning between the two $\tilde{\mathcal{N}}$ states, $\Delta^{\mathcal{N}}$, coupling to differences in laser beam properties (pointing, power, spatial) of the two probe ($\hat{X}$ and $\hat{Y}$) laser beams [6]. These effects are removed by the $\tilde{\mathcal{P}}$ and $\tilde{\mathcal{R}}$ switches, but will cause noise in the $\omega^{\mathcal{N}}$ channel if the timescale of the $\Delta^{\mathcal{N}}$ variation is faster than that of the $\tilde{\mathcal{P}}$ and $\tilde{\mathcal{R}}$ switches. Such noise is caused primarily by ∼1–100 ms excursions in the frequency of the Ti:S readout laser, with magnitude $\Delta^{\mathcal{N}} \sim$ 400–600 kHz. To ensure this noise does

not contribute to $\omega^{\mathcal{NE}}$, we verified that the correlation coefficient between $\omega^{\mathcal{NE}}$ and $\omega^{\mathcal{N}}$ (i.e. $S_{\omega^{\mathcal{N}}} = \partial\omega^{\mathcal{NE}}/\partial\omega^{\mathcal{N}}$) for the eEDM dataset is consistent with zero.

5.15 $\mathcal{A}^{\mathcal{NE}}$ ASYMMETRY EFFECTS

We also describe effects that were not observed to shift $\omega^{\mathcal{NE}}$, but have an effect on the other parity components. The $\tilde{\mathcal{P}}$- and $\tilde{\mathcal{R}}$- odd components of the frequency, $\omega^{u\mathcal{PR}}$, contain understood nonzero offsets that were observed and explained in ACME I [6]. These nonzero components result from differences in the properties (spatial profile, power and pointing) of the $\hat{X}$ and $\hat{Y}$ readout beams and are proportional to correlated detuning components Δ^u. The $\tilde{\mathcal{P}}$ and $\tilde{\mathcal{R}}$ switches, which interchange the roles of the $\hat{X}$ and $\hat{Y}$ beams, prevent offsets in $\omega^{u\mathcal{PR}}$ from contaminating ω^u. When combined with $\Delta^{\mathcal{NE}}$ (which arises due to $\mathcal{E}^{\mathrm{nr}}$; see Section 5.3), the residual differences in the $\hat{X}$ and $\hat{Y}$ readout beams create $\sim 8\ \sigma_{\omega^{\mathcal{NE}}}$ offsets in the $\omega^{\mathcal{NEPR}}$ channel.

We verified numerically that the value of $\omega^{\mathcal{NEPR}}$ is consistent with our model, given the measured size of experimental imperfections that it couples to (pointing between $\hat{X}$ and $\hat{Y}$, $\mathcal{E}^{\mathrm{nr}}$). By putting bounds on the possible size of correlations between $\omega^{\mathcal{NEPR}}$ and $\omega^{\mathcal{NEP}}$ (i.e., $\partial\omega^{\mathcal{NEPR}}/\partial\omega^{\mathcal{NEP}}$), and between $\omega^{\mathcal{NEPR}}$ and $\omega^{\mathcal{NER}}$ (i.e. $\partial\omega^{\mathcal{NEPR}}/\partial\omega^{\mathcal{NER}}$), we measured a suppression factor of possible leakage from $\omega^{\mathcal{NEPR}}$ to $\omega^{\mathcal{NE}}$ of > 500. Systematic checks in which we deliberately exaggerate $\omega^{\mathcal{NEPR}}$ by increasing the difference in the parameters between the $\hat{X}$ and $\hat{Y}$ beams (power, pointing asymmetry) give similar or better bounds. The systematic contribution due to $\omega^{\mathcal{NEPR}}$ is therefore limited to < 10 μrad/s. Including this term in the systematic error budget would increase its uncertainty by less than 1%. We did not include it, however, since we did not see direct evidence of these effects shifting $\omega^{\mathcal{NE}}$ near current sensitivity.

5.16 Search for correlations

In addition to searching for variation of $\omega^{\mathcal{NE}}$ with various experimental parameters, we also looked for unexplained statistically nonzero correlation coefficients for the block and superblock switches. We performed this analysis for important measurement quantities ω, $\mathcal{C}$ and also a large range of auxiliary measured parameters.

Figure 5.16.1 shows correlation coefficients between parity channels of frequency, ω, and contrast, $\mathcal{C}$. The magnitudes of the correlation coefficients are normalized by their uncertainties. The only significant correlation between different frequency channels occurs at high magnetic field, $1\mathcal{B}$, where the Zeeman precession phase $\sim \pi/4$. Here, we observe a significant correlation between $\omega^{\mathcal{N}}$ and $\omega^{\mathcal{NB}}$, due to leakage in the $\omega^{\mathcal{NB}}$ channel from the large offset and noisy $\omega^{\mathcal{B}}$ channel, due to insufficient $\tilde{\mathcal{N}}$ switch suppression limited by the Δg difference between the $\tilde{\mathcal{N}} = \pm 1$ states (see Section 4.4). There are no significant correlations between $\omega^{\mathcal{NE}}$ and any of the other measurement channels.

The significantly non-zero correlations between $\omega^{\mathcal{NE}}$ and $\mathcal{C}^{\mathcal{NE}}$ and $\mathcal{C}^{\mathcal{NEB}}$ have already been described in Section 5.7 and are part of the systematic error bar. In addition, the data at the larger magnitude of $1\mathcal{B}$ shows correlations between experiment frequency channels and contrast channels with a large offset due to the large Zeeman precession angle ($\sim \pi/4$) in the $1\mathcal{B}$ configuration.

In addition to correlations between measured data channels, we have also examined correlations between monitored parameters. The left panel in Figure 5.16.2 shows components of monitored parameters that are correlated with block experiment switches ($\tilde{\mathcal{N}}, \tilde{\mathcal{E}}, \tilde{\theta}, \tilde{\mathcal{B}}$). The correlated components are expected. For example, we perform the $\tilde{\mathcal{N}}$ switch by tuning the refinement/readout Ti:S 703 nm laser, so there is and should be a large component of the Ti:S 703 nm laser with $\tilde{\mathcal{N}}$. The correlations in the measured fluorescence signal with $\tilde{\theta}$ are consistent with changes in laser power and pointing, when performing the $\tilde{\theta}$ switch. The

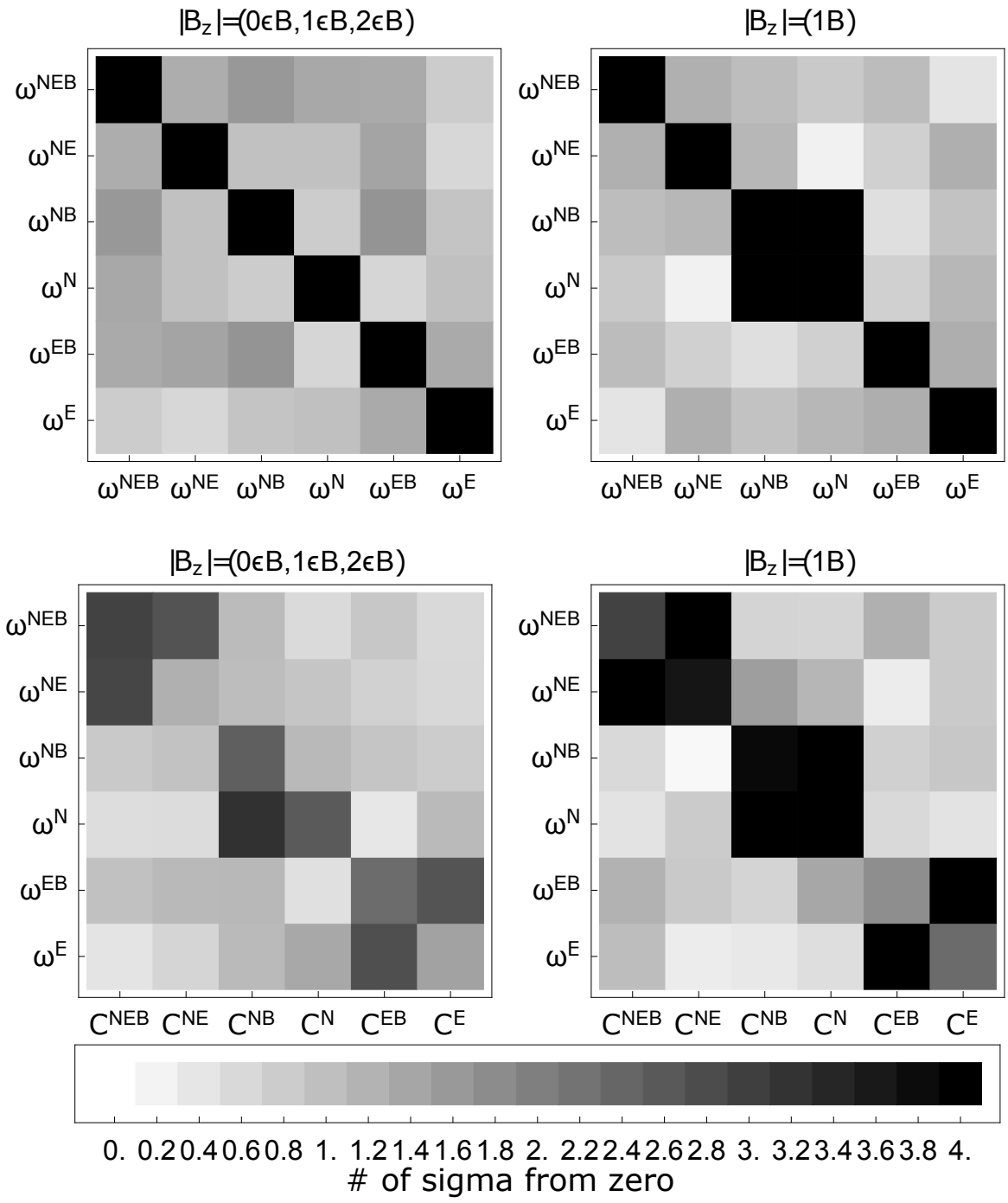

Figure 5.16.1: **Correlations between frequency and contrast parity sum channels.** The top two tables show correlations between 6 frequency channels. The bottom two table show correlations between 6 frequency channels and contrast channels. The left tables are taken with low magnetic field values $(0\epsilon\mathcal{B}, 1\epsilon\mathcal{B}, 2\epsilon\mathcal{B})$, where the Zeeman precession angle is close to zero, and the right tables are taken with higher magnetic field $(1\mathcal{B})$, where the Zeeman precession angle is $\sim \pi/4$. All shown parameters are odd in superblock switches $\tilde{\mathcal{P}}$, $\tilde{\mathcal{L}}$, $\tilde{\mathcal{R}}$. The magnitude of the correlation coefficients normalized by their uncertainties are shown on a gray-scale from 0 to 4, where coefficients larger than 4 are shown in black.

$\tilde{\mathcal{N}}$-correlated fluorescence component arises due to the $\Delta^{\mathcal{N}}$ correlated detuning in the read-out laser and the $\tilde{\mathcal{N}}\tilde{\mathcal{E}}$-correlated fluorescence component is consistent with the amount of intrinsic $\Delta^{\mathcal{N}\mathcal{E}}$ present in the precession region (due to $\mathcal{E}^{\mathrm{nr}}$). The $\tilde{\mathcal{B}} = \pm 1$ states have slightly different amounts of Zeeman phase precession, causing slightly different fluorescence levels. None of the correlated parity sum parameter channels were found to be correlated with $\omega^{\mathcal{N}\mathcal{E}}$, as shown in the right panel of Fig. 5.16.2. We have also searched for new, unexpected effects, by computing correlation coefficients with many other parameters and in various configurations, not shown here, such as for all superblock parity sums, asymmetry, contrast and phase.

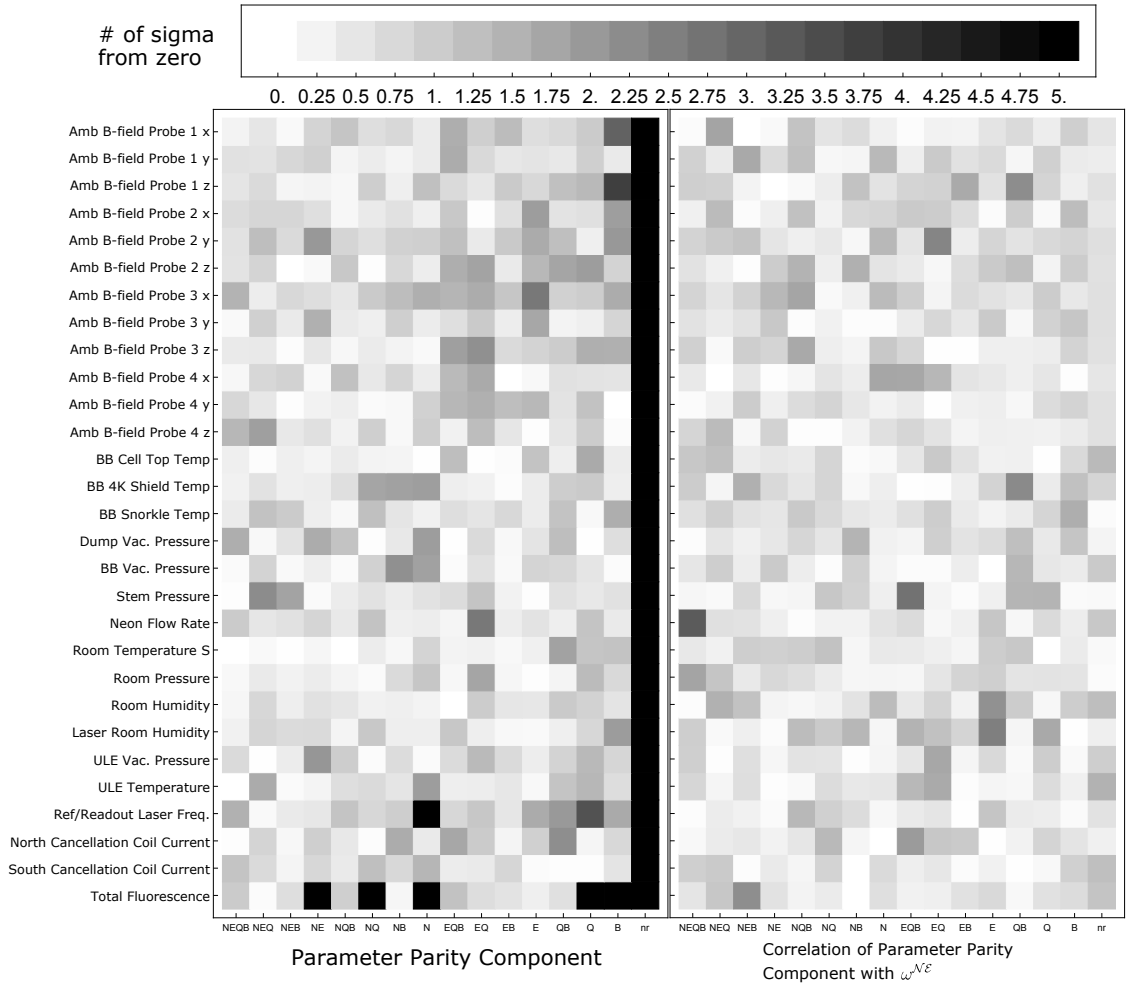

Figure 5.16.2: **Monitored parameter correlations.** Left panel shows components of monitored parameters that are correlated with block esperiment switches. Q refers to the $\tilde{\theta}$ switch used to measure the contrast. Most of the parameters only have a non-correlated, "nr", component, although we explain the mechanism behind the correlated parts in the text. The right panel shows correlations between these components and $\omega^{\mathcal{NE}}$. There are no significantly non-zero correlation channels. The magnitude of the correlation coefficients normalized by their uncertainties are shown on a gray-scale from 0 to 5, where coefficients larger than 5 are shown in black.

But there's no sense crying
over every mistake.
You just keep on trying
'til you run out of cake.
And the science gets done.

GlaDOS, *Portal*

6

An order of magnitude improved eEDM limit

Precise measurements of the eEDM represent stringent probes of physics beyond the Standard Model. This thesis focused on describing the ACME II measurement of the electric dipole moment of the electron. We explained the unique properties of the ThO molecules used to enhance the ACME II sensitivity to the eEDM. We described the robust and efficient experimental methods and apparatus required for performing the precise measurement. We discussed the mechanisms leading to systematic effects and our procedure to bound them to values that are much lower than the statistical uncertainty.

The result of this second generation eEDM measurement using ThO in units of precession

frequency is

$$\omega^{\mathcal{NE}} = (-510 \pm 373_{\text{stat}} \pm 310_{\text{syst}})\ \mu\text{rad/s}. \tag{6.1}$$

Using $d_e = -\hbar\omega^{\mathcal{NE}}/\mathcal{E}_{\text{eff}}$ and $\mathcal{E}_{\text{eff}} = 78$ GV/cm [39, 40] results in

$$d_{\text{e}} = (4.3 \pm 3.1_{\text{stat}} \pm 2.6_{\text{syst}}) \times 10^{-30}\ e \cdot \text{cm}, \tag{6.2}$$

where the combined statistical and systematic uncertainty, $\sigma_{d_e} = 4.0 \times 10^{-30}\ e \cdot \text{cm}$, is a factor of 12 smaller than the previous best result, from ACME I [5, 6].

Feldman-Cousins limit

An upper limit on $|d_e|$ is computed using the Feldman-Cousins prescription [6, 114]. The Feldman-Cousins method constructs confidence intervals that are independent of the result, by unifying the case when a measurement is consistent with zero and therefore reported as an upper bound and the case when a measurement is a few sigma from zero and therefore reported as a mean and two-sided confidence interval. We apply the Feldman-Cousins prescription to a folded normal distribution

$$P(x|\mu) = \frac{1}{\sqrt{2\pi}\sigma}\left[e^{-\frac{(x-\mu)^2}{2\sigma^2}} + e^{-\frac{(x+\mu)^2}{2\sigma^2}}\right], \tag{6.3}$$

where μ is the unknown true magnitude of $\omega_T^{\mathcal{NE}}$ and σ is the measurement scale parameter that we set as equal to the quadrature sum of the statistical and systematic uncertainties given in Eq. 6.2. We use a numerical method which we described in a previous publication [6] to extract the Feldman-Cousins limits for several different confidence intervals, as shown in Figure 6.0.1. For the 90% confidence interval that we chose to report our result, the switch between reporting an upper bound and a two-sided confidence interval occurs when the mean value of $\omega^{\mathcal{NE}}$ becomes larger than 1.64σ.

Using our measured ratio of $\mu/\sigma = 1.08$ with the Feldman-Cousins method, we obtain a

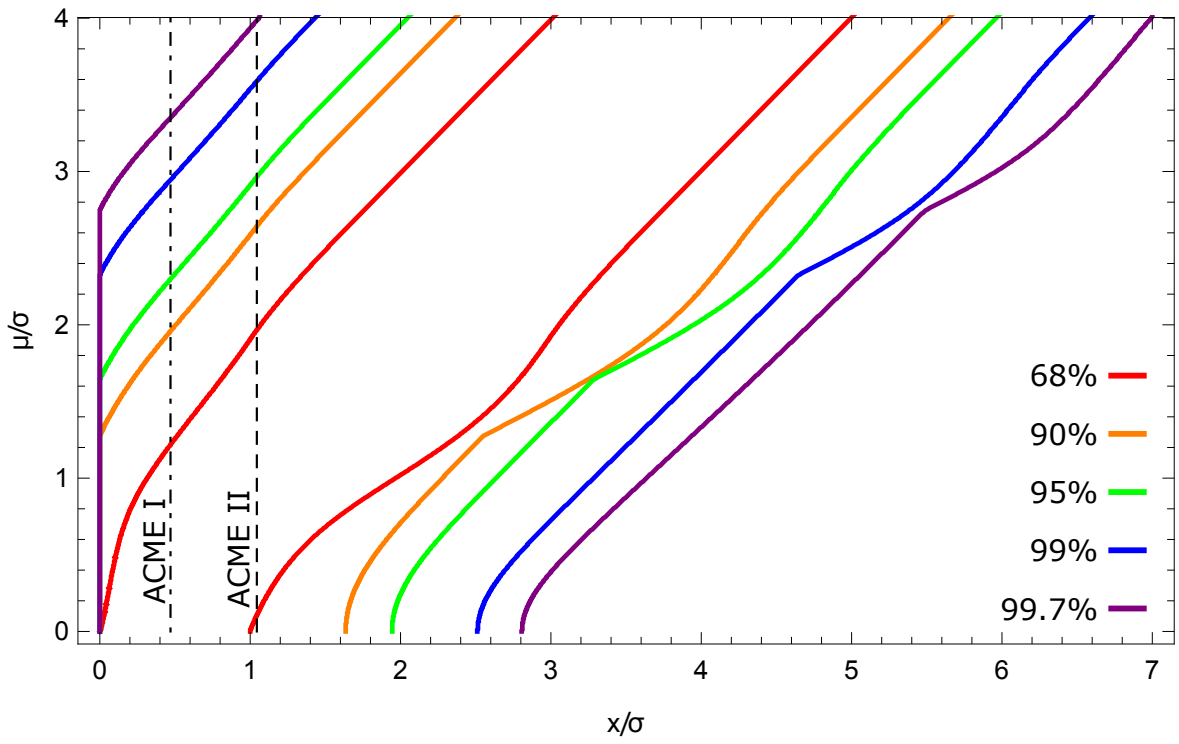

Figure 6.0.1: **Feldman-Cousins confidence bands for a folded normal distribution.** Each pair of same-color lines indicates the upper and lower bounds of the confidence band associated with each choice of confidence level. The lower bound is zero for all points that are to the left of lower band intercept with the $x-$axis. We show vertical result lines for the measured x/σ values of the ACME I and ACME II measurements. The μ value obtained from the intersection of these result lines and the 90% confidence band is used to calculate the eEDM limit in both ACME I and ACME II measurements.

limit on the eEDM at

$$|d_e| < 1.1 \times 10^{-29}\ e \cdot \text{cm (90\% c. l.)}, \tag{6.4}$$

which is 8.6 times smaller than the best previous limit, from ACME I [5, 6].

Though our reported d_e limit is computed using the Feldman-Cousins prescription [6, 114], previous eEDM experiments [43, 56, 115] reported limits based on a direct folded Gaussian distribution. To facilitate comparison with those experiments, we note that our limit computed in this way would be $|d_e| < 9.6 \times 10^{-30}\ e \cdot \text{cm}$ (90% c. l.).

Limit on C_S parameter

Because paramagnetic molecules are sensitive to multiple T-violating effects [116], our measurement can be more generally interpreted as $\hbar\omega^{\mathcal{NE}} = -d_e\mathcal{E}_{\text{eff}} + W_S C_S$, where C_S is a dimensionless T-violating electron-nucleon coupling and $W_S = -2\pi\hbar \times 282$ kHz is a molecule-specific constant [39, 40, 117]. For the d_e limit above, we assume $C_S = 0$. Assuming $d_e = 0$ instead gives

$$|C_S| < 7.3 \times 10^{-10} \text{ (90\% c. l.)}, \tag{6.5}$$

which is 8.6 times smaller than the previous best limit, from ACME I [5, 6].

Conclusion

Our new limit on the size of the electron's electric dipole moment [9] is

$$|d_e| < 1.1 \times 10^{-29}\ e \cdot \text{cm (90\% c. l.)}, \tag{6.6}$$

an order of magnitude lower than the previous ACME I bound [6].

Since the values of d_e and C_S predicted by the Standard Model are many orders of magnitude below our sensitivity [7, 8], this measurement is a background-free probe for new physics beyond the Standard Model. Nearly every extension to the Standard Model [10, 12–14] introduces the possibility for new particles and new T-violating phases, ϕ_{T}, that can lead to measurably large eEDMs. Within typical extensions to the Standard Model, an eEDM arising from new particles with rest-mass energy Λ in an n-loop Feynman diagram will have size [16, 28, 29]

$$\frac{d_e}{e} \sim \kappa \left(\frac{\alpha_{\text{eff}}}{2\pi}\right)^n \left(\frac{m_e c^2}{\Lambda^2}\right) \sin(\phi_{\text{T}})(\hbar c), \tag{6.7}$$

where α_{eff} (4/137 for electroweak interactions) encodes the strength with which the electron couples to new particles, m_e is the electron mass and $\kappa \sim 0.1$ to 1 is a dimensionless prefactor whose value depends on the specific model of new physics. In typical models where 1- or 2-loop diagrams produce d_e, with $\sin(\phi_{\text{T}}) \sim 1$, our result typically limits T-violating new physics to energy scales above $\Lambda \sim 30$ TeV or 3 TeV, respectively [10–16].

The future of ACME

Despite continuing success of ACME I and ACME II in reducing the eEDM limit by more than two orders of magnitude compared to previous measurements, we believe significant sensitivity improvements are still possible in the future. We are continuing to develop the ACME technique to reach these sensitivities.

The upgrades that we are considering include:

1. **Noise reduction.** ACME II was limited by excess noise that increased our uncertainty by a factor of 1.7 above shot noise. After acquiring the ACME II dataset, we have investigated and understood the mechanism leading to the excess noise (see Section 4.10). The noise contaminates the measurement of the asymmetry and is due to a combination of timing noise in the DAQ digitizer used, a time offset between the $\hat{X}$ and $\hat{Y}$ polarization switching signals and time dependence of the detected fluorescence signal due to the fast polarization switching scheme used for the phase measurement. We show that the noise can be suppressed by reducing the two experimental imperfections that contribute to it and by integrating over a larger sub-bin within the polarization switching signal (more detail in Section 4.10). We demonstrate suppression of this source of noise at the ACME II level of sensitivity, but also expect this source of noise to be suppressed by a few orders of magnitude, below the projected ACME III statistical uncertainty. Suppressing this noise already represents a factor of 3 gain in signal for a future generation compared to ACME II and opens the door to future signal gains contributing directly to measurement signal to noise.

Noise could also be reduced by performing one of our experiment switches on timescales faster than that of variations in the parameter(s) causing the noise, therefore removing noise by fast differential measurements. This could be performed in ACME by switching $\tilde{\mathcal{N}}$ on fast timescales (>1 kHz), for example by using AOMs to tune the experiment laser frequencies. Such switching should not only suppress noise coming from sources affecting the asymmetry, but also phase and frequency. Fast $\tilde{\mathcal{N}}$ switching would also reduce noise due to fluctuations in the velocity of the molecular beam (see Section 4.10). Implementing fast $\tilde{\mathcal{N}}$ switching schemes in our system might prove challenging because the switching of the laser frequency corresponding to the $\tilde{\mathcal{N}}$ switch would need to be performed in both the state preparation and state readout laser beams. This would likely require increased laser power compared to the current ACME II configuration. Furthermore, velocity dispersion in the molecular beam could make the different $\tilde{\mathcal{N}}$ states overlap in time, which will limit our ability to time-resolve them. Other schemes might be preferable to use for distinguishing between the populations of the $\tilde{\mathcal{N}} = \pm 1$ states.

2. **Reduction of the ellipticity gradients-$\mathcal{E}^{\mathrm{nr}}$ systematic.** Most of the systematic effects that we have observed and expected in ACME I and ACME II have been or can be further suppressed below the expected ACME III sensitivity. However, as discussed in Section 5.3.1, ellipticity gradients in the experiment lasers can combine with $\mathcal{E}^{\mathrm{nr}}$ to cause systematic shifts. These ellipticity gradients were caused in ACME I by thermal stress induced birefringence in the glass due to the optical power deposited by the lasers. We have reduced thermal stress induced birefringence to levels that are low enough to limit the systematic effect contribution to below statistical sensitivity. The larger effect causing birefringence in the glass is now due to mechanical stress.

   One option we are investigating to reduce the mechanical stress is to use glass with

a lower stress birefringence coefficient[1]. In addition, we are investigating transitions that would allow us to perform STIRAP through the field plates, which is not possible currently due to the large intensity of the $H-C$ Stokes laser (1 W/mm^2 at 1090 nm). Having the Stokes STIRAP beam propagate through the field plates, along z, allows for full control over the angle of the linear polarization in the xy plane. Aligning this linear polarization axis with the birefringence axis minimizes the effect of the glass birefringence on the polarization of the laser beams, heavily suppressing the ellipticity systematic effects.

Some of the candidates for a STIRAP scheme that requires lower laser power and could be performed through the field plates are $X-A-H$, $X-L-H$ or $X-U-H$. The $X-A$ transition (943 nm) was used for state preparation in ACME I [6] and some of the properties of the latter two intermediary states L and U have been spectroscopically measured and characterized recently [75]. Performing STIRAP on strong transitions, with robust lasers that allow access to high Rabi frequencies with low intensity has a number of additional advantages. Firstly, we can implement STIRAP with higher than the 75 % transfer efficiency achieved in ACME II [73], for a signal gain of up to 1.2 over ACME II. In addition, it is possible to build a more robust optical setup than in ACME II due to less stringent requirements for the spatial intensity profile of the laser beams required to achieve sufficient intensity for saturation. Larger area laser beams ($\sim$ 1 mm instead of 100 μm waist used in ACME II [73]) also reduce sensitivity of the STIRAP transfer efficiency to variations in the laser beam intensity profiles caused by alignment variations due to environmental effects, such as thermal drift or mechanical vibrations. This could also make the STIRAP prepared spin-aligned state be more reliably aligned along the direction of the Stokes 1090 nm laser polarization, reducing our reliance on the refinement laser beam to clean up the STIRAP prepared spin-aligned state. The implementation of STIRAP through

[1]Schott SF57HTUltra.

the field plates requires modifying our current rotational cooling scheme to instead transfer population to a single superposition of the $|X, J = 1, M = \pm 1\rangle$ quantum states, but we estimate that such schemes can achieve molecular populations which are comparable to the ACME II rotational cooling scheme.

3. **Optical cycling.** In ACME II, the readout laser beams create at most one fluorescence photon per molecule. About 20% of the photons are collected and reach the PMTs and the quantum efficiency of the PMTs is 25%. These two factors combined lead to a total detection efficiency of 5%. By using optical cycling, we expect to produce multiple photons per molecule. Optical cycling first requires the shelving of the orthogonal $\hat{X}, \hat{Y}$ quadratures by using opposite parity excited states, $P = -1$ and $P = +1$, to rotational levels $\{J0, J2\}$ and $J1$, respectively. A second set of lasers, at 512 nm, would cycle photons on the $X - I$ transition, which could allow for up to 10 photons to be cycled based on the measured 91% branching ratio [75].

   Since the new states that encode spin-alignment information, i.e. the rotational levels of the ground X state, are not sensitive to electric or magnetic fields, detection could also be performed outside of the interaction region μ-metal shielded chamber. The detection could then be performed in an improved collection optics geometry, where more photons could be directed to the detecting PMTs. New photodetectors with higher quantum efficiency could also be used to improve detection efficiency even further.

4. **Molecular beam lensing.** One upgrade that we built and tested for ACME II was based on a quadrupole electrostatic lens for guiding molecules in the ground state X. However, voltage breakdown and the presence of Bremsstrahlung X-rays prevented that project from increasing the number of measured molecules [100]. We are investigating performing the guiding while the molecules are in the Q state, which has larger electric and magnetic dipole moments. This larger moments allow for larger

forces to be applied to the molecules, improving the number of guided ThO molecules that are useful for the ACME precession measurement by up to a factor of 10. To take advantage of this signal gain factor, we would need to first use STIRAP to transfer population from the ground state X to the Q state before the lensing and transfer the population back to the $H^3\Delta_1$ experiment state after the guiding step.

5. **Reduced beamline length.** Future experiments might reduce the length of the stem vacuum chamber or remove it entirely, if parts of the rotational cooling scheme can be performed inside the beam source. The feasibility of this scheme would have to be tested experimentally, as it is unclear at the moment if collisions between the ThO molecules and the neon buffer gas that is present at high pressures in the proximity of the the cell would remix the populations of the various J rotational levels. The gain due to this further optimization would likely be limited to at most a factor of 2 in signal.

6. **Faster target replacement.** The molecular flux of the ACME beam source decreased by a factor of 2-3 after 3-6 days of continuous running. A method of replacing the targets on faster timescales (every week rather than every month in ACME II) could increase ACME signal by up to a factor of 2. Implementations of such schemes would need to allow for target replacement without warming up the cryogenic beam source, which typically takes 1-2 days.

We expect that future ACME experiments could reduce the uncertainty of the eEDM measurement by another order of magnitude, either finding a nonzero value of d_e, or constraining it to be below 10^{-30} $e \cdot \mathrm{cm}$ (with 90 % confidence), thus probing one-loop interactions at energy scales in excess of 100 TeV.

A

$\omega^{\mathcal{NE}}$ systematic from $P^{\mathcal{NE}}$ due to AC Stark shifts

During ACME II, we observed a depedence of $\omega^{\mathcal{NE}}$ on an intentionally applied $P^{\mathcal{NE}}$ in the refinement laser beam. The true mechanism leading to that effect is described in Section 5.6. We describe here models we used initially to investigate the observed shift, that matched some of the characteristics but didn't fully capture the behavior of the observed systematic. These models were based on the framework describing AC Stark shift effects that were dominant in ACME I. The mechanism and derivation of the terms that lead to observable effects are described in detail in a previous publication [6]. As shown in Eq. 77

in [6], contributions to the $\omega^{\mathcal{NE}}$ eEDM channel might arise from terms

$$\omega_{\text{AC Stark}-P} = cP(d\theta_{\text{ref}} - g\mu_{\text{B}}\mathcal{B}_z\tilde{\mathcal{B}}t), \tag{A.1}$$

where $d\theta_{\text{ref}}$ is an imperfection in our system that quantifies the amount of linear polarization gradient in the polarization of the refinement laser beam, t is the molecule-laser beam interaction time and c is the coupling constant given by the total power offset and the profile of the laser beam intensity.

An applied or residual $P^{\mathcal{NE}}$ will then cause two contributions to the measured correlated frequencies: one due to the first term in Eq. A.1, $\omega^{\mathcal{NE}}_{\text{AC Stark}-P^{\mathcal{NE}}} = cP^{\mathcal{NE}}d\theta_{\text{ref}}$, and one due to the second term $\omega^{\mathcal{NEB}}_{\text{AC Stark}-P^{\mathcal{NE}}} = cP^{\mathcal{NE}}g\mu_{\text{B}}\mathcal{B}_z t$. We have observed the second term in both ACME I and ACME II data as a slope in the $\omega^{\mathcal{NEB}}$ vs $P^{\mathcal{NE}}$, $S^{\omega^{\mathcal{NEB}}}_{P^{\mathcal{NE}}}$. The magnitude of $S^{\omega^{\mathcal{NEB}}}_{P^{\mathcal{NE}}}$ was consistent with the expected based on our laser beam parameters.

We investigated whether the first term might be responsible for the observed $S^{\omega^{\mathcal{NE}}}_{P^{\mathcal{NE}}}$ in ACME II. At $1\mathcal{B}$, the molecules precess by $\pi/4$ over a distance of 20 cm, so the Zeeman precession term magnitude is $d\phi_{\mathcal{B}}/dx \sim 4$ mrad/mm. Since we measured the magnitude of $S^{\omega^{\mathcal{NE}}}_{P^{\mathcal{NE}}}$ to be about 10 times smaller than $S^{\omega^{\mathcal{NEB}}}_{P^{\mathcal{NE}}}$, the magnitude of the linear polarization gradient required to quantitatively explain the $\omega^{\mathcal{NE}}$ dependence on $P^{\mathcal{NE}}$ is $d\theta_{\text{ref}}/dx \sim 400$ μrad/mm.

We used two methods to measure the magnitude of linear polarization gradients in the laser beam, $d\theta_{\text{ref}}/dx$. The first one was based on our polarimetry measurements of circular polarization gradients [101]. The second method used a high-extinction ratio polarizing beam-spliter and a camera to directly measure the linear polarization gradients. Both methods convinced us that the amount of linear polarization gradients present in the ACME II refinement laser beam is too small to correctly describe the observed $P^{\mathcal{NE}}$ systematic.

A.1 Linear polarization gradients from circular polarization measurements

Our polarimetry system was designed to be have high sensitivity when measuring circular polarization, in particular. While it is able to perform well for linear polarization, better limits can be placed on the linear polarization components from the circular polarization measurements [101]. This argument was initially made by Vitaly Andreev and is reproduced here.

In our polarimetry measurements, we were able to limit circular polarization gradients to below 0.1% in the relative fraction of circular polarization (S/I). The birefringence effect that changes the polarization properties of our laser beams is largest when the axis of linear polarization of the incoming light is perfectly misaligned with the birefringence axis of the glass, i.e. at 45 degrees. At this angle, the incoming Stokes vector is $\vec{S}_{\text{in}} = \{I, M, C, S\} = \{1, 0, 1, 0\}$ and the outgoing Stokes vector can be obtained by multiplying the Mueller matrix corresponding to the glass with birefringence δ at an angle β with respect to this 45 degree reference axis:

$$\vec{S}_{\text{out}} = \Gamma(\delta, \beta) \cdot \vec{S}_{\text{in}} = \begin{pmatrix} 1 \\ \sin(4\beta)\sin^2(\delta/2) \\ \cos^2(2\beta)\cos\delta + \sin^2(2\beta) \\ -\cos(2\beta)\sin\delta \end{pmatrix}. \tag{A.2}$$

Allowing for small misalignment, $\Delta\beta \ll 1$, and also assuming that the retardance is small, $\delta \ll 1$, we can expand $\vec{S}_{\text{out}}$ to second order in δ to obtain

$$\vec{S}_{\text{out}} \approx \begin{pmatrix} 1 \\ \delta^2 \Delta\beta \\ 1 - \delta^2(1 - 4\Delta\beta^2)/2 \\ -\delta(1 - 2\Delta\beta^2) \end{pmatrix}. \tag{A.3}$$

The linear polarization rotation angle is given by $\tan 2\theta = M/C$. Assuming θ is small,

$$d\theta \approx \delta^2 \Delta\beta/2. \tag{A.4}$$

Since we are interested in the gradient in θ along x,

$$d\theta/dx = \delta(\Delta\beta)\frac{d\delta}{dx} + 1/2\delta^2 \frac{d(\Delta\beta)}{dx}. \tag{A.5}$$

We can estimate $d\delta/dx$ from our measurements of S/I across the refinement laser window (Fig 4.4b in [118]). There, since the measurement was performed at 45 degrees as above, $S/I \approx -\delta + 2\delta\Delta\beta^2$. Based on this measurement, we can then estimate $\delta = 0.1$ and $d\delta/dx \approx 10^{-3}$ /mm. Furthermore, $d(\Delta\beta)/dx$ should not be much larger than 0.002 rad/mm. It is possible $\Delta\beta$ is misaligned by as much as 0.1 rad. Plugging these very rough estimate numbers in, we obtain that $d\theta_{\text{prep}}/dx < 20$ μrad/mm, which is at least an order of magnitude lower than it would need to be to explain our observed systematic effect.

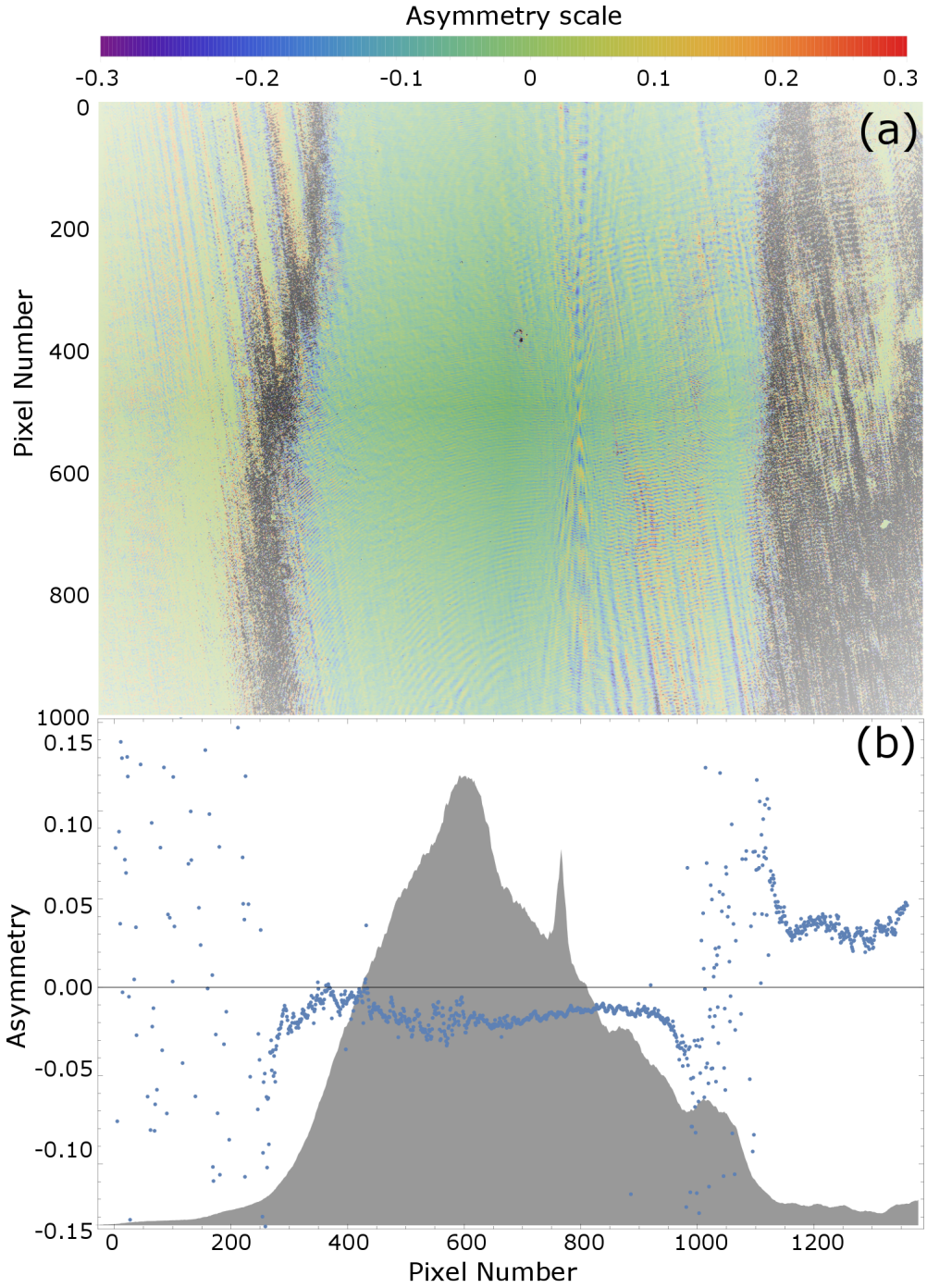

Figure A.1.1: **Measurement of linear polarization gradients in the refinement laser beam. (a)** Top figure shows the computed asymmetry between $\tilde{\theta} = \pm 1$ states for the entire 1360×1024 camera image. **(b)** The bottom figure shows the asymmetry as a function of x (horizontal) pixel number. The spatial intensity profile of the laser light along x during these measurements is shown in gray in the background.

A.2 Direct measurement of linear polarization gradients

In addition to the estimates above, we have set up a measurement of the linear polarization gradient of the refinement laser beam, after passing through the field plates. The measurement uses a high extinction ratio Glan Laser polarizing beamsplitter (PBS), which can be rotated using a high precision (better than 10^4 angle accuracy) rotation stage. A CCD camera is placed after the PBS. We rotate the PBS such that the transmission is maximized. We dither the angle of the PBS around the angle of maximum transmission by $\tilde{\psi}\psi = \pm 2$ degrees. We expect the linear polarization gradients due to birefringence, $d\theta/dx$, to be much smaller than ψ. The intensity of the laser light at each of the CCD pixels is given by

$$I(\theta, \psi) = \sin^2(\theta + \tilde{\psi}\psi) \tag{A.6}$$

$$\approx \theta^2 + \psi^2 + 2\theta\tilde{\psi}\psi, \tag{A.7}$$

where we have used the fact that both θ and ψ are small angles. Computing the asymmetry between the two $\tilde{\psi} = \pm 1$ configurations, we obtain

$$\mathcal{A} = \frac{I(\theta, \tilde{\psi} = +1) - I(\theta, \tilde{\psi} = -1)}{I(\theta, \tilde{\psi} = +1) + I(\theta, \tilde{\psi} = -1)} \tag{A.8}$$

$$= \frac{4\theta\psi}{2\psi^2 + 2\theta^2} \tag{A.9}$$

$$\approx \frac{2\theta}{\psi}. \tag{A.10}$$

To first order, the polarization angle is then simply given by

$$\theta \approx \frac{\mathcal{A}\psi}{2}. \tag{A.11}$$

The asymmetry data is shown in Figure A.1.1a, for each point within the CCD camera

image (1360x1024 pixels). We have checked for variation of the asymmetry shape along the vertical direction y, the direction along which the laser beam is elongated, and have not observed significant changes in the asymmetry. Figure A.1.1b shows the variation in the asymmetry along x, where we have averaged over the vertical y dimension. We can convert asymmetry variation along x into an linear polarization gradient using Eq. A.11. Without models to understand the mechanisms leading to the small observed variation in asymmetry, we can limit $d\theta/dx < 100$ μrad/s. This measured value of $d\theta/dx$ is too small to explain the size of the $S_{P\mathcal{N}\mathcal{E}}^{\omega\mathcal{N}\mathcal{E}}$ slope observed in ACME II. Instead, the $S_{P\mathcal{N}\mathcal{E}}^{\omega\mathcal{N}\mathcal{E}}$ effect is explained by the model described in Section 5.6.

B

Steps performed during data analysis

The data analysis used for the ACME II measurement is described in detail in Chapter 4. We provide here a summary of the steps in the order in which they were performed in the data analysis routine. The order of certain steps could vary for different analysis routines, but the end result is completely independent of such choices.

If this section is read by a future student looking to write their own ACME analysis routine, I recommend they first try to come up with their own sequence of steps, before reading this section too carefully. That mindset will hopefully allow them to better understand how the analysis procedure is constructed, what steps have to be done to obtain an eEDM number from the raw data and what analysis choices can be made.

Block Analysis.

1. Load all data corresponding to one block (in ".bin" format) and sum all 8 PMT channels after scaling their voltage by the individually measured PMT gain weigths (photoelectron countrate/ voltage for each PMT). Keep the data in a countrate vs time format, for each of the 64 traces in a block.

2. Subtract background [for each trace]:

   (a) Given the polarization switching rate and the sample rate, figure out how many trace points correspond to a full $\hat{X} - \hat{Y}$ polarization switching cycle - 80 in ACME II.

   (b) Average together background data corresponding to one $\hat{X} - \hat{Y}$ polarization cycle from the first 0.5 to 2.5 ms (400 cycles), to obtain a "typical background". This makes the uncertainty in the background very small, $> 10\times$ smaller, compared to the uncertainty of the trace.

   (c) Subtract background by taking the difference between the data trace and the background, point by point, for the whole trace.

3. Compute asymmetry points [for each trace]:

   (a) Decide which points in the $\hat{X} - \hat{Y}$ polarization bin belong to the sub-bin over which we want to integrate data, both for $\hat{X}$ and for $\hat{Y}$ polarization. The $\hat{X}$ and $\hat{Y}$ sub-bins should be synchronized with the timing of the $\hat{X}$ and $\hat{Y}$ fluorescence pulses.

   (b) Sum all points in the chosen sub-bin, for each $\hat{X}$ and each $\hat{Y}$ polarization cycles independently. Keep the two lists of points corresponding to signal belonging to $\hat{X}$ and $\hat{Y}$ quadratures in different arrays. Each list will have 160000/80/2=1000 points of fluorescence signal values F_x and F_y.

(c) Compute the point by point asymmetry, by: $\mathcal{A} = (F_x - F_y)/(F_x + F_y)$, where F_x and F_y are the values of the points from the previous step.

(d) Also compute the total signal, by $F_{\text{total}} = (F_x + F_y)/2$.

4. Compute asymmetry groups and assign error bars to the asymmetry groups [for each trace]:

   (a) Group N (typically 20) consecutive asymmetry points.

   (b) For each asymmetry group, perform a linear fit. The group mean is the value of the fit at the middle fit point. The uncertainty is the standard deviation of the fit residuals divided by $\sqrt{N-2}$ (typically $\sqrt{18}$).

   (c) Also compute the total signal for each group by averaging together the points in that group, F_{total}.

5. Won't need this until later, but it's a good time to perform the signal cut [for each trace].

   (a) Using the trace total signal, F_{total}, cut out any groups that:

      i. Are below 15% (typically) of the peak trace signal.

      ii. Are below 8 MHz count rate. This rarely does anything as our peak values are typically above 150 MHz, so the proportional signal cut is typically more stringent, but is there to ensure the statistics remains Gaussian even if signals become lower, such as due to depleting targets.

   (b) Take the interception of all groups that have survived the signal cut for all traces. If there are less than 5 groups in this interception, flag and throw the block away. This almost never happens, as there are typically tens of groups in the high signal region.

6. Average together the degenerate asymmetry traces [there are 16 $\tilde{\mathcal{N}}\tilde{\mathcal{E}}\tilde{\theta}\tilde{\mathcal{B}}$ states in a block, each with a degeneracy of 4, making up the total of 64 traces]:

   (a) Load in the header and read the assignment of the 4 block switches $\tilde{\mathcal{N}}\tilde{\mathcal{E}}\tilde{\theta}\tilde{\mathcal{B}}$, for each trace in the block.

   (b) Group the traces by state. That is, each state (for example $\tilde{\mathcal{N}}\tilde{\mathcal{E}}\tilde{\theta}\tilde{\mathcal{B}}$=++-+) will have 4 traces.

   (c) Check that the values of the traces in one state agree well by computing a χ^2_r. We rarely (once every 100 blocks) see that one trace has a much differing asymmetry. This is typically caused by the velocity making a large sudden jump or the waveplate controller failing to do the flip. If the other three asymmetry traces are good, I keep those and remove the bad trace.

   (d) Average together the 4 degenerate traces (for each asymmetry group), by doing a standard weighted average.

7. Compute contrast and mean asymmetry [for each of the 8 $\tilde{\mathcal{N}}\tilde{\mathcal{E}}\tilde{\mathcal{B}}$ states]:

   (a) Again, using the header, find the pair of states that have opposite waveplate states ($\tilde{\theta}$), but identical $\tilde{\mathcal{N}}\tilde{\mathcal{E}}\tilde{\mathcal{B}}$ states.

   (b) Compute contrast and mean asymmetry using the pairs of opposite states and the total waveplate polarization dither angle of $d\theta$:

      i. $\mathcal{C} = -1/(2d\theta)(\mathcal{A}(\tilde{\mathcal{N}}\tilde{\mathcal{E}}\tilde{\mathcal{B}}, \tilde{\theta} = +1) - \mathcal{A}(\tilde{\mathcal{N}}\tilde{\mathcal{E}}\tilde{\mathcal{B}}, \tilde{\theta} = -1))$

      ii. $\mathcal{A} = 1/2(\mathcal{A}(\tilde{\mathcal{N}}\tilde{\mathcal{E}}\tilde{\mathcal{B}}, \tilde{\theta} = +1) + \mathcal{A}(\tilde{\mathcal{N}}\tilde{\mathcal{E}}\tilde{\mathcal{B}}, \tilde{\theta} = -1))$

   (c) Propagate errors using standard Gaussian error propagation.

8. Compute phase, Φ, and contrast corrected asymmetry, $\mathcal{A}^{\mathcal{C}}$ [for each of the 8 $\tilde{\mathcal{N}}\tilde{\mathcal{E}}\tilde{\mathcal{B}}$ states]:

   (a) Do the calculation group by group, for each $\tilde{\mathcal{N}}\tilde{\mathcal{E}}\tilde{\mathcal{B}}$ state:

i. $\Phi = \mathcal{A}/(2\mathcal{C})$

ii. $\mathcal{A}^{\mathcal{C}} = \mathcal{A}\text{sign}(\mathcal{C})$

(b) Error propagation using standard Gaussian error propagation.

9. Compute parity sums [per block]:

   (a) For the phase, $\Phi^{p}(\mathcal{N},\mathcal{E},\mathcal{B}) = \frac{1}{2^8}\sum_{\tilde{\mathcal{N}}',\tilde{\mathcal{E}}',\tilde{\mathcal{B}}'=\pm 1}(\tilde{\mathcal{N}}')^{\frac{1-\mathcal{N}}{2}}(\tilde{\mathcal{E}}')^{\frac{1-\mathcal{E}}{2}}(\tilde{\mathcal{B}}')^{\frac{1-\mathcal{B}}{2}}\Phi(\tilde{\mathcal{N}}\tilde{\mathcal{E}}\tilde{\mathcal{B}})$.

   (b) Same for contrast.

10. Calculate τ, the block precession time , from $\Phi^{\mathcal{B}}$ [per block]:

    $\tau = \text{Round}[g_H\mu_B\mathcal{B}_z/(\pi/4)]\pi/4 + \Phi^{\mathcal{B}}/(\mu_B g_H \mathcal{B}_z)$.

11. Calculate precession frequencies [for each $\tilde{\mathcal{N}}\tilde{\mathcal{E}}\tilde{\mathcal{B}}$ correlated phase channel]:

    (a) Calculate frequencies group by group (without averaging over time) for each $\mathcal{N}\mathcal{E}\mathcal{B}$ channel by:

    $\omega^{\mathcal{N}\mathcal{E}\mathcal{B}} = \Phi^{\mathcal{N}\mathcal{E}\mathcal{B}}/\tau$ (shown here for $\omega^{\mathcal{N}\mathcal{E}\mathcal{B}}$).

    (b) Standard error propagation.

    (c) Need to be very careful to blind the eEDM channel, that is:

    $\omega^{\mathcal{N}\mathcal{E}}_{\text{blinded}} = \omega^{\mathcal{N}\mathcal{E}} + \omega_{\text{blind}}$.

12. Now that we have τ, can also compute parity sums for the C-corrected asymmetry:

    (a) Same formula as before for parity sums.

    (b) Asymmetry blind is:

    $\mathcal{A}^{\mathcal{N}\mathcal{E}}_{\text{blinded}} = \mathcal{A}^{\mathcal{N}\mathcal{E}} + 2\omega_{\text{blind}}\tau\mathcal{C}$.

13. Also blind the phase:

    $\Phi^{\mathcal{N}\mathcal{E}}_{\text{blinded}} = \Phi^{\mathcal{N}\mathcal{E}} + \omega_{\text{blind}}\tau$.

14. For diagnostics, calculate eta:

    $\eta = -\omega^{\mathcal{N}\mathcal{B}}/(\mu_B|\mathcal{E}_z||\mathcal{B}_z|)$.

15. Average $\omega, \Phi, \mathcal{A}$ and $\mathcal{C}$ in time after ablation, for the groups that survived the signal cut computed previously. Use standard weighted averaging to average all groups.

16. At the end of block analysis, there is now a value with an error bar for each $\omega, \Phi, \mathcal{A}, \mathcal{C}$ quantities for each parity sum ($\mathcal{NEB}$), for each block.

Superblock analysis.

1. Average together degenerate blocks:

   (a) Each superblock has 16 blocks and only 8 states (corresponding to binary switches $\tilde{\mathcal{P}}\tilde{\mathcal{L}}\tilde{\mathcal{R}}$), so there is a degeneracy of 2.

   (b) Using the header, determine which blocks are degenerate and average them together using standard error propagation.

2. Compute parity sums for the superblock:

   (a) Entirely analogous to block parity sums, compute parity sums in the $\mathcal{NEBPLR}$ basis, for frequencies, phases, asymmetries, contrast.

   (b) For example, I take $\omega^{\mathcal{NE}}$ for the 8 superblock states (corresponding to $\tilde{\mathcal{P}}, \tilde{\mathcal{L}}, \tilde{\mathcal{R}} = \pm 1$) and then do a parity sum on that to obtain all $\omega^{\mathcal{NE}}$ superblock parity sums for all combinations of $\tilde{\mathcal{P}}, \tilde{\mathcal{L}}, \tilde{\mathcal{R}} = \pm 1$ ($\omega^{\mathcal{NEPLR}}, \omega^{\mathcal{NEPL}}, \omega^{\mathcal{NEPR}}$ etc.).

3. At the end of superblock analysis, there is now a value with an error bar for each $\omega, \Phi, \mathcal{A}, \mathcal{C}$ quantities for each parity sum ($\mathcal{NEBPLR}$), for each superblock.

Systematic check analysis.

1. A typical systematic check has data with a parameter P that is an exaggerated imperfection, or just a different value than typical running configuration.

2. Create a table of all the superblocks relevant to that systematic check. The table includes both "normal data" (I use run 112 along with the daily data from that

systematic), and the superblocks corresponding to the exaggerated parameter P. The table contains, for each superblock, the value of applied P, the mean $\omega^{\mathcal{NE}}$ and the uncertainty in $\omega^{\mathcal{NE}}$.

3. Compute a slope and an uncertainty in the slope for the data in the table, in units of $\omega^{\mathcal{NE}}$/ (units of parameter).

4. If the slope is smaller than the uncertainty, compute the total systematic error contribution to $\omega^{\mathcal{NE}}$ by using the value of the parameter under typical running conditions.

5. If the slope is significantly larger than the uncertainty, understand systematic mechanism.

Bibliography

[1] D. Hanneke, S. Fogwell, and G. Gabrielse, "New Measurement of the Electron Magnetic Moment and the Fine Structure Constant," Phys. Rev. Lett. **120801**, 1–4 (2008).

[2] B. Odom, D. Hanneke, B. D. Urso, and G. Gabrielse, "New Measurement of the Electron Magnetic Moment Using a One-Electron Quantum Cyclotron," Phys. Rev. Lett. **030801**, 6–9 (2006).

[3] R. H. Parker, C. Yu, W. Zhong, B. Estey, and H. Müller, "Measurement of the fine-structure constant as a test of the Standard Model," Science **360**, 191–195 (2018).

[4] T. Aoyama, M. Hayakawa, T. Kinoshita, and M. Nio, "Tenth-Order QED Contribution to the Electron g-2 and an Improved Value of the Fine Structure Constant," Phys. Rev. Lett. **111807**, 13–16 (2012).

[5] J. Baron, W. C. Campbell, D. DeMille, J. M. Doyle, G. Gabrielse, Y. V. Gurevich, P. W. Hess, N. R. Hutzler, E. Kirilov, I. Kozyryev, B. R. O'Leary, C. D. Panda, M. F. Parsons, E. S. Petrik, B. Spaun, A. C. Vutha, and A. D. West, "Order of magnitude smaller limit on the electric dipole moment of the electron." Science **343**, 269–72 (2014).

[6] ACME Collaboration, J. Baron, W. C. Campbell, D. DeMille, J. M. Doyle, G. Gabrielse, Y. V. Gurevich, P. W. Hess, N. R. Hutzler, E. Kirilov, I. Kozyryev, B. R. O'Leary, C. D. Panda, M. F. Parsons, B. Spaun, A. C. Vutha, A. D. West, and E. P. West, "Methods, Analysis, and the Treatment of Systematic Errors for the Electron Electric Dipole Moment Search in Thorium Monoxide," New J. Phys. **19**, 073029 (2016).

[7] M. E. Pospelov and I. B. Khriplovich, "Electric dipole moment of the W boson and the electron in the Kobayashi-Maskawa model," Sov. J. Nucl. Phys. **53**, 638–640 (1991).

[8] M. Pospelov and A. Ritz, "CKM benchmarks for electron electric dipole moment experiments," Phys. Rev. D **89**, 1–7 (2014), arXiv:1311.5537 .

[9] ACME Collaboration, V. Andreev, D. G. Ang, D. DeMille, J. M. Doyle, G. Gabrielse, J. Haefner, N. R. Hutzler, Z. Lasner, C. Meisenhelder, B. R. O'Leary, C. D. Panda, A. D. West, E. P. West, and X. Wu, "Improved limit on the electric dipole moment of the electron," Nature **562**, 355–360 (2018).

[10] C. Cesarotti, Q. Lu, Y. Nakai, A. Parikh, and M. Reece, "Interpreting the Electron EDM Constraint," arXiv (2018), arXiv:1810.07736 .

[11] G. Panico, A. Pomarol, and M. Riembau, "EFT approach to the electron Electric Dipole Moment at the two-loop level," arXiv (2018), arXiv:1810.09413 .

[12] Y. Nakai and M. Reece, "Electric dipole moments in natural supersymmetry," J. High Energy Phys. **2017** (2017).

[13] S. M. Barr, "A review of CP violation in atoms," Int. J. Mod. Phys. A **08**, 209–236 (1993).

[14] M. Pospelov and A. Ritz, "Electric dipole moments as probes of new physics," Ann. Phys. **318**, 119–169 (2005).

[15] J. Engel, M. J. Ramsey-Musolf, and U. van Kolck, "Electric dipole moments of nucleons, nuclei, and atoms: The Standard Model and beyond," Prog. Part. Nucl. Phys. **71**, 21–74 (2013).

[16] W. Bernreuther and M. Suzuki, "The electric dipole moment of the electron," Rev. Mod. Phys. **63**, 313–340 (1991).

[17] R. G. Sachs, *The Physics of Time Reversal*, 1st ed. (University of Chicago Press, London, 1987).

[18] C. S. Wu, E. Ambler, R. W. Hayward, D. D. Hoppes, and R. P. Hudson, "Experimental test of parity conservation in beta decay," Phys. Rev. **105**, 1413–1415 (1957).

[19] J. H. Christenson, J. W. Cronin, V. L. Fitch, and R. Turlay, "Evidence for the 2π Decay of the K_2^0 Meson," Phys. Rev. Lett. **13**, 138–140 (1964).

[20] M. Sozzi, *Discrete Symmetries and CP Violation* (Oxford University Press, New York, USA, 2008).

[21] J. P. Lees, V. Poireau, V. Tisserand, J. Garra Tico, E. Grauges, A. Palano, G. Eigen, B. Stugu, D. N. Brown, L. T. Kerth, Y. G. Kolomensky, G. Lynch, H. Koch, T. Schroeder, D. J. Asgeirsson, C. Hearty, T. S. Mattison, J. A. McKenna, R. Y. So, A. Khan, V. E. Blinov, A. R. Buzykaev, V. P. Druzhinin, V. B. Golubev, E. A. Kravchenko, A. P. Onuchin, S. I. Serednyakov, Y. I. Skovpen, E. P. Solodov, K. Y. Todyshev, A. N. Yushkov, M. Bondioli, D. Kirkby, A. J. Lankford, M. Mandelkern, H. Atmacan, J. W. Gary, F. Liu, O. Long, G. M. Vitug, C. Campagnari, T. M. Hong, D. Kovalskyi, J. D. Richman, C. A. West, A. M. Eisner, J. Kroseberg, W. S. Lockman, A. J. Martinez, B. A. Schumm, A. Seiden, D. S. Chao, C. H. Cheng, B. Echenard, K. T. Flood, D. G. Hitlin, P. Ongmongkolkul, F. C. Porter, A. Y. Rakitin, R. Andreassen, Z. Huard, B. T. Meadows, M. D. Sokoloff, L. Sun, P. C. Bloom, W. T. Ford, A. Gaz, U. Nauenberg, J. G. Smith, S. R. Wagner, R. Ayad, W. H. Toki, B. Spaan, K. R. Schubert, R. Schwierz, D. Bernard, M. Verderi, P. J.

Clark, S. Playfer, D. Bettoni, C. Bozzi, R. Calabrese, G. Cibinetto, E. Fioravanti, I. Garzia, E. Luppi, M. Munerato, L. Piemontese, V. Santoro, R. Baldini-Ferroli, A. Calcaterra, R. De Sangro, G. Finocchiaro, P. Patteri, I. M. Peruzzi, M. Piccolo, M. Rama, A. Zallo, R. Contri, E. Guido, M. Lo Vetere, M. R. Monge, S. Passaggio, C. Patrignani, E. Robutti, B. Bhuyan, V. Prasad, C. L. Lee, M. Morii, A. J. Edwards, A. Adametz, U. Uwer, H. M. Lacker, T. Lueck, P. D. Dauncey, U. Mallik, C. Chen, J. Cochran, W. T. Meyer, S. Prell, A. E. Rubin, A. V. Gritsan, Z. J. Guo, N. Arnaud, M. Davier, D. Derkach, G. Grosdidier, F. Le Diberder, A. M. Lutz, B. Malaescu, P. Roudeau, M. H. Schune, A. Stocchi, G. Wormser, D. J. Lange, D. M. Wright, C. A. Chavez, J. P. Coleman, J. R. Fry, E. Gabathuler, D. E. Hutchcroft, D. J. Payne, C. Touramanis, A. J. Bevan, F. Di Lodovico, R. Sacco, M. Sigamani, G. Cowan, D. N. Brown, C. L. Davis, A. G. Denig, M. Fritsch, W. Gradl, K. Griessinger, A. Hafner, E. Prencipe, R. J. Barlow, G. Jackson, G. D. Lafferty, E. Behn, R. Cenci, B. Hamilton, A. Jawahery, D. A. Roberts, C. Dallapiccola, R. Cowan, D. Dujmic, G. Sciolla, R. Cheaib, D. Lindemann, P. M. Patel, S. H. Robertson, P. Biassoni, N. Neri, F. Palombo, S. Stracka, L. Cremaldi, R. Godang, R. Kroeger, P. Sonnek, D. J. Summers, X. Nguyen, M. Simard, P. Taras, G. De Nardo, D. Monorchio, G. Onorato, C. Sciacca, M. Martinelli, G. Raven, C. P. Jessop, J. M. Losecco, W. F. Wang, K. Honscheid, R. Kass, J. Brau, R. Frey, N. B. Sinev, D. Strom, E. Torrence, E. Feltresi, N. Gagliardi, M. Margoni, M. Morandin, A. Pompili, M. Posocco, M. Rotondo, G. Simi, F. Simonetto, R. Stroili, S. Akar, E. Ben-Haim, M. Bomben, G. R. Bonneaud, H. Briand, G. Calderini, J. Chauveau, O. Hamon, P. Leruste, G. Marchiori, J. Ocariz, S. Sitt, M. Biasini, E. Manoni, S. Pacetti, A. Rossi, C. Angelini, G. Batignani, S. Bettarini, M. Carpinelli, G. Casarosa, A. Cervelli, F. Forti, M. A. Giorgi, A. Lusiani, B. Oberhof, E. Paoloni, A. Perez, G. Rizzo, J. J. Walsh, D. Lopes Pegna, J. Olsen, A. J. Smith, A. V. Telnov, F. Anulli, R. Faccini, F. Ferrarotto, F. Ferroni, M. Gaspero, L. Li Gioi, M. A. Mazzoni, G. Piredda, C. Bünger, O. Grünberg, T. Hartmann, T. Leddig, H. Schröder, C. Voss, R. Waldi, T. Adye, E. O. Olaiya, F. F. Wilson, S. Emery, G. Hamel De Monchenault, G. Vasseur, C. Yèche, D. Aston, D. J. Bard, R. Bartoldus, J. F. Benitez, C. Cartaro, M. R. Convery, J. Dorfan, G. P. Dubois-Felsmann, W. Dunwoodie, M. Ebert, R. C. Field, M. Franco Sevilla, B. G. Fulsom, A. M. Gabareen, M. T. Graham, P. Grenier, C. Hast, W. R. Innes, M. H. Kelsey, P. Kim, M. L. Kocian, D. W. Leith, P. Lewis, B. Lindquist, S. Luitz, V. Luth, H. L. Lynch, D. B. MacFarlane, D. R. Muller, H. Neal, S. Nelson, M. Perl, T. Pulliam, B. N. Ratcliff, A. Roodman, A. A. Salnikov, R. H. Schindler, A. Snyder, D. Su, M. K. Sullivan, J. Va'Vra, A. P. Wagner, W. J. Wisniewski, M. Wittgen, D. H. Wright, H. W. Wulsin, C. C. Young, V. Ziegler, W. Park, M. V. Purohit, R. M. White, J. R. Wilson, A. Randle-Conde, S. J. Sekula, M. Bellis, P. R. Burchat, T. S. Miyashita, E. M. Puccio, M. S. Alam, J. A. Ernst, R. Gorodeisky, N. Guttman, D. R. Peimer, A. Soffer, P. Lund, S. M. Spanier, J. L. Ritchie, A. M. Ruland, R. F. Schwitters, B. C. Wray, J. M. Izen, X. C. Lou, F. Bianchi, D. Gamba, S. Zambito, L. Lanceri, L. Vitale, J. Bernabeu, F. Martinez-Vidal, A. Oyanguren, P. Villanueva-Perez, H. Ahmed, J. Albert, S. Banerjee, F. U. Bernlochner, H. H. Choi, G. J. King, R. Kowalewski, M. J. Lewczuk, I. M. Nugent, J. M. Roney, R. J. Sobie, N. Tasneem,

T. J. Gershon, P. F. Harrison, T. E. Latham, H. R. Band, S. Dasu, Y. Pan, R. Prepost, and S. L. Wu, "Observation of time-reversal violation in the B0 meson system," Phys. Rev. Lett. **109**, 0–7 (2012), arXiv:1207.5832 .

[22] O. W. Greenberg, "*CPT* Violation Implies Violation of Lorentz Invariance," Phys. Rev. Lett. **89**, 231602 (2002).

[23] V. A. Kostelecký and N. Russell, "Data tables for Lorentz and *CPT* violation," Rev. Mod. Phys. **83**, 11–31 (2011).

[24] A. D. Sakharov, "Violation of CP invariance, C asymmetry and baryon asymmetry of the universe," Pisma Zh. Eksp. Teor. Fiz. **5**, 1967 (1967).

[25] N. Cabibbo, "Unitary Symmetry and Leptonic Decays," Phys. Rev. Lett. **10**, 531–533 (1963).

[26] M. Kobayashi and T. Maskawa, "CP-Violation in the Renormalizable Theory of Weak Interaction," Progr. Theor. Phys **49**, 652–657 (1973), arXiv:0403184v2 .

[27] W. Bernreuther, "CP Violation and Bariogenesis," Lect. Notes Phys. **591** (2002).

[28] I. B. Khriplovich and S. K. Lamoreaux, *CP Violation Without Strangeness* (Springer, New York, 1997).

[29] N. Fortson, P. Sandars, and S. Barr, "The search for a permanent electric dipole moment," Phys. Today **56**, 33–39 (2003).

[30] J. M. Pendlebury, S. Afach, N. J. Ayres, C. A. Baker, G. Ban, G. Bison, K. Bodek, M. Burghoff, P. Geltenbort, K. Green, W. C. Griffith, M. van der Grinten, Z. D. Grujić, P. G. Harris, V. Hélaine, P. Iaydjiev, S. N. Ivanov, M. Kasprzak, Y. Kermaidic, K. Kirch, H.-C. Koch, S. Komposch, A. Kozela, J. Krempel, B. Lauss, T. Lefort, Y. Lemière, D. J. R. May, M. Musgrave, O. Naviliat-Cuncic, F. M. Piegsa, G. Pignol, P. N. Prashanth, G. Quéméner, M. Rawlik, D. Rebreyend, J. D. Richardson, D. Ries, S. Roccia, D. Rozpedzik, A. Schnabel, P. Schmidt-Wellenburg, N. Severijns, D. Shiers, J. A. Thorne, A. Weis, O. J. Winston, E. Wursten, J. Zejma, and G. Zsigmond, "Revised experimental upper limit on the electric dipole moment of the neutron," Phys. Rev. D **92**, 92003 (2015).

[31] C. A. Baker, D. D. Doyle, P. Geltenbort, K. Green, M. G. D. van der Grinten, P. G. Harris, P. Iaydjiev, S. N. Ivanov, D. J. R. May, J. M. Pendlebury, J. D. Richardson, D. Shiers, and K. F. Smith, "Improved Experimental Limit on the Electric Dipole Moment of the Neutron," Phys. Rev. Lett. **97**, 131801 (2006).

[32] R. Chislett, "The muon EDM in the g-2 experiment at Fermilab," EPJ Web of Conferences **118**, 01005 (2016), arXiv:arXiv:1701.02807v1 .

[33] B. Graner, Y. Chen, E. G. Lindahl, and B. R. Heckel, "Reduced Limit on the Permanent Electric Dipole Moment of ^{199}Hg," Phys. Rev. Lett. **116**, 161601 (2016).

[34] R. H. Parker, M. R. Dietrich, M. R. Kalita, N. D. Lemke, K. G. Bailey, M. Bishof, J. P. Greene, R. J. Holt, W. Korsch, Z.-T. Lu, P. Mueller, T. P. O'Connor, and J. T. Singh, "First Measurement of the Atomic Electric Dipole Moment of ^{225}Ra," Phys. Rev. Lett. **114**, 233002 (2015).

[35] L. I. Schiff, "Measurability of Nuclear Electric Dipole Moments," Phys. Rev. **132**, 2194–2200 (1963).

[36] E. E. Salpeter, "Some Atomic Effects of an Electronic Electric Dipole Moment," Phys. Rev. **112**, 1642–1648 (1958).

[37] P. G. H. Sandars, "The electric dipole moment of an atom," Phys. Lett. **14**, 194–196 (1965).

[38] E. D. Commins, J. D. Jackson, and D. P. DeMille, "The electric dipole moment of the electron: An intuitive explanation for the evasion of Schiff's theorem," Am. J. Phys. **75**, 532–536 (2007).

[39] M. Denis and T. Fleig, "In search of discrete symmetry violations beyond the standard model: Thorium monoxide reloaded," J. Chem. Phys. **145** (2016).

[40] L. V. Skripnikov, "Combined 4-component and relativistic pseudopotential study of ThO for the electron electric dipole moment search," J .Chem. Phys. **145** (2016).

[41] B. L. Roberts and W. J. Marciano, *Lepton Dipole Moments*, 1st ed. (World Scientific, Singapore, 2009).

[42] V. V. Flambaum, "On Enhancement of the electron Electric Dipole Moments in Heavy Atoms," Sov. J. Nucl. Phys. **24** (1976).

[43] B. C. Regan, E. D. Commins, C. J. Schmidt, and D. DeMille, "New Limit on the Electron Electric Dipole Moment," Phys. Rev. Lett. **88**, 071805 (2002).

[44] D. M. Kara, I. J. Smallman, J. J. Hudson, B. E. Sauer, M. R. Tarbutt, and E. A. Hinds, "Measurement of the electron's electric dipole moment using YbF molecules: Methods and data analysis," New J. Phys. **14** (2012).

[45] D. F. Nelson, A. A. Schupp, R. W. Pidd, and H. R. Crane, "Search for an electric dipole moment of the electron," Phys. Rev. Lett. **2**, 492–495 (1959).

[46] D. Wilkinson and H. Crane, "Precision Measurement of the g Factor of the Free Electron," Phys. Rev. **130**, 852 (1963).

[47] P. Sandars and E. Lipworth, "Electric dipole moment of the cesium atom. A new upper limit to the electric dipole moment of the free electron," Phys. Rev. Lett. **13**, 718–720 (1964).

[48] E. Ensberg, "Experimental Upper Limit for the Permanent Electric Dipole Moment of Rb by Optical-Pumping Techniques," Phys. Rev. **153**, 36–43 (1967).

[49] M. Weisskopf, J. Carrico, H. Gould, E. Lipworth, and T. Stein, "Electric dipole moment of the cesium atom. A new upper limit to the electric dipole moment of the electron," Phys. Rev. Lett. **21**, 1645–1648 (1968).

[50] S. A. Murthy, D. Krause, Z. L. Li, and L. R. Hunter, "New limits on the electron electric dipole moment from cesium," Phys. Rev. Lett. **63**, 965–968 (1989).

[51] M. A. Player and P. G. H. Sandars, "An experiment to search for an electric dipole moment in the 3 P 2 metastable state of xenon," J. Phys. B **3**, 1620–1635 (1970).

[52] S. K. Lamoreaux, J. P. Jacobs, B. R. Heckel, F. J. Raab, and N. Fortson, "New constraints on time-reversal asymmetry from a search for a permanent electric dipole moment of Hg199," Phys. Rev. Lett. **59**, 2275–2278 (1987).

[53] D. Cho, K. Sangster, and E. A. Hinds, "Tenfold Improvement of Limits on T Violation in Thallium Fluoride," Phys. Rev. Lett. **63**, 2559–2562 (1989).

[54] S. B. Ross and H. Gould, "Limit on the Electron Electric Dipole Moment," Phys. Rev. Lett. **65**, 2347–2350 (1990).

[55] D. Commins, B. Ross, and D. Demille, "Improved Experimental Limit on the electric dipole moment of the electron," Phys. Rev. A **50** (1994).

[56] W. B. Cairncross, D. N. Gresh, M. Grau, K. C. Cossel, T. S. Roussy, Y. Ni, Y. Zhou, J. Ye, and E. A. Cornell, "Precision Measurement of the Electron's Electric Dipole Moment Using Trapped Molecular Ions," Phys. Rev. Lett. **119**, 1–5 (2017).

[57] A. C. Vutha, *A search for the electric dipole moment of the electron using thorium monoxide*, Ph.D. thesis, Yale University (2011).

[58] Y. V. Gurevich, *Preliminary Measurements for an Electron EDM Experiment in ThO*, Ph.D. thesis, Harvard University (2012).

[59] N. R. Hutzler, *A New Limit on the Electron Electric Dipole Moment: Beam Production, Data Interpretation, and Systematics*, Ph.D. thesis, Harvard University (2014).

[60] P. W. Hess, *Improving the Limit on the Electron EDM : Data Acquisition and Systematics Studies in the ACME Experiment*, Ph.D. thesis, Harvard University (2014).

[61] B. N. Spaun, *A Ten-Fold Improvement to the Limit of the Electron Electric Dipole Moment*, Ph.D. thesis, Harvard University (2014).

[62] J. M. Brown and A. Carrington, *Rotational Spectroscopy of Diatomic Molecules*, Cambridge Molecular Science (Cambridge University Press, 2003).

[63] A. C. Vutha, W. C. Campbell, Y. V. Gurevich, N. R. Hutzler, M. Parsons, D. Patterson, E. Petrik, B. Spaun, J. M. Doyle, G. Gabrielse, and D. DeMille, "Search for the electric dipole moment of the electron with thorium monoxide," J. Phys. B **43**, 074007 (2010), arXiv:0908.2412 .

[64] S. Bickman, P. Hamilton, Y. Jiang, and D. DeMille, "Preparation and detection of states with simultaneous spin alignment and selectable molecular orientation in PbO," Phys. Rev. A **80**, 023418 (2009).

[65] S. Eckel, P. Hamilton, E. Kirilov, H. W. Smith, and D. DeMille, "Search for the electron electric dipole moment using Ω-doublet levels in PbO," Phys. Rev. A **87**, 1–19 (2013).

[66] E. Kirilov, W. C. Campbell, J. M. Doyle, G. Gabrielse, Y. V. Gurevich, P. W. Hess, N. R. Hutzler, B. R. O'Leary, E. Petrik, B. Spaun, A. C. Vutha, and D. DeMille, "Shot-noise-limited spin measurements in a pulsed molecular beam," Phys. Rev. A **88**, 013844 (2013).

[67] G. Herzberg, *Molecular spectra and molecular structure: spectra of diatomic molecules*, 2nd ed. (Krieger, Malabar, 1989).

[68] A. N. Petrov, L. V. Skripnikov, A. V. Titov, N. R. Hutzler, P. W. Hess, B. R. O'Leary, B. Spaun, D. DeMille, G. Gabrielse, and J. M. Doyle, "Zeeman interaction in ThO $H^3\Delta_1$ for the electron electric-dipole-moment search," Phys. Rev. A **89**, 062505 (2014).

[69] N. R. Hutzler, H. I. Lu, and J. M. Doyle, "The buffer gas beam: An intense, cold, and slow source for atoms and molecules," Chem. Rev. **112**, 4803–4827 (2012).

[70] D. Patterson and J. M. Doyle, "Bright, guided molecular beam with hydrodynamic enhancement," J. Chem. Phys. **126**, 1–6 (2007).

[71] S. E. Maxwell, N. Brahms, R. Decarvalho, D. R. Glenn, J. S. Helton, S. V. Nguyen, D. Patterson, J. Petricka, D. DeMille, and J. M. Doyle, "High-flux beam source for cold, slow atoms or molecules," Phys. Rev. Lett. **95**, 1–4 (2005).

[72] N. R. Hutzler, M. F. Parsons, Y. V. Gurevich, P. W. Hess, E. Petrik, B. Spaun, A. C. Vutha, D. DeMille, G. Gabrielse, and J. M. Doyle, "A cryogenic beam of refractory, chemically reactive molecules with expansion cooling," Phys. Chem. Chem. Phys. **13**, 18976 (2011).

[73] C. D. Panda, B. R. O'Leary, A. D. West, J. Baron, P. W. Hess, C. Hoffman, E. Kirilov, C. B. Overstreet, E. P. West, D. DeMille, J. M. Doyle, and G. Gabrielse, "Stimulated Raman adiabatic passage preparation of a coherent superposition of ThO $H^3\Delta_1$ states for an improved electron electric-dipole-moment measurement," Phys. Rev. A **93**, 1–9 (2016).

[74] H. R. Gray, R. M. Whitley, and C. R. Stroud, "Coherent trapping of atomic populations," Opt. Let. **3**, 218 (1978).

[75] D. L. Kokkin, T. C. Steimle, and D. DeMille, "Branching ratios and radiative lifetimes of the U, L, and I states of thorium oxide," Phys. Rev. A **90**, 062503 (2014).

[76] D. L. Kokkin, T. C. Steimle, and D. DeMille, "Characterization of the $I(|\Omega| = 1) - X\,^1\Sigma^+(0,0)$ band of thorium oxide," Phys. Rev. A **91**, 042508 (2015).

[77] E. Petrik West, *A Thermochemical Cryogenic Buffer Gas Beam Source of ThO for Measuring the Electric Dipole Moment of the Electron*, Ph.D. thesis, Harvard University (2017).

[78] K. Bergmann, H. Theuer, and B. W. Shore, "Coherent population transfer among quantum states of atoms and molecules," Rev. Mod. Phys. **70**, 1003–1023 (1998).

[79] U. Gaubatz, P. Rudecki, S. Schiemann, and K. Bergmann, "Population transfer between molecular vibrational levels by stimulated Raman scattering with partially overlapping laser fields. A new concept and experimental results," J .Chem. Phys. **92**, 5363 (1990).

[80] K.-K. Ni, S. Ospelkaus, M. H. G. de Miranda, A. Pe'er, B. Neyenhuis, J. J. Zirbel, S. Kotochigova, P. S. Julienne, D. S. Jin, and J. Ye, "A high phase-space-density gas of polar molecules." Science **322**, 231–235 (2008).

[81] J. G. Danzl, E. Haller, M. Gustavsson, M. J. Mark, R. Hart, N. Bouloufa, O. Dulieu, H. Ritsch, and H. C. Nagerl, "Quantum gas of deeply bound ground state molecules," Science **321**, 1062–1066 (2008).

[82] A. S. Parkins, P. Marte, P. Zoller, and H. J. Kimble, "Synthesis of arbitrary quantum states via adiabatic transfer of Zeeman coherence," Phys. Rev. Lett. **71**, 3095–3098 (1993).

[83] M. Hennrich, T. Legero, A. Kuhn, and G. Rempe, "Vacuum-stimulated Raman scattering based on adiabatic passage in a high-finesse optical cavity," Phys. Rev. Lett. **85**, 4872–4875 (2000).

[84] J. Sørensen, D. Møller, T. Iversen, J. Thomsen, F. Jensen, P. Staanum, D. Voigt, and M. Drewsen, "Efficient coherent internal state transfer in trapped ions using stimulated Raman adiabatic passage," New J. Phys. **8**, 261 (2006).

[85] D. Møller, J. L. Sørensen, J. B. Thomsen, and M. Drewsen, "Efficient qubit detection using alkaline-earth-metal ions and a double stimulated Raman adiabatic process," Phys. Rev. A **76**, 062321 (2007).

[86] D. Farkas, *An Optical Reference and Frequency Comb for Improved Spectroscopy of Helium*, Ph.D. thesis, Harvard University (2006).

[87] R. W. P. Drever, J. L. Hall, F. V. Kowalski, J. Hough, G. M. Ford, A. J. Munley, and H. Ward, "Laser phase and frequency stabilization using an optical resonator," Appl. Phys. B **31**, 97–105 (1983).

[88] V. Romanenko and L. Yatsenko, "Adiabatic population transfer in the three-level Λ-system: two-photon lineshape," Opt. Commun. **140**, 231–236 (1997).

[89] L. P. Yatsenko, B. W. Shore, and K. Bergmann, "Detrimental consequences of small rapid laser fluctuations on stimulated Raman adiabatic passage," Phys. Rev. A **89**, 013831 (2014).

[90] J. R. Kuklinski, U. Gaubatz, F. T. Hioe, and K. Bergmann, "Adiabatic population transfer in a three-level system driven by delayed laser pulses," Phys. Rev. A **40**, 6741–6744 (1989).

[91] T. Halfmann, T. Rickes, N. V. Vitanov, and K. Bergmann, "Lineshapes in coherent two-photon excitation," Opt. Commun. **220**, 353–359 (2003).

[92] R. W. Nicholls, "Approximate formulas for Franck–Condon factors," J .Chem. Phys. **74**, 6980 (1981).

[93] G. Edvinsson and A. Lagerqvist, "A low-lying $\Omega = 2$ state in the ThO molecule," J. Mol. Spectrosc. **113**, 93–104 (1985).

[94] I. I. Boradjiev and N. V. Vitanov, "Stimulated Raman adiabatic passage with unequal couplings: Beyond two-photon resonance," Phys. Rev. A **81**, 053415 (2010).

[95] M. Stappel, R. Steinborn, D. Kolbe, and J. Walz, "A high power, continuous-wave, single-frequency fiber amplifier at 1091 nm and frequency doubling to 545.5 nm," Laser Phys. **23**, 3866–3871 (2013).

[96] Y. A. L. Iu, R. S. U. Ongtao, P. M. A. Engfei, X. I. W. Ang, H. A. Z. Hang, P. U. Z. Hou, L. S. I. Ei, Y. Liu, R. Su, P. Ma, X. Wang, H. Zhang, P. Zhou, and L. Si, "Maintained fiber amplifiers with wavelength spanning from 1065 to 1090 nm," Appl. Opt. **56**, 4213–4218 (2017).

[97] U. Schunemann, H. Engler, R. Grimm, M. Weidemuller, and M. Zielonkowski, "Simple scheme for tunable frequency offset locking of two lasers," Rev. Sci. Instrum. **70**, 242–243 (1999).

[98] F. Robben, "Noise in the measurement of light with photomultipliers," Appl. Opt. **10**, 776–796 (1971).

[99] B. R. O'Leary, *In search of the electron's electric dipole moment in thorium monoxide: An improved upper limit, systematic error models, and apparatus upgrades*, Ph.D. thesis, Yale University (2017).

[100] A. D. West, Z. Lasner, D. Demille, E. P. West, C. D. Panda, J. M. Doyle, G. Gabrielse, A. Kryskow, and C. Mitchell, "An underappreciated radiation hazard from high voltage electrodes in vacuum," Health Phys. **112**, 33–41 (2017), arXiv:1607.01389 .

[101] V. Andreev, C. D. Panda, P. W. Hess, B. Spaun, and G. Gabrielse, "A self-calibrating polarimeter to measure Stokes parameters," (2017), arXiv:1703.00963 .

[102] C. Abel, N. J. Ayres, G. Ban, G. Bison, K. Bodek, V. Bondar, M. Daum, M. Fairbairn, V. V. Flambaum, P. Geltenbort, K. Green, W. C. Griffith, M. Van Der Grinten, Z. D. Grujić, P. G. Harris, N. Hild, P. Iaydjiev, S. N. Ivanov, M. Kasprzak, Y. Kermaidic, K. Kirch, H. C. Koch, S. Komposch, P. A. Koss, A. Kozela, J. Krempel, B. Lauss, T. Lefort, Y. Lemiére, D. J. Marsh, P. Mohanmurthy, A. Mtchedlishvili, M. Musgrave, F. M. Piegsa, G. Pignol, M. Rawlik, D. Rebreyend, D. Ries, S. Roccia, D. Rozp dzik, P. Schmidt-Wellenburg, N. Severijns, D. Shiers, Y. V. Stadnik, A. Weis, E. Wursten, J. Zejma, and G. Zsigmond, "Search for axionlike dark matter through nuclear spin precession in electric and magnetic fields," Phys. Rev. X **7**, 1–9 (2017), arXiv:1708.06367 .

[103] T. Ruf, "The Lomb-Scargle periodogram in biological rhythm research: analysis of incomplete and inequally spaced time-series," Biol. Rhythm Res. **30**, 178–201 (1999).

[104] N. R. Lomb, "Least-squares frequency analysis of unequally spaced data," Astrophys. Space Sci. **39**, 447–462 (1976).

[105] J. D. Scargle, "Studies in astronomical time series analysis," Astrophys. J. **263**, 835–853 (1982).

[106] J. H. Horne and S. L. Baliunas, "A prescription for period analysis of unevenly sampled time series," Astrophys. J **302**, 757–763 (1986).

[107] P. J. Huber, "Robust Estimation of a Location Parameter," Ann. Math. Stat. **35**, 73–101 (1964).

[108] B. Efron, "Bootstrap Methods: Another Look at the Jackknife," Ann. Stat. **7**, 1–26 (1979).

[109] B. Efron and R. Tibshirani, "Bootstrap Methods for Standard Errors, Confidence Intervals, and Other Measures of Statistical Accuracy," Stat. Sci. **1**, 54–75 (1986).

[110] N. R. Draper and H. Smith, *Applied Regression Analysis*, 3rd ed. (John Wiley Sons, 1998).

[111] J. F. Kenney and E. S. Keeping, *Mathematics of Statistics: Part One*, 4th ed. (Chapman Hall, LTD., London, 1954) p. 221.

[112] W. C. Griffith, M. D. Swallows, T. H. Loftus, M. V. Romalis, B. R. Heckel, and E. N. Fortson, "Improved limit on the permanent electric dipole moment of Hg199," Phys. Rev. Lett. **102**, 1–4 (2009).

[113] N. A. Robertson, J. R. Blackwood, S. Buchman, R. L. Byer, J. Camp, D. Gill, J. Hanson, S. Williams, and P. Zhou, "Kelvin probe measurements: Investigations of the patch effect with applications to ST-7 and LISA," Class. Quantum Grav. **23**, 2665–2680 (2006).

[114] G. J. Feldman and R. D. Cousins, "Unified approach to the classical statistical analysis of small signals," Phys. Rev. D **57**, 3873–3889 (1998), arXiv:9711021 .

[115] J. J. Hudson, D. M. Kara, I. J. Smallman, B. E. Sauer, M. R. Tarbutt, and E. A. Hinds, "Improved measurement of the shape of the electron." Nature **473**, 493–496 (2011).

[116] M. G. Kozlov and L. N. Labzowsky, "Parity violation effects in diatomic molecules," J. Phys. B **28**, 1933–1961 (1995).

[117] V. A. Dzuba, V. V. Flambaum, and C. Harabati, "Relations between matrix elements of different weak interactions and interpretation of the parity-nonconserving and electron electric-dipole-moment measurements in atoms and molecules," Phys. Rev. A **84**, 1–9 (2011).

[118] V. Andreev, *Polarimetry on the Advanced Cold Molecule Electron Electric Dipole Moment Experiment* (Masters Thesis, Technische Universitat Munchen, 2016).

Colophon

This thesis was typeset using LaTeX, originally developed by Leslie Lamport and based on Donald Knuth's TeX. The formatting for this thesis is adapted from a template released under the permissive MIT (X11) license that be found online at github.com/suchow/ or from the author at suchow@post.harvard.edu.